Mathematical Modelling and Stability Analysis for Grid-Connected Cascaded H-bridge Converter

Xiaoyi Bai

Submitted to the University of Nottingham for the Degree of Doctor of Philosophy,
September 2018.

Abstract

When power converters are employed to connect the renewable power resources to the grid, the grid inductance can typically be quite significant because wind farms and solar power stations are located far away from the converters. The non-negligible grid inductance interacts with the Phase Locked Loop (PLL) which is assisting the grid side current controller with the phase angle of grid voltage and furthermore interacts with the DC-link voltage controller. It is known that the inductance of the grid side transmission line would distort the input voltage of PLL at the point of common coupling and this interference can even lead to the instability of the converter operation. However, the accurate prediction of the stability thresholds of the PLL configuration related to the grid inductance was missing which requires advanced modelling techniques.

The key technique is a new mathematical approach to calculating the spectra, which is more sophisticated and more flexible than existing methods. The Harmonic Balance Technique is powerful for modelling the steady state of the periodic waveform and is already a sophisticated technique in other fields but occasionally adopted on power electronics. This study aims to adopt this modelling approach to obtain a detailed description of the operation of the converter steady state thus the stability of its steady state can be investigated.

The stability analysis is conducted for the periodic steady state employing the Floquet theorem. The stability analysis indicates that for a single-phase grid-connected cascaded H-bridge rectifier, the interactions between control loops and PLL can be affected by grid side inductance, and their interactions can even lead to instability of the system. Notably, the instability boundaries are predicted for PLL bandwidth about three different grid strengths. These thresholds have been verified with both simulation and experimental results.

Acknowledgements

Firstly, I would also like to thank Dr Alan Watson for being my internal assessor and Dr Alessandro Lidozzi for being my external examiner and for sparing their time on this work.

Secondly, I would like to thank the University of Nottingham for the scholarship for my PhD. Likewise, I want to give my sincere gratitude to my supervisors Prof. Zanchetta Pericle and Dr Stephen Cox for their guidance and patience throughout this work.

Moreover, I feel deeply indebted to my dear Mom and Dad. Your love is the endless power to me, and also you were financially supporting me during PhD. I know these years have been trying for you, too. My sincere gratitude is beyond the words' description.

Last but not the least, thanks also give to colleagues I've had in PEMC group at the University of Nottingham. Thank for making my life fun. I enjoyed all the technical discussions and all the parties in the group, and I wish we can cross paths again and keep working together in the future.

List of Terms

CHB - Cascaded H-Bridge

CPL - Constant Power Load

CE - Chip Enable

CCS - Code Composer Studio

CPU - Central Processing Unit

DCC - Diode Clamped Converter

DBC - Dead Beat Controller

DSK - DSP Starter Kit

DSP - Digital Signal Processor

DAB - Dual Active Bridge

ESR - Equivalent Series Resistance

EMIF - External Memory Interface

EMI - Electromagnetic Interference

EMC - Electromagnetic Compliance

FCC - Flying Capacitor Converter

FPGA - Field Programmable Gate Array

FACTS - Flexible AC Transmission

GPC - Generalized Predictive Controller

HBT - Harmonic Balancing Technique

HPI - Host Port Interface

HVDC - High Voltage Direct Current

IGBT - Insulated-Gate Bipolar Transistor

LTP - Linear Time Periodic

LSC-PWM - Level Shifted Carrier PWM

MC - Multilevel Converter

MMC, M2LC - Modular Multilevel Converter

MPC - Model Predictive Controller

MATLAB - Matrix Laboratory (Simulation Software)

NPC - Neutral Point Converter

NLTP - Non-linear Time Periodic

ODE - Ordinary Differential Equation

PI - Proportional plus Integral

PR - Proportional Resonant

PCC - Point of Common Coupling

PSC-PWM - Phase Shifted Carrier PWM

PLECS - Piecewise Linear Electrical Circuit Simulation

PCB - Printed Circuit Board

PVS - Precision Voltage Source

PLL - Phase Locked Loop

SOGI - Second Order Generalised Integrator

SM - Sub-Module

SHE-PWM - Selective Harmonic Elimination

SVM - Space Vector Modulation

SPWM - Sinusoidal PWM

STATCOM - Static Var Compensation

SST - Solid State Transformer

THD - Total Harmonic Distortion

TFS - Truncated Fourier Series

TI - Texas Instrument

UNIFLEX-PM - Universal and Flexible Power Management

C_n - n_{th} cell DC side capacitor

I_L - Supply Current

I_{dc} - H-Bridge DC Side Current

I_R - H-Bridge DC Side Load Current

I_C - H-Bridge DC Side Capacitor Current

k_p - Proportional Coefficient of PI (Total DC voltage)

k_i - Integral Coefficient of PI (Total DC voltage)

$k_p^{'}$ - Proportional Coefficient of PI (PLL)

$k_i^{'}$ - Integral Coefficient of PI (PLL)

L - Line Inductance

m - Modulating Signal

N - Number of H-bridge cells per phase

r - Line inductance ESR

R_n - n_{th} Cell DC Side Load Resistance

T_s - Sampling time

U - Output of PI controller

$V_{Cn}(n = 1, 2, 3)$ - DC Link Capacitor Voltage of n_{th} Cell

V_C - Total DC Link Capacitor Voltage

V_{CONV} - Converter AC Side Applied Voltage

V_S - Supply Voltage

V_{spk} - Peak Supply Voltage

Contents

1 Introductions **22**

1.1 Background Introduction 22

1.2 Mathematical Modelling Overview 26

1.2.1 Switching and Averaged Model 27

1.2.2 Perturbation Theory 27

1.2.3 Harmonic Balance Technique 28

1.3 Stability Analysis Overview 29

1.3.1 Stable, Unstable and Asymptotically Stable 30

1.3.2 Stability of Linear System 32

1.3.2.1 Solution of Linear Dynamic System 32

1.3.2.2 Phase Portrait 34

1.3.3 Stability of Non-linear System 35

1.3.3.1 Linearisation Technique 35

1.3.3.2 Bifurcation Map 37

1.4 Contribution to Knowledge 38

1.5 Thesis Plan 38

1.6 Summary 40

2 Multilevel Converters 42

2.1 Multilevel Topologies 42

2.1.1 Diode Clamped Converter 45

2.1.2 Flying Capacitor Converter 45

2.1.3 Cascaded H-bridge Converter 45

2.1.4 Modular Multilevel Converter 46

2.2 Modulation Strategies for Multilevel Converters 47

2.2.1 Sinusoidal PWM 48

2.2.1.1 Level Shifted Carrier PWM Modulation 48

2.2.1.2 Phase Shifted Carrier PWM Modulation 49

2.2.2 Selective Harmonic Elimination PWM 50

2.2.3 Space Vector PWM 51

2.2.4 Summary of Modulating Methods 51

2.3 Applications of Multilevel Converters 51

2.3.1 Reactive Power Compensation 52

2.3.2 Solid State Transformer 53

2.3.3 Comparison of Topologies and Modulation Strategies 53

2.4 Converter Structure Proposed in This Thesis 54

2.5 Summary 60

3 Control Design of Cascaded H-bridge Converter 61

3.1 Introduction 61

3.2 Overall Control Scheme Applied for Single-Phase CHB Rectifier . . . 64

3.3 Proportional-Integral (PI) Voltage Controller Design 65

3.3.1 Plant Transfer Function 66

3.3.2 PI Parameters Tuning 67

3.4 Deadbeat Current Controller Design 70

3.4.1 Phase-Locked Loop 70

3.4.2 Deadbeat Control Law Derivation 73

3.4.3 Simulation Results of Control Scheme 77

3.5 Summary 79

4 Stability Analysis of Buck Converter with Constant Power Load 80

4.1 Introduction 80

4.2 System Description 81

4.2.1 System Averaged Model 82

4.3 Stability of Equilibrium Point and *Hopf Bifurcation* 83

4.3.1 Equilibrium Point and Eigenvalues 83

4.3.2 Eigenvalue Observations and *Hopf Bifurcation* 84

4.4 Mathematical Weakly Non-linear Method 90

4.4.1 At the leading order $O(\varepsilon^0)$ 91

4.4.2 At $O(\varepsilon)$ order 92

4.4.3 At $O(\varepsilon^2)$order 93

4.4.4 At $O(\varepsilon^3)$ order 94

4.4.5 Composite Perturbation Solution 97

4.4.6 Limit Cycle Size 97

4.5 Summary 100

5 Mathematical Modelling for Cascaded H-bridge Converter 101

5.1 Open Loop Modelling 103

5.1.1 Converter Averaged Model 103

5.1.2 Voltage and Current Spectra 106

5.1.2.1 State Variables Assumption 106

5.1.2.2 Input Signals Assumption 107

5.1.2.3 Harmonic Balance Method 107

5.2 Closed Loop Modelling with Simplified Control Scheme 110

5.2.1 Closed Loop Averaged Model 110

5.2.2 Steady State Model 111

5.2.2.1 Steady State Derivations 112

5.2.2.2 *Bifurcation* of Solutions 113

5.2.2.3 Steady State Solutions 116

5.2.3 Models Validation 116

5.3 Modelling for Weak Grid 118

5.3.1 System Equations 118

5.3.2 Steady State Operation Modelling 120

5.4 Summary 125

6 Stability of Controlled Multilevel Cascaded H-bridge Converter 126

6.1 Introduction of the Floquet's Theorem 127

6.2 Stability Analysis of the Simplified Closed Loop 129

6.2.1 Linearisation of System Governing Equations 129

6.2.2 Stability Analysis of the Simplified Model 130

6.2.3 Evaluate the Eigenvalues and Decide Stability 130

6.3 Stability Analysis of the Full System 138

6.3.1 The Effect of PI Bandwidth on Stability 139

6.3.2 The Effect of Grid Strength and PLL Bandwidth On Stability 139

6.4 Simulation Verification of the Parametric Thresholds 143

6.4.1 The Verification of PI Bandwidth Stability-Threshold 143

6.4.2 The Verification of Grid Strength and PLL Bandwidth Stability-Threshold 143

6.5 Summary 149

7 Converter Hardware Design and Practical Control Implementation 150

7.1 Overall Rig Structure 150

7.2 Converter Design 153

7.2.1 IGBT Module 153

7.2.2 Gate Drive Board 153

7.2.3 Dead Time Circuit 155

7.3 Transducers 155

7.4 Passive Components 157

7.4.1 Line Inductance Selection 157

7.4.2 DC Capacitor Selection 158

7.5 FPGA/DSP Control Platform 159

7.6 Summary 162

8 Experimental Validations **163**

8.1 Introduction 163

8.2 Stable Operation of the System Experimental Results 164

8.3 Experiment Results of the Unstable Operation of the System 169

8.3.1 The Experimental Results Showing Effect of Voltage PI Bandwidth on the Stability of the Closed-loop System 170

8.3.2 The Experimental Results Showing Effect of Grid Strength and PLL Bandwidth on the Stability of the Closed-loop System . . 170

8.4 Summary 177

9 Conclusions **178**

9.1 Summary of Achievements 180

9.2 Further Work 181

A Matlab Codes For Buck CPL **197**

B Matlab Scripts For CHB (Simplified Model) **202**

C Matlab Scripts of the Full Model **210**

List of Figures

1.3.1 Illustration of the definition of stability[36] 31

1.3.2 Illustration of the definition of asymptotic stability [36] 31

1.3.3 Responses of linear dynamic systems 33

1.3.4 Stability classification of fixed points 35

1.3.5 General stability analysis method 36

2.1.1 One phase leg of an inverter with (a) two levels, (b) three levels, (c) n levels. 43

2.1.2 Basic topology of multilevel converters. (a) Three-level neutral-point inverter (b) Three-level "Flying"-capacitor inverter (c) Three-level cascaded H-bridge inverter. 44

2.1.3 Three-phase five-level topology for a cascaded H-Bridge inverter . . . 46

2.1.4 Three-phase Modular Multilevel Converter (MMC) schematic 47

2.2.1 Classification of multilevel converter modulation methodologies 48

2.2.2 Level-shifted PWM modulation implementation for the five-level cascaded H-bridge converter (Frequency=500Hz, MI=0.5) 49

2.2.3 Phase-shifted PWM modulation implementation for the five-level cascaded H-bridge converter.(Frequency=500Hz, MI=0.5) 50

2.3.1 Phaser diagram for reactive power compensation 52

2.4.1 Schematic of a single-phase three-cell CHB rectifier 54

2.4.2 Phase-shifted PWM modulation implementation for the 7-level cascaded H-bridge converter 55

2.4.3 Switching signals generated based on the PSCPWM for 7-level CHB . 56

2.4.4 The switching function of an H-bridge cell for describing its operating states 57

2.4.5 Modulated voltages produced by the converter (Switching frequency=2kHz, MI=0.5 58

2.4.6 Overlaid AC and DC side current of CHB converter by applying PSC-PWM 59

2.4.7 Zoomed-in part of Fig.2.4.6 showing phase-shifted DC currents 60

3.1.1 Stationary reference frame control strategy with global DC-link control[88] 62

3.1.2 Natural reference frame control strategy with DC-link voltage control per phase[88] 63

3.2.1 Schematic of overall control scheme applied in this work 64

3.3.1 Block diagram regarding DC-link voltage control 65

3.3.2 Schematic of H-bridge DC side 66

3.3.3 Step response of the closed-loop PI control system of the DC-link voltage 68

3.3.4 Bode plot of the open-loop control system for controlling DC-link voltage 69

3.4.1 Three-phase PLL structure[94] 70

3.4.2 Single-phase PLL structure 71

3.4.3 Simulation results of the single-phase phase-locked loop 73

3.4.4 AC side of the rectifier schematic 74

3.4.5 Block diagram of deadbeat control methodology applied for the single-phase CHB rectifier 76

3.4.6 Simulation results of the current deadbeat controller 78

4.2.1 Voltage-current characteristic of CPL 81

4.2.2 Topology of a buck converter with a CPL load 82

4.2.3 Two working modes of the buck converter 82

4.3.1 Locus of the complex eigenvalue pair corresponding to Table.4.3 . . . 87

4.3.2 Effect of eigenvalues on system responses and phase portrait 88

4.3.3 Illustration of limit cycle 89

4.3.4 Limit cycle 89

4.3.5 3D view of the *Hopf Bifurcation* 90

4.4.1 Comparison of the exact solution by solving system ODEs with the solution by using perturbation method 98

4.4.2 Comparison of the exact solution by solving system ODEs with the solution by using perturbation method 99

4.4.3 Size of limit cycle 99

5.0.1 Schematic of CHB rectifier connected to weak grid 103

5.1.1 Comparison of switching model and averaged model for the open-loop operating CHB rectifier. 105

5.1.2 Comparison of harmonic amplitudes from analytical solution (MATLAB) and simulation FFT results (PLECS) 109

5.2.1 Solutions of the quadratic equation. 114

5.2.2 Bifurcation map regarding four system parameters 115

5.2.3 Comparison of close loop operation system response of switching model (PLECS simulation), averaged model built with simplified control scheme, and steady state model derived from the simplified averaged model. . 117

5.3.1 Comparison of seven state variables responses of averaged model and truncated model 123

5.3.2 Model compare of switching model, averaged model and steady state model for converter connected to weak grid. 124

6.2.1 System eigenvalue maps regarding four essential parameters 133

6.2.2 Time responses of under and above V_{S1} threshold showing stable and unstable converter operations 134

6.2.3 Time responses of under and above V_{ref} threshold showing stable and unstable converter operations 135

6.2.4 Time responses of under and above R threshold showing stable and unstable converter operations 136

6.2.5 Time responses of under and above r threshold showing stable and unstable converter operations 137

6.3.1 Eigenvalue map with increasing bandwidth of the DC-link PI controller from 50 Hz to 80 Hz. 140

6.3.2 Eigenvalue maps of varying PLL bandwidth regarding different grid strength. 142

6.4.1 Simulated time response of CHB converter operation with varying PI bandwidth condition 145

6.4.2 Simulated time response of CHB converter operation of varying PLL bandwidths when $L_S = 0$ 146

6.4.3 Simulated time response of CHB converter operation of varying PLL bandwidth when $L_S = 3$ mH 147

6.4.4 Simulated time response of CHB converter operation of varying PLL bandwidth when $L_S = 6$ mH. 148

7.1.1 Overview of experiment set-up 151

7.1.2 Functional block diagram of hardware subsystems 152

7.1.3 Photo of rig 152

7.2.1 SEMIKRON SK30GH123 (a)power module and (b)pin configuration . 153

7.2.2 Highlight of the gate drive circuit 154

7.2.3 Dead time circuit 155

7.3.1 Voltage transducer LV-25P connection 156

7.5.1 Schematic of hardware control platform 160

7.5.2 Digital implementation of dead beat control 161

8.2.1 Experiment start-up waveforms 164

8.2.2 Steady-state experimental DC-link voltages. 166

8.2.3 Results of current control: current reference and measured current when connected to a strong grid. 167

8.2.4 Waveform of converter applied voltage under strong grid condition. . 168

8.2.5 Output of PLL when CHB connected to strong grid 168

8.3.1 Experimental results of CHB converter operation time response with varying PI bandwidth, for verifying the analysed PI bandwidth instability threshold 173

8.3.2 Experimental results of CHB converter operation time response with varying PLL bandwidth when grid inductance is negligible, for verifying the analysed PLL bandwidth instability threshold when grid inductance is negligible 174

8.3.3 Experimental results of CHB converter operation time response with varying PLL bandwidth when $L_S = 3$ mH, for verifying the analysed PLL bandwidth instability threshold when $L_S = 3$ mH 175

8.3.4 Experimental results of CHB converter operation time response with varying PLL bandwidth when $L_S = 6$ mH, for verifying the analysed PLL bandwidth instability threshold when $L_S = 6$ mH 176

List of Tables

1.1 How eigenvalues decide system response 33

2.1 Comparison of power component requirements per phase leg among three multilevel converters 54

2.2 Possible voltage levels of a three-cell CHB converter consists of the output AC terminal three-level voltage 58

3.1 PI coefficient values for different bandwidths of the DC-link voltage controller 69

3.2 PI controller coefficient values for different bandwidths within the PLL structure 72

4.1 System parameters 85

4.2 Some important results corresponding to parameters set in Table 4.1 85

4.3 Eigenvalue showing dependence on P_L 86

5.1 Open loop configurations 106

5.2 Closed loop configurations 122

6.1 Eigenvalues of the closed-loop system with varying PLL bandwidths when the converter is connected to the ideal grid 141

6.2 Eigenvalues of the closed-loop system with varying PLL bandwidths when L_S equals 3 mH. 141

6.3 Eigenvalues of the closed-loop system with varying PLL bandwidths when L_S equals 6 mH 141

8.1 IGBT Module SK30GH123 169

Chapter 1

Introductions

1.1 Background Introduction

Power electronic systems rely on both power converter and control scheme to fulfil their functions. Power converters are normally stable by themselves due to the constraints design and constructions. However, when they are connected to various kinds of sources and loads, their operating conditions may be affected and even leading to instability. Therefore the active control is usually applied to the converters to enhance their functionalities under the requirements, but the control can, in turn, worsen the stability of the power converter. Meanwhile, there are cases that electrical engineers tend to design their controller parameters rigorously. For example, when tuning a classic PI controller or implementing a predictive controller, one might still need to adjust the calculated parameters on some extent to achieve superior performance of the controller. However, the tuning process is carried out without knowing precisely where the stability boundaries for the parameters are. The fuzzy control parameter design can even cause new stability issues to the system. Hence an exact prediction of the parameter stable boundaries is needed.

Voltage-Sourced Converters (VSC) is a commonly applied class of converters in power

systems nowadays. They have been widely used in the interfacing the renewable energies with the grid[1][2]. Multilevel converters are an advanced family among VSCs and are commonly used in High-Voltage Direct-Current (HVDC) applications[3][4], Flexible AC Transmission Systems (FACTS)[5] and since modular approach can be used to meet the high voltage and high current requirements. Cascaded H-bridge converter which is considered in this thesis is an emerging multilevel topology in medium or high voltage and high power applications [6], such as VAR compensation [7], photovoltaic [8] and wind power integrating, or Solid State Transformer (SST) [9].

This thesis mainly considers when CHB converters used in the distributed systems, the Distributed Energy Resources (DER) or Distributed Energy Storages (DES) such as wind farms and solar generation resources are normally located far away from the load centres, thus the transmission line can be in the long distance. As a result, the grid side impedance is big and can not be ignored leading to the VSCs connected to the weak grid. It is known that the Phase Locked Loop (PLL) is strongly affected by the grid strength and even is likely to cause the instability of the system[10][11][12].

The stability analysis for multilevel converters can be justified by applying Lyapunov stability criterion. For instance, in [13] an open-loop controller using an estimation of steady-state solutions of the dynamic equations was applied to a modular multilevel converter. The controller was proved to be effective. And the stability of the system is based on Lyapunov theory, a rigorous way that proves when the open loop strategy is used, the system becomes globally asymptotically stable, without any special restrictions of parameter values.

The stability analysis can also be conducted in a phasor-based framework so that the system can be regarded as time-invariant. For example, in [14] also a modular multilevel converter was being studied. The MMC was vector-controlled and the stability analysis of fundamental frequency phasor-based averaged model can be conducted in a traditional linear time-invariant framework through eigenvalue computation. However, the gain parameter of the circulating current controller can affect the system

stability. This leads to the requirements of linear time-periodic modelling technique.

It can be observed that the modelling process is either conducted in *dq* reference frame so the variables are all DC quantities, or the stability analysis is conducted rigorously without an accurate model of the system *dq* reference frame is not applicable for certain systems. In these literatures, there lacking an accurate method of system modelling. Meanwhile, techniques such as converting to *dq* reference frame or using phasors are possible solutions. Each of them has its advantages and applications but also has their limitations [15]. For instance, the *dq* reference frame cannot be applied when connected to an asymmetrical three-phase or a single-phase grid. As a result, it is necessary to have a precise way of modelling using more advanced mathematical tools.

In this thesis, the *harmonic linearisation technique* will be applied to the cascaded H-bridge system to obtain the time-periodic steady state formula. And the stability analysis will be conducted from this time-periodic model. Since the steady-state trajectory is known, upon linearisation, a linear time-periodic model is derived from the averaged model. Then the *Floquet theory* will be applied to justify the stability of the CHB system. Floquet theory has been a powerful tool of analysing the stability of linear time-periodic systems. The *Floquet multipliers* are indicative of system instability corresponding to system parameters. It has also been applied to other power systems and some prove that Floquet theory is more accurate than traditional methods.

In [16], Floquet theory has been applied to analyse the stability of non-linear composite right left-handed transmission lines. Based on the values of the Floquet multipliers, different bifurcation mechanisms can be identified. It was shown that the transmission line can be rigorously analysed using Floquet and bifurcation theories. The link between parametric generation and system instability suggests that non-linear system theory is a valuable tool necessary for investigating such systems where non-linearity can be substantial.

In [17] the stability of the grid-connected inverter with LCL-filter has been conducted by applying Floquet theory. The resonance of the LCL-filter can lead to the instability of such a system, the damping resistor within the LCL-filter is normally designed with reference to the Routh-Hurwitz stability criterion. In this work harmonic balance technique was applied to get an approximate model of the inverter. The stability is conveyed according to the Floquet theory. The results have shown that the resistance obtained by the novel analysis is more practical than the resistance got by Routh-Hurwitz stability criterion. Because in practice, the resistance should be bigger than the designed value (based on the Routh-Hurwitz stability criterion) to make the inverter stable and reliable, but the resistance obtained by Floquet theory is more practical.

These provided methods will be applied to the cascaded H-bridge converter system, whose stability is a very important issue in many application fields. The focus will be on the stability analysis of the multilevel cascaded H-bridge converter with power control on both AC source and DC load sides. The equations for the closed loop would be a non-linear time periodic system, which is more complicated than the linear time-invariant system that is usually dealt with in the classic control.

The steady state stability analysis contains two steps: 1) establishing the mathematical model of the steady-state operation and 2) judging if this steady state is stable or not. In this chapter, in the first section, a number of mathematical modelling methods which can be applied to power electronic systems will be reviewed. The general switching model and averaged model will be first introduced in section 1.2.1. A more powerful modelling tool by applying perturbation series suitable for modelling DC power systems will be proposed in section 1.2.2. Then the methods can be used for AC time-periodic systems will be brought in another advanced harmonic balance modelling technique in section 1.2.3.

In the second section, the methods to justify the stable and unstable operation of a system will be reviewed firstly from the perspective of Lyapunov. Stability for the linear dynamic system will then be analysed and stability of the non-linear system

can be studied locally around an equilibrium by applying linearisation technique and some aided graphical tools such as phase portrait and bifurcation map. Finally, for time-periodic system, its stability can be investigated by using a Floquet theory, the application of the Floquet theory for studying the stability of time-periodic systems will be briefly literature reviewed.

1.2 Mathematical Modelling Overview

The initial step of mathematical modelling is using differential equations to describe the system since almost all the physical activities in nature can be described by differential equations [18]. Particularly for power electronic systems, the state variables are typically chosen to be the properties of energy storage components in the circuit, such as the voltage across the capacitor or the current flows through the inductor.

The simplest model may be encountered for power electronic systems is the linear time-invariant systems that are often dealt with in classic control theory. However, power electronic systems are abundant in non-linear dynamic behaviours due to the cyclic switching of circuit topologies [19] as a result of applying the PWM modulation. Thus they are regarded as *piece-wise* linear systems. Besides, many power electronic systems are time-periodic. Thus it requires more advanced approaches for both modelling and stability.

In classic control theory, a single input single output(SISO) linear system is described by a transfer function, and then it is easy to apply Routh-Hurwitz stability criteria [20, 21, 22] and Nyquist stability[23, 24, 25] to decide the stability. Nyquist is an even more commonly used technique since it can not only decide the stability but also tell where to improve the stability [26]. However, these methods don't apply for non-linear and time-variant systems.

1.2.1 Switching and Averaged Model

Many different modelling techniques have been established in literature[27]. The first one to be discussed is the *switching model* which can be obtained by directly applying Kirchhoff's Laws to the electronic circuit, the state variables in the switching model are all instantaneous values, which is the most fundamental way of modelling, switching model describes precisely the behaviour of the electronic system and can be applied to almost any power electronic system.

Another more commonly used model is the *average model*, which is derived from the switching model by ignoring the high frequency switching details. It describes the relationship of input and output of the converter more simply than switching model. It should also be noted that the averaged model is only valid when the system remains in continuous mode, and the switching frequency is relatively high.

The averaged model generally allows one to locate slow instabilities, while fast instabilities require the switching model.

1.2.2 Perturbation Theory

A more advanced method called *weakly non-linear perturbation* can thus be applied for studying the detailed behaviour of the system when close to losing stability. Perturbation theory is applicable if the problem at hand cannot be solved exactly but can be formulated by adding a small term to the mathematical description of the exactly solvable problem or the problem naturally possesses a small parameter[28][29][30]. It comprises mathematical methods for finding an approximate solution to a problem, by starting from the exact solution of a related, simpler problem.

Perturbation theory leads to an expression for the desired solution in the form of a power series in some "small" parameter - known as perturbation series - that quantifies the deviation from the exactly solvable problem. Formally, we have for the

approximation to the full solution $\mathbf{x}$, a series in the small parameter (here called ε), like the following:

$$\mathbf{x} = \mathbf{x}_0 + \varepsilon^1 \mathbf{x}_1 + \varepsilon^2 \mathbf{x}_2 ...$$

The leading term in this power series is the solution of the exactly solvable problem, namely the equilibrium point. The higher order terms describe the deviation in the solution, may be found iteratively by some systematic procedures, these higher order terms in the series become successively smaller.

By solving the higher terms around the equilibrium point, the more detailed information can be revealed. For example, in chapter 4 of buck converter with constant power load case study, the system losses its stability via a limit cycle becoming unstable from stable. We will show that by applying the perturbation theory, the size of the limit cycle can be calculated.

1.2.3 Harmonic Balance Technique

Harmonic Balance Technique (HBT) is another advanced technique for modelling time-periodic systems by capturing the harmonic spectra of the harmonic order of interest. It was introduced to analyse low-frequency electromagnetic field problems in the later 1980's[31]. The HBT is used in the electrical system such as analysing the nonlinear electromagnetic field for DC biased HVDC transformer[32] but have seldom been applied for power electronics.

HBT method is robust for determining the periodic steady-state. It models the power electronic converter in the frequency domain based on the knowledge that according to the Fourier theorem any periodic signal is made up of sinusoidal signals at various frequencies and magnitudes.

The technique is conceptually simple, by making the assumptions that all periodic state variables are in the form of truncated Fourier series, exciting the system under-

studied with harmonic perturbations, collecting the variables of interest, and extracting the corresponding components at the perturbation frequency by the harmonic balance principle.

The HBT method will be applied for the CHB converter to mathematically model the converter both in open-loop and closed-loop operation for steady-state operation. The validation of the method will be verified by comparing the magnitudes of dominant harmonics found by analysis and the FFT results of simulation of the exact model.

1.3 Stability Analysis Overview

Stability is especially important for control systems, an unstable control system cannot fulfil its task and has the potential danger as well. Hence it is a vital task of how to judge a system whether it's stable or unstable and how to improve its stability. Generally speaking, if a system starts working from one expected operating condition, and it can always keep working close to that operating point when it's perturbed by some small quantity perturbations, we say that this system is stable, otherwise, it is unstable.

Linear systems can be classified into time-invariant and time-variant systems. Similarly, a non-linear system is called *autonomous* system if it only contains the time-dependent variables but the coefficients do not explicitly depend on the time variable t, otherwise it is called *non-autonomous* system. The difference between the an autonomous system and non-autonomous system is that the states of autonomous systems are independent of time, but for the non-autonomous system the start time needs to be considered when performing stability analysis.

1.3.1 Stable, Unstable and Asymptotically Stable

Since 1892 a Russian mathematician Aleksandr Lyapunov published his book *The General Problem of Stability of Motion* [33], his method of studying stability problem became the most applicable and important one for the non-linear system.

Consider an autonomous system

$$\dot{\mathbf{x}} = f(\mathbf{x}) \tag{1.3.1}$$

where $\mathbf{x}$ is a vector of state variables of time t and $\dot{\mathbf{x}}$ is its derivative. The steady state is which satisfies $\dot{\mathbf{x}} = 0$. In DC distributed systems, the steady state is called *equilibrium point* or *critical point* or *fixed point*. The equilibrium $\mathbf{x}_e$ is derived by:

$$f(\mathbf{x}_e) = 0 \tag{1.3.2}$$

All stability problem is about a steady state. A critical point can be classified to be *stable*, *unstable* and *asymptotically stable*. For simplicity of explanation, we assume the equilibrium is at the origin since any equilibrium can be translated to the origin by proper transformation [34].

An equilibrium is *stable* if as shown in Fig1.3.1, by choosing the initial conditions in a sufficiently small spherical neighbourhood of radius δ, we can force the trajectory of the system for all time $t \geq t_0$ to lie entirely in a given cylinder of radius ε [35]. On the contrary, an equilibrium is *unstable* if the trajectories move away from the critical point to infinitely far away.

Furthermore, an equilibrium is *asymptotically stable* if as illustrated in Fig1.3.2, by choosing the initial conditions in a sufficiently small spherical neighbourhood of radius δ, we can force the trajectory of the system for all time $t \geq t_0$ to come back to zero eventually, which is a stricter requirement than *stable*.
The above stability definition is made by assuming the DC power system. Similarly, for AC distributed system, the asymptotic stability is about trajectories converging (or not) to the stable trajectory as time progresses.

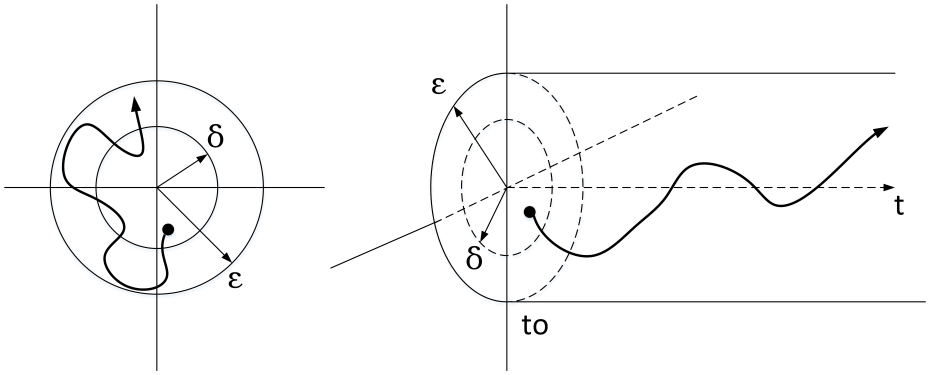

Figure 1.3.1 Illustration of the definition of stability[36]

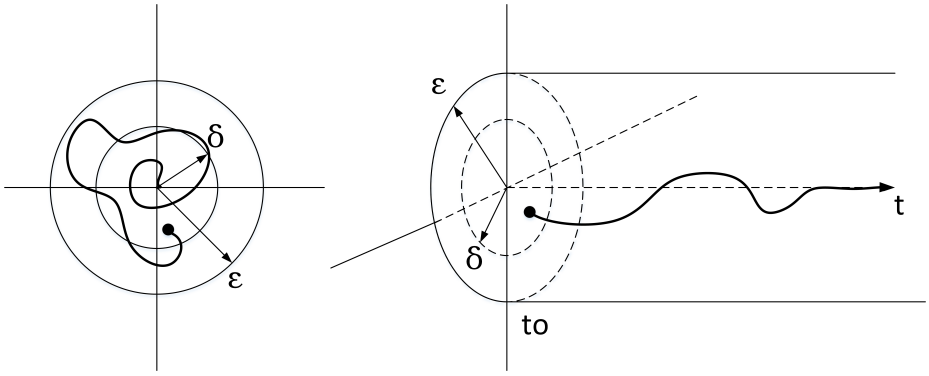

Figure 1.3.2 Illustration of the definition of asymptotic stability [36]

Mathematically, Lyapunov stability of a system is investigated by finding and validating the *Lyapunov functions*. However, there are no general methods for finding the Lyapunov functions, and Lyapunov functions only exist for the system with unique features.

Although Lyapunov stability has limitations of applying to all non-linear systems, it provides a fundamental definition for the system stability. The stability for the linear dynamic system is another branch of stability. The theories of linear systems are mutually developed and can be applied to non-linear dynamic systems close to equilibria by applying *linearisation* technique.

1.3.2 Stability of Linear System

Consider the system described in (1.3.1), the left side of the equation is the changing rate of the state variables, the right side of is a function involving the state variables and the inputs. The dynamic system can be classified into linear and non-linear systems depending on function f. If it contains all linear terms, the system is a linear dynamic system; if it contains non-linear terms, the system is a non-linear dynamic system.

It should be noted that for a linear system, there is only one equilibrium or time-periodic trajectory so that the overall stability of the system can be studied. However for non-linear DC system, there can be more than one equilibrium, each equilibrium point may have distinct stability characteristics; hence they must be studied individually.

1.3.2.1 Solution of Linear Dynamic System

If the system defined in (1.3.1) is linear, an n-order system is normally written in the form of (1.3.3), where the function f is replaced by an $n \times n$ matrix A of the constant coefficients times $\mathbf{x}$. $\mathbf{x}(t)$ is the $n \times 1$ vector of the state variables.

$$\dot{\mathbf{x}} = \mathbf{A}\mathbf{x} \tag{1.3.3}$$

Thus the rate of change of the nth variable x_k is determined by all the variables whose coefficient is non-zero since the coefficient can be either positive or negative, it is hard to tell whether a small perturbation from the equilibrium would result in an increase or decrease of the derivative. The simplest case is where its diagonal eigenvalue matrix replaces the matrix A. Hence, the change of kth variable is only decided by x_k alone with the coefficient of λ_k, then the solution of the linear system is in the form of

$$\mathbf{x}_k = \mathbf{r}_k e^{\lambda_k t} \tag{1.3.4}$$

where λ_k is the eigenvalue of the matrix A, $\mathbf{r}_k$ is its corresponding eigenvector. And the general solution for $\mathbf{x}$ is a linear combination of the individual solutions.

The linear dynamic system responses can be classified depending on the type of the eigenvalues as summarised in Table1.1 and Fig1.3.3. If the eigenvalues are real negative numbers or complex numbers with negative real parts, the system is stable and will converge to a steady state. However, if at least one eigenvalue is a positive real number or complex number with a positive real part, the system would diverge to infinity and being an unstable system; if all eigenvalues are pure imaginary numbers, there would be stable oscillation.

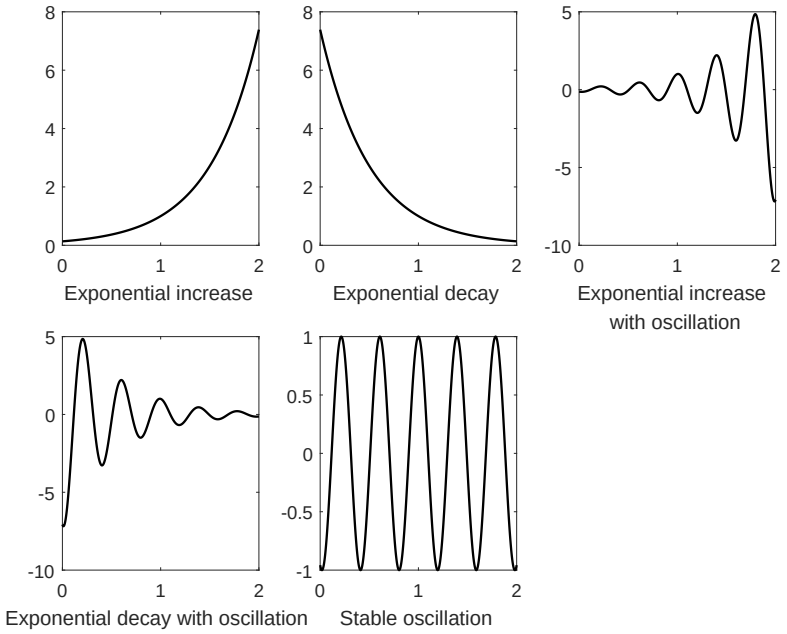

Figure 1.3.3 Responses of linear dynamic systems

Table 1.1 How eigenvalues decide system response

Eigenvalue	System Time Response
Positive real number	Exponential increase
Negative real number	Exponential decay
Complex, positive real number	Increase with oscillation
Complex, negative real number	Decay with oscillation
Imaginary number	Stable oscillation

1.3.2.2 Phase Portrait

Now we introduce an alternative graphics tool for studying differential equations, which is called *phase portrait*, is typically used for autonomous second order system. Its central idea is to draw the moving trajectories from many initial points in the state space, and then tell the characteristics of the system concerning the geometric characteristic of the phase portrait.

On the phase plane, the axes are of state variables, the phase portrait plots the curves or trajectories $(x, y) = (x_1(t), x_2(t))$, $t_0 < t < \infty$ from any initial point. Then it can be visualised how the system would behave in the long run.

The phase portrait can be drawn electronically by the aid of some software for the known systems, firstly the *direction field* (a map with the derivative of each point shown by short arrows on the phase plane) is sketched, it is then easy to draw the solution of the system from an initial point. An alternative way of drawing phase portrait is to use the eigenvalues to indicate stability locally around an equilibrium on the phase plane.

For example, for a second-order linear differential system (1.3.3), its characteristic equation can be written as

$$\lambda^2 - \tau\lambda + \Delta = 0 \tag{1.3.5}$$

where τ is the trace of matrix A, $\tau = \lambda_1 + \lambda_2$, and Δ is the determinant of matrix A, $\Delta = \lambda_1\lambda_2$. Fig1.3.4 indicates the phase portrait of classification of the fixed point according to the values of τ and Δ, as they are enough to indicate the categories of the two eigenvalues.

Give an example, if Δ is positive, indicating that two eigenvalues are with the same sign. And if τ is positive, then both eigenvalues are positive, if above the quadratic curve $\tau^2 - 4\Delta$, then they are two real numbers, the fixed point is unstable node, the trajectories starting from close to equilibrium will get far away from it; when under the $\tau^2 - 4\Delta$ curve, indicating two complex eigenvalues with positive real part, the

fixed point is an unstable spiral, the trajectories starting from close to the equilibrium will get away from it with spirals.

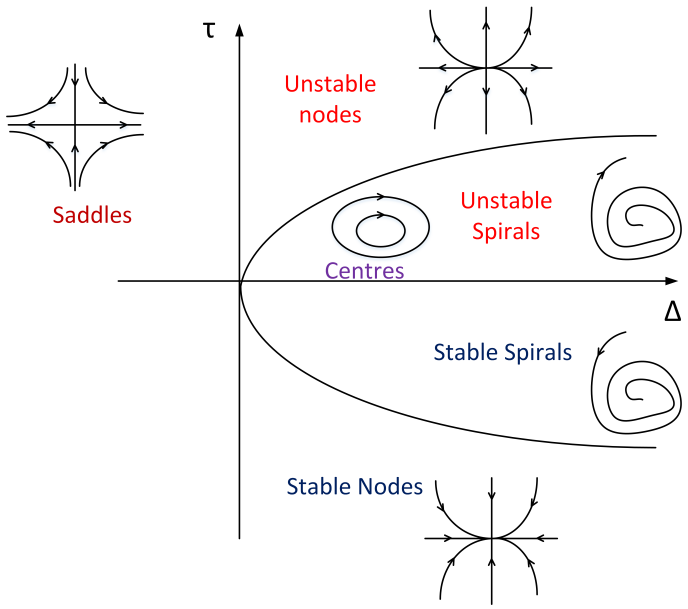

Figure 1.3.4 Stability classification of fixed points

Fig1.3.4 accords with the results in Fig1.3.3. The exponential decrease or increase in time-domain plot correspond to the stable or unstable node on phase portrait. If the eigenvalue has an imaginary part, the phase diagram will have a spiral. Moreover, the stable oscillation correlates with the centre on the phase plane. In summary, we see that the stability of the equilibrium then can be seen and judged from the phase portrait, and eigenvalues decide the shape of the phase portrait.

1.3.3 Stability of Non-linear System

1.3.3.1 Linearisation Technique

Linear dynamic systems can be solved precisely since their analytic solutions can be given, nonetheless, for the non-linear systems the analytic solutions usually cannot be found. Hence it is hard to know the global characteristic of the non-linear dynamical

system.

It is then a conventional technique for engineers to locally linearise a non-linear system to be a linear system. The linearisation technique applies to both time-invariant and time-variant systems. For the time-invariant system, the linearisation is about a fixed point; for the time-dependent system, in general, one linearises about a time-dependent solution rather than an equilibrium. The general method of conducting stability analyses of a non-linear system is depicted in Fig1.3.5.

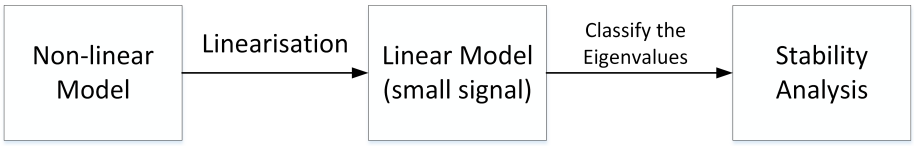

Figure 1.3.5 General stability analysis method

A DC non-linear power system, for example, as represented by (1.3.1) can be linearised to a linear system which is represented by (1.3.6)

$$\dot{\mathbf{x}} = \mathbf{J}\mathbf{x} \tag{1.3.6}$$

Where **J** is the Jacobian matrix calculated at a fixed point. The Jacobian matrix is derived from Taylor series approximation of a function at a fixed point. Generally, for an n-order system, it is an $n \times n$ matrix calculating the partial derivatives from each function of each state variable as in (1.3.7).

$$\mathbf{J} = \begin{bmatrix} \frac{\partial f_1}{\partial x_1} & \cdots & \frac{\partial f_1}{\partial x_n} \\ \vdots & & \vdots \\ \frac{\partial f_n}{\partial x_1} & \cdots & \frac{\partial f_n}{\partial x_n} \end{bmatrix} \tag{1.3.7}$$

Similarly, the Taylor series expansion can be applied for AC power systems about a time-dependent solution to obtain the linearised small signal model.

1.3.3.2 Bifurcation Map

In non-linear systems, a *bifurcation map* is usually used to describe the situation that there is a qualitative change of system solutions according to the change of parameters. The qualitative change can refer to either the number of solutions change or the stability of the equilibrium change.

Various DC-DC converters usually have been studied for the non-linear systems demonstrations because they are representative and straightforward. Such as in [37] a free-running Ćuk converter was studied, the analysis was carried out with large-signal analysis. Namely, there is no linearisation but directly analysing the describing non-linear state equations of the system by drawing the phase portrait. Analysis of the non-linear averaged model shows that the system loses stability via a supercritical Hopf bifurcation. The occurrence of such kinds of bifurcation in autonomous DC-DC converters has been rarely known in power electronics.

In chapter 4, we will analyse a sample buck converter with a constant power load system. The analysis contains the application of some powerful methods of analysing the stability of nonlinear systems mentioned above. The analysis will indicate that the system will lose stability via a Hopf bifurcation. Various types of bifurcations have been classified. A Hopf bifurcation is also known as a Poincare-Andronov-Hopf bifurcation, named after Henri Poincare, Eberhard Hopf, and Aleksandr Andronov [38][39]. A Hopf bifurcation is a local bifurcation in which a fixed point of a dynamical system loses stability, as a pair of complex conjugate eigenvalues (of the linearisation around the fixed point) cross the complex plane imaginary axis. Under reasonably assumptions about the dynamical system, a small-amplitude limit cycle branches from the fixed point.

1.4 Contribution to Knowledge

Some contributions to knowledge in terms of the modelling and stability techniques are listed in the following:

• By applying harmonic balance technique to model the steady state of the power converter and applying Floquet theory to justify the stability, thus the single-phase power converter with a controller designed in the natural reference frame can be studied. Hence the accurate stable boundary for the system parameters is derived.

• By applying the method in this thesis, it is easy to include all the controllers in the natural reference frame and PLL into the model and study the interactions between all the control loops. This is not yet considered in other studies for the interaction's effect on the stability problem.

1.5 Thesis Plan

Chapter 1 is a general introduction to background system stability, which also gives an overview of the stability analysing methods applied to the non-linear time-invariant and time-periodic power electronic systems. The Lyapunov stability is first introduced as the fundamental definition of the system stability. Then the stability of the linear system is illustrated. For the more complicated non-linear systems, except for linearisation technique, some specific methods are introduced such as phase portrait analysis and perturbation method.

Chapter 2 gives a review on multilevel converters. Four most commonly seen multilevel topologies: diode-clamped multilevel, flying capacitor multilevel, cascaded H-bridge multilevel, and the modular multilevel converter will be introduced concerning circuit schematics, devices requirements, PWM modulations and applications. In the end, the topology proposed in this thesis, a single-phase 7-level CHB rectifier will be introduced in detail with simulating operating waveforms.

Chapter 3 illustrates the control design of the proposed converter. A brief review of the control scheme for the CHB converter will be shown first. The control implemented in this thesis is a classic 2-loop structure, the outer loop is for controlling the total DC link voltage by a PI controller, the inner loop is a fast-speed predictive deadbeat controller. The control design procedures will be shown step by step. Finally, the control design will be validated with simulations.

Chapter 4 studies an example system which is a buck converter with a constant power load system as an introduction of the mathematical method. The averaged model is firstly derived and used to predict that the system would lose its stability via the Hopf bifurcation if the power of CPL is beyond the analysed threshold. Then the weakly non-linear perturbation method is applied to solve the solution for the system. The analysis provides more information about the locally of bifurcation point, indicating that there is a limit cycle at the bifurcation point and the size of this limit cycle can also be calculated.

Chapter 5 derives the mathematical model for the CHB converter with closed-loop control. The model of the open-loop converter will be built first by evaluating each spectrum of harmonics. The result is compared with simulation FFT result, proving that the harmonic balance technique is valid and accurate. Then the control equations are included in the analysis by some simplifying assumptions. Again the harmonic balance principle will be applied to establish the formula for steady state periodic operation. The analysed results will be compared to both the averaged model and switching model time responses.

Chapter 6 carries out stability analysis of CHB converter steady state which is obtained from chapter 5 by applying Floquet theory. The basic theory of Floquet theory will be explained and the general steps of applying Floquet theory to analysing linear time-periodic system will be given. The averaged model of our system is linearised, and the LTP small signal model will be derived. Then compute the Floquet multipliers, namely the eigenvalues of the monodromy matrix, by varying the system parameters of interest. Make conclusions of system stability by observing the distri-

bution of eigenvalues regarding the unit circle.

Chapter 7 is about the experimental hardware set up. The overall experimental rig is illustrated, and then several important parts are explained individually, such as the gate drive circuit and the dead time circuit of the converter. Also, the theory of the voltage/current transducers. The control is implemented on the DSP/FPGA platform designed by the PEMC group of the University of Nottingham. The theory of the co-operation between the DSP and FPGA will also be explained.

Chapter 8 shows the experimental results from running a 2 kW test. The waveforms from working on the nominal system configurations will be shown to verify that the control design is functioning. Then the experimental results of unstable waveforms when we set the parameter of interest close to the analysed threshold value will be shown to verify our stability analysis. The PI bandwidth effect and common effect of grid strength and PLL bandwidth on the stability of the system are verified with the parameter varying in steps.

Chapter 9 gives the conclusions of the thesis with a list of achievements and future work.

1.6 Summary

In this chapter, the background of the study is described as well as a general review of modelling and stability analysis techniques for various systems. It is clarified that this thesis aims to analyse the stability of the grid-connected CHB rectifier. There are two problems with the existing methods: if we apply Lyapunov theory, the exact boundary of the parameter can't be derived; while if using phasor method it can't be applied for the single-phase converter and not applicable for the model-based controllers which are designed in the natural reference frame. Hence it is necessary to propose the harmonic balance technique and Floquet theorem which are applicable for time-periodic dynamic systems.

Meanwhile, the modelling methods and stability verifying approaches have been simply reviewed as the topic background. For the mathematical modelling methods, switching and averaged model are introduced as they are the basic models of the system that are dealt with in this study. Furthermore, the perturbation theory is introduced as a powerful modelling technique which will be shown in the example of a buck converter with constant power load. The harmonic balance technique is also demonstrated as it is the method used in the steady-state modelling for the CHB converter. In the stability section, the definition is firstly given for stable and unstable operation with Lyaponov theory, and stability for linear and non-linear systems are reviewed separately with their commonly used methods.

Given the background and bring out the advanced analysing techniques, it can be seen that the advanced analyse techniques bring in many benefits which are listed in the contribution to knowledge.

Chapter 2

Multilevel Converters

2.1 Multilevel Topologies

Multilevel Converters (MCs) have gained much attention nowadays in medium or high voltage and high power applications [6, 9, 7, 8, 40]. The voltage ratings of present power semiconductors such as Isolated Gate Bipolar Transistors (IGBT) are not comparable to the medium or high voltage, hence they can not be directly connected to the grid but need to be stacked up or used to form some advanced topologies. As a result, the multilevel converter families were born. The main advantages of the multilevel converters include lower voltage stress on power switches, lower dv/dt ratio to supply lower harmonic contents in output voltage and current thus less filtering requirement and less Electromagnetic Interference (EMI), et cetera.

In this chapter the most four common multilevel topologies that can be found in the literature are reviewed: a)Diode-Clamped Converter (DCC) or Neutral Point Converter (NPC), b)Flying-Capacitors Converter (FCC), and c)Cascaded H-bridge Converter (CHB) [41, 42], d)Modular Multilevel Converter(MMC). Usually, NPC, FCC, and CHB are found discussed in the literature of multilevel converter family. However, MMC is nowadays a vital topology mostly used for High Voltage Direct

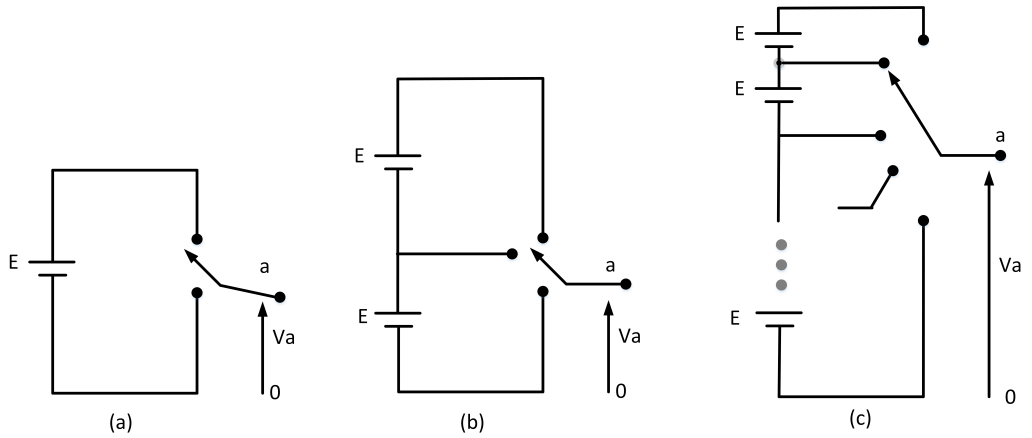

Figure 2.1.1 One phase leg of an inverter with (a) two levels, (b) three levels, (c) n levels.

Current (HVDC) applications, the main difference of it from the other topologies is it has no DC link. These four topologies will be demonstrated in the following, but multilevel converters are not only these four types, other types such as T-Type, E-Type, Asymmetric and hybrid MLCs are also commonly referred to in this topic[43, 44].

As shown in Fig.2.1.1, the basic idea of multilevel converters is synthesising the staircase voltage waveform from several DC capacitor voltages [42], one phase leg of an inverter with two levels, three levels and n levels. An ideal switch with several positions represents the action of the power semiconductors. The two-level inverter has only one DC-link level, and the switch has two positions so that the output voltage V_a has two voltage levels for the capacitor negative terminal. The three-level inverter has two DC-link levels with a middle point between the two capacitors. With an increase in the number of the DC levels, the output voltage is possible to synthesise voltage with more steps. Their basic structures are illustrated in Fig.2.1.2 for a three-level phase voltage generation[45]. The DC source of NPC inverter and FCC inverter E is divided into two DC sources E/2 by adding a neutral point N in the middle of capacitors. NPC inverter uses diodes to clamp the DC voltage levels, and FCC uses auxiliary capacitors to clamp different voltage levels.

According to Fig2.1.2, for NPC the output voltage V_0 has three states: $E/2$, 0, and

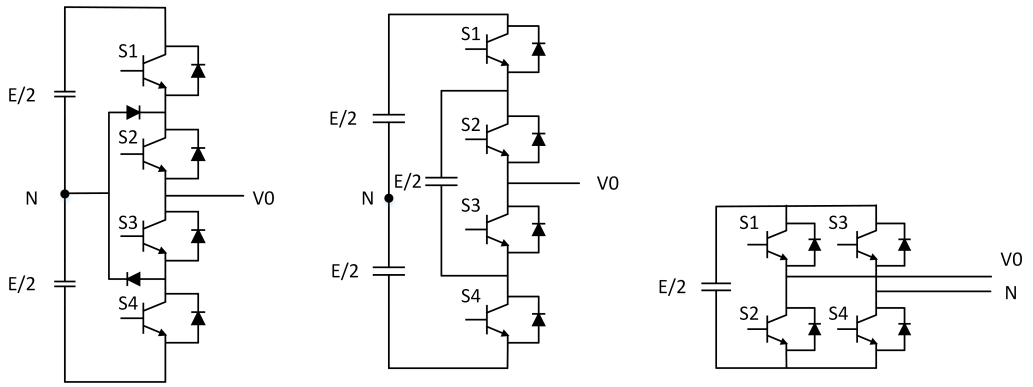

Figure 2.1.2 Basic topology of multilevel converters. (a) Three-level neutral-point inverter (b) Three-level "Flying"-capacitor inverter (c) Three-level cascaded H-bridge inverter.

$-E/2$. For voltage level $E/2$, switches S_1 and S_2 need to be turned on; for $-E/2$, switches S_3 and S_4 need to be turned on; and for the 0 level, S_2 and S_3 need to be turned on.

As for FCC, for voltage level $E/2$, switches S_1 and S_2 need to be turned on; for $-E/2$, switches S_3 and S_4 need to be turned on; and for the 0 level, either pair (S_1 S_3) or (S_2 S_4) needs to be turned on. Clamping capacitor is charged when S_1 and S_3 are turned on and is discharged when S_2 and S_4 are turned on. The charge of clamping capacitor can be balanced by proper selection of the 0-level switch combination.

CHB inverter is based on the series connection of single-phase inverters with separate DC sources. Fig2.1.2 shows a single cell which generates a three-level output voltage.

A simplest multilevel scenario for three-level inverters has been illustrated, adding more number of DC link capacitors can generate more levels than the three. It can be seen that the flying capacitor inverter and cascaded H-bridge has more switching state for $V_0 = 0$ than diode-clamped multilevel.

A demonstration of topology structures, modulation strategies, and operation of the multilevel converters are given in the following. Then single phase cascaded H-bridge converter, whose stability is studied in this thesis, is described in detail. A thorough understanding of its operating principles is necessary preparation for its mathematical

modelling and stability analysis in later chapters.

2.1.1 Diode Clamped Converter

The Diode Clamped Converter (DCC) is the origin of the multilevel topologies and was proposed by Nabae, Takashi, and Akagi in 1981[46]. DCC is suitable for working in fundamental switching frequency, which usually causes the high THD of voltage and current waveforms[41].

2.1.2 Flying Capacitor Converter

An alternative topology is the Flying Capacitor Converter (FCC), which was introduced in 1992 by Meynard[47]. Similar with NPC topology, the m-level topology needs $m-1$ DC link capacitors, but extra $(m-1)(m-2)/2$ auxiliary capacitors [48, 49]. FCC topology has more flexibility with switching states compared with NPC[42], which gives more redundancy of the selection of switching states.

2.1.3 Cascaded H-bridge Converter

A relatively new modular multilevel topology is the Cascaded H-bridges (CHB), namely connecting H-bridge cells in series, in this topology each H-bridge cell requires isolated DC source, and each cell can generate three levels. As Fig2.1.3 depicts a three-phase five-level topology for a Y-configured CHB inverter, each phase is identical. On AC side the output terminals of the H-bridges are connected in series and synthesis the staircase waveform using the different DC levels. Thus the DC sources must be isolated from each other. Because of this property, the CHB converters are suitably used with fuel cells or photovoltaic arrays[40, 50, 51]. Generally, having N cell per phase will result $(2N+1)$ levels of the voltage waveform[41, 42].

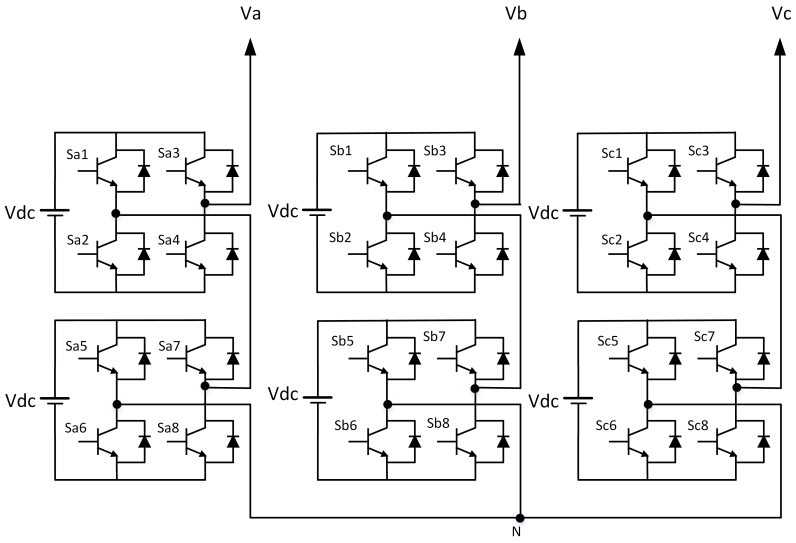

Figure 2.1.3 Three-phase five-level topology for a cascaded H-Bridge inverter

2.1.4 Modular Multilevel Converter

Modular Multilevel Converter (MMC or M2LC) is another common multilevel topology. Fig2.1.4 shows a schematic diagram of a three-phase MMC inverter. Each phase has two legs, and each leg consists of an identical number of Sub-Modules (SM) connected in series. For each leg, a choke inductor L_O is required to limit the AC.

The SMs of MMC can be realised by various circuits, such as 1) the half-bridge circuit, 2) the full-bridge circuit, 3) the clamp diode circuit, 4) the three level converter circuit, 5) the five-level cross-connected circuit, etc.[52]. Among these circuits, the half-bridge and full-bridge are the most commonly seen. Moreover, the half-bridge circuit is most adopted by MMC [53, 54] with respect to the number of components and power losses[52]. Due to the various SM topologies, each cell can have the voltage level of two, three or five, and the synthesised multilevel voltage will be generated as a result of applying the modulation technique.

The challenges related to MMC include circulating current control[55, 56, 57], precharging the SM capacitors[58, 59] and SM capacitor voltage ripple reduction[60, 61], etc.

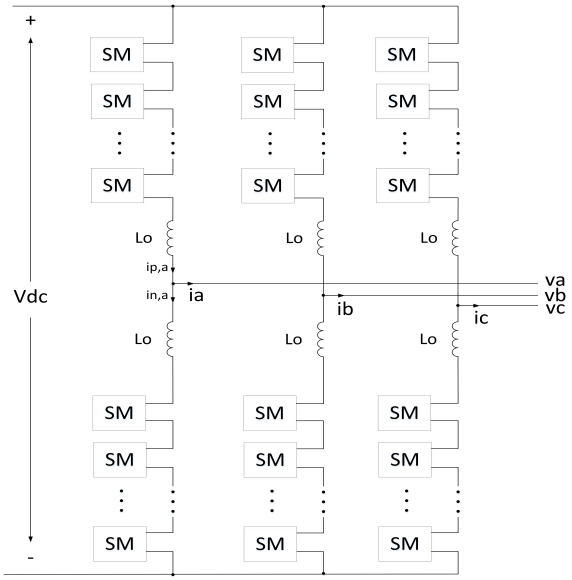

Figure 2.1.4 Three-phase Modular Multilevel Converter (MMC) schematic

2.2 Modulation Strategies for Multilevel Converters

The modulation strategy is an essential selection regarding the switching loss and THD reduction for the converter[41]. The conventional modulation techniques applied for multilevel converters are Selective Harmonic Elimination PWM (SHE-PWM), Sinusoidal PWM (SPWM), Space Vector Modulation (SVM), etc. One classification of modulation strategies for multilevel is the fundamental switching frequency modulation and high switching frequency modulation. Fundamental switching frequency modulation is where each converter only has one commutation per fundamental cycle, and high switching frequency is where each converter has several commutations per fundamental cycle[62]. As illustrated in Fig2.2.1, the fundamental switching frequency techniques include SVM and SHE-PWM, the high switching frequency category has SVM, SHE-PWM and SPWM.

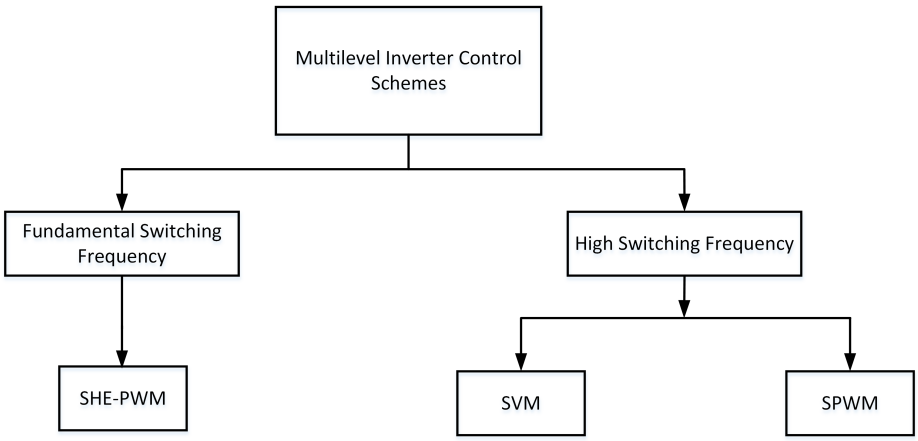

Figure 2.2.1 Classification of multilevel converter modulation methodologies

2.2.1 Sinusoidal PWM

Sinusoidal PWM (SPWM) is the most common PWM technique which generates switching signals by comparing a sinusoidal modulating signal with a triangle carrier, and the switching occurs when there is an intersection of the modulating signal and the carrier[63, 64]. The SPWM is easy to be implemented. Furthermore, multi-carrier PWM techniques have been developed for multilevel converters to improve their performance[65, 66]. The multi-carrier modulation is an extension of Sinusoidal PWM (SPWM)[67] and has been classified into two categories: Level Shifted Carrier PWM (LSC-PWM) and Phase-Shifted Carrier PWM (PSC-PWM) [68, 69]. PSC-PWM is only useful for CHB and FCC, while LSC-PWM is more useful for NPC[70].

2.2.1.1 Level Shifted Carrier PWM Modulation

LSC-PWM uses a number of carriers shifted vertically as shown in Fig2.2.2 for a 5-level cascaded H-bridge converter, V_1 and V_2 are the converter applied voltage on the AC side of the two cells, V_O is the synthesised 5-level voltage. As we can see this technique produces uneven conduction time and power share among cells[71], which is the main drawback of the LSC-PWM.

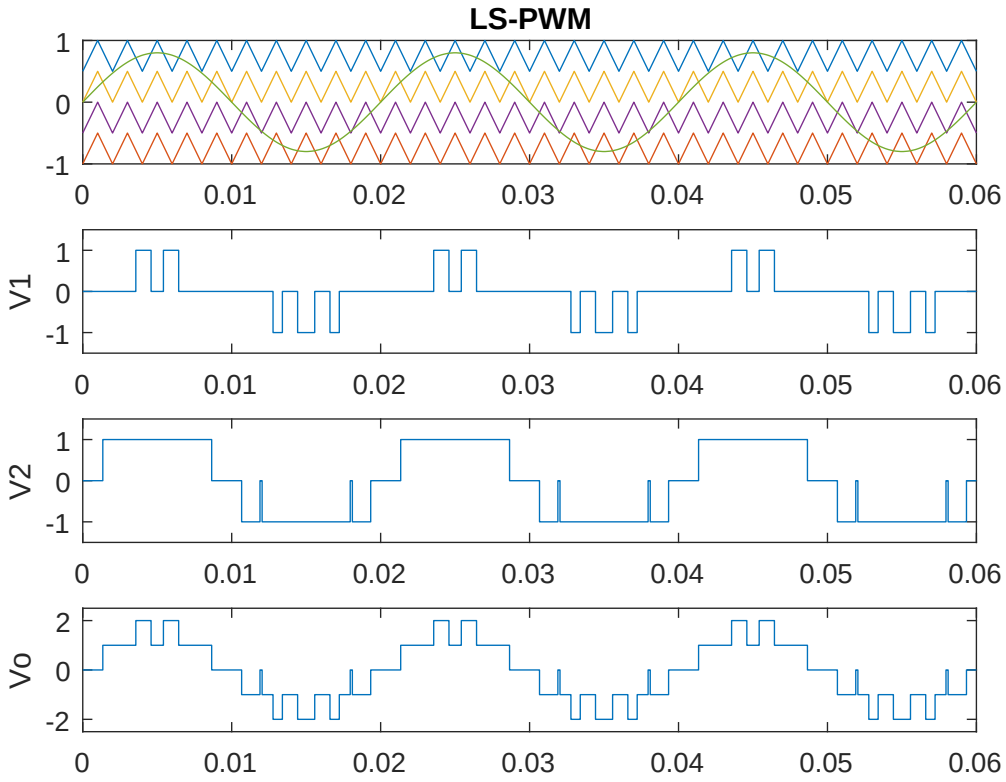

Figure 2.2.2 Level-shifted PWM modulation implementation for the five-level cascaded H-bridge converter (Frequency=500Hz, MI=0.5)

2.2.1.2 Phase Shifted Carrier PWM Modulation

An alternative to LSC-PWM is the PSC-PWM, which uses carriers with horizontally phase shift to each other. Generally, N carriers(triangular) are used for N cells for CHB topology, with phase shifted between each other with:

$$phase = \frac{\pi}{N} \tag{2.2.1}$$

The PSC-PWM for a 5-level CHB (2-cell) converter is illustrated in Fig2.2.3, where two carriers phase shifted with 90 degrees are applied and compared to the same modulating signal.

Generally, the factors that would affect the THD level are the number of levels, the switching frequency f_s and the modulating index m_i[41]. Generally, the more of the

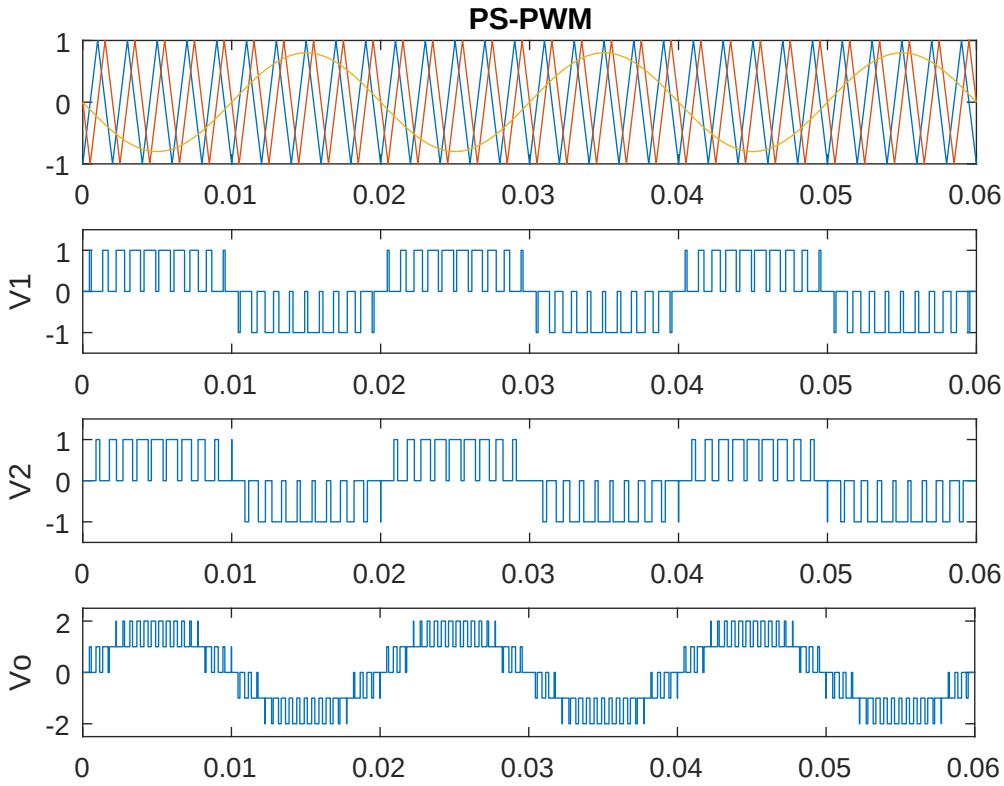

Figure 2.2.3 Phase-shifted PWM modulation implementation for the five-level cascaded H-bridge converter.(Frequency=500Hz, MI=0.5)

number of levels of voltage waveform, the bigger the switching frequency, and the bigger the modulating index are, the lower the THD is.

2.2.2 Selective Harmonic Elimination PWM

The SHE PWM modulation method is proposed in 1974 by Patel[72] aiming to eliminate the specific order of harmonics. The method is to pre-calculate the switching angles and obtain the Fourier expansions of the output voltage. SVM usually is applied as a fundamental switching frequency modulation method.

2.2.3 Space Vector PWM

Another common PWM technique is space vector PWM (SVPWM), which uses the control variables and gives the switching vectors directly[73, 74]. The ON time of the desired voltage reference vector is generated by synthesising the adjacent three vectors. As the number of level increases, the computational burden of SVPWM may become a problem, the usage of digital hardware can easily overcome this. The advantages of SVPWM include: good dc-link voltage utilisation, low current ripple, and easy hardware implementation; and the harmonic elimination is better than that obtained by applying SPWM. These advantages make it suitable for the high-voltage high-power applications[75, 76, 77].

2.2.4 Summary of Modulating Methods

In summary, each modulation method has its own advantages and disadvantages. For example, by using level shifted PWM, it is easy to be implemented, but the conduction times of the switching devices are not equal and the power share between the cells are unbalanced, thus an additional swapping scheme between the cells is needed. The space vector PWM doesn't need a modulator to be implemented and generates switching signals without comparing a carrier and a modulating signal. The SHE method can eliminate the specific order of harmonics but involves complicated mathematical calculus. In this project, the PSC-PWM has finally been selected among the others due to its advantage of balancing the power flow between the cells in nature and easy to be implemented.

2.3 Applications of Multilevel Converters

The applications of the multilevel converters include high-frequency drives and motor drives, renewable energy sources interconnection to the grid, Flexible AC Trans-

mission System (FACTS). In this section, a simple introduction is made of its two common applications as STATCOM and used in the back-to-back SST topology.

2.3.1 Reactive Power Compensation

One of the typical applications of multilevel converters is used as Static Var Generator (SVG)[8]. All three multilevel topologies can be used in reactive power compensation[42]. They can be directly connected to the grid without the need of step-down transformer[7] compared to the traditional var compensator. Fig2.3.1 shows the phaser diagram for reactive power compensation, the relationship is $V_S = V_{CONV} + jXI_L$, where X is the impedance of the grid inductance. When there is a leading reactive power, the amplitude of V_{CONV} is more prominent than V_S, and when there is a lagging reactive power, the amplitude of V_{CONV} is smaller than V_S, thus it can be concluded that the polarity and amplitude of the reactive current is controlled by the magnitude of the multilevel converter, which is further controlled by the DC voltage level and the modulation index.

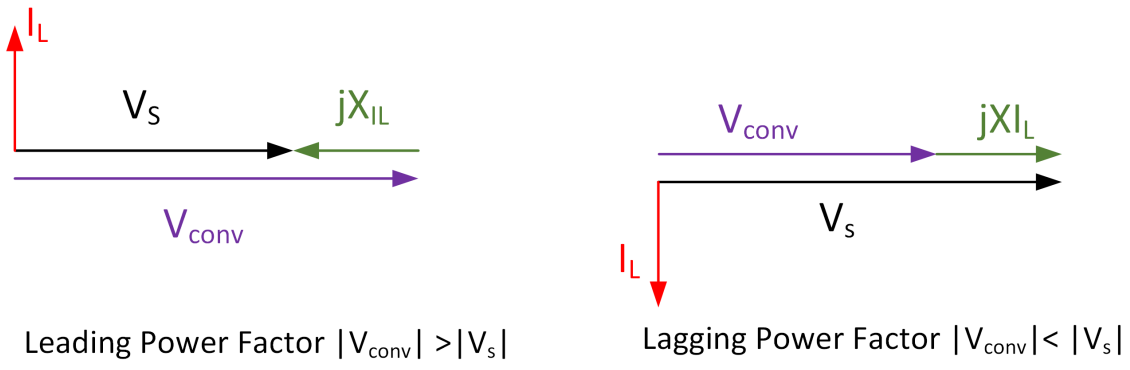

Figure 2.3.1 Phaser diagram for reactive power compensation

2.3.2 Solid State Transformer

Another main application for multilevel converters is the power electronics-based transformer, or Solid State Transformer (SST), which can be treated as a frequency changer, a phase shifter, or a power flow controller in electricity networks[42].

According to [9], in a three-stage SST schematic, the input stage implemented by a multilevel converter is of the most interest[9], and then the HVDC to LVDC stage is implemented by a Dual Active Bridge (DAB), and then the LVDC to LVAC stage is implemented by a PWM inverter. This three-stage SST topology receives most attention because of its advantages of controllability to fulfil the functionality of the SST [78]. The main drawback is an increasing number of components which may decrease the efficiency[9]. A 300 kVA back-to-back multilevel prototype has been build for the Universal and Flexible Power Management (UNIFLEX-PM) project in University of Nottingham[79, 80, 81].

2.3.3 Comparison of Topologies and Modulation Strategies

MMC gains much attention these years especially for application on HVDC transmissions[82, 83], and CHB topology stands out for its inherent modular structure[84, 85].

NPC converters have been widely used in motor drives with SHE-PWM. The NPC topology is efficient working in fundamental frequency with SHE-PWM or SVPWM, but the complexity would increase if the level exceeds three. The other applications of NPC include the active filters and STATCOM.

The FCC is similar to NPC, but requires more auxiliary capacitors to generate the staircase waveform. Hence it is hard to control the accurate of capacitors charging and discharging. FCC is mostly used in motor drives and active filter applications.

The CHB topology requires the least number of devices compared to the other two

according to Table 2.1. It was firstly designed for motor drive and active filter applications, but due to its inherent requirements of isolated DC sources, it is now widely used for interconnecting the renewable sources into the grid. SPWM is the most applied modulation technique for CHB because of its simplicity.

Table 2.1 Comparison of power component requirements per phase leg among three multilevel converters

Topology	DCC	FCC	CHB
Main Switching Devices	(N-1)/2	(N-1)/2	(N-1)/2
Main Diodes	(N-1)/2	(N-1)/2	(N-1)/2
Clamping Diodes	(N-1)*(N-2)	0	0
DC Bus Capacitors	(N-1)	(N-1)	(N-1)/2
Balancing Capacitors	0	(N-1)*(N-2)/2	0

2.4 Converter Structure Proposed in This Thesis

As shown in Fig2.4.1, a single phase 3-cell CHB rectifier is proposed and studied in this work, based on the fact that when the three phase is connected with a neutral point, each phase is identical and can be analysed and controlled separately. This structure can also be regarded as the rectifying stage in a back-to-back application. From the

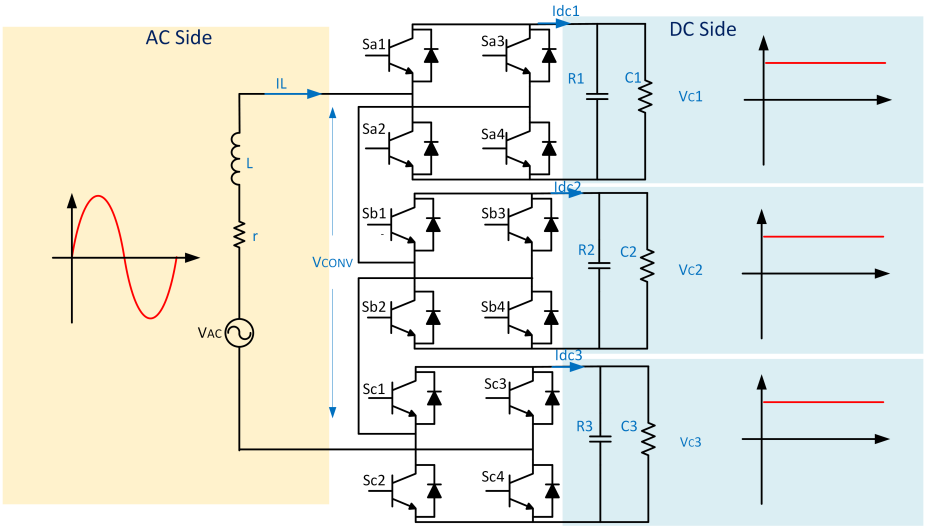

Figure 2.4.1 Schematic of a single-phase three-cell CHB rectifier

AC side, the converter is interfaced with the voltage source V_S, which is referred to as the *AC-side voltage source*. The connection between the AC-side terminal and the AC-side voltage source is through a series rL branch as the input filter to enable power factor control at the grid and provide an acceptable attenuation of the current harmonics. L and r, respectively, represent the inductance and the internal resistance of the interface.

The converter is composed of three H-bridge cells connected in series. The AC side terminal voltage is denoted as V_{CONV} and the positive direction of the AC side current is indicated as I_L. From the DC side, each H-bridge is loaded with a capacitor and a resistor connected in parallel. Assume that the identical DC loads are applied, thus C_1=C_2=C_3=C, R_1=R_2=R_3=R. The voltages across the capacitors V_{C1}, V_{C2} and V_{C3} are taken as the output voltages. Also the positive directions of the DC side current of each H-bridge are indicated as I_{dc1}, I_{dc2}, I_{dc3}.

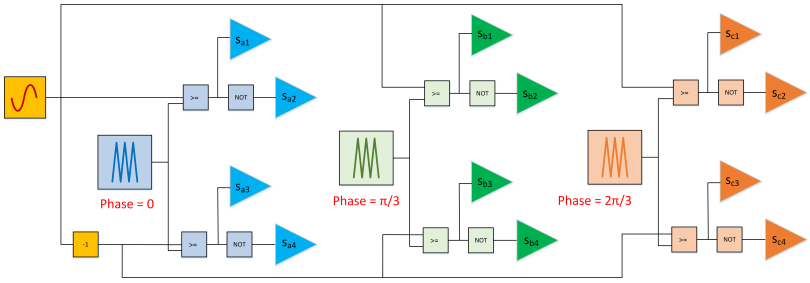

Figure 2.4.2 Phase-shifted PWM modulation implementation for the 7-level cascaded H-bridge converter

The PSC-PWM is selected to be applied for the CHB rectifier for its advantage of balanced power-sharing between cells. Fig.2.4.2 gives the generation schematic of the PSC-PWM for the 3-cell cascaded H-bridge converter. The unipolar PWM [86] is applied for each cell for its less THD compared to bipolar PWM. Hence, two opposite sinusoidal modulating reference waveforms (180 degrees shifted in phase) are used for a full H-bridge cell. As the figure shows, same modulating signals are used for all three cells, guaranteeing the same fundamental voltage of each cell. Three phase-shifted triangular carriers are applied, the second carrier is shifted $\pi/3$ rad for the first carrier, the third carrier is shifted $\pi/3$ rad for the second carrier, and $2\pi/3$ rad

to the first carrier. The produced switching signals s_{a1-4}, s_{b1-4} and s_{c1-4} are given to the CHB as labelled in Fig2.4.1.

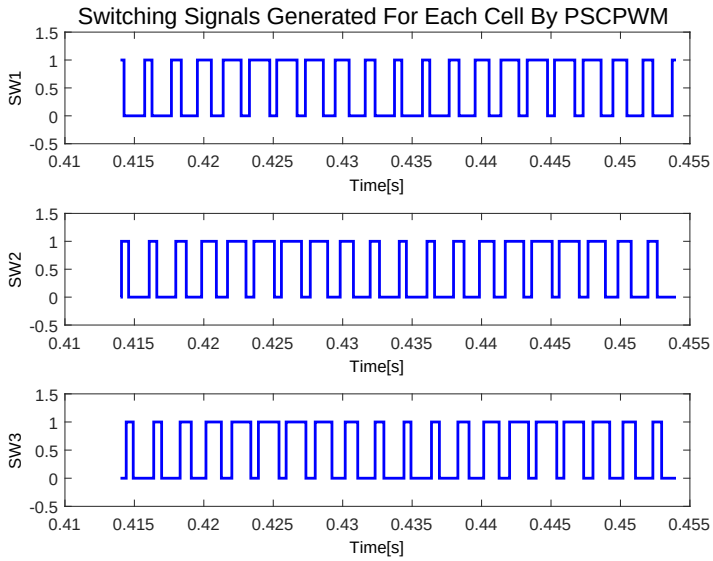

Figure 2.4.3 Switching signals generated based on the PSCPWM for 7-level CHB

Fig.2.4.3 indicates the produced gating signals s_{a1}, s_{b1} and s_{c1}. Note that the fundamental component of each switching signal is the same, while the switching instants occur with a phase shift between cells. It is necessary to investigate the converter waveforms due to the PSC-PWM since it is the modulation method applied in this study. Each H-bridge has three switching states, take the first cell in Fig.2.4.1 as an example, a switching function S_1 is defined for describing these three states [87, 87], similar for the second and third cell we define S_2 and S_3, where S_1, S_2, S_3= $-1, 0, 1$.

As shown in Fig2.4.4, when s_{a1} is conducting (thus s_{a2} is blocking) and s_{a4} is conducting (thus s_{a3} is blocking), $V_{CONV1} = V_{C1}$ ($S_1 = 1$); When s_{a1} and s_{a3} are conducting (s_{a2} and s_{a4} are blocking) or s_{a2} and s_{a4} are conducting (s_{a1} and s_{a3} are blocking), $V_{CONV1} = 0$ ($S_1 = 0$); When s_{a2} is conducting (thus s_{a1} is blocking) and s_{a3} is conducting (thus s_{a4} is blocking), $V_{CONV1} = -V_{C1}$ ($S_1 = -1$).

Hence the switching model describing the relationship between input and output

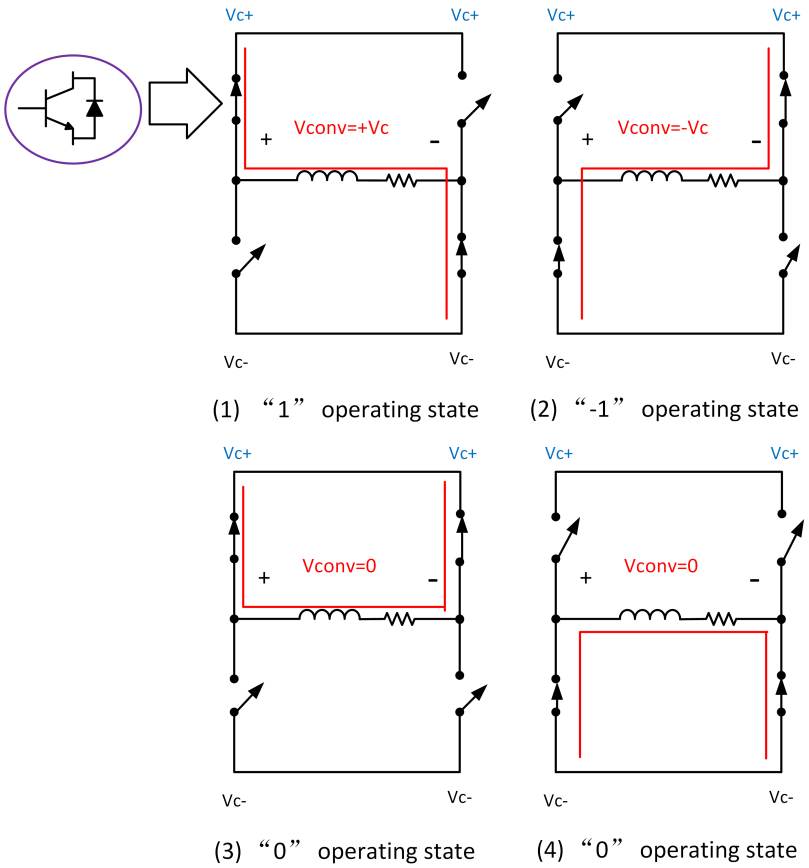

Figure 2.4.4 The switching function of an H-bridge cell for describing its operating states

voltages of each cell can be written by switching functions:

$$V_{CONV1} = S_1 V_{C1} \tag{2.4.1}$$
$$V_{CONV2} = S_2 V_{C2}$$
$$V_{CONV3} = S_3 V_{C3}$$

The AC terminal voltage V_{CONV} applied by the converter is the sum of

$$V_{CONV} = S_1 V_{C1} + S_2 V_{C2} + S_3 V_{C3} \tag{2.4.2}$$

Table 2.2 gives the possible values of V_{CONV} as a result of all the possible working states of a single H-bridge. Assume the ideal case when identical DC loads for each H-bridge or DC voltages balance scheme is applied and $V_{C1} = V_{C2} = V_{C3} = V_C$. So V_{CONV} has up to 7 levels in consequence, and each level is at the same voltage.

Table 2.2 Possible voltage levels of a three-cell CHB converter consists of the output AC terminal three-level voltage

V_{CONV}	H-bridges States
$3V_C$	(111)
$2V_C$	(110) (101) (011)
V_C	(100) (010) (001) (11-1) (1-11) (-111)
0	(000) (10-1) (-101) (1-10) (-110) (01-1) (0-11)
$-V_C$	(-100) (0-10) (00-1) (-1-11) (-11-1) (1-1-1)
$-2V_C$	(-1-10) (-10-1) (0-1-1)
$-3V_C$	(-1-1-1)

Simulation results for the multilevel voltages applied from each cell, and the AC terminal are shown in Fig.2.4.5. The voltage applied by the converter of each cell $V_{CONV1-3}$ is 3-level, with the same fundamental voltage. The sum up of the three voltages V_{CONV} is 7-level, and closer to a sinusoidal waveform. The equivalent switching frequency is triple of that of a single cell.

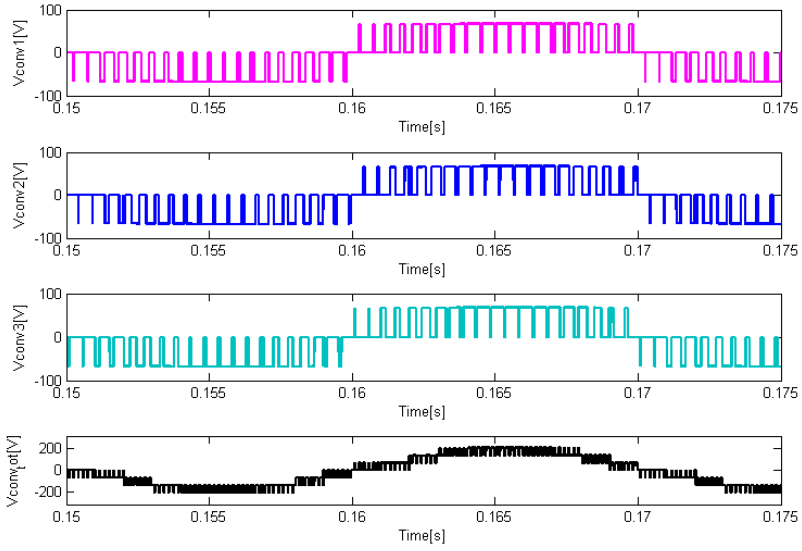

Figure 2.4.5 Modulated voltages produced by the converter (Switching frequency=2kHz, MI=0.5

The relationships of the current between the AC/DC side can be similarly derived by

the switching functions as:

$$I_{dc1} = S_1 I_L$$
$$I_{dc2} = S_2 I_L$$
$$I_{dc3} = S_3 I_L \tag{2.4.3}$$

As the equations indicate, the same current is flowing through all the cells on the AC side. Fig.2.4.6 is the simulation waveforms from PLECS of a CHB rectifier working in unity power factor, the average of the switching function, namely the sinusoidal modulating signal, is slightly ahead of I_L in phase with the amplitude of 0.8. Noted that there is a small negative area of I_{DC} during the zero crossing of I_L, this is due to the slight phase shift between the modulating signal and grid current.

A zoomed-in plot of the DC currents of each cell from the location of Fig.2.4.6 is shown in Fig.2.4.7, the switched DC currents are phase shifted but with the same fundamental waveform.

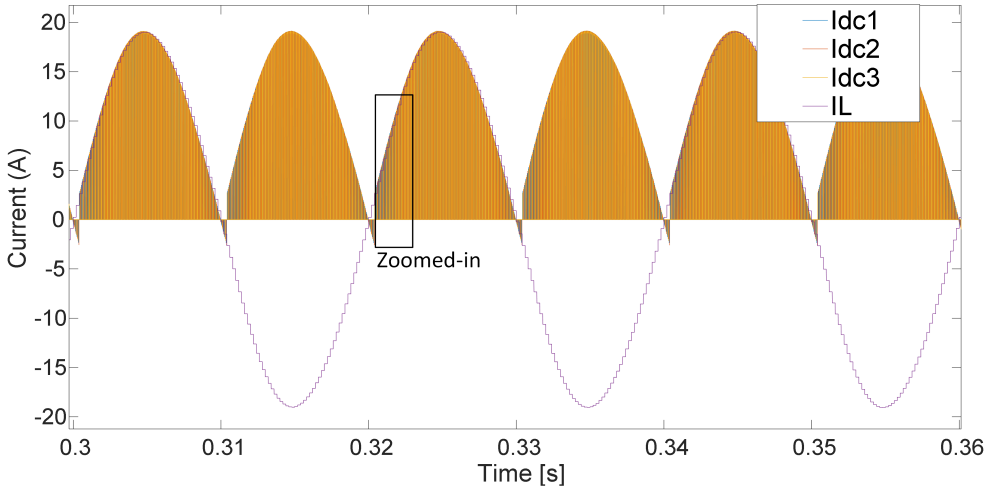

Figure 2.4.6 Overlaid AC and DC side current of CHB converter by applying PSC-PWM

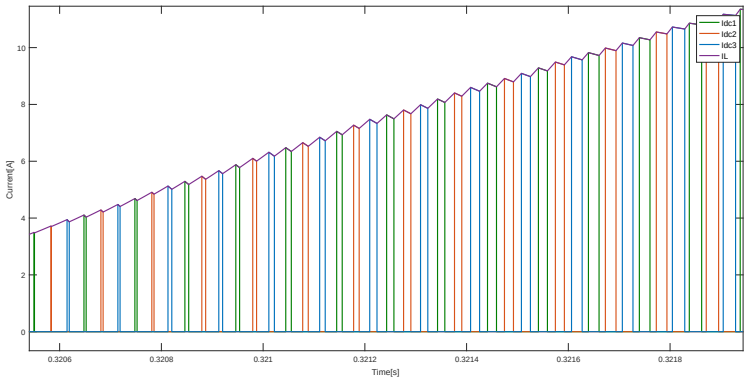

Figure 2.4.7 Zoomed-in part of Fig.2.4.6 showing phase-shifted DC currents

2.5 Summary

Multilevel converters are emerging technologies in grid integration, HVDC and many applications. This chapter gave a review of circuits, modulation, control and applications of the most known four multilevel topologies: DCC, FCC, CHB, and MMC. The four topologies are compared regarding losses and efficiency.

Finally, a single phase 3-cell 7-level CHB rectifier has been focused as the proposed topology, with the modulation strategy of PSC-PWM. The fundamental simulation waveforms are shown with the working concepts. In the next chapter, the control is included to regulate the AC current and DC voltage to complete the system whose stability is verified in this thesis.

Chapter 3

Control Design of Cascaded H-bridge Converter

3.1 Introduction

Various control schemes are under consideration for three-phase CHB converter and can be found in the literature. These control schemes can primarily be classified due to different reference frames: synchronous reference frame (dq) with Proportional plus Integral (PI) controllers; stationary reference frame ($\alpha\beta$) with Proportional Resonant controllers (PR); natural reference frame (abc) with predictive controllers.

Fig3.1.1 and Fig3.1.2 demonstrate two examples of control schemes that can be applied for three-phase CHB converter. In Fig3.1.1 the current is controlled in $\alpha\beta$ reference frame with PR controllers, the output is wanted voltages which are converted back to natural reference frame demands feeding the modulator; Fig3.1.2 applies a natural reference frame control and regulates the current of each phase individually. Since natural reference frame controllers have the flexibility of controlling each phase individually, it can be a big benefit when there are asymmetrical faults[81] or some single phase converter applications.

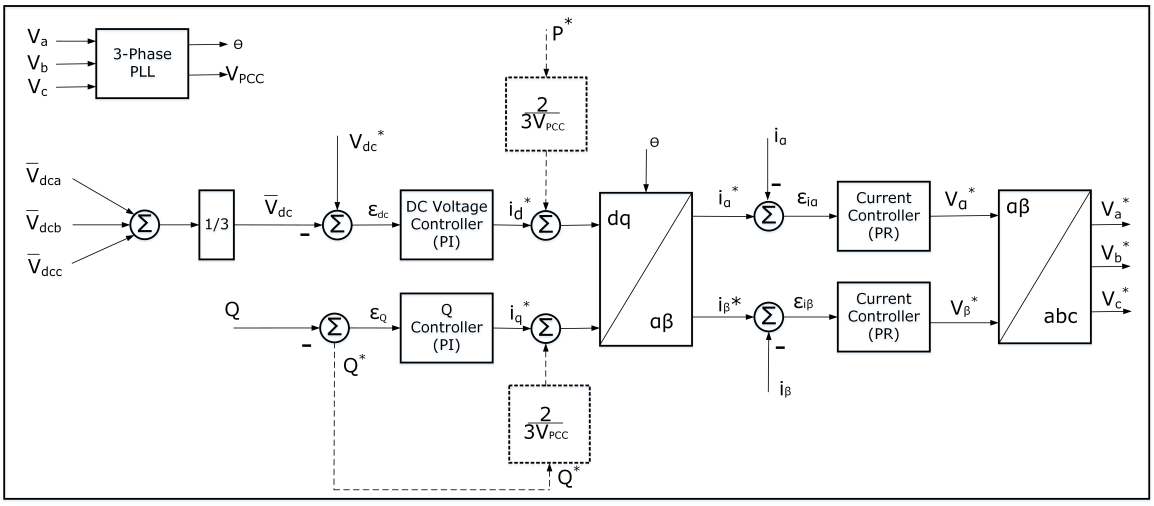

Figure 3.1.1 Stationary reference frame control strategy with global DC-link control[88]

Whereas this study is about the single-phase CHB scenario, the natural reference frame controller has been selected among others. The current in the natural frame is in AC form and requires a controller which can regulate AC signal. A fast PI controller can regulate the current to the AC reference. After all, in this study, a predictive Dead Beat Controller (DBC) is implemented to control the current. DBC is well-known for its breakneck speed which is far more than our need. The reason for using the predictive controller is that these controllers are becoming more and more widely used and their model-based nature brings more opportunities for instability phenomenon. Another benefit is its easy digital implementation.

Predictive controllers have become more and more widely used in power converters and drives due to several intrinsic characteristics of power electronics and modern control platform. Such as the non-linear characteristic and a finite number of switching states characteristic of power converters and drives[89]. Also, the discrete-time implementation and known models of converters and drives of present control systems all make the predictive controller a suitable solution[89].

Predictive control comprises Deadbeat Control (DBC), Model Predictive Control (MPC), and Generalized Predictive Control (GPC)[89]. DBC uses the model of the converter to calculate the voltage that makes the error zero at the next sampling

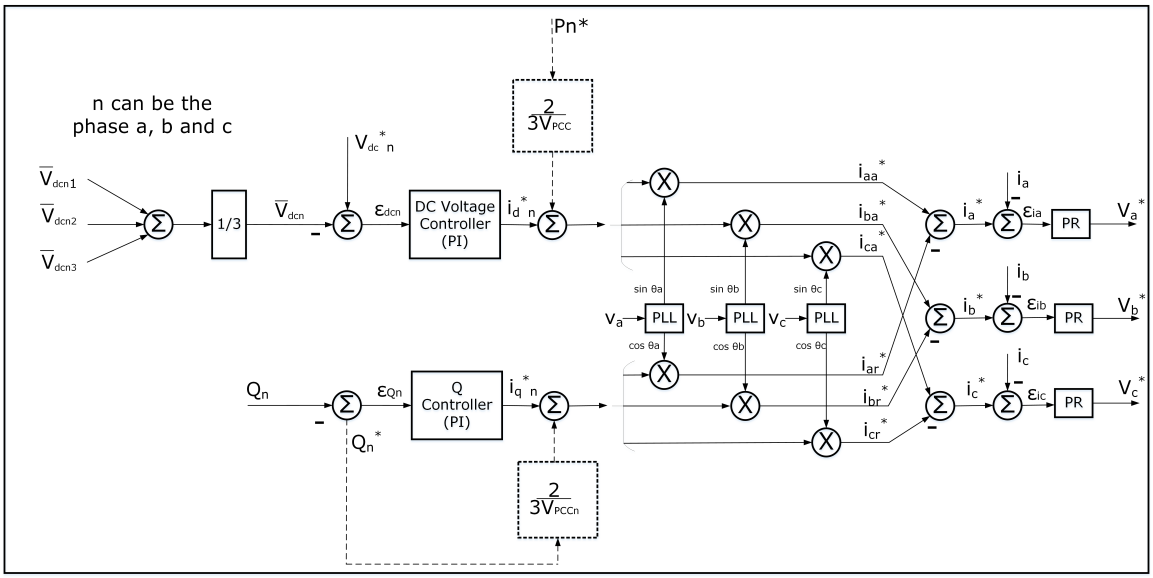

Figure 3.1.2 Natural reference frame control strategy with DC-link voltage control per phase[88]

time. This voltage is then applied to the converter via a modulator. DBC is known as the fastest control strategy since the controlled quantity can achieve its desired reference for only one sampling time. Another different but powerful predictive control is MPC[90, 91], which doesn't need a modulator but generates a vector that can be applied to the converter directly. This vector is chosen by minimising a cost function which represents the error. In [92] DBC and MPC applied to CHB are compared, indicating that DBC gives better current and power quality for MPC.

In this chapter, the design of the control of a single-phase 7-level CHB rectifier is illustrated. A traditional 2-loop control scheme has been applied. The inner loop is for imposing the desired grid current, under this condition the outer loop regulates the total DC link voltages to the reference. The outer loop controller is a classic PI; the inner loop is implemented by a fast deadbeat controller.

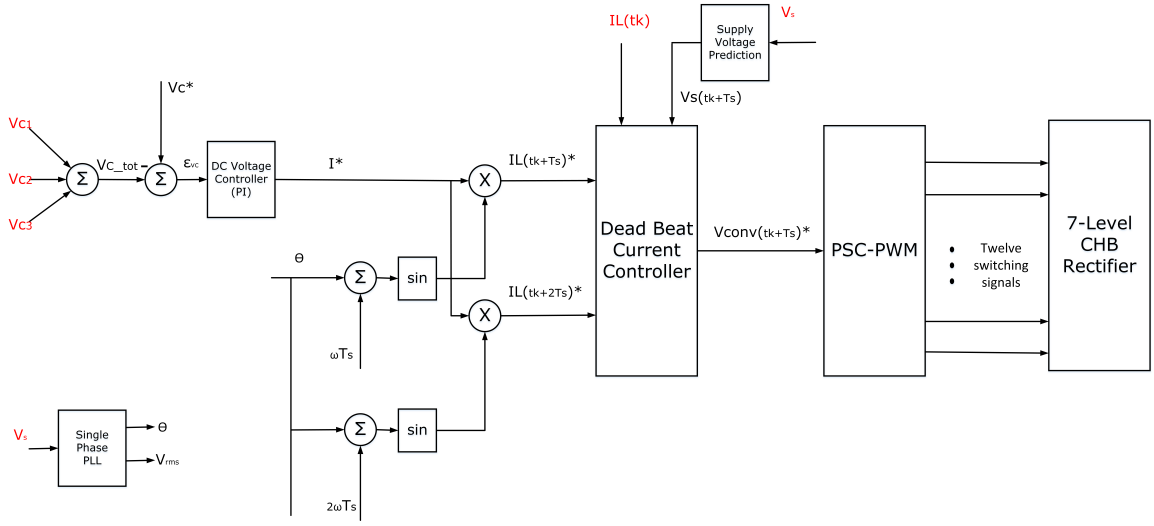

Figure 3.2.1 Schematic of overall control scheme applied in this work

3.2 Overall Control Scheme Applied for Single-Phase CHB Rectifier

The overall control scheme is presented in Fig.3.2.1. The voltages of the DC-link on each cell V_{C1}, V_{C2}, V_{C3} are measured and summed up giving the total DC-link voltage V_C. V_C is subtracted by the DC voltage reference V_{ref}, this gives the error signal ε_{VC} as the input of PI controller. The output of the PI controller is the desired amplitude of the AC current I^*.

In the inner current control loop, the current predictions after one and two sampling time $I_L(t_k + T_s)^*$, $I_L(t_k + 2T_s)^*$ are made by multiplying I^* with corresponding sinusoidal signals. The angle of the sinusoidal signal is decided by a Phase Lock Loop (PLL), which is capable of detecting the real-time phase angle of the grid voltage. The controller also requires the prediction of the supply voltage $V_S(t_k + T_s)$ at the next sampling made from the measurement of current sampling time $V_S(t_k)$, and the measurement of the current at the present sampling time $I_L(t_k)$. The output of DBC is the voltage reference of the next sampling time $V_{conv}(t_k + T_s)^*$, which is divided by V_{ref} is the modulating signal feeding the PSC-PWM modulator. The modulator generates the switching signals for the CHB converter. The AC current is thus regulated

to its reference with one or two samples delay when looked from the outer voltage loop.

The DC voltage controller and AC current controller can be designed separately due to their significant discrepancy of bandwidth, the bandwidth of the PI controller is much smaller than that of the DBC. In other words, the inner loop DBC is assumed to regulate the AC current very fast while the DC voltage is changing very slowly.

3.3 Proportional-Integral (PI) Voltage Controller Design

A classic PI controller is used to control the total DC-link voltage as PI is ideal for DC variable regulating. As its name indicates, PI is consist of a proportional part plus an integral part, by introducing this integrator in the loop gain, the open loop DC gain becomes infinity; hence the closed loop gain is 1, indicating a perfect reference tracking. The controller needs to be designed with steady-state accuracy, desired transient response and also with the chosen stability margins.

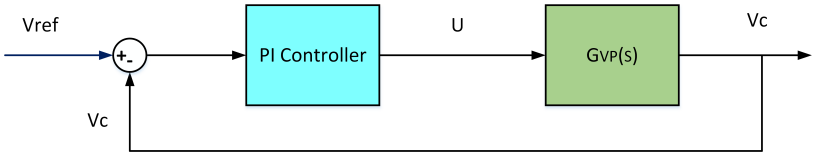

Figure 3.3.1 Block diagram regarding DC-link voltage control

The block diagram of PI control is shown in Fig.3.3.1. The PI transfer function is defined in s domain as:

$$PI(s) = \frac{U(s)}{V_{ref}(s) - V_C(s)} = k_p + \frac{k_i}{s} \tag{3.3.1}$$

Where k_p is the proportional gain and k_i is the integral gain, their values are to be decided by the closed loop dynamic requirements, s is the Laplace operator.

3.3.1 Plant Transfer Function

The first step is to find the transfer function of the plant $G_{VP}(s)$.

Single H-bridge DC Side Modelling

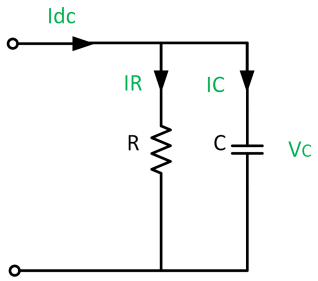

Figure 3.3.2 Schematic of H-bridge DC side

Consider the DC side of the *ith* H-bridge cell as shown in Fig.3.3.2, by applying Kirchhoff's current law then a linear time domain model can be derived as:

$$I_{dci}(t) = I_{Ri}(t) + I_{Ci}(t) = C\frac{dV_{Ci}(t)}{dt} + \frac{V_{Ci}(t)}{R}_{i=1,2,3} \tag{3.3.2}$$

To derive the transfer function of the model, the Laplace transform is applied to the differential equation:

$$I_{dci}(s) = sCV_{Ci}(s) + \frac{V_{Ci}(s)}{R}_{i=1,2,3} \tag{3.3.3}$$

Thus the plant transfer function of DC side of single cell is found to be:

$$G_{VPi}(s) = \frac{V_{Ci}(s)}{I_{dci}(s)} = \frac{1}{sC + 1/R} \tag{3.3.4}$$

$G_{VPi}(s)$, is always a stable transfer function since it has only a left-hand side pole, the explanation for this is that a converter in open loop is a physical system that is stable by construction.

Cascaded H-bridge DC Side Modelling

Then consider the DC side of a cascaded H-bridge converter, assume same DC loads are applied for each cell. Thus equation(3.3.3) can be summed up:

$$\sum_{i=1,2,3} I_{dci}(s) = sC \sum_{i=1,2,3} V_{Ci}(s) + \frac{1}{R} \sum_{i=1,2,3} V_{Ci}(s) \tag{3.3.5}$$

Define the total DC link voltage as V_C:

$$V_C = V_{C1} + V_{C2} + V_{C3} \tag{3.3.6}$$

The average of DC link current is identical, indicated as I_{dc}, then equation (3.3.5) can be further simplified as:

$$3I_{dc}(s) = sCV_C(s) + \frac{V_C(s)}{R} \tag{3.3.7}$$

The transfer function for the plant of total DC voltage of cascaded H-bridge converter is thus:

$$G_{VP}(s) = \frac{V_C(s)}{I_{dc}(s)} = \frac{3}{sC + 1/R} \tag{3.3.8}$$

3.3.2 PI Parameters Tuning

Consider a system configured as $R = 20\Omega$, $C = 2000\mu F$. The plant transfer function in s domain can be obtained:

$$G_{VP}(s) = \frac{3}{0.002s + 0.05}$$

Then the open loop transfer function can be written as:

$$OL(s) = \frac{k_p s + k_i}{s} \times \frac{3}{Cs + 1/R} \tag{3.3.9}$$

and the closed loop transfer function is thus:

$$CL(s) = \frac{OL(s)}{1 + OL(s)} = \frac{3(k_p s + k_i)}{s(sC + \frac{1}{R}) + 3(k_p s + k_i)} \tag{3.3.10}$$

An easy way to calculate the parameters of the PI controller is to compare the closed-loop gain with the well-known form of the standard second-order system:

$$G(s) = \frac{\omega_0^2}{s^2 + 2\zeta\omega_0 + \omega_0^2} \tag{3.3.11}$$

where the natural frequency ω_0 determines the speed of the system and the damping factor ζ represents the overshoot of a step response. Comparing the denominator of (3.3.10) and (3.3.11) k_p and k_i can be decided by:

$$2\zeta\omega_0 = \frac{1}{CR} + \frac{3k_p}{C} \tag{3.3.12}$$

$$\omega_0^2 = \frac{3k_i}{C} \tag{3.3.13}$$

In our design we choose the damping ζ to be 1, and choose the bandwidth of PI to be 5 Hz, thus ω_0 is 31 rad/s. These specifications give $k_p = 0.0166$, $k_i = 0.374$.

Fig.3.3.3 shows the step response of the closed-loop system, and the rise time is about 0.1 s, the steady-state error is zero. Fig.3.3.4 shows the bode plot for the open loop

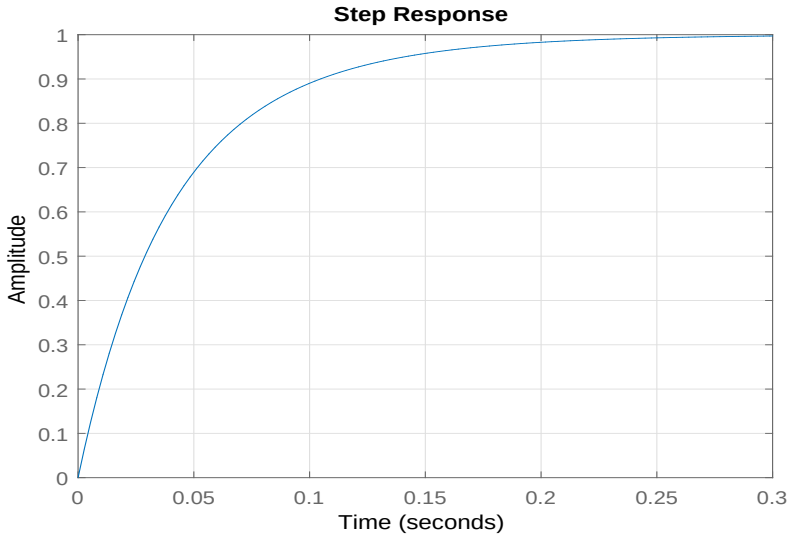

Figure 3.3.3 Step response of the closed-loop PI control system of the DC-link voltage

transfer function. The gain margin is infinity, and the phase margin is 87 degree so that the closed loop is within safety margins for the robustness of the system.

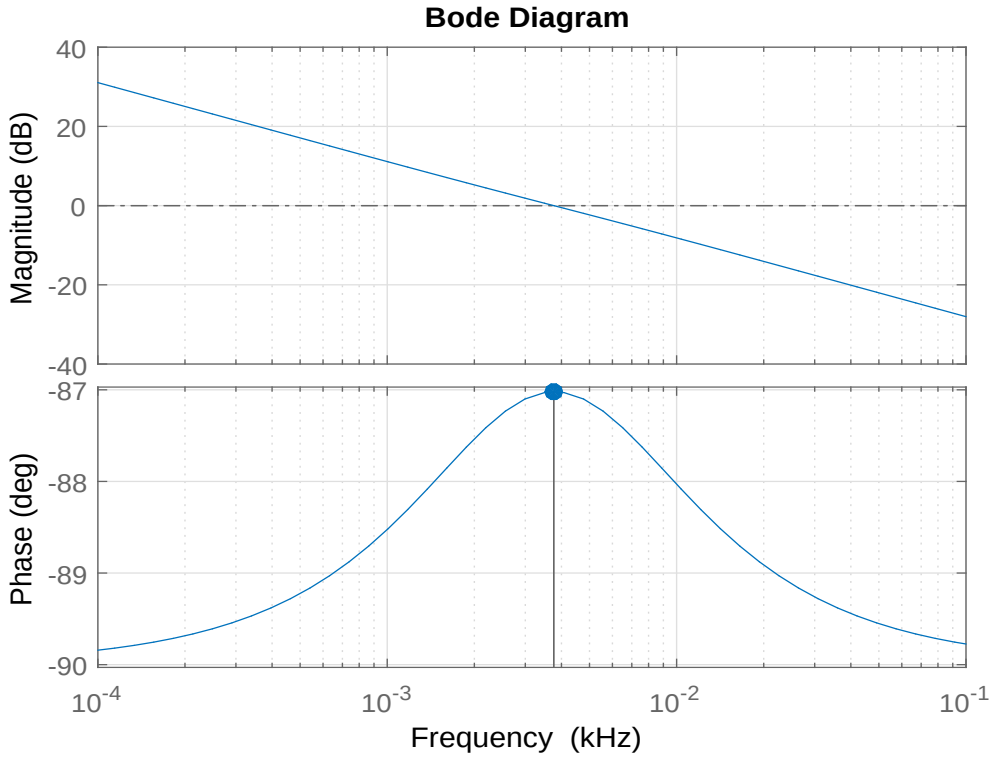

Figure 3.3.4 Bode plot of the open-loop control system for controlling DC-link voltage

The other alternative tuning method is frequency domain tuning. The frequency domain tuning is convenient for designing for more than one operating point. In this case, bode function in Matlab can be used. The open loop gain of the voltage loop is known, with desired phase margin (70 degrees in our calculation), crossover frequency (which is the desired bandwidth of the PI controller), and the switching frequency, the bode function can help to calculate the proportional gain k_p and the integral gain k_i. In table 3.2 k_p and k_i are calculate for a couple of different PI bandwidths using this tuning method.

Table 3.1 PI coefficient values for different bandwidths of the DC-link voltage controller

	50 Hz	60 Hz	70 Hz	80 Hz
k_p	0.0903	0.1112	0.1322	0.1531
k_i	59.6002	85.1959	115.3503	150.0632

3.4 Deadbeat Current Controller Design

The design of deadbeat control is a model based design in the discrete time domain. It has four main subsystems: PLL, desired current prediction, supply voltage prediction, and calculation of control law. An additional z domain analysis is presented to investigating its realisation.

3.4.1 Phase-Locked Loop

The angle and amplitude is essential feed-forward information for the power factor controllers to control the grid-connected rectifiers. In our case, to synchronise the converter with the grid, we need to generate the current reference in the same angle with the grid voltage in the deadbeat control. PLL is commonly utilised for detecting the phase angle[93]. PLL is a vital part of the control loop since its quality affects the control performance directly[93]. Fig3.4.1 shows one PLL structure applied for

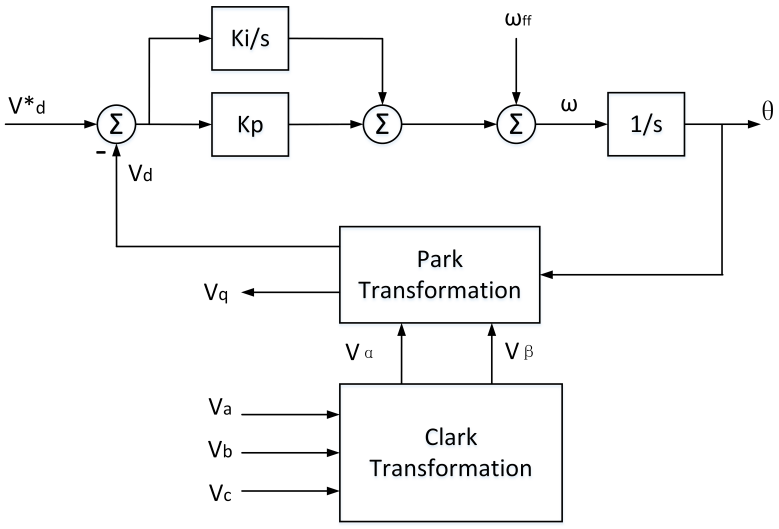

Figure 3.4.1 Three-phase PLL structure[94]

the three-phase system, which was introduced in [95], where ω_{ff} is the feed-forward frequency, the three-phase voltages are first transformed to two-phase voltages via the Clark transformation, and then transformed to stationary reference frame by

using Park transformation. The direct component V_d is controlled to be zero by a PI controller, resulting in the lock-in of the PLL output θ on the phase of the voltage vector. The phase signal, the instantaneous frequency (ω) and amplitude of the grid voltage can be known as well. The tuning of the $k_p^{'}$ and $k_i^{'}$ are based on the small signal model of the three-phase structure[94].

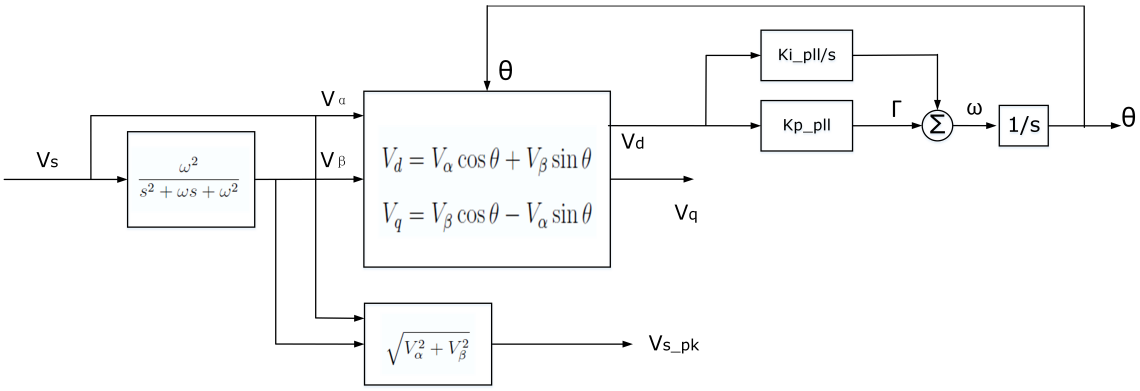

Figure 3.4.2 Single-phase PLL structure

In our case, single-phase PLL is required since that in this study single-phase converter is connected to single-phase grid. Implementation of single-phase PLL can be more challenging than the implementation for the three-phase PLL since there is less information regarding the grid condition and there is a lack of grid voltage vector. The single-phase PLL is derived from the three-phase structure, and one possible schematic is exhibited in Fig3.4.2. The method is to generate a fictitious orthogonal system like the $\alpha - \beta$ system in the three phase. Align the real grid voltage to α axis and a fake orthogonal voltage on the β axis 90 degrees ahead of the real grid voltage. The peak amplitude of the supply voltage can be calculated by:

$$V_{Spk} = \sqrt{V_{S\alpha}^2 + V_{S\beta}^2} \tag{3.4.1}$$

The orthogonal voltage can be formed by applying a Second Order Generalised Integrator(SOGI) method from [96]. The transfer functions of SOGI can be represented by:

$$\frac{V_{S\beta}}{V_S} = \frac{k\omega^2}{s^2 + k\omega s + \omega^2} \tag{3.4.2}$$

Where k is a coefficient affecting the bandwidth of the closed loop of SOGI, selection of k value would vary the dynamic of the SOGI system, in our case the value of k is 1[96], and ω is the angular frequency of the input voltage of 50 Hz, small variations in the 50 Hz grid haven't been considered. Since that it could greatly complicate the instability study of the converter and as a result, an ideal 50 Hz supply was considered in simulations, and also the grid was implemented using a programmable AC supply practically so the there is no variation in the supply voltage.

An alternative method to generate the orthogonal voltage is to use an all-pass filter[45], whose transfer function is given by:

$$H(s) = \frac{s - \omega}{s + \omega} \tag{3.4.3}$$

Where omega is the angular frequency of supply voltage. This all-pass filter has 0 dB gain for all the frequency, and 90 degrees for the wanted 50 Hz input.

The tuning of the PI controller is similar to the tuning of the voltage loop PI controller. Only except that the open loop gain is different, for the PI inside PLL design, the open loop gain merely is an integrator. A couple of the calculated results are given in Table 3.2 for the PLL bandwidths of interest. These values are also accepted in the implementation of stability analysis in the later chapters.

Table 3.2 PI controller coefficient values for different bandwidths within the PLL structure

	40 Hz	45 Hz	50 Hz	55 Hz	60 Hz
$k_p^{'}$	125.6637	141.3717	157.0796	172.7876	188.4956
$k_i^{'}$	5.4703e4	6.9233e4	8.5473e4	1.0342e5	1.2308e5

The results of single-phase PLL are displayed in Fig.3.4.3. The angle is detected in radiance within the range of [0, 2π]. The RMS value of the input voltage is also measured with a delay because of the SOGI, but this delay is allowable as it is fast enough concerning the closed-loop control.

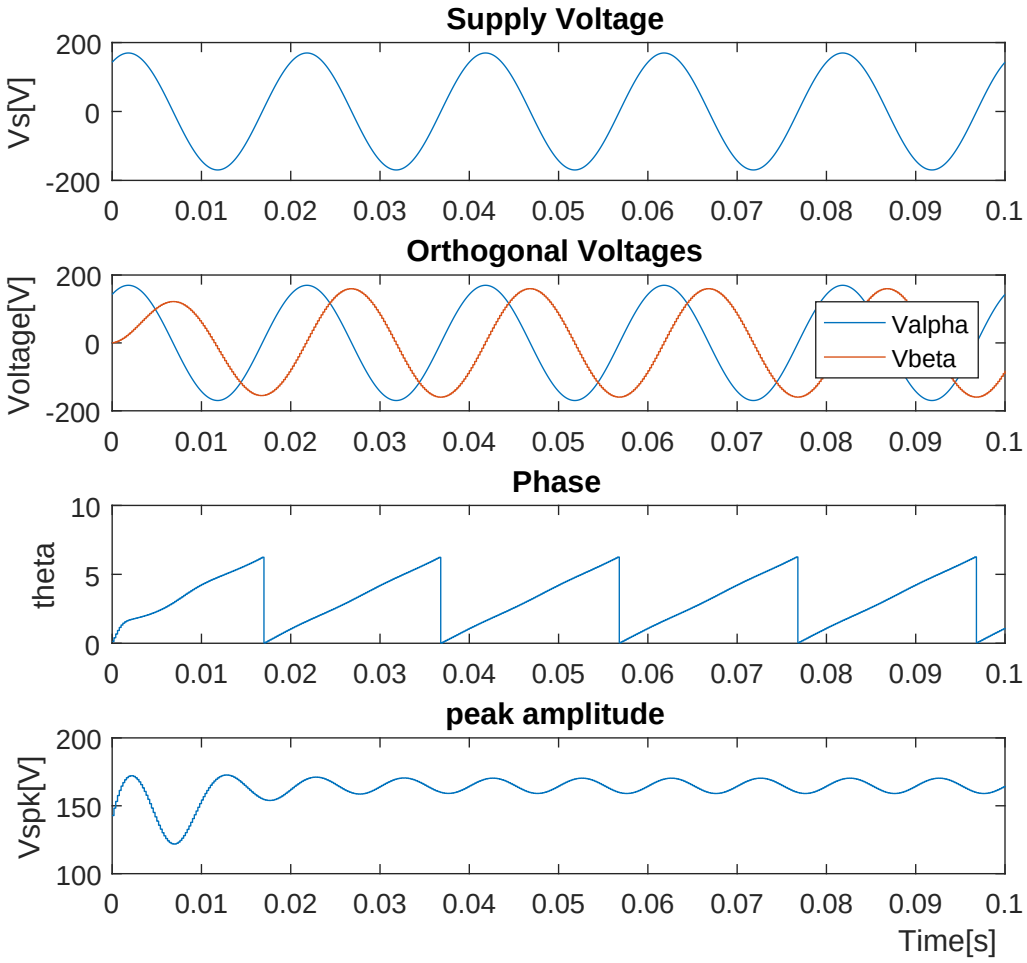

Figure 3.4.3 Simulation results of the single-phase phase-locked loop

3.4.2 Deadbeat Control Law Derivation

Deadbeat control is employed for the inner current control loop for its high bandwidth and reliable accuracy. Deadbeat control is based on the discretised modelling of the system; therefore the discretising method applied to the continuous model is a vital factor in the quality of the control. In this section, the derivation of classic control law and an improved control law will be delivered. The improved dead beat control is proposed in [97], and it has better accuracy and suitable with low switching frequency. Generally, in high power applications, a lower switching frequency is yearned for better

efficiency[97], and the reduced switching frequency can worsen the performance of the deadbeat control dramatically.

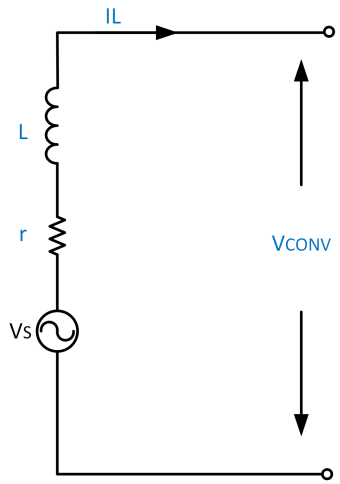

Figure 3.4.4 AC side of the rectifier schematic

On the AC side of the rectifier as shown in Fig.3.4.4, apply Kirchhoff's voltage law the ODE of the plant for the current controller can be obtained:

$$V_S(t) - V_{CONV}(t) = L\frac{dI_L(t)}{dt} + rI_L(t) \tag{3.4.4}$$

To implement the dead beat control in DSP, discretisation of the AC side continuous model is needed.[98, 99]. At time t_k discretion the model as:

$$V_S(t_k) - V_{CONV}(t_k) = L\frac{dI_L(t)}{dt}_{t=t_k} + rI_L(t_k) \tag{3.4.5}$$

From (3.4.5) it can be seen that a good approximation of the derivative of I_L at time t_k is vital on obtaining an accurate discrete model.

By applying the Taylor series expansion formula, the current value at the next sampling time can be derived from the current value and its derivatives at the current sampling by:

$$I_L(t_k + T_S) = \sum_{i=0}^{\infty} \frac{I_L^{(i)}(t_k)}{i!} T_S^i \tag{3.4.6}$$

Where $i!$ denotes the factorial of i and $I_L^{(i)}(t_k)$ denotes the ith derivative of I_L evaluated at t_k, T_S^i denotes T_S to the ith power. The derivative of order zero of I_L is defined to be itself, and T_S^0 and 0! are both defined to be 1. We don't need to do the expansions with an infinite number of terms, a truncated number of terms is employed for the approximation of modelling, for example, the truncated series with four terms are usually good enough as in equation (3.4.7). So the error between this approximation and the accurate solution is of order T_S^4, denoted by $O(T_S^4)$, means that as T_S approaching 0, the remaining part of the series is proportional to T_S^4.

$$I_L(t_k + T_S) = I_L(t_k) + T_S I'_L(t_k) + \frac{T_S^2}{2} I''_L(t_k) + \frac{T_S^3}{6} I'''_L(t_k) + O(T_S^4) \tag{3.4.7}$$

First Order Approximation: Classic dead beat

If only two terms are remained in the truncated series:

$$I_L(t_k + T_S) = I_L(t_k) + T_S I'_L(t_k) + O(T_S^2) \tag{3.4.8}$$

An approximation of the first order derivative can be represented as:

$$I'_L(t_k) + O(T_S) = \frac{I_L(t_k + T_S) - I_L(t_k)}{T_S} \tag{3.4.9}$$

Thus the derivative of the line current can be approximated by:

$$\frac{dI_L(t)}{dt}_{t=t_k} = \frac{I_L(t_k + T_S) - I_L(t_k)}{Ts} + O(T_S) \tag{3.4.10}$$

The error between the first order approximation and the continuous model is proportional to the sampling time T_S. Substitute (3.4.10) to (3.4.4) thus the classic dead beat control law in discrete time domain at the kth sampling time can be derived as:

$$V^*_{CONV}(t_k) = V_S(t_k) - \frac{L}{Ts}[I_L(t_k + T_S) - I_L(t_k)] - rI_L(t_k) \tag{3.4.11}$$

Second Order Approximation: Improved dead beat

Truncate the Taylor series backward for two terms:

$$I_L(t_k - T_S) = I_L(t_k) - T_S I'_L(t_k) + O(T_S^2) \tag{3.4.12}$$

Subtract (3.4.12) from (3.4.8), then a second order approximation of the derivative of I_L is shown as following (the order of error increases by 1, because the even order terms are cancelled out by subtraction in the remained part of the truncated series):

$$I'_L(t_k) + O(T_S^2) = \frac{I_L(t_k + T_S) - I_L(t_k - T_S)}{2T_S} \tag{3.4.13}$$

Follow this pattern, the derivative of I_L at time $t_k + T_S$ is:

$$\frac{dI_L(t)}{dt}_{t=t_k+T_S} = \frac{I_L(t_k + 2T_S) - I_L(t_k)}{2Ts} + O(T_S^2) \tag{3.4.14}$$

The error of the second order Taylor approximation is proportional to the square of sampling time, thus more accurate than the first order Taylor approximation. Thus an improved deadbeat control law derived from the second-order approximation can be derived as:

$$V^*_{CONV}(t_k + T_S) = V_S(t_k + T_S) - \frac{L}{2Ts}[I_L(t_k + 2T_S) - I_L(t_k)] + rI_L(t_k + T_S) \tag{3.4.15}$$

A block diagram for implementing the improved dead beat (3.4.15) is illustrated in

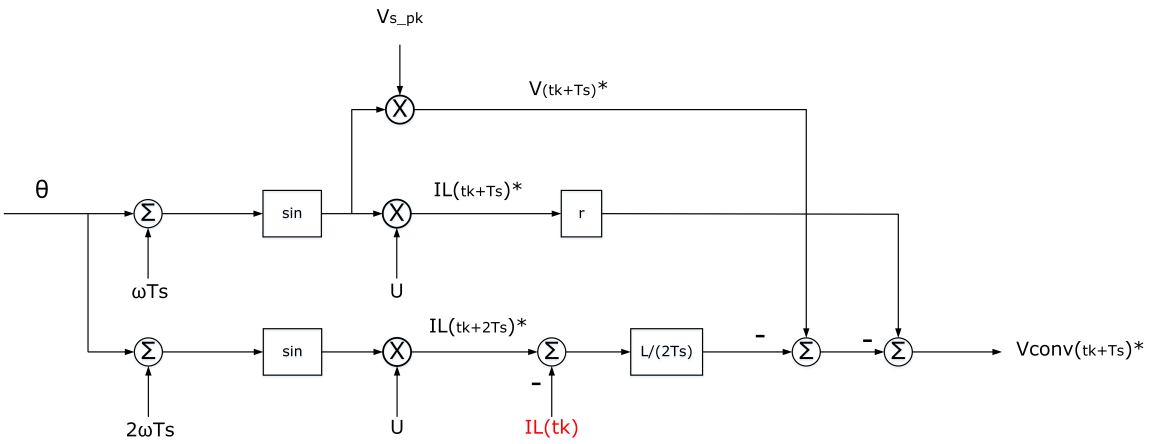

Figure 3.4.5 Block diagram of deadbeat control methodology applied for the single-phase CHB rectifier

Fig3.4.5.

3.4.3 Simulation Results of Control Scheme

The classic deadbeat control law can be implemented by ignoring the intrinsic delay of the real control response. Consequently, the current would equal its desired current at the next sampling time. However, in reality, the operating of DSPs would always bring in a delay, which is at least one sample time.

So it is better to implement the deadbeat control law (3.4.15). In this case, the grid current tracks its reference after two sampling time. The calculated desired voltage is imposed on the modulator one sampling period after sampling.

The control law (3.4.11) and (3.4.15) are both simulated in PLECS, their current tracking ability is shown in Fig.3.4.6a. They both regulate the line current to the sinusoidal reference. Fig.3.4.6b is the zoomed-in plot, which clearly shows that with classic control law the grid current gets its reference within one sampling time. Moreover, with the improved control law, the grid current gets its reference after two sampling periods.

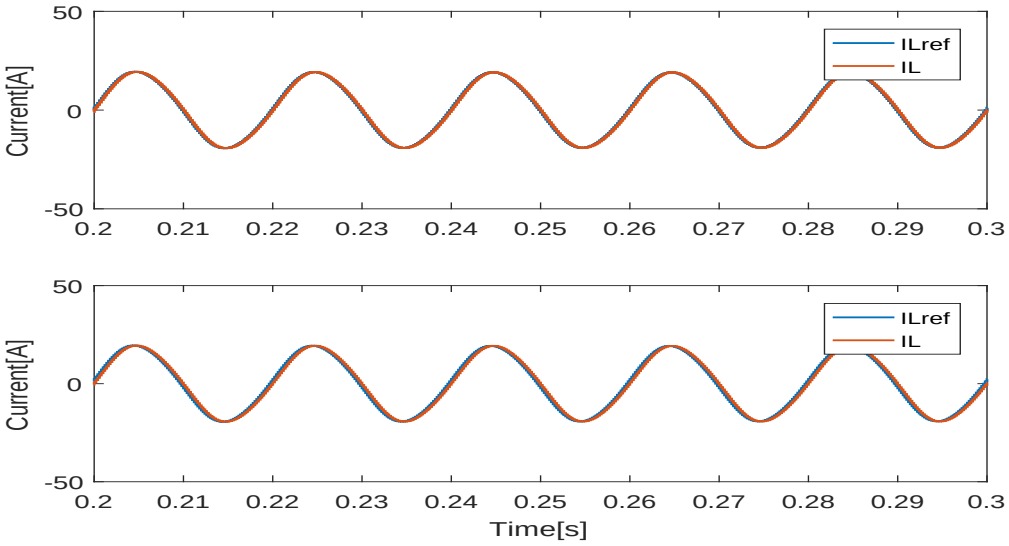

(a) Overlaid current reference and actual current

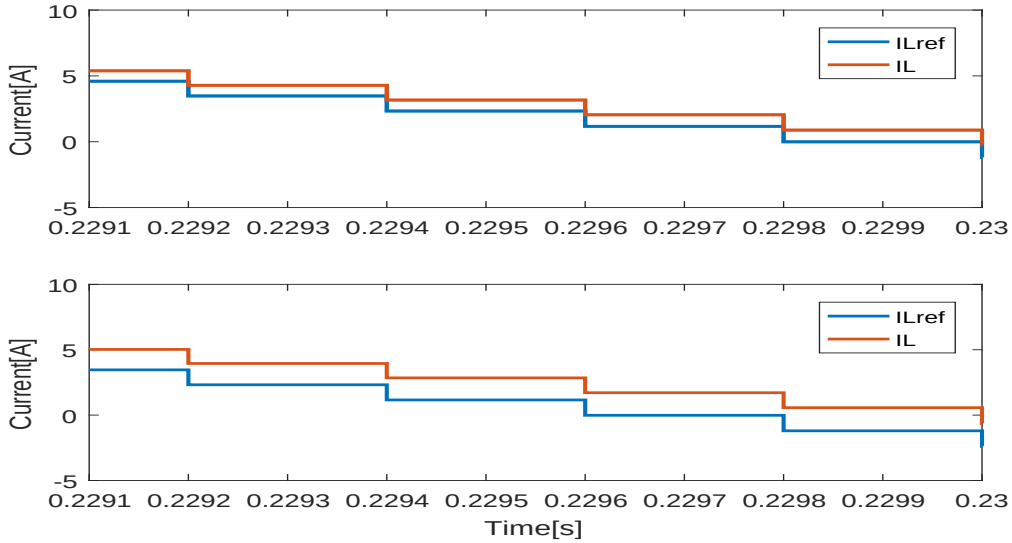

(b) Zoomed-in plot of current reference and actual current

Figure 3.4.6 Simulation results of the current deadbeat controller

3.5 Summary

This chapter delivers a detailed process of the control design and implementation. The final goal is to fulfil the unity power factor operation of the rectifier. At the same time, the total DC link voltage has been controlled at a level required by the active power and the AC current has the allowed THD level.

In the design, it is assumed that the voltages of DC link on each cell are at the same level, while this is normally not true even though the same configured DC link parameters are set up because of the differences of manufacturing of each device. Hence the balancing control of the DC link control is also an essential issue. Some relevant DC balance schemes can be found in [100, 101], with the specific PWM method. However, the DC balance scheme appears "invisible" to the whole control; thus it is convenient to do the analysis assuming the DC link voltages of each cell are already balanced. It will also be verified by practical implementation of the converter that the balancing scheme is not needed in this study because even if it's missing in the experiment, the experimental results show that the voltages on each cell are balanced.

So far, the 2-loop control has been designed for the grid-connected CHB rectifier. The simulation results indicate that the designed control can work to the expectations. However, the input of the PLL can be distorted by the transmission line impedance, and it might further distort the model based current controller. In the following analysis, the effect of the control loop on the stability of the system is further investigated.

Chapter 4

Stability Analysis of Buck Converter with Constant Power Load

4.1 Introduction

This chapter is to present the stability study of an ideal and elemental implementation of a Buck converter. The aim is to give a simple example to test the application of the stability analysis methods with an example system of a DC-DC buck converter with constant power load (CPL).

The system is non-linear because of the characteristic of the CPL, the commonly-used linearisation approach implies that there is *Hopf Bifurcation* phenomenon and that the system may be unstable when the load power is beyond its maximum threshold. So a novel perturbation method is applied for developing the mathematical model for the system where it is close to the unstable condition. Therefore provided a detailed description of the system's operation and a thorough understanding of the instability.

4.2 System Description

The system schematic is shown in Fig.4.2.2; a step-down DC-DC buck converter is connected with a constant power load (CPL). Buck converter is a common used DC-DC converter for converting higher DC input voltage to lower DC output voltage. In practical, CPLs can be referred to the highly regulated converters as loads connected to AC or DC power systems [102, 103]. In our case, the CPL is connected in parallel with the convention resistive load to bring in non-linearity to the system.

One crucial characteristic of CPL is its negative input impedance[104], Fig.4.2.1 gives its voltage-current characteristic plot, which is a hyperbola and the slope of the curve indicates the resistance value. The instantaneous impedance depends on the operating point, for example, R_1 and R_2 on the figure are two different impedances of two different operating points.

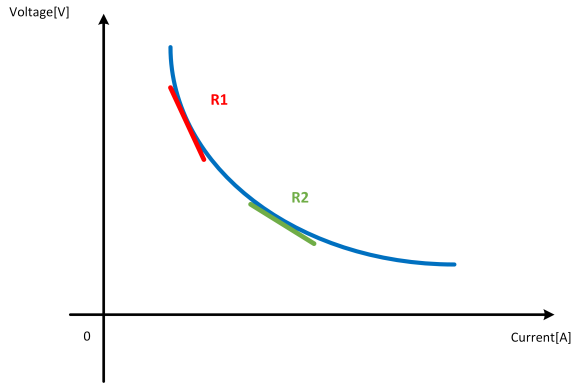

Figure 4.2.1 Voltage-current characteristic of CPL

The buck converter is assumed to be an ideal circuit, which consists of a fully-controlled-switch (in our case turned on/off by a constant-duty-cycle PWM signal), an ideal diode, an inductor L, a capacitor C, and a load resistor R. The CPL is represented by a controlled current source, whose input power is constant.

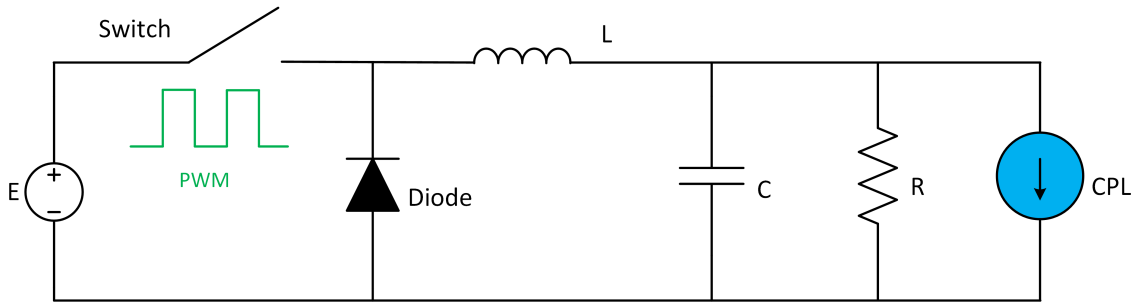

Figure 4.2.2 Topology of a buck converter with a CPL load

4.2.1 System Averaged Model

The operation of the converter can be regarded as having two phases depends on the state of the switch shown in Fig.4.2.3. Phase one: when the switch is turned on, namely during time $nT < t < (n + D)T, 0 < D < 1$ where D (0¡D¡1) is the duty cycle, T is the switching period; Phase two: when the switch is turned off, when $(n+D)T < t < (n+1)T$. The state space equations of two phases with instantaneous

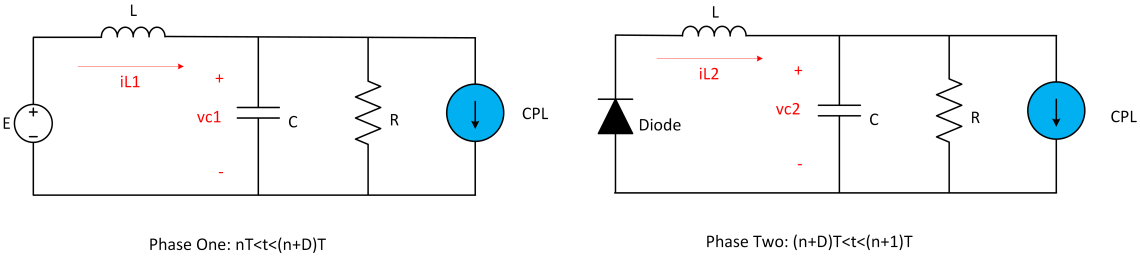

Figure 4.2.3 Two working modes of the buck converter

state variables are:

$$(1)\frac{\mathrm{d}v_{c1}}{\mathrm{d}t} = \frac{i_{L1}(t) - v_{c1}(t)/R - P_L/v_{c1}(t)}{C} \qquad (2)\frac{\mathrm{d}v_{c2}}{\mathrm{d}t} = \frac{i_{L2}(t) - v_{c2}(t)/R - P_L/v_{c2}(t)}{C}$$

$$\frac{\mathrm{d}i_{L1}}{\mathrm{d}t} = \frac{E - v_{c1}(t)}{L} \qquad \frac{\mathrm{d}i_{L2}}{\mathrm{d}t} = \frac{-v_{c2}(t)}{L}$$

Where E is the supply DC voltage, P_L is the power of CPL. Take the averages of the state variables during one switching period, denote the averages as V and I:

$$V = Dv_{c1} + (1 - D)v_{c2} \tag{4.2.1}$$

$$I = Di_{L1} + (1 - D)i_{L2} \tag{4.2.2}$$

Assume that the switching frequency is very high, we could suppose that the state variables change slightly between the two operating modes and make the assumptions:

$$i_{L1} = i_{L2} = I$$

$$v_{c1} = v_{c2} = V$$

Thus:

$$\begin{aligned}\frac{dV}{dt} &= \frac{d(Dv_{c1} + (1-D)v_{c2})}{dt} \\ &= D\frac{dv_{c1}}{dt} + (1-D)\frac{dv_{c2}}{dt} \\ &= D\frac{i_{L1} - v_{c1}/R - P_L/v_{c1}}{C} + (1-D)\frac{i_{L2} - v_{c2}/R - P_L/v_{c2}}{C}\end{aligned}$$

With the assumptions, it can be simplified to:

$$\frac{\mathrm{d}V}{\mathrm{d}t} = \frac{I - V/R - P_L/V}{C} \tag{4.2.3}$$

Similarly, we get

$$\frac{\mathrm{d}I}{\mathrm{d}t} = \frac{DE - V}{L} \tag{4.2.4}$$

Equations (4.2.3) and (4.2.4) are called the averaged model of the system.

4.3 Stability of Equilibrium Point and *Hopf Bifurcation*

4.3.1 Equilibrium Point and Eigenvalues

The equilibrium point is derived by making the derivatives in equation(4.2.3)(4.2.4) to be zero, then we get (4.3.1)(4.3.2). It is noted that the equilibrium current exists for all values of P_L, while the equilibrium voltage is independent of P_L.

$$V_0 = DE \tag{4.3.1}$$

$$I_0 = \frac{DE}{R} + \frac{P_L}{DE} \tag{4.3.2}$$

To examine the stability of the equilibrium point, we linearise around the equilibrium by calculating its *Jacobian matrix*, which is in the form of:

$$J = \begin{pmatrix} \frac{-1}{CR} + \frac{P_L}{CV^2} & \frac{1}{C} \\ \frac{-1}{L} & 0 \end{pmatrix} = \begin{pmatrix} \frac{-1}{CR} + \frac{P_L}{CD^2E^2} & \frac{1}{C} \\ \frac{-1}{L} & 0 \end{pmatrix} \tag{4.3.3}$$

The eigenvalues can be calculated by the determinant of the system:

$$det(\lambda I - J) = 0, \tag{4.3.4}$$

This gives the characteristic equation of the system in equ(4.3.5) and the expression of eigenvalues in equ(4.3.6).

$$\lambda^2 - (\frac{-1}{CR} + \frac{P_L}{CD^2E^2})\lambda + \frac{1}{LC} = 0 \tag{4.3.5}$$

$$\lambda_{1,2} = \frac{(\frac{-1}{CR} + \frac{P_L}{CD^2E^2}) \pm \sqrt{(\frac{-1}{CR} + \frac{P_L}{CD^2E^2})^2 - \frac{4}{LC}}}{2} \tag{4.3.6}$$

4.3.2 Eigenvalue Observations and *Hopf Bifurcation*

We next show that the equilibrium point is stable for small P_L. We discuss a particular case about the characteristic equation when P_L is very close to zero, the equation (4.3.5) then has a simpler form (4.3.7), and the new eigenvalues are then expressed as equ(4.3.8).

$$\lambda^2 + \frac{1}{CR}\lambda + \frac{1}{LC} \approx 0 \tag{4.3.7}$$

$$\lambda = \frac{-\frac{1}{CR} \pm \sqrt{\frac{1}{C^2R^2} - \frac{4}{LC}}}{2} \tag{4.3.8}$$

Plus, we can know the relationship between the two eigenvalues from the equation:

$$\lambda_1 + \lambda_2 = -\frac{1}{CR} \tag{4.3.9}$$

$$\lambda_1\lambda_2 = \frac{1}{LC} \tag{4.3.10}$$

There are two possibilities; either both eigenvalues are real negative numbers, or two eigenvalues are a pair of complex conjugate numbers and their real parts are negative. Whichever the above case, the system is always stable. However, the system can become unstable either when the real λs passes through zero or when the real part of complex λs passes through zero. Note that we cannot have any eigenvalue to be 0 since their multiplication is nonzero. But we can have $\lambda_1 = j\omega$, and $\lambda_2 = -j\omega$ where ω is real. Substitute these to equation (4.3.9) and (4.3.10) we can get:

$$\omega^2 = \frac{1}{LC} \tag{4.3.11}$$

$$P_L = \frac{D^2E^2}{R} \tag{4.3.12}$$

(4.3.12) is the maximum value of the load power that can be loaded to the buck converter. If load power is bigger than this, the buck converter becomes unstable.

We now use computer simulations to study the local trajectories and *Hopf bifurcation*. In the simulation, the system parameters are set referring to Table.4.1. Correspondingly, some important variables are shown in Table.4.2.

Table 4.1 System parameters

Names	Values
Switching Period T	20 μs
Duty Cycle D	0.5
Input Voltage E	120 V
Load Resistance R	100Ω
Inductance L	37.5mH
Capacitance C	420μF

Table 4.2 Some important results corresponding to parameters set in Table 4.1

Names	Values
Equilibrium V_0	$60V$
Equilibrium I_0	$1.2A$
Maximum Load Power P_0	$36W$
ω	$252rad/s$

Since the maximum load power of CPL is $36W$, we give a range of P_L around P_0 and their corresponding eigenvalues in Table 4.3. It can be seen that when P_L is below

P_0, the eigenvalues are a pair of complex conjugate numbers with negative real parts, indicating stable equilibrium point; when P_L is equal to P_0, the eigenvalues are two purely imaginary numbers, showing an occurrence of the *hopf bifurcation*; and when P_L is above P_0, the eigenvalues are a pair of complex conjugate numbers with positive real parts, thus the equilibrium become unstable. Fig.4.3.1 shows the locus of the complex eigenvalue pair corresponding to Table.4.3, and Fig.4.3.5 shows the 3D view of the eigenvalues dependent on the values of P_L, the conjugate eigenvalue pair is moving from the left-hand-side of the imaginary axis to the right-hand-side of it as P_L is increasing, crossing it when P_L equals $36W$.

Table 4.3 Eigenvalue showing dependence on P_L

$P_L(W)$	Eigenvalues	Remarks
31	$-1.6534 \pm j251.97$	Stable Equilibrium Point
32	$-1.3228 \pm j251.97$	Stable Equilibrium Point
33	$-0.9920 \pm j251.97$	Stable Equilibrium Point
34	$-0.6614 \pm j251.98$	Stable Equilibrium Point
35	$-0.3307 \pm j251.98$	Stable Equilibrium Point
36	$0 \pm 251.98j$	Threshold
37	$0.33069 \pm 251.98j$	Unstable Equilibrium Point

Eigenvalues also give information about the dynamic of the system. The value of the real part of the eigenvalue determines the decay rate of the system response, the imaginary part of the eigenvalue determines the oscillating rate. In Fig.4.3.2 we plot the dynamic time responses and the local trajectories or *phase portrait* for three different eigenvalues, respectively. For eigenvalues are conjugate with negative real parts, the dynamic is decaying, the phase portrait is spiralling into a stable point. For eigenvalues are purely imaginary, the dynamic has no decay but only oscillates, the phase portrait is a periodic one; for eigenvalues are conjugate with positive real parts, the system has a divergent and unstable response, and the phase portrait is spiralling out. We could see that there seems a limit cycle on the phase portrait plane, inside the limit cycle local trajectories are spiralling in, while outside this cycle local trajectories are spiralling outward. Thus this limit cycle is unstable, and we call it *subcritical Hopf bifurcation*.

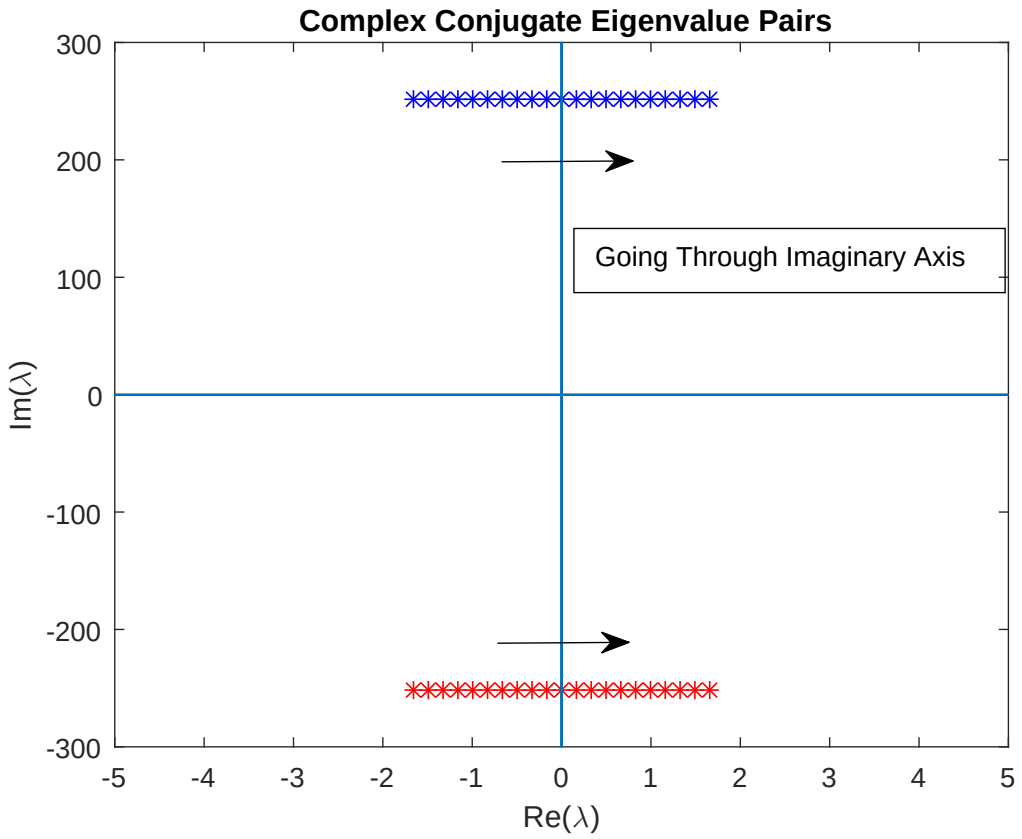

Figure 4.3.1 Locus of the complex eigenvalue pair corresponding to Table.4.3

Fig.4.3.5 shows a better description for the *Hopf bifurcation*. It plots the phase portrait against P_L in a 3D view. The starting conditions for all the phase portraits are at the same point. We see that the phase portraits all spirals in if below P_0, and all spirals out if above P_0. It indicates the existence of the limit cycle boundary of the stability.

In the above analysis, the loci of the eigenvalues and the local trajectories are studied. Computer simulations are performed to capture the effects of the variation of P_L on the qualitative behaviour of the system. In particular, it is shown that simple averaged models can be used to predict the occurrence of *Hopf bifurcation* in such systems.

Usually, an engineer would stop here since the average model can predict that there is a threshold value for the load power P_L if the load power is bigger than this value

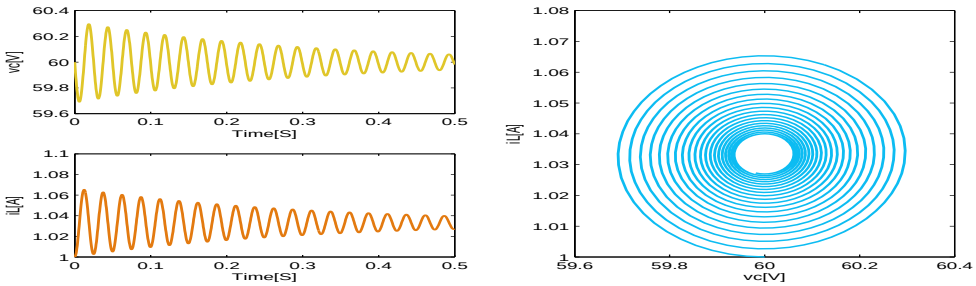

(a) Pair of eigenvalues has negative real parts

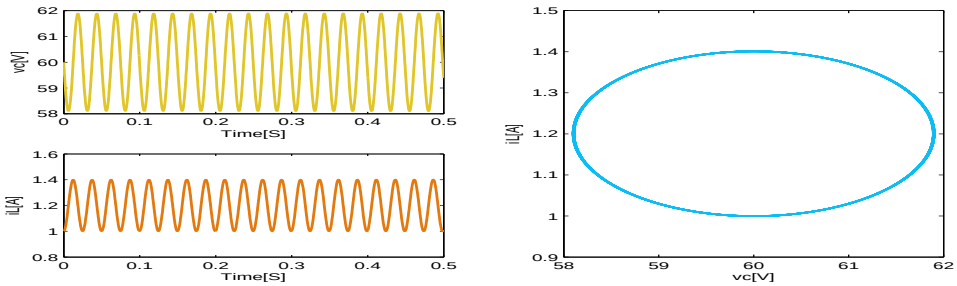

(b) Eigenvalues are purely imaginary numbers

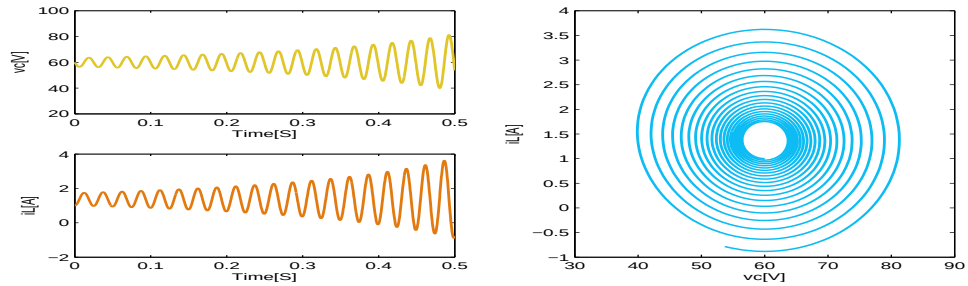

(c) Pair of eigenvalues has positive real parts

Figure 4.3.2 Effect of eigenvalues on system responses and phase portrait

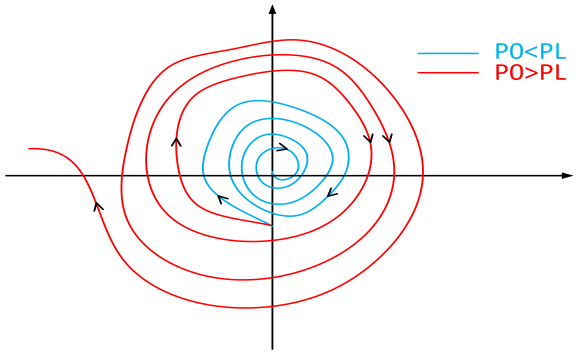

Figure 4.3.3 Illustration of limit cycle

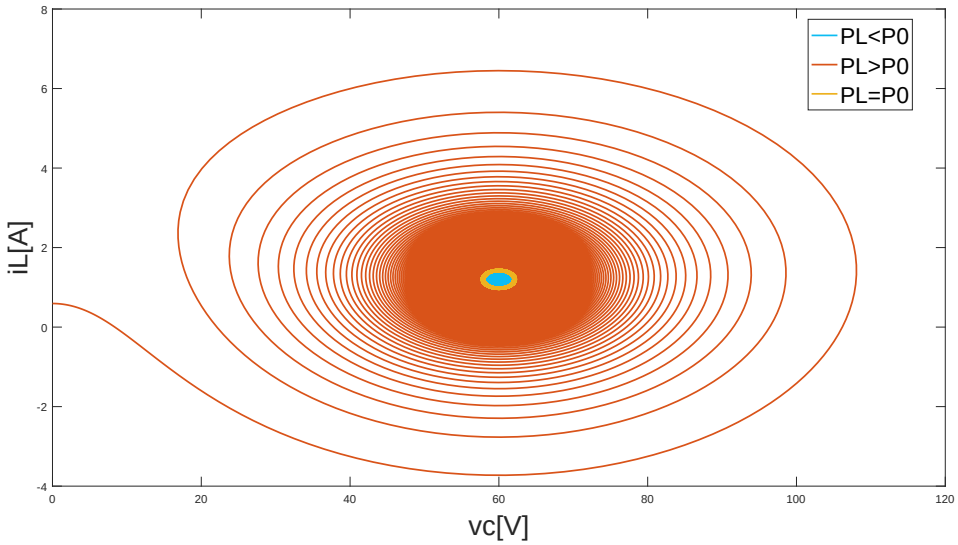

Figure 4.3.4 Limit cycle

the system would become unstable. However, the things that happen close to this threshold we can not know just by the average model. So in the following, we are applying a mathematical approach which helps us look at in more detail what happens close to the threshold and also give some information about the initial conditions.

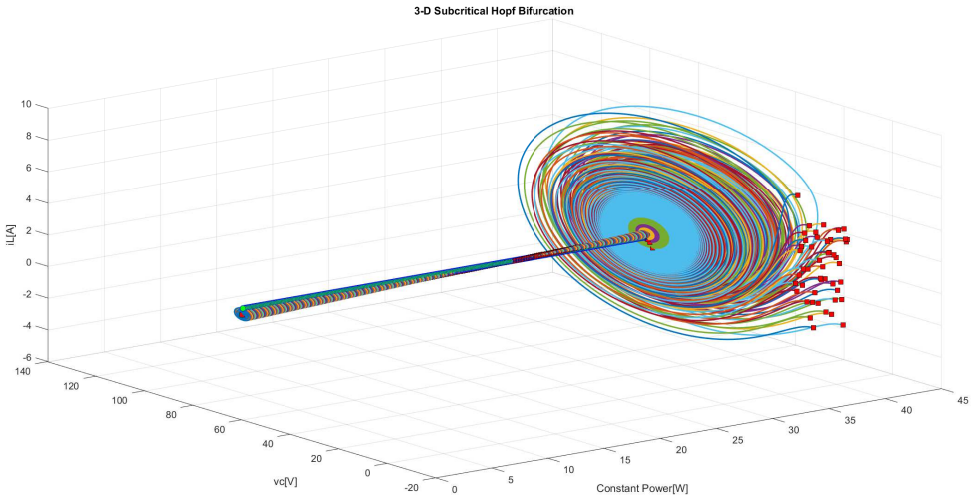

Figure 4.3.5 3D view of the *Hopf Bifurcation*

4.4 Mathematical Weakly Non-linear Method

We now extend the linear stability analysis of the previous section to derive weakly non-linear expressions for the solutions for the analysis of the instability. We apply a method with a perturbation expansion to obtain an approximate solution to the full problem.

The result is an approximation to the solution when the load power is very close to the threshold, and the starting point is from the limit cycle.

First we introduce a Landau symbol *big O*, we say $f(\varepsilon) = O(g(\varepsilon))$ *as* $\varepsilon \to 0$ if for some non-zero constant A:

$$\lim_{\epsilon \to 0} \frac{f(\epsilon)}{g(\epsilon)} = A$$

We aim to find the system's solution in the form of power series perturbation expansion:

$$V = V_0 + \varepsilon V_1 + \varepsilon^2 V_2 + \varepsilon^3 V_3 + \cdots \tag{4.4.1}$$

$$I = I_0 + \varepsilon I_1 + \varepsilon^2 I_2 + \varepsilon^3 I_3 + \cdots \tag{4.4.2}$$

Where ε is a very small value ($0 < \varepsilon \ll 1$), V_0 represents the solution at order $O(\varepsilon^0)$, V_1, V_2.V_3 indicates the perturbation solutions at order $O(\varepsilon^1)$, $O(\varepsilon^2)$, $O(\varepsilon^3)$, respectively. And similar for (4.4.2).
We regard the constant load power P_L as our bifurcation parameter and consider values of P_L very close to threshold P_0, so assume that:

$$P_L = P_0 + \varepsilon^2 P_2 \tag{4.4.3}$$

The approach is to substitute these assumptions to the system ODEs (4.2.3)(4.2.4), and solve the equations by each order. The non-linear term P_L/V can be simplified with the assistance of the Taylor series. Thus we get two governing equations (4.4.5)(4.4.5).

$$\begin{aligned} & C(\varepsilon\frac{\mathrm{d}V_1}{\mathrm{d}t} + \varepsilon^2\frac{\mathrm{d}V_2}{\mathrm{d}t} + \varepsilon^3\frac{\mathrm{d}V_3}{\mathrm{d}t} + \cdots) \\ = \;& I_0 + \varepsilon I_1 + \varepsilon^2 I_2 + \varepsilon^3 I_3 - \frac{1}{R}(V_0 + \varepsilon V_1 + \varepsilon^2 V_2 + \varepsilon^3 V_3 + \cdots) - \\ & \frac{P_0 + \varepsilon^2 P_2}{V_0}[1 - \varepsilon\frac{V_1}{V_0} - \varepsilon^2\frac{V_2}{V_0} - \varepsilon^3\frac{V_3}{V_0} + \varepsilon^2\frac{V_1^2}{V_0^2} + 2\varepsilon^3\frac{V_1 V_2}{V_0^2} - \varepsilon^3\frac{V_1^3}{V_0^3}] \end{aligned} \tag{4.4.4}$$

$$L(\varepsilon\frac{\mathrm{d}I_1}{\mathrm{d}t} + \varepsilon^2\frac{\mathrm{d}I_2}{\mathrm{d}t} + \varepsilon^3\frac{\mathrm{d}I_3}{\mathrm{d}t}) = DE - V_0 - \varepsilon V_1 - \varepsilon^2 V_2 - \varepsilon^3 V_3 \tag{4.4.5}$$

By collecting terms order-by-order, we can obtain the state space equations for each order and do the analysis respectively.

4.4.1 At the leading order $O(\varepsilon^0)$

Collect the terms in (4.4.5) (4.4.5) of the order of $O(\varepsilon^0)$ then we get:

$$\begin{aligned} C\frac{\mathrm{d}V_0}{\mathrm{d}t} &= I_0 - \frac{V_0}{R} + \frac{P_0}{V_0} \\ L\frac{\mathrm{d}I_0}{\mathrm{d}t} &= DE - V_0 \end{aligned} \tag{4.4.6}$$

By making these two differential equations equal zero, the solutions are the equilibria, namely the voltage and current values for the steady state as before:

$$V_0 = DE \tag{4.4.7}$$

$$I_0 = \frac{DE}{R} + \frac{P_0}{DE} = 2\frac{DE}{R} \tag{4.4.8}$$

4.4.2 At $O(\varepsilon)$ order

Collecting the terms of $O(\varepsilon)$ order in (4.4.5) (4.4.5), the state-space equation can be written as:

$$C\frac{\mathrm{d}V_1}{\mathrm{d}t} = I_1 - \frac{V_1}{R} - \frac{P_0}{V_0^2}V_1 \tag{4.4.9}$$

$$L\frac{\mathrm{d}I_1}{\mathrm{d}t} = -V_1 \tag{4.4.10}$$

If we seek solutions in the form of:

$$\begin{pmatrix} V_1 \\ I_1 \end{pmatrix} = \begin{pmatrix} \bar{V_1} \\ \bar{I_1} \end{pmatrix} \mathrm{e}^{\lambda t} \tag{4.4.11}$$

Where $\bar{V_1}$ and $\bar{I_1}$ are the amplitude of the perturbation. Substitute the solution to (4.4.10), yields:

$$L\lambda\bar{I_1} = -\bar{V_1} \tag{4.4.12}$$

We study the situation when the *Hopf bifurcation* occurs, that is when the responses of the system do not decay but only do the stable oscillation around the equilibrium point. so $\lambda = \pm j\omega$. For

$$\lambda = j\omega, Lj\omega\bar{I_1} = -\bar{V_1}$$

The corresponding eigenvector is

$$\begin{pmatrix} -Lj\omega \\ 1 \end{pmatrix}$$

Similarly, for

$$\lambda = -j\omega, -Lj\omega\bar{I_1} = -\bar{V_1}$$

The corresponding eigenvector is

$$\begin{pmatrix} Lj\omega \\ 1 \end{pmatrix}$$

With their corresponding eigenvector we can write at $0(\varepsilon)$ the solution takes the following form according to the superposition property:

$$\begin{pmatrix} V_1 \\ I_1 \end{pmatrix} = A \begin{pmatrix} -j\omega L \\ 1 \end{pmatrix} e^{j\omega t} + A^* \begin{pmatrix} j\omega L \\ 1 \end{pmatrix} e^{-j\omega t} \tag{4.4.13}$$

A and A^* are a pair of complex conjugate numbers. For the convenience of calculation, we write A in the form of $re^{j\theta}$, where r is the amplitude of A which decides the amplitude of the current spectra. In the following calculations in higher orders, we would be able to decide the value of r. Observing the linear voltage and current plots, it seems that there are two different time scales: one is the normal amplitude decay time scale, the other is a much slower oscillating time scale, with much higher frequency. Assume $T_0 = \varepsilon^0 t = t$, the original time scale and $T_2 = \varepsilon^2 t$. The oscillation is verified with $A(T_2)$ and $A^*(T_2)$.

Also, if we substitute the solution to (4.4.5), we can get the same threshold value of ω and P_0 as in (4.3.11)(4.3.12).

4.4.3 At $O(\varepsilon^2)$order

At O(ε^2)order the state-space equation can be written as:

$$C\frac{\mathrm{d}V_2}{\mathrm{d}t} = I_2 - \frac{P_0}{V_0^3}V_1^2 - \frac{P_2}{V_0} \tag{4.4.14}$$

$$L\frac{\mathrm{d}I_2}{\mathrm{d}t} = -V_2 \tag{4.4.15}$$

There is only one non-linear term V_1^2 which can be calculated as:

$$V_1^2 = -L^2\omega^2 A^2 e^{2j\omega t} + 2 \mid A \mid^2 L^2\omega^2 - L^2\omega^2 A^{*2} e^{-2j\omega t}$$

Since V_2 and I_2 contain the terms of $e^{\pm 2j\omega}$ and constants, so put

$$V_2 = \alpha_1 e^{2j\omega t} + \alpha_2 + \alpha_3 e^{-2j\omega t}$$
$$I_2 = \beta_1 e^{2j\omega t} + \beta_2 + \beta_3 e^{-2j\omega t}$$

Substitute V_2 and I_2 to equation(4.4.15) and equation(4.4.14) we have the solution at O(ε^2)order:

$$V_2 = \frac{-2jA^2L^3\omega^3}{3V_0R} e^{2j\omega t} + \frac{2jA^{*2}L^3\omega^3}{3V_0R} e^{-2j\omega t} \tag{4.4.16}$$
$$I_2 = \frac{A^2L^2\omega^2}{3V_0R} e^{2j\omega t} + \frac{A^{*2}L^2\omega^2}{3V_0R} e^{-2j\omega t} + \frac{P_2}{V_0} + \frac{2 \mid A \mid^2 L^2\omega^2}{V_0R} \tag{4.4.17}$$

The $e^{\pm 2j\omega t}$ terms represent the second harmonics, the above equations indicate an existing constant perturbation to I, but no perturbation to V. This is consistent with the fact that the equilibrium V is independent of P_L but that the equilibrium I depends on P_L.

4.4.4 At $O(\varepsilon^3)$ order

Collect the terms of the order of $O(\varepsilon^3)$ of the expansion expressions and get the equations:

$$C\frac{\mathrm{d}V_3}{\mathrm{d}t} = I_3 + \frac{P_2V_1}{V_0^2} - \frac{2V_1V_2}{V_0R} + \frac{V_1^3}{V_0^2R} \tag{4.4.18}$$
$$L\frac{\mathrm{d}I_3}{\mathrm{d}t} = -V_3 \tag{4.4.19}$$

The *forcing terms* (those are proportional to V_1V_2 and V_1^3) include terms of both $e^{\pm j\omega t}$ terms and $e^{\pm 3j\omega t}$ terms.

$e^{\pm j\omega t}$ terms are called secular or resonant terms, and $e^{\pm 3j\omega t}$ terms are called non-secular terms. The secular forcing terms proportional to $e^{\pm j\omega t}$ generate a resonant response proportional to $te^{\pm j\omega t}$, whose amplitude grows linearly with time. The linear growth eventually causes the asymptotic expansion upon which the analysis is based to become invalid. Hence such terms must be suppressed.

Then we get a reasonable agreement with the exact solution and no secular growth, but the phase is slightly wrong. However, we do not care much about the frequency but only the amplitude of the approximate solution. So if we consider:

$$C\frac{\mathrm{d}V_3}{\mathrm{d}t} = I_3 + \Delta e^{j\omega t} + \Delta^* e^{-j\omega t} \tag{4.4.20}$$

$$L\frac{\mathrm{d}I_3}{\mathrm{d}t} = -V_3 \tag{4.4.21}$$

Here Δ is the coefficient of the $e^{j\omega t}$ terms, and Δ^* is the conjugate coefficient of the $e^{-j\omega t}$ terms. Observing the above equations we can assume that V_3 and I_3 are in the form of:

$$V_3 = \alpha e^{j\omega t} + \alpha^* e^{-j\omega t} \tag{4.4.22}$$

$$I_3 = \beta e^{j\omega t} + \beta^* e^{-j\omega t} \tag{4.4.23}$$

And also from (4.4.18) we have

$$Cj\omega\alpha = \beta + \Delta \tag{4.4.24}$$

Δ is the coefficient of the $e^{\pm j\omega t}$ terms in the state-space equation, we find Δ by taking into account derivatives with respect to T_2. So we can assume that:

$$V = V(T_0, T_2) \tag{4.4.25}$$

$$I = I(T_0, T_2) \tag{4.4.26}$$

Then we can use the chain rule to get the new expression:

$$C\frac{\partial V(T_0, T_2)}{\partial t} = C\frac{\partial V}{\partial T_0}\frac{\partial T_0}{\partial t} + C\frac{\partial V}{\partial T_2}\frac{\partial T_2}{\partial t} \tag{4.4.27}$$

After substitution, (4.4.18) stays the same, (4.4.19) becomes:

$$L\frac{dI_3}{dt} + L\frac{dA}{dT_2}e^{j\omega t} + L\frac{dA^*}{dT_2}e^{-j\omega t} = -V_3 \tag{4.4.28}$$

which gives

$$Lj\omega\beta + L\frac{dA}{dT_2} = -\alpha \tag{4.4.29}$$

From (4.4.24)(4.4.29), hence

$$LC\omega^2\beta - LCj\omega\frac{dA}{dT_2} = \beta + \Delta \tag{4.4.30}$$

We know that $\omega^2 = LC$ get an expression for Δ

$$\Delta = -LCj\omega\frac{dA}{dT_2} \tag{4.4.31}$$

Find the coefficient of $e^{j\omega t}$ terms we can get the second formula for Δthat

$$\Delta = (\frac{-4\omega^2L^3}{3V_0^2R^2C} - \frac{3j\omega^3L^3}{V_0^2R})A^2A^* - \frac{Lj\omega}{V_0^2}AP_2 + LCj\omega\frac{dA}{dT_2} \tag{4.4.32}$$

Equating the two expressions for Δ (4.4.31) and (4.4.32) gives

$$2LCj\omega\frac{dA}{dT_2} = \frac{Lj\omega}{V_O^2}AP_2 - (\frac{-4\omega^2L^3}{3V_0^2R^2C} - \frac{3j\omega^3L^3}{V_0^2R})A^2A^* \tag{4.4.33}$$

Put $A = r(T_2)e^{j\theta(T_2)}$ gives

$$\frac{\mathrm{d}A}{\mathrm{d}T_2} = (\frac{\mathrm{d}r}{\mathrm{d}T_2} + jr\frac{\mathrm{d}\theta}{\mathrm{d}T_2})e^{j\theta} \tag{4.4.34}$$

Thus

$$\frac{dr}{dT_2} = \frac{P_2}{2V_0C}r + \frac{3\omega^2L^2}{2CV_0^2R}r^3 \tag{4.4.35}$$

$$= \frac{P_2}{2V_0C}r + \frac{3L}{2C^2V_0^2R}r^3 \tag{4.4.36}$$

This gives two equilibrium points:

(1)

$$r = 0$$

Namely the equilibrium point, exists for all the values of P_2;or

(2)

$$r = \sqrt{-\frac{RC}{3L}P_2}$$

Exists only for $P_2 < 0$, hence this is the sub-critical bifurcation.

4.4.5 Composite Perturbation Solution

We now can go back to calculate the amplitudes of I_1 and V_1 since we have known the amplitude of A, referring to equation(4.4.13) we could have:

$$I_1 = 2rcos(\omega t + \theta) \tag{4.4.37}$$

$$V_1 = 2\omega Lrsin(\omega t + \theta) \tag{4.4.38}$$

Similarly, calculate the amplitudes of I_2 and V_2 according to (4.4.16)(4.4.17) so that we can have the composite solution in the form of (4.4.1) (4.4.2). In Fig.4.4.1 the perturbation solution is plotted together with the exact solution, we can see that the amplitude of the perturbation solution agrees with the exact solution, but the phase does not, which is as expected.

4.4.6 Limit Cycle Size

Having the mathematical model by the non-linear perturbation method allows us to calculate the size of the limit cycle. We now predict that on the current axis, the distance from the edge of the limit cycle to the equilibrium is:

$$max(I - I_{eq}) = \varepsilon max(I_1) \tag{4.4.39}$$

$$= 2\varepsilon r \tag{4.4.40}$$

Similarly, for the voltage the distance is predicted as:

$$max(V - V_{eq}) = \varepsilon max(V_1) \tag{4.4.41}$$

$$= 2\omega L\varepsilon r \tag{4.4.42}$$

To verify our prediction about the size of the limit cycle, we check the size of the limit cycle on the phase plot. As in Fig.4.4.3, the equilibrium point on the phase portrait is at the point $(60, 1.2)$, we set P_L as $35W$, and ε to be 0.001, thus we see the distance from the edge of the limit cycle to the equilibrium is that $60 - 48.47 =$

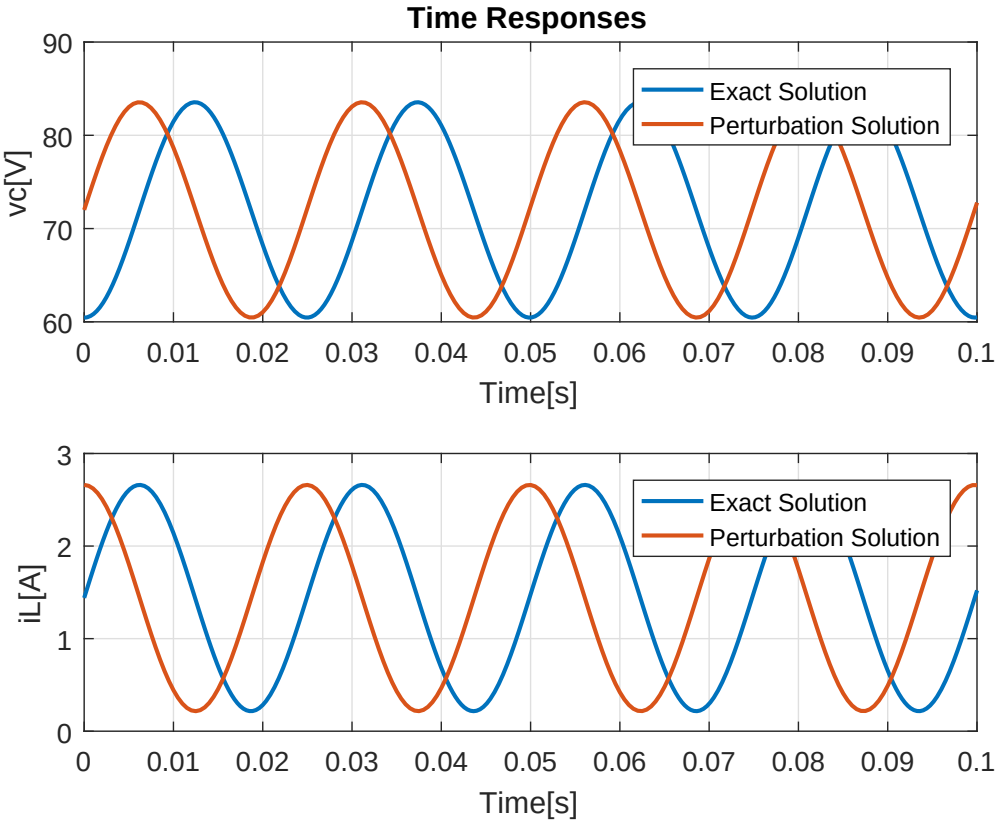

Figure 4.4.1 Comparison of the exact solution by solving system ODEs with the solution by using perturbation method

$71.53 - 60 = 11.53V$ and $2.42 - 1.2 = 1.2 - (-0.02) = 1.22A$, and 11.53 is the value of $2\omega L\varepsilon r$, 1.22 is the value of $2\varepsilon r$, respectively, as expected.

The size of the limit cycle gives us information about the initial conditions. Namely, to ensure the stability of such a system, for example, a system configured with parameters in Table4.1, the initial conditions must be inside the limit cycle. That is to say, the initial voltage must be no less than $48.47V$ and no more than $71.53V$. So the initial current must be no less than $-0.02A$ and no more than $2.42A$, otherwise the system becomes unstable.

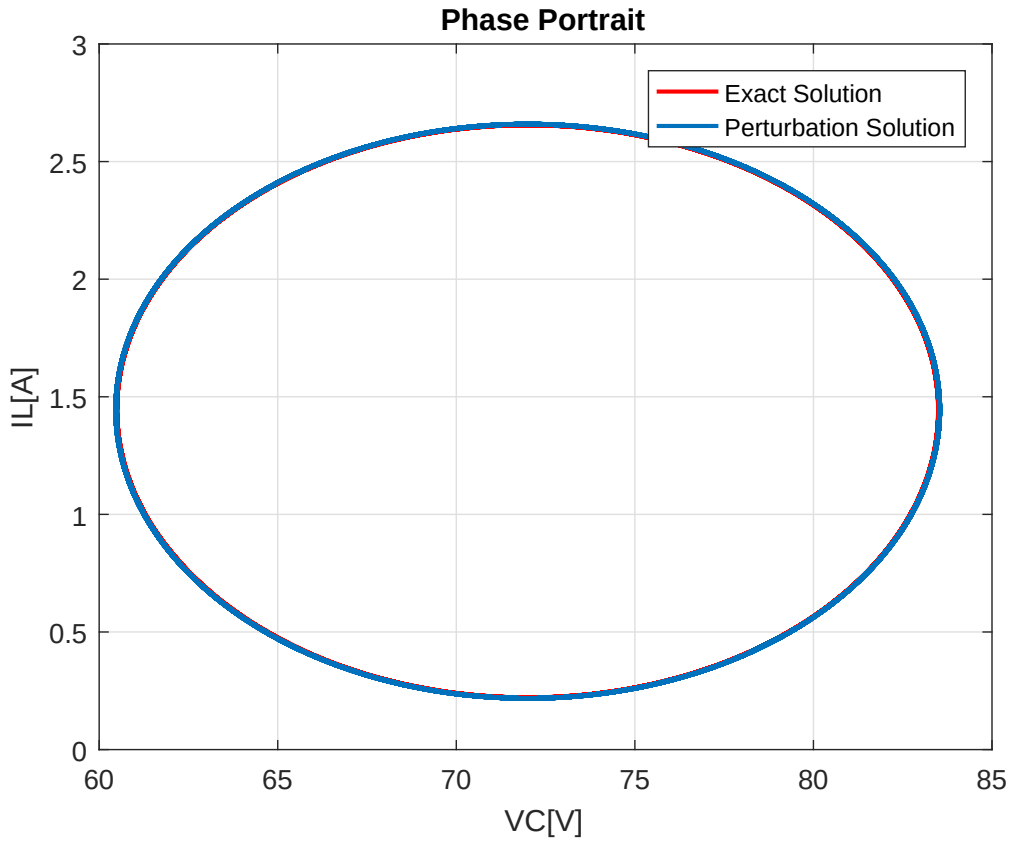

Figure 4.4.2 Comparison of the exact solution by solving system ODEs with the solution by using perturbation method

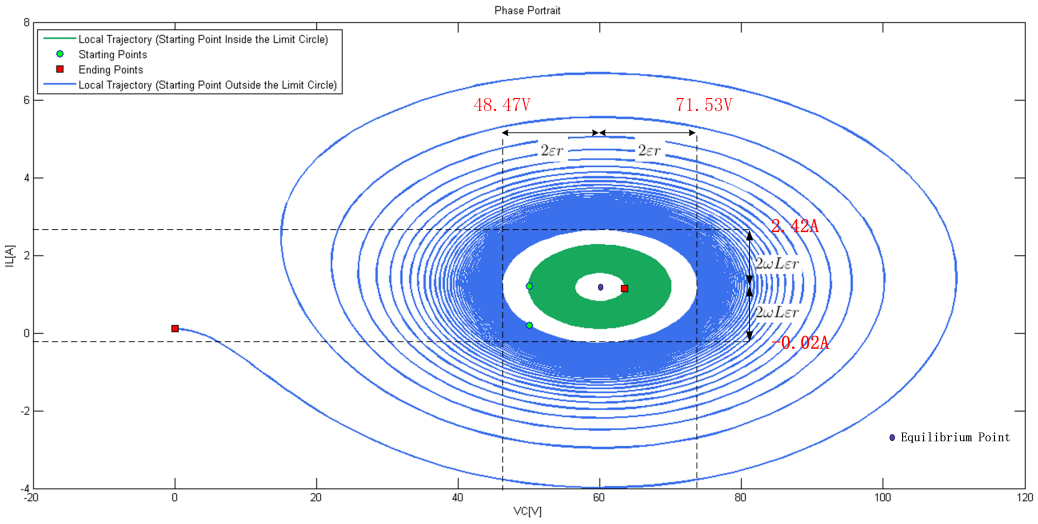

Figure 4.4.3 Size of limit cycle

4.5 Summary

In this chapter, the stability of a DC-DC buck converter with a constant power load system has been studied. This example serves as a demonstrating example of some techniques for analysing non-linear systems. DC-DC converters are widely used in power electronic systems and are rich in non-linear dynamics. When the cascaded connection of DC-DC converters is implemented, the downstream converter can play as a constant power load. This example shows a sample for the steps of analysing our CHB system's stability. The stability analysis gives the maximum input power value that the CPL can hold. Also, the stable range for the initial voltage and current is given to ensure the stable operation of the system by a novel mathematical perturbation method. It is shown that by applying more advanced mathematical method, it is possible to discover more precise of the stability boundary of the power electronic systems.

Chapter 5

Mathematical Modelling for Cascaded H-bridge Converter

Time-periodic systems require more advanced techniques for modelling than a time-invariant system because the equilibrium of the time-invariant system is merely a point, while the steady state of time-periodic system would be trajectories. Hence time-periodic systems, usually AC systems, require some more advanced modelling techniques.

Hence the Truncated Fourier Series (TFS) approximation and Harmonic Balancing Technique(HBT) is applied to model the CHB with its dominant harmonic components. This method predicts the intrinsic harmonics of the state variables, namely the frequency components of the output signals or state variables at multiples of the fundamental frequency of a sinusoidal input signal. This model could capture the primary source of the model non-linearity.

PLL has a smaller effect on the stability of the system rather than the DC link voltage and AC current control. However, when the converter is connected to the weak grid, the high impedance can bring in many distortions in the voltage measured from the Point of Common Coupling (PCC), which is the input voltage of the PLL. Thus the

performance of PLL is worsened and also of the whole control system.

There only exists a few studies investigating the current controller performance and stability for the voltage source converters connected to the weak grid and the interaction between the converter and the grid impedance[105, 106]. Although in [107], different current control strategies have been studied when the converter is connected to the weak grid. Trail and error simulations have investigated the limits of stable operation of the converter in lack of mathematical models with general validity under weak grid conditions. Also, the stability of DC-link voltage control has been studied when VSC is connected to weak grid[108]. It is revealed that the effect of control loops' interactions on dc-link stability reaches largest when the bandwidth of PLL is close to that of the dc-link voltage control.

For this reason, a full detailed model of the system is going to be built including the two-loop control scheme and the PLL structure to study their possible effect on the stability of the system. The process is going to be from simplified case to full-detailed case, in section 5.1 the model of the converter itself is analysed without control, the converter itself is a second-order ODE system; then in section 5.2 the simplified control is going to be added to the model regardless of the grid strength. Thus it becomes a third-order system with periodic coefficient decided by the deadbeat control equation. This model is efficient to predict threshold values for several systematic parameters; in section 5.3 the full seven-order ODE system regarding the grid strength as shown in Fig5.0.1 is built, which is used for studying the effect of the PLL on the stability of the system.

As shown in Fig5.0.1 where the CHB rectifier is connected to a weak grid, in reality, a higher filter is likely to be used in the implementation of a grid-connected converter but that an inductive filter has been used for simplicity in the stability analysis. The inductance of the supply is significant and cannot be ignored, and it is represented by L_S, and its series resistance is labelled as r_s. The input of the PLL is thus changed from the measurement of V_S to V_M, which is the actual input voltage of the filter and converter from the grid side.

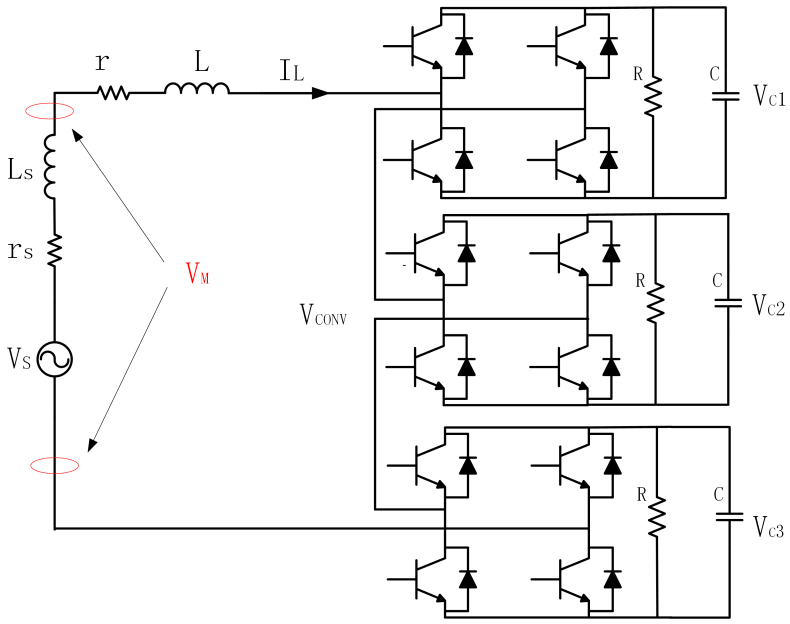

Figure 5.0.1 Schematic of CHB rectifier connected to weak grid

5.1 Open Loop Modelling

The mathematical method has been first applied to a simple scenario that the CHB rectifier works in open loop excluding the control loop. A sinusoidal modulating signal of which the phase angle is synchronised with the supply voltage is used as the input of the PSC-PWM modulator.

5.1.1 Converter Averaged Model

The control plants derived in chapter 3 is the switching model of the CHB converter, representing instantaneous state variables having switching characteristics. The averaged model can be obtained by directly replacing the instantaneous variables with the averaged variables. Hence the following 4 Ordinary Differential Equations (ODEs) regarding the AC current and DC link voltage on each cell have been derived as the

averaged model of the CHB:

$$C\frac{\mathrm{d}V_{C1}}{\mathrm{d}t} = m(t)I_L - \frac{V_{C1}}{R} \tag{5.1.1}$$

$$C\frac{\mathrm{d}V_{C2}}{\mathrm{d}t} = m(t)I_L - \frac{V_{C2}}{R} \tag{5.1.2}$$

$$C\frac{\mathrm{d}V_{C3}}{\mathrm{d}t} = m(t)I_L - \frac{V_{C3}}{R} \tag{5.1.3}$$

$$L\frac{\mathrm{d}I_L}{\mathrm{d}t} = v_S - m(t)(V_{C1} + V_{C2} + V_{C3}) - rI_L \tag{5.1.4}$$

Where the state variables are instantaneous values averaged over a switching period T_S as:

$$V_{C_{1,2,3}} = \frac{1}{T_S}\int_t^{t+T_S} v_{C_{1,2,3}}(\tau)\mathrm{d}\tau$$

$$I_L = \frac{1}{T_S}\int_t^{t+T_S} i_L(\tau)\mathrm{d}\tau$$

$$m(t) = \frac{1}{T_S}\int_t^{t+T_S} S(\tau)\mathrm{d}\tau$$

Where $v_{C_{1,2,3}}, i_L$ are instantaneous values of the DC link voltages and AC current, S is the switching function, its average is the sine-wave modulating signal $m(t)$. It should be noted that only the low-frequency components of the variables remain after averaging. The averaged model is used in all the study for the modelling and stability study.

Since the DC loads are assumed identical for each H-bridge, (5.1.1)-(5.1.3) may be added and the system averaged model is simplified to only two equations regarding the total DC link voltage and AC current as:

$$C\frac{\mathrm{d}V_C}{\mathrm{d}t} = 3mI_L - \frac{V_C}{R} \tag{5.1.5}$$

$$L\frac{\mathrm{d}I_L}{\mathrm{d}t} = V_S - mV_C - rI_L \tag{5.1.6}$$

The averaged model (written in MATLAB scripts) is compared with the switching model (simulated in PLECS) with configurations defined in Table5.1. The responses of the two models are depicted together in Fig5.1.1a. It is shown that the two models agree well not only in the steady state but also during the transient. The discrepancy

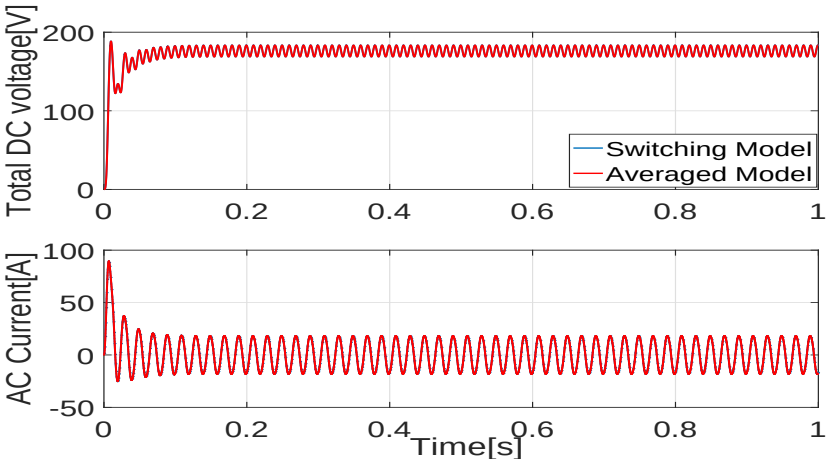

(a) Total DC-link voltage and AC current response

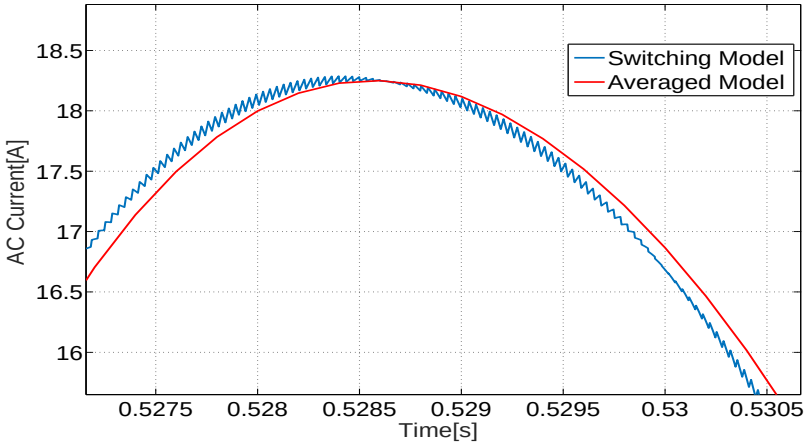

(b) Zoomed-in of current response

Figure 5.1.1 Comparison of switching model and averaged model for the open-loop operating CHB rectifier.

between the two models can only be seen in a smaller time scale as shown in Fig5.1.1b, where the current waveform around the peak area is magnified, it thus can be seen a difference between the switching model and averaged model. The averaged model waveform is smooth, and the switching model waveform is switched. It is also observed that the averaged model current waveform slightly lags behind the switching model, which is an artefact of the averaging. The lag varies in proportion to the switching period.

In summary, the averaged model describes the system behaviour as good as switching

Table 5.1 Open loop configurations

Parameters	Values
Switching Frequency f_s	$5kHz$
Fundamental Frequency	$50Hz$
Cell Load Capacitance C	$5000\mu F$
Cell Load Resistance R	20Ω
Supply Voltage Amplitude As	$120\sqrt{2}V$
AC Side Inductance L	$5mH$
Inductance Series Resistance r	0.6Ω
Modulating Index M	0.8

model in the system operating time scale and has the elegance and simplicity of representing the input-output relationships of the system. However, it can only describe the behaviour of the system well when the operating frequency of the converter is much lower than the switching frequency[109, 110].

5.1.2 Voltage and Current Spectra

In this section, the steady state of the converter is modelled in the form of spectra since the steady state of the system is periodic from observation. Hence the TFS method is applied for the steady-state modelling.

5.1.2.1 State Variables Assumption

Assume the solution of V_C and I_L are in the Fourier series form of:

$$V_C = \sum_{-\infty}^{+\infty} V_n e^{jn\omega t} \tag{5.1.7}$$

$$I_L = \sum_{-\infty}^{+\infty} I_n e^{jn\omega t} \tag{5.1.8}$$

Where n is the harmonic order. V_n and I_n are the amplitudes of the corresponding $e^{jn\omega t}$ terms. V_n and V_{-n}, I_n and I_{-n} are complex conjugate pairs.

5.1.2.2 Input Signals Assumption

The inputs of the CHB, V_S and m of real trigonometric function, are converted to the complex exponential functions by applying Euler formulas, complying with the series form of the variables in the whole analysis. The input conditions of the converter can be represented as:

$$V_S = V_{S1}\sin(\omega t) = \frac{V_{S1}}{2j}(e^{j\omega t} - e^{-j\omega t}) \tag{5.1.9}$$

$$m = m_1\sin(\omega t) = \frac{m_1}{2j}(e^{j\omega t} - e^{-j\omega t}) \tag{5.1.10}$$

Where V_{S1} stands for the peak amplitude of the input voltage, m_1 represents the amplitude for the modulation signal, and ω is the fundamental frequency of the supply voltage, j is the imaginary unit.

5.1.2.3 Harmonic Balance Method

Substitute the assumed Fourier series solutions and the inputs to the averaged model (5.1.5)(5.1.6) of the converter. By substituting and collecting the coefficients of the $e^{nj\omega t}$ terms is obtained a general formula:

$$jCn\omega V_n = \frac{3m_1}{2j}(I_{n-1} - I_{n+1}) - \frac{1}{R}V_n \tag{5.1.11}$$

$$jLn\omega I_n = \frac{V_{S1}}{2j}\varepsilon(n) - \frac{m_1}{2j}V_{n-1} + \frac{m_1}{2j}V_{n+1} - rI_n \tag{5.1.12}$$

Where a function $\varepsilon(n)$ is defined by:

$$\varepsilon(n) = \begin{cases} 1, & \text{if n=1} \\ -1, & \text{if n=-1} \\ 0, & \text{otherwise} \end{cases}$$

As n increases, the values of the variables would become very small and insignificant. Thus it is sufficient to study only four significant low order harmonics: the DC voltage V_0, the second order harmonic of voltage V_2, the fundamental harmonic of current

I_1, and the third order harmonic I_3. Ignore all the higher order harmonics in the calculation.

Put $n = 0$ in (5.1.11), put $n = 2$ in (5.1.11), put $n = 1$ in (5.1.12), and put $n = 3$ in (5.1.12) and set $V_4 = 0$ gives the following:

$$0 = \frac{3m_1}{2j}(I_{-1} - I_1) - \frac{V_0}{R} \tag{5.1.13}$$

$$2j\omega CV_2 = \frac{3m_1}{2j}(I_1 - I_3) - \frac{V_2}{R} \tag{5.1.14}$$

$$j\omega LI_1 = \frac{V_{S1}}{2j} - \frac{m_1}{2j}V_0 + \frac{m_1}{2j}V_2 - rI_1 \tag{5.1.15}$$

$$3j\omega LI_3 = -\frac{m_1}{2j}V_2 - rI_3 \tag{5.1.16}$$

To solve the above equations, treat the variables as complex values, convert 4 complex equations for 4 complex unknowns to 7 real equations for 7 real unknowns(one quantity is purely real, hence 7, not 8). The amplitudes of each order harmonic are twice the module of the corresponding complex number. Thus the four state variables are assumed to be:

$$V_0 = V_0 \tag{5.1.17}$$

$$I_1 = I_{1a} + jI_{1b} \tag{5.1.18}$$

$$V_2 = V_{2a} + jV_{2b} \tag{5.1.19}$$

$$I_3 = I_{3a} + jI_{3b} \tag{5.1.20}$$

Substitute these variables to the above equations a seven order matrix can be derived. Matlab can compute this matrix with configurations shown in Table5.1.

$$\begin{bmatrix} -m_1/2 & L\omega & r & m_1/2 & 0 & 0 & 0 \\ 0 & r & -L\omega & 0 & -m_1/2 & 0 & 0 \\ 0 & 0 & 0 & -m_1/2 & 0 & 3L\omega & r \\ 0 & 0 & 0 & 0 & m_1/2 & r & -3L\omega \\ 1/R & 0 & 3m_1 & 0 & 0 & 0 & 0 \\ 0 & 3m_1/2 & 0 & 2C\omega & 1/R & -3m_1/2 & 0 \\ 0 & 0 & -3m_1/2 & 1/R & -2C\omega & 3m_1/2 & 0 \end{bmatrix} \begin{bmatrix} V_0 \\ I_{1a} \\ I_{1b} \\ V_{2a} \\ V_{2b} \\ I_{3a} \\ I_{3b} \end{bmatrix} = \begin{bmatrix} -V_S/2 \\ 0 \\ 0 \\ 0 \\ 0 \\ 0 \\ 0 \end{bmatrix}$$

To verify the accuracy of this converter frequency model, in Fig.5.1.2 plotting the absolute values of V_0, I_1, V_2 and I_1 with the amplitudes of harmonics of the switching model(by FFT in PLECS) for a range of modulation indices. It can be seen that they are in good agreement and the spectra model is more accurate and closer to the switching model if truncating the Fourier series with more terms.

Hence it can be concluded that by applying the TFS method to the averaged model and HBT to the system ODEs, the steady state can be modelled with reasonable accuracy. However, a little disagreement shows with the 3rd harmonic of the inductor current. The reason is that the Fourier series expansion has only been truncated to the 3rd order harmonic, so the third order solution is with the more significant error than harmonics of lower orders. The accuracy can be improved if more harmonic orders were included in the analysis.

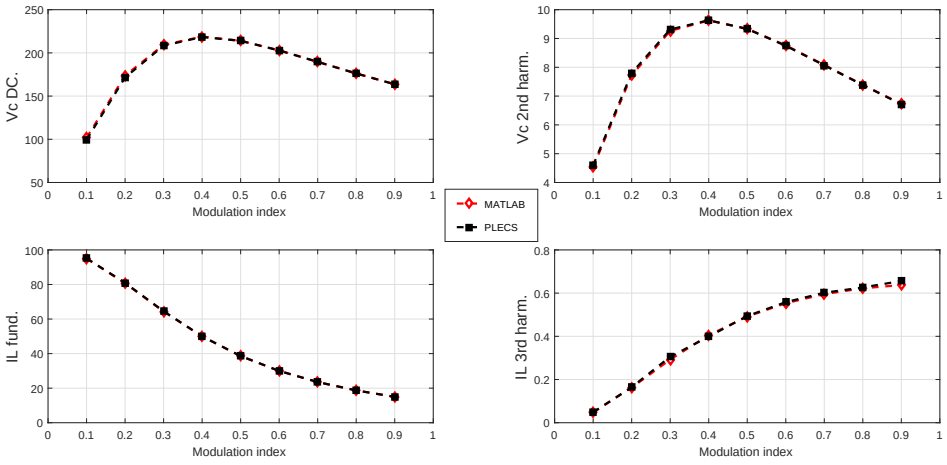

Figure 5.1.2 Comparison of harmonic amplitudes from analytical solution (MATLAB) and simulation FFT results (PLECS)

5.2 Closed Loop Modelling with Simplified Control Scheme

5.2.1 Closed Loop Averaged Model

In this section, the control algorithm is considered into the system of mathematical modelling. Assume the PLL functions well, and the deadbeat controller tracks its desired reference within one sampling time. Hence these two control equations can be included:

$$\frac{dU}{dt} = -\frac{k_p}{C}(3mI_L - \frac{V_C}{R}) + k_i(V_{ref} - V_C) \tag{5.2.1}$$

$$m = \frac{1}{V_{ref}}(V_S - rI_L - \frac{L}{T_S}(U\sin(\omega(t+T_S)) - I_L)) \tag{5.2.2}$$

(5.2.1) is the total DC voltage PI controller, (5.2.2) is the dead beat current controller.

Making some arrangements for the equations for the controllers, they need to be converted to continuous time domain equations to comply with the ODEs of the CHB converter. The PI is designed in s domain and has been converted to a differential equation. The deadbeat current controller is designed in discrete time domain and has been approximated to be continuous at the constraint that the switching frequency is much higher than that of the grid frequency, and m does not vary too much during a switching period T_S, therefore, approximately making T_k as t.

Equations (5.1.5)(5.1.6) with (5.2.1)(5.2.2) are labelled as the *governing equations*, or *closed loop averaged model* since they can fully describe the operation of our system. The governing equations are solved using MATLAB with system configurations.

5.2.2 Steady State Model

From the averaged model both the transient and steady state can be known. However, for stability analysis purpose it is required to find these steady-state solutions for the closed-loop system by ignoring the transient of the time response.

The steady states or stable operating points of the system are periodic solutions for CHB rectifier. Hence the similar TFS solutions and HBT in the open loop modelling is applied to the closed loop.

Observation from simulation and experience is that in the steady state an only small number of harmonics dominant. Also from the results of open loop modelling, the truncated result with only dominant harmonics matches well enough with the switching model. So it is reasonable to use only dominant harmonics for the steady state modelling for closed-loop modelling. In the later section of the model validation figure 5.2.3a also shows this simplified assumption is valid.

For the total DC link voltage, the dominant components are the DC V_0 and the 2nd order harmonic V_{C2}. For the PI output U, the dominant component is its DC harmonic, denoted by U_0. For the AC current, modulating signal and grid voltage, the dominant is their 1st order harmonics. So assumptions for the steady state variables (with a bar sign) can be made as follows:

$$\begin{aligned}
\bar{V_C} &= V_{C0} + \frac{1}{2j}V_{C2}e^{2j\omega t} - \frac{1}{2j}V_{C2}^{*}e^{-2j\omega t} \\
\bar{U} &= U_0 \\
\bar{I_L} &= \frac{1}{2j}I_{L1}e^{j\omega t} - \frac{1}{2j}I_{L1}^{*}e^{-j\omega t} \\
\bar{m} &= \frac{1}{2j}m_1 e^{j\omega t} - \frac{1}{2j}m_1^{*}e^{-j\omega t} \\
\bar{V_S} &= \frac{1}{2j}V_{S1}e^{j\omega t} - \frac{1}{2j}V_{S1}^{*}e^{-j\omega t}
\end{aligned} \tag{5.2.3}$$

5.2.2.1 Steady State Derivations

The next step is to substitute the assumptions to the closed loop averaged model. This derivation process involves many mathematical calculations. The results can be found in section *Results of Steady State Solutions*.

Substituting $\bar{V_C}$, $\bar{I_L}$ and $\bar{m}$ in (5.2.3) to (5.1.5) hence get two equations (5.2.4)(5.2.6) regarding V_{C0} and V_{C2}:

$$Re(m_1 I_{L1}^*) = \frac{2V_{C0}}{3R} \tag{5.2.4}$$

(where Re stands for the real part of the complex number.)

$$V_{C2} = \frac{-3m_1 I_{L1}}{4(C\omega - j\frac{1}{2R})} \tag{5.2.5}$$

Substitute (5.1.6) with the assumed solutions in (5.2.3), the equation regarding I_{L1} can be derived:

$$(j\omega L + r)I_{L1} = V_{S1} - m_1 V_{C0} \tag{5.2.6}$$

Substitute equation (5.2.1) with the assumed solution and get:

$$V_{C0} = V_{ref} \tag{5.2.7}$$

Substitute equation (5.2.2):

$$(r - \frac{L}{T_S})I_{L1} = V_{S1} - m_1 V_{C0} - \frac{L}{T_S}U_0 e^{j\omega T_S} \tag{5.2.8}$$

From (5.2.6) and (5.2.8) derived the formula for I_{L1}:

$$I_{L1} = \frac{U_0 e^{j\omega T_S}}{1 + j\omega T_S} \tag{5.2.9}$$

Correspondingly, its conjugate can be represented as:

$$I_{L1}^* = \frac{U_0 e^{-j\omega T_S}}{1 - j\omega T_S} \tag{5.2.10}$$

Furthermore the expression of m_1 can be derived as:

$$m_1 = \frac{V_{S1}}{V_{ref}} - \frac{(r + j\omega L)U_0 e^{j\omega T_S}}{V_{ref}(1 + j\omega T_S)} \tag{5.2.11}$$

So the expression for $m_1 I_{L1}^*$ is:

$$m_1 I_{L1}^* = \frac{V_{S1} U_0 e^{-j\omega T_S}}{V_{ref}(1 - j\omega T_S)} - \frac{(r + j\omega L)U_0^2}{V_{ref}(1 + \omega^2 T_S^2)} \tag{5.2.12}$$

which can be further simplified as:

$$m_1 I_{L1}^* \approx \frac{V_{S1} U_0}{V_{ref}} - \frac{(r + j\omega L)U_0^2}{V_{ref}} \tag{5.2.13}$$

The proof of this simplification is that apply *Taylor expansion* to term $e^{-j\omega T_S} \approx 1 - j\omega T_S$, and since $\omega T_S \ll 1$, the approximation of truncating to two terms is good, also, $1 + \omega^2 T_S^2$ can be approximated as 1. Thus:

$$Re(m_1 I_{L1}^*) = \frac{V_{S1} U_0}{V_{ref}} - \frac{r U_0^2}{V_{ref}} \tag{5.2.14}$$

Compared with (5.2.4) the following quadratic equation regarding U_0:

$$\frac{r}{V_{ref}} U_0^2 - \frac{V_{S1}}{V_{ref}} U_0 + \frac{2V_{ref}}{3R} = 0 \tag{5.2.15}$$

Also, U_0 has two possible solutions as given in (5.2.16), need to verify which should be selected, later it will show the smaller one is the stable solution.

$$U_0 = \frac{V_{S1}}{2r}\left(1 \pm \sqrt{1 - \frac{8rV_{ref}^2}{3RV_{S1}^2}}\right) \tag{5.2.16}$$

5.2.2.2 *Bifurcation* of Solutions

Bifurcation is a terminology used to describe the phenomena that as the parameter in the equation varying, the number of the solution of the equation changes correspondingly. We say that there is a change in the qualitative behaviour of solutions, and call the boundary point where *bifurcation* has taken place as the *bifurcation point*.

To make quadratic equation (5.2.15) valid, its discriminant must satisfy the condition "$b^2 - 4ac \geqslant 0$", this constraint gives us the thresholds of system parameters V_{ref}, V_{S1}, R and r and causes the *bifurcation* phenomenon of the system solution.

From "$b^2 - 4ac$" $= \dfrac{V_{S1}^2}{V_{ref}^2} - \dfrac{8r}{3R} \geqslant 0$ the effective parameter range can be derived as:

$$\begin{aligned} V_{S1min} &= \sqrt{\frac{8rV_{ref}^2}{3R}} \\ V_{refmax} &= \sqrt{\frac{3RV_{S1}^2}{8r}} \\ R_{min} &= \frac{8rV_{ref}^2}{3V_{S1}^2} \\ r_{max} &= \frac{3RV_{S1}^2}{8V_{ref}^2} \end{aligned} \tag{5.2.17}$$

To illustrate the number of solutions with the value of parameters, define the left side of the quadratic equation as:

$$Y = \frac{r}{V_{ref}} U_0^2 - \frac{V_{S1}}{V_{ref}} U_0 + \frac{2V_{ref}}{3R}$$

In Fig5.2.15 Y is plotted against U_0 by varying the value of V_{S1}. The solutions of the

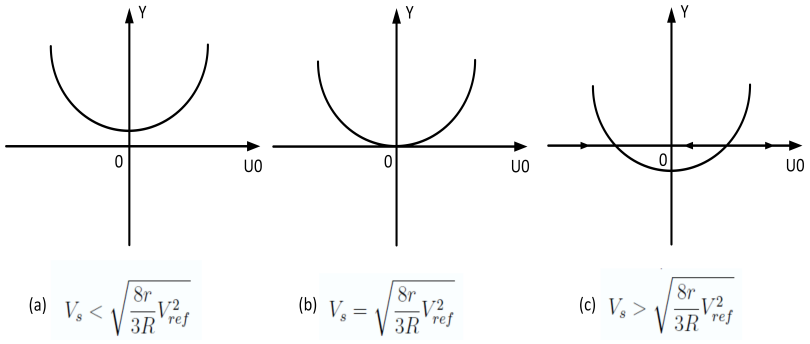

Figure 5.2.1 Solutions of the quadratic equation.

quadratic equation will then be graphically represented by the crossings of the plot with the x-axis. It is can be seen that when $V_{S1} < V_{S1min}$, there is no solution for U_0; when $V_{S1} = V_{S1min}$, there is only one solution for U_0; when $V_{S1} > V_{S1min}$, there are two solutions for U_0.

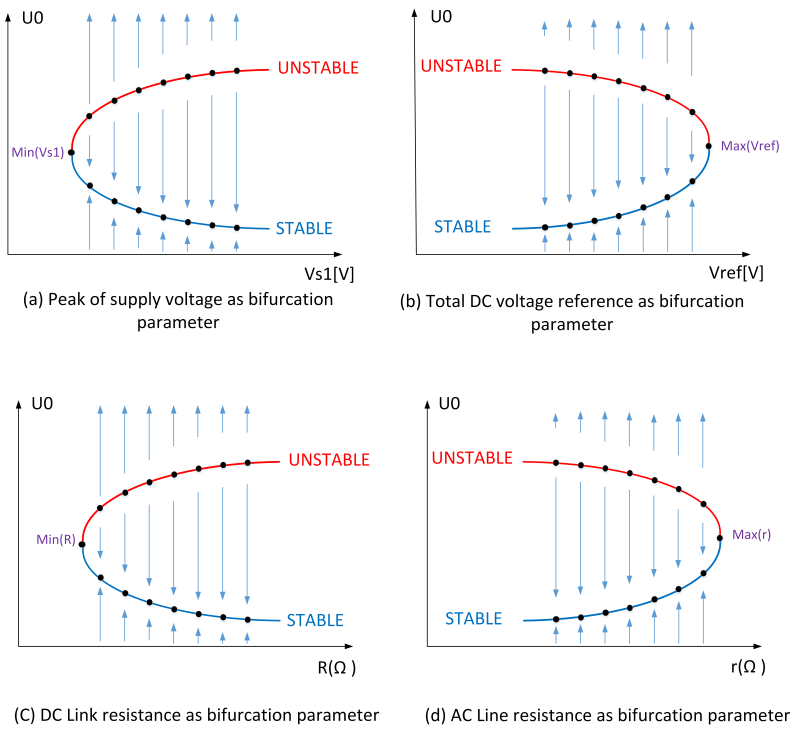

Figure 5.2.2 Bifurcation map regarding four system parameters

In Fig5.2.1(c) the right arrow on the x-axis indicates the solution is increased, the left arrow indicates the solution is decreasing. Thus the smaller solution for U_0 is stable because the other solutions are approaching it, the bigger solution for U_0 is unstable because the solutions close to it are getting away from it.

Then, seen in Fig.5.2.2, the solutions of U_0 against four parameters appearing in the quadratic equation are plotted respectively, this is called the *bifurcation map*.

Map Fig5.2.1 to Fig5.2.2(a) but plot the solution of U_0 against the bifurcation parameter. It can be seen that as the values of V_{S1} vary, the number of the solutions may change from none to two, one is stable(in blue) the other is unstable(in red). The bifurcation maps for other three parameters can be obtained by the same method, and they are shown in Fig5.2.2(b)(c)(d).

A notable observation from the four plots is that among the two solutions always the

smaller solution for U_0 is stable, the bigger one is unstable. Thus the solution for U_0 is selected to be:

$$U_0 = \frac{V_{S1}}{2r}\left(1 - \sqrt{1 - \frac{8rV_{ref}^2}{3RV_{S1}^2}}\right) \tag{5.2.18}$$

5.2.2.3 Steady State Solutions

Summarize the formulas for the steady state model here:

$$\begin{aligned} V_{C0} &= V_{ref} \\ U_0 &= \frac{V_{S1}}{2r}\left(1 - \sqrt{1 - \frac{8rV_{ref}^2}{3RV_{S1}^2}}\right) \\ I_{L1} &= \frac{U_0 e^{j\omega T_S}}{1 + j\omega T_S} \\ m_1 &= \frac{V_{S1}}{V_{ref}} - \frac{(r + j\omega L)U_0 e^{j\omega T_S}}{V_{ref}(1 + j\omega T_S)} \\ V_{C2} &= \frac{-3m_1 I_{L1}}{4(C\omega - j\frac{1}{2R})} \end{aligned} \tag{5.2.19}$$

These equations give the amplitudes of the dominant harmonics. The periodic time solutions are computed with the expressions in (5.2.3).

5.2.3 Models Validation

In this section the validation of three mathematical models are verified. The first is the averaged model(5.1.5)(5.1.6)(5.2.1)(5.2.2) of system, solved numerically in MATLAB; the second is the reduced order steady state model (5.2.3) with (5.2.19), the third is the switching model built with blocks.

In Fig.5.2.3 the time responses of the closed-loop system V_C and I_L, from three mathematical models are plotted together for a time duration of 5 seconds. It is

seen that they match each other with good agreement for the steady-state operation. To verify the three models better, a zoomed-in plot during steady-state operation is shown in Fig5.2.3b. The transient responses are different of the averaged model and switching model since the averaged model is by its very nature intended to simulate (only) the steady-state behaviour, so behaviour on short-time scales cannot be resolved in the averaged model.

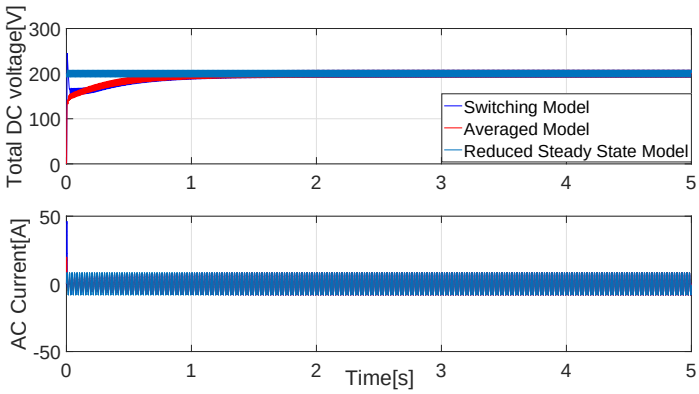

(a) Transient and steady state

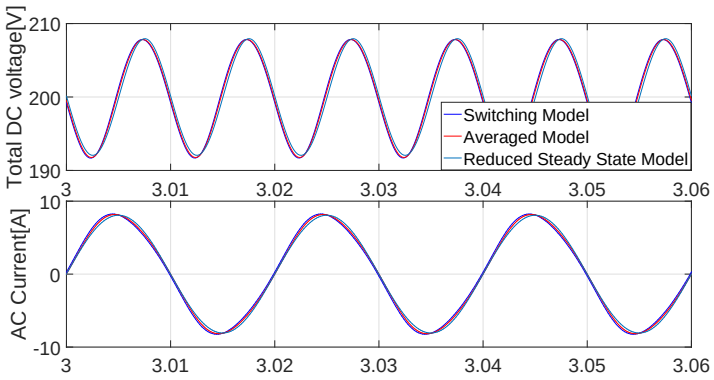

(b) Zoomed-in view of the steady state

Figure 5.2.3 Comparison of close loop operation system response of switching model (PLECS simulation), averaged model built with simplified control scheme, and steady state model derived from the simplified averaged model.

5.3 Modelling for Weak Grid

The control system should be designed under any grid condition. Typically, the supply side inductance is small, and this is called a strong grid; otherwise, if the impedance is significant between the supply and converter, it is called a weak grid. In this section, a more detailed seven-order model of the system is going to be built including the PLL. Thus the effect of the PLL to the stability of the system can then be studied through the mathematical model. The PLL is based on a PI controller eliminating the steady state error of the estimated phase angle.

5.3.1 System Equations

A 7-order state equation can model the complete control system with 7 state variables defined as:

$$\begin{pmatrix} x_1 \\ x_2 \\ x_3 \\ x_4 \\ x_5 \\ x_6 \\ x_7 \end{pmatrix} = \begin{pmatrix} V_C \\ I_L \\ U \\ V_\beta \\ V_{d\beta} \\ \theta \\ \Gamma \end{pmatrix}$$

where $V_{d\beta}$ represents the derivative of V_β. θ is the output of PLL, and Γ is a variable defined for the convenience of calculation.

The governing equations are derived from the above control block diagrams and can

be summarised by (5.3.1).

$$\begin{aligned} V_S &= A_S \sin(\theta) = A_S \sin(\omega t + \phi) \\ V_\alpha &= V_m \\ I_{Lref1} &= x_3 \sin(x_6 + \omega T_S) \\ I_{Lref2} &= x_3 \sin(x_6 + 2\omega T_S) \\ V_{Spk} &= \sqrt{V_S^2 + x_4^2} \\ V_{Sref} &= V_{Spk} \sin(x_6 + \omega T_S) \\ V_{CONVref} &= V_{Sref} - \frac{L}{2T_S}(I_{Lref2} - x_2) - rI_{Lref1} \\ m &= V_{CONVref}/V_{ref} \end{aligned} \tag{5.3.1}$$

ϕ is the initial phase of the supply voltage from the above equations that a compact equation for the modulating signal m can be derived in (5.3.2), where for simplification of calculation, the known amplitude of the supply voltage A_S is directly used rather than using PLL to detect the amplitude.

$$m = \frac{1}{V_{ref}}(As \sin(x_6 + \omega Ts) - \frac{L}{2T_S}(x_3 \sin(x_6 + 2\omega T_S) - x_2) - rx_3 \sin(x_6 + \omega T_S)) \tag{5.3.2}$$

The differential equations for the system can be summarised as follows:

$$\dot{x_1} = -\frac{1}{RC}x_1 + \frac{3m}{C}x_2 \tag{5.3.3}$$

$$\dot{x_2} = -\frac{m}{L_S + L}x_1 - \frac{r + r_s}{L_S + L}x_2 + \frac{V_S}{L_S + L} \tag{5.3.4}$$

$$\dot{x_3} = (\frac{k_p}{CR} - k_i)x_1 - \frac{3mk_p}{C}x_2 + k_i V_{Cref} \tag{5.3.5}$$

$$\dot{x_4} = x_5 \tag{5.3.6}$$

$$\dot{x_5} = -\omega^2 x_4 - \omega x_5 + \omega^2 V_\alpha \tag{5.3.7}$$

$$\dot{x_6} = x_7 + k_p^{'} \cos(x_6)V_\alpha + k_p^{'} \sin(x_6)x_4 \tag{5.3.8}$$

$$\dot{x_7} = k_i^{'} \cos(x_6)V_\alpha + k_i^{'} \sin(x_6)x_4 \tag{5.3.9}$$

Where V_m is the input voltage of the PLL, measured from the PCC. Its equation is:

$$V_m = V_S - r_s I_L - L_S \dot{I_L} = V_S - r_s x_2 - L_S(-\frac{m}{L + L_S}x_1 - \frac{r + r_s}{L + L_S}x_2 + \frac{V_S}{L + L_S}) \tag{5.3.10}$$

5.3.2 Steady State Operation Modelling

From observation the assumption for the most dominant harmonics for each variable can be made:

$$\begin{aligned}
\bar{V_C} &= V_{C0} \\
\bar{I_L} &= \frac{I_{L1}e^{j\omega t} - I_{L1}^* e^{-j\omega t}}{2j} \\
\bar{U} &= U_0 \\
\bar{x_4} &= \frac{x_{41}e^{j\omega t} - x_{41}^* e^{-j\omega t}}{2j} \\
\bar{x_5} &= \frac{x_{51}e^{j\omega t} - x_{51}^* e^{-j\omega t}}{2j}
\end{aligned} \tag{5.3.11}$$

And $\bar{x_6} = \omega t + x_{60}$, and $\bar{x_7}$ is a constant, its value to be defined.

Meanwhile, the additional assumptions are made for supply voltage and modulating signal:

$$\begin{aligned}
\bar{V_S} &= \frac{V_{S1}e^{j\omega t} - V_{S1}^* e^{-j\omega t}}{2j} \\
\bar{m} &= \frac{m_1 e^{j\omega t} - m_1^* e^{-j\omega t}}{2j}
\end{aligned} \tag{5.3.12}$$

Substitute the assumptions made in (5.3.3) (5.3.12) and that for $\bar{x_6}$ and $\bar{x_7}$ to the system NLTP equations and (5.3.2) and got the results for steady state operations:

$$\begin{aligned}
Re(m_1 I_{L1}^*) &= \frac{2V_{C0}}{3R} \\
(j\omega(L + L_S) + (r + r_s))I_{L1} &= -m_1 V_{C0} + V_{S1} \\
V_{C0} &= V_{ref} \\
A_S \sin(x_6 + \omega T_S) - m_1 V_{ref} &= \frac{L}{2T_S}(U \sin(x_6 + 2\omega T_S) - I_L) + rU \sin(x_6 + \omega T_S) \\
x_{51} &= j\omega x_{41} \\
jx_{41} &= V_{\alpha 1}
\end{aligned} \tag{5.3.13}$$

where Re indicates the real part. For the convenience of calculation, represent the complex quantities as $X_1 = X_{1a} + jX_{1b}$, where $X = m, I_L, x_4, x_5, V_S$ Additionally, it

is known that:

$$\begin{aligned} V_{S1a} &= A_S \cos(\phi) \\ V_{S1b} &= A_S \sin(\phi) \end{aligned} \tag{5.3.14}$$

Thus the (5.3.13) can be transformed to:

$$\begin{aligned} m_{1a}I_{L1a} + m_{1b}I_{L1b} &= \frac{2V_{C0}}{3R} \\ (r+r_s)I_{L1a} - \omega(L+L_S)I_{L1b} &= V_{S1a} - m_{1a}V_{C0} \\ (r+r_s)I_{L1b} + \omega(L+L_S)I_{L1a} &= V_{S1b} - m_{1b}V_{C0} \\ V_{C0} &= V_{ref} \\ A_S\cos(\phi+\omega T_S) - m_{1a}V_{ref} &= \frac{L}{2T_S}(U_0\cos(\phi+2\omega T_S) + I_{L1a}) + rU_0\cos(\phi+\omega T_S) \\ A_S\sin(\phi+\omega T_S) - m_{1b}V_{ref} &= \frac{L}{2T_S}(U_0\sin(\phi+2\omega T_S) + I_{L1b}) + rU_0\sin(\phi+\omega T_S) \\ x_{51a} &= -\omega x_{41b} \\ x_{51b} &= \omega x_{41a} \\ -x_{41b} &= (1-\frac{L_S}{L+L_S})V_{S1a} + \frac{L_S}{L+L_S}m_{1a}V_{C0} + (\frac{r+r_s}{L+L_S} - r_s)I_{L1a} \\ x_{41a} &= (1-\frac{L_S}{L+L_S})V_{S1b} + \frac{L_S}{L+L_S}m_{1b}V_{C0} + (\frac{r+r_s}{L+L_S} - r_s)I_{L1b} \end{aligned} \tag{5.3.15}$$

Now the above ten equations can be solved in Matlab. Besides, substitute $\bar{x_6} = \omega t + x_{60}$ and $\bar{x_7} = const.$ to (5.3.8-5.3.9):

$$\begin{aligned} \omega &= \bar{x_7} + k_p^{'}\cos(\bar{x_6})V_\alpha + k_p^{'}\sin(\bar{x_6})x_4 \\ 0 &= k_i^{'}\cos(\bar{x_6})V_\alpha + k_i^{'}\sin(\bar{x_6})x_4 \end{aligned} \tag{5.3.16}$$

This gives:

$$\begin{aligned} x_{60} &= \phi \\ \bar{x_7} &= \omega \end{aligned} \tag{5.3.17}$$

Additionally, the second order harmonic of DC-link voltage V_{C2} and the third order

harmonic of current can be included to the truncated model by:

$$V_{C2} = \frac{-3 * m_1 I_{L1}}{4(C\omega - \frac{j}{2R})}$$
$$I_{L3} = \frac{-m_1 V_{C2}}{3j\omega(L + L_S) + (r + r_s)} \tag{5.3.18}$$

The steady state model is solved by Matlab script in ss_seven. The simulations are

Table 5.2 Closed loop configurations

Parameters	Values
Switching Frequency f_s	$5kHz$
Fundamental Frequency	$50Hz$
Cell Load Capacitance C	$2000\mu F$
Cell Load Resistance R	20Ω
Supply Voltage Amplitude As	$120\sqrt{2}V$
Total Voltage Reference V_{ref}	$200V$
Grid Inductance L_S	$3.35mH$
Grid Inductance Series Resistance r_S	0.4Ω
Filter Inductance L	$3.75mH$
Filter Inductance Series Resistance r	0.6Ω
Total Voltage PI Controller k_p	0.0166
Total Voltage PI Controller k_i	0.374
PI Controller in PLL $k_p^{'}$	9.2
PI Controller in PLL $k_i^{'}$	422.3

conducted using the system parameters configured in Table(5.2). Meanwhile, the averaged model has been solved numerically with the scriptseven_state_variables_average_model in the appendix. The seven state variables have been plotted individually. The averaged model is plotted together with a truncated model of the steady state in Fig5.3.1. It can be observed that the two models are with good agreement. Noted that "theta" is a mathematical variable here, so it appears as an infinite value only for validating the accuracy of the averaged model, in practice, it should be limited from 0 to 2π.

Furthermore, the averaged model and the model for the steady state are plotted together with the simulation results from PLECS, concerning the total DC-link voltage and the AC side current in Fig5.3.2. As the figure indicates, after the system going into the steady state, the three models start to have a good agreement. Again the

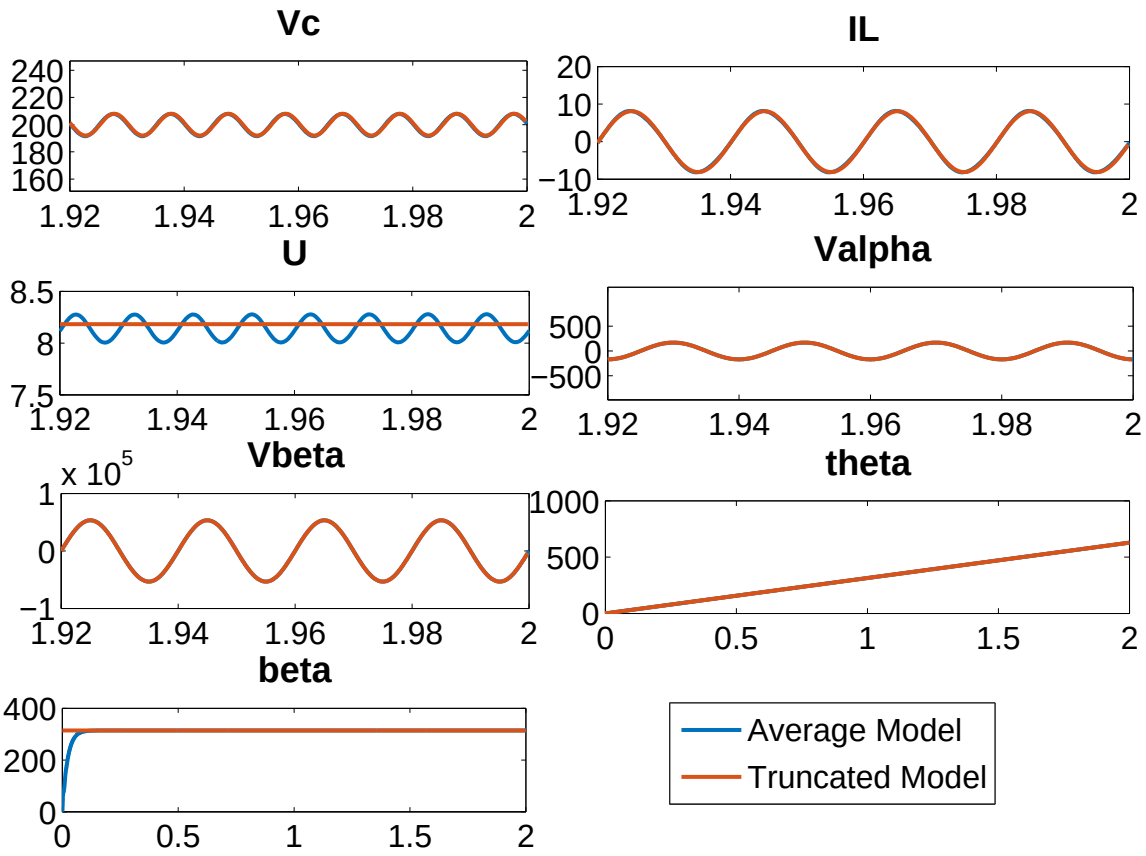

Figure 5.3.1 Comparison of seven state variables responses of averaged model and truncated model

transients of the three models don't match because the averaged model and switching model have different starting conditions. Also, the steady state model inherently matches only in the steady state. All in all, our stability analysis is only about steady state stability but not considering transient stability, so this won't affect.

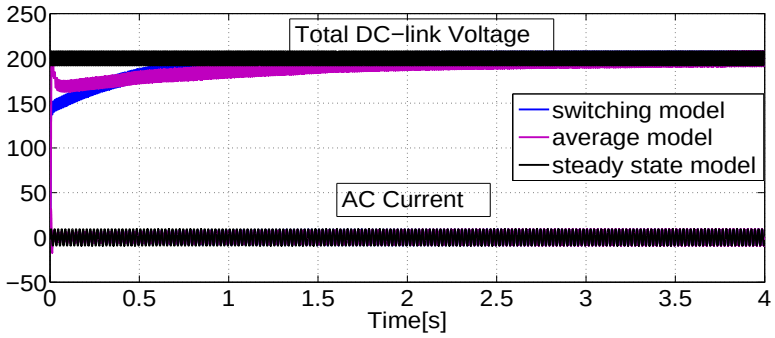

(a) Simulation for four seconds

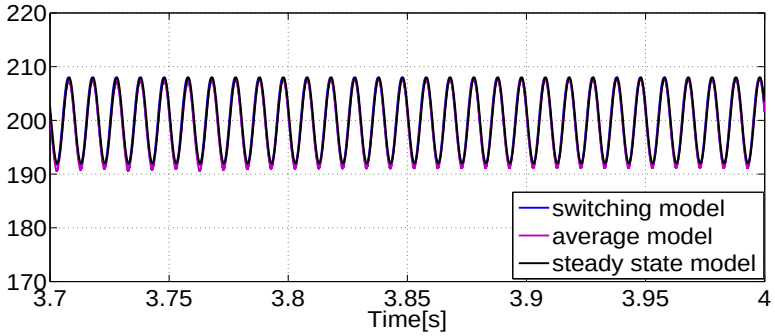

(b) Zoomed-in of steady dynamics of total DC-link voltage

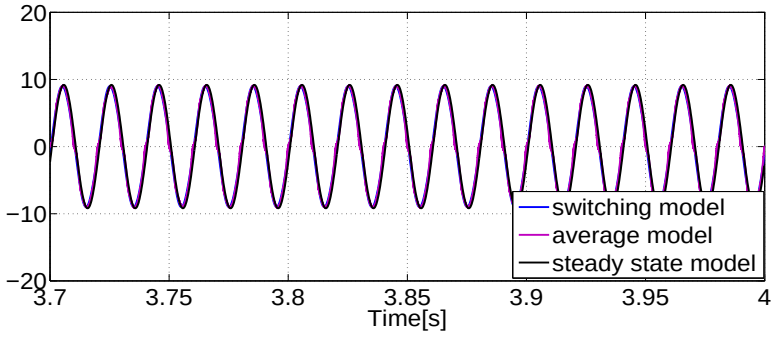

(c) Zoomed-in of steady dynamics of AC current

Figure 5.3.2 Model compare of switching model, averaged model and steady state model for converter connected to weak grid.

5.4 Summary

In this chapter, the grid-connected converter system has been mathematically modelled. The converter itself working in open loop is firstly modelled, then the simplified control loop is included, and finally, the full detailed model is built. In each section, the averaged model is first derived. Moreover, then the steady-state model is derived from the averaged model by applying the truncated Fourier series approximation and harmonic balance technique. In this way, it is necessary to capture the main nonlinearity of the system. The averaged model and the steady-state model are then compared with the switching (electromagnetic) model. The comparison proves that the models are accurate and reliable. Hence the stability analysis can then be carried out based on these models. Matlab scripts realise the modelling process, some of them are shown in the appendix.

Chapter 6

Stability of Controlled Multilevel Cascaded H-bridge Converter

The time-periodic steady state has been resolved in the last chapter. In this chapter, the aim is to examine whether or not this state is stable. Theoretically, for a periodic orbit if a small perturbation is added and the solution converges back to the orbit, it is stable otherwise it is not.

Suppose that this state is perturbed, that each state variable is perturbed by a small-signal perturbation quantity. Hence a linearised model is derived just as for the time-invariant system. Hence the non-linear time-periodic inhomogeneous system is linearised to a linear time-periodic homogeneous system regarding the perturbations. Then a *Floquet theory* is applied to investigate the time-periodic state's stability by observing the distribution of the eigenvalues of the *monodromy matrix*.

Since the steady states of the system are AC variables, traditional stability analysis methods used for DC dynamic systems are not applicable any more. For this reason, the *Floquet theory* [111, 112, 113] which is applicable for the time-periodic system is applicable.

The general steps of analysing the stability of an AC system can be summarised as follows:

• Derive the averaged model of the system;

• Apply *Harmonic Linearisation* to the averaged model and derive the time-periodic steady state;

• Add small signal perturbations to the steady state, derive the state space equation about the perturbations, which would be a linear time-periodic (LTP) system;

• Apply *Floquet theory* to validate stability: if all the eigenvalues of the *monodromy matrix* are inside the unit circle, the steady state is stable; otherwise, if there is one or more than one eigenvalues are outside the unit circle, the steady state is unstable.

6.1 Introduction of the Floquet's Theorem

This section introduces the main theorem used in the stability analysis in this study for our LTP system. The main theorem of Floquet theory, due to Gaston Floquet (1883)[114, 115, 116, 117], has played a very important role in the analysis in LTP systems[111, 112, 113], and will be reviewed in the following.

Firstly, the definition of the periodic function is given as: a function is periodic with T if $T \in \Re^+$ is the smallest number such that

$$f(t) = f(t+T), \forall t$$

Where $\forall$ stands for "for all". Floquet theory is relating to the solutions to periodic linear differential equations of the form:

$$\dot{x}(t) = A(t)x(t)$$

Where $x(t) \in \Re^n$. The elements of matrix $A(t)$ are known, real-valued, piece-wise continuous, T-periodic functions defined in $\Re^+$, and defines the state of the stability of solutions.

Any non-singular solution of the homogeneous differential system is known as its *fundamental matrix*. Define an $n \times n$ matrix $\phi(t)$, each column is a fundamental

matrix, $\phi(t)$ satisfies

$$\dot{\phi}(t) = A(t)\phi(t) \tag{6.1.1}$$

for which assume the initial condition is an n order identity matrix.

$$\phi(t, t_0) = I \tag{6.1.2}$$

This unique matrix is called the *state transition matrix*. Without losing generality, $t_0 = 0$ is assumed. For the stability of the LTP system, it is essential to calculate the transition matrix. In most cases, transition matrix cannot be solved in closed form[14]. Fortunately the *monodromy matrix* introduced next is enough for determining stability. From the state transition matrix:

$$\vec{x}(t) = \phi(t)\vec{x}(0) \tag{6.1.3}$$

and from the periodic condition it can be derived:

$$\vec{x}(t+T) = \phi(t+T)\vec{x}(0) \tag{6.1.4}$$

$$= \phi(t)\phi(T)\vec{x}(0) \tag{6.1.5}$$

Now choose $\vec{x}(0)$ to be an eigenvector of the *monodromy matrix* $\phi(T)$ with eigenvalue λ, then it is derived that:

$$\phi(T)\vec{x}(0) = \lambda\vec{x}(0) \tag{6.1.6}$$

Hence,

$$\vec{x}(t+T) = \lambda\phi(t)\vec{x}(0) = \lambda\vec{x}(t) \tag{6.1.7}$$

Therefore stability can be determined by examining the magnitudes of the eigenvalues λ of the monodromy matrix, The eigenvalues of the monodromy matrix are called the *Floquet Multipliers*. If the absolute value of the eigenvalues of the monodromy matrix is all less than one, then the perturbations will converge, and thus the system is asymptotically stable. However, if the magnitudes of any eigenvalue are bigger than one, then there is instability.

The monodromy matrix can be solved numerically by solving $\Delta\dot{x}(t) = A(t)\Delta x(t)$ n times with n different initial conditions. The ith $(i = 1, 2, ...n)$ initial condition is the ith column of the identity matrix, solve the equation for T and get the solution $x_i(t), i = 1, 2, ...n$. Then the monodromy matrix is given by

$$\phi(T, 0) = [x_1(T)x_2(T)...x_n(T)] \tag{6.1.8}$$

6.2 Stability Analysis of the Simplified Closed Loop

6.2.1 Linearisation of System Governing Equations

In this section, the system being studied is a simplified closed-loop system, which is efficient for predicting the instability points for some crucial system parameters. Denote the steady state solutions with bar signs. Suppose each state variables is perturbed by a small quantity, denote the perturbations with Δ signs. The perturbed solutions are:

$$V_C(t) = \bar{V_C}(t) + \Delta V_C(t) \tag{6.2.1}$$

$$I_L(t) = \bar{I_L}(t) + \Delta I_L(t) \tag{6.2.2}$$

$$U(t) = \bar{U}(t) + \Delta U(t) \tag{6.2.3}$$

$$m(t) = \bar{m}(t) + \Delta m(t) \tag{6.2.4}$$

By using conventional linearisation methods, substitute the perturbed solutions for the system averaged model (inhomogeneous time-varying). It can easily be shown that the perturbations can be modelled by a homogeneous linear time-varying model yields:

$$C\Delta\dot{V_C} = 3\bar{m}\Delta I_L + 3\Delta m\bar{I_L} - \frac{\Delta V_C}{R} \tag{6.2.5}$$

$$L\Delta\dot{I_L} = -r\Delta I_L - \bar{m}\Delta V_C - \Delta m\bar{V_C} \tag{6.2.6}$$

$$\Delta\dot{U} = -\frac{k_p}{C}(3\bar{m}\Delta I_L + 3\Delta m\bar{I_L} - \frac{\Delta V_C}{R}) - k_i\Delta V_C \tag{6.2.7}$$

where

$$\Delta m = \frac{1}{V_{ref}}[-r\Delta I_L - \frac{L}{T_S}[\Delta U \sin(\omega(t+T_S) - \Delta I_L]] \tag{6.2.8}$$

substitute Δm to $\Delta V_C, \Delta U, \Delta I_L$, obtain three ODEs regarding the perturbations with periodic coefficient in the vector form of:

$$\dot{\vec{x}} = A(t)\vec{x} \tag{6.2.9}$$

where $\vec{x} = \begin{pmatrix} \Delta V_C \\ \Delta I_L \\ \Delta U \end{pmatrix}$

and $A(t) = \begin{pmatrix} -\frac{1}{CR} & \frac{3\bar{m}}{C} - \frac{3r\bar{I_L}}{CV_{ref}} + \frac{3L\bar{I_L}}{CV_{ref}T_S} & -\frac{3L\bar{I_L}\sin(\omega(t+T_S))}{CT_SV_{ref}} \\ -\frac{\bar{m}}{L} & -\frac{r}{L} + \frac{r\bar{V_C}}{LV_{ref}} - \frac{\bar{V_C}}{V_{ref}T_S} & \frac{\bar{V_C}\sin(\omega(t+T_S))}{T_SV_{ref}} \\ \frac{k_p}{CR} - k_i & -\frac{3k_p\bar{m}}{C} + \frac{3rk_p\bar{I_L}}{CV_{ref}} - \frac{3k_pL\bar{I_L}}{CT_SV_{ref}} & \frac{3k_pLI_L\sin(\omega(t+T_S))}{CT_SV_{ref}} \end{pmatrix}$

6.2.2 Stability Analysis of the Simplified Model

The monodromy matrix of (6.2.9) is defined as a 3×3 matrix which satisfies

$$\dot{\phi}(t) = A(t)\phi(t) \tag{6.2.10}$$

And its initial condition is an 3×3 identity matrix.

The monodromy matrix has been solved numerically in MATLAB by solving (6.2.9) three times for T($2\pi/\omega$) with one column of the identity matrix each time, then three vectors of $x(t)$ can be calculated, forming a 3×3 monodromy matrix, as well as its three eigenvalues. The MATLAB code can be found in the Appendix.

6.2.3 Evaluate the Eigenvalues and Decide Stability

Now it is possible to predict the stability by observing the distribution of Floquet multipliers on the z plane. Fig(6.2.1a)-(6.2.1d) are the eigenvalue maps in terms of

four parameters V_{S1}, V_{ref}, R and r. In each figure, the parameter is in a selected proper range. The distribution of three eigenvalues is plotted individually on the left. The biggest eigenvalue is plotted against the bifurcation parameter on the right for all four figures.

With the system configuration defined in chapter 5, the corresponding thresholds for the system are $V_{S1min} = 56.57$ V, $V_{refmax} = 600$ V, $R_{min} = 2.22\Omega$ and $r_{max} = 5.4\Omega$, respectively. The eigenvalues start to escape the unit circle and lose stability at predicted bifurcation points. The reason is that if parameters are selected values beyond these thresholds, there are no real solutions for the system. For verify the predictions about the thresholds of the parameters, the system time evolutions are simulated under the conditions that the parameters are around the calculated thresholds for both stable and unstable operation. Thus the stability of the system can be observed intuitively. The total DC voltage and AC current are plotted as the system response.

Such as the amplitude of the grid voltage is studied as a systematic parameter and the minimum threshold for it is calculated to be 56.5685 V. In Fig6.2.2, the switching model is simulated assuming the peak amplitude is 57 V for stable operation (Fig6.2.2a); and 56 V for unstable case. It can be seen from Fig6.2.2b that the magnitudes of the DC total voltage and AC current are increasing, indicating an unstable system. Eventually, V_C would get to zero the system would stop working. The averaged model (Matlab) also gives the same simulation results. Secondly, consider the reference value for the total DC-link voltage as a varying parameter. It has a maximum threshold of 600 V, in Fig6.2.3a V_{ref} is 599 V and the converter is stable, in Fig6.2.3b the system is operating when configuring V_{ref} as $601V$, the system is divergent and unstable. The two simulations also indicate the accuracy of the stability threshold.

The third parameter to be verified is the DC side load resistance R at each cell. From the previous prediction, it has a minimum threshold of 2.222Ω. So the simulation is run with $R = 2.1\Omega$ and $R = 2.2\Omega$, very close to the threshold. From Fig6.2.4b it can be observed that the magnitudes of DC voltage and AC current keep increasing until

the DC voltage touches zero at about 5.7 s. Then the DC voltage of averaged model goes to negative and finally breaks down, and the switching model stops simulating at about 2.2 s because of error of negative voltage on DC capacitors.

The fourth systematic parameter verified is the grid series resistance r, which has a maximum threshold of 5.4Ω. The simulation is ran in Fig6.2.5b when set r to be 5.3Ω and 5.6Ω. From $0-8.4$ s, the DC voltage is stable, but the magnitude of AC current is increasing, then the DC voltage starts to go down, and both averaged model and switching model stops operating. A zoom-in plot indicates this process more clearly.

In this section, four parameters have been verified having their thresholds in design to guarantee stable time responses of the closed form system. The eigenvalue analysis is based on the simplified control system, in which the phase locked loop has not been taken into account and the ideal deadbeat control neglecting the sample delay is used. This simplified model is enough to predict the effect of the system passive components and the inputs of the system.

The simulation results from the electromagnetic model prove that if the system parameters are used beyond the predicted thresholds, the DC-link voltage and current will diverge until eventually collapse. However, it is hard to verify the analysis results in the experiment due to the current rating of the IGBT power module used.

Furthermore, the effect of the phase locked loop when the converter is connected to the weak grid cannot be studied using the simplified model. Thus in the next section, a full-detailed 7-order averaged model is built. This model is capable of including the model of PLL and model of the real two-sampling-time delay deadbeat control law.

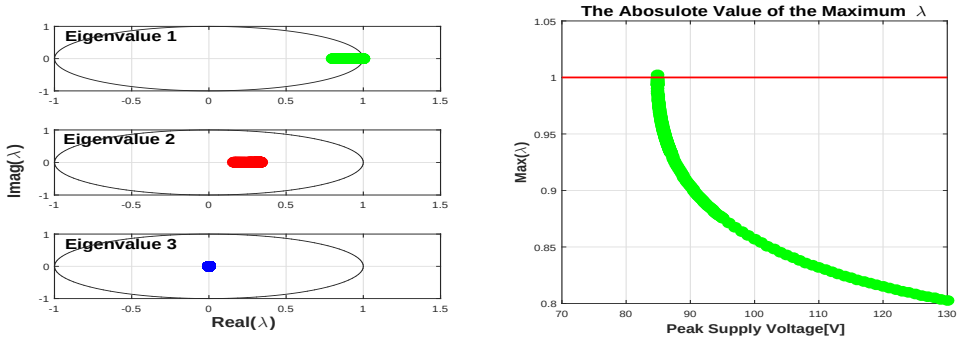

(a) Eigenvalue map varying V_{S1}

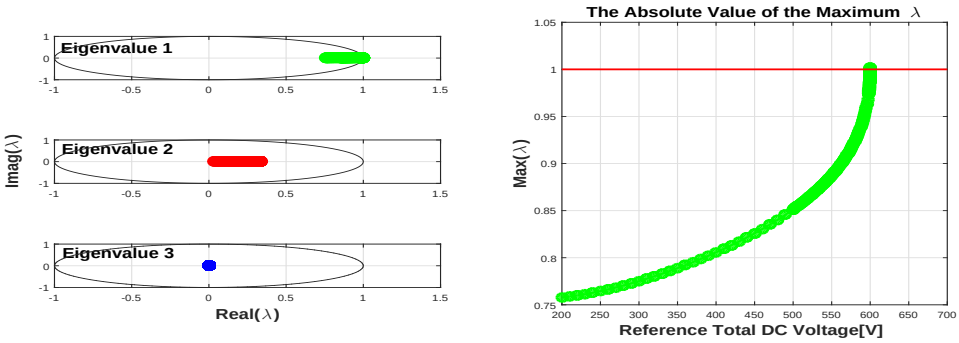

(b) Eigenvalue map varying V_{ref}

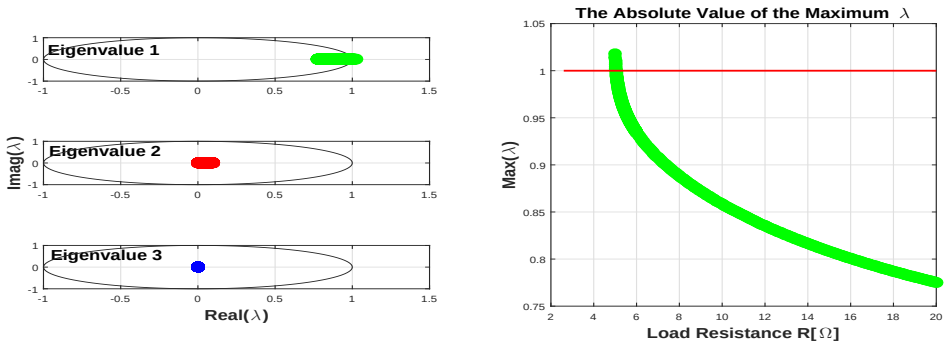

(c) Eigenvalue map varying R

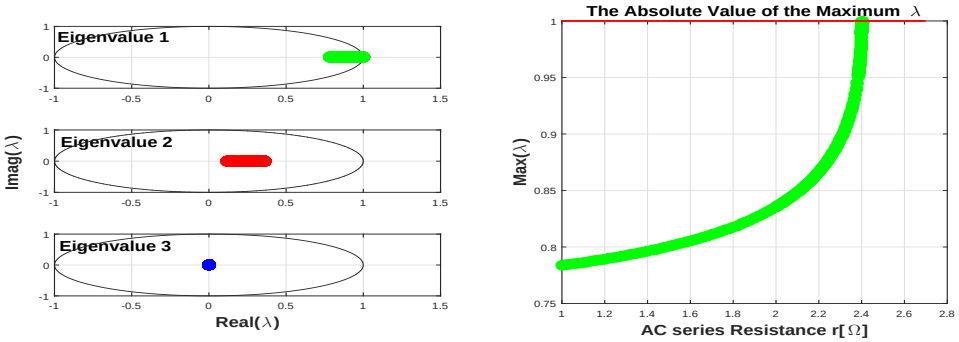

(d) Eigenvalue map varying r

Figure 6.2.1 System eigenvalue maps regarding four essential parameters

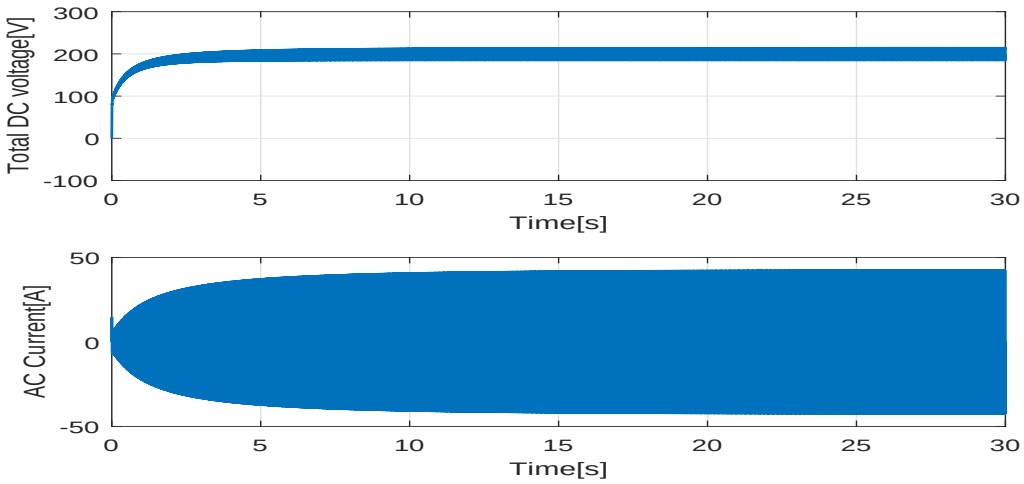

(a) Simulation results when V_{S1} is 57 V

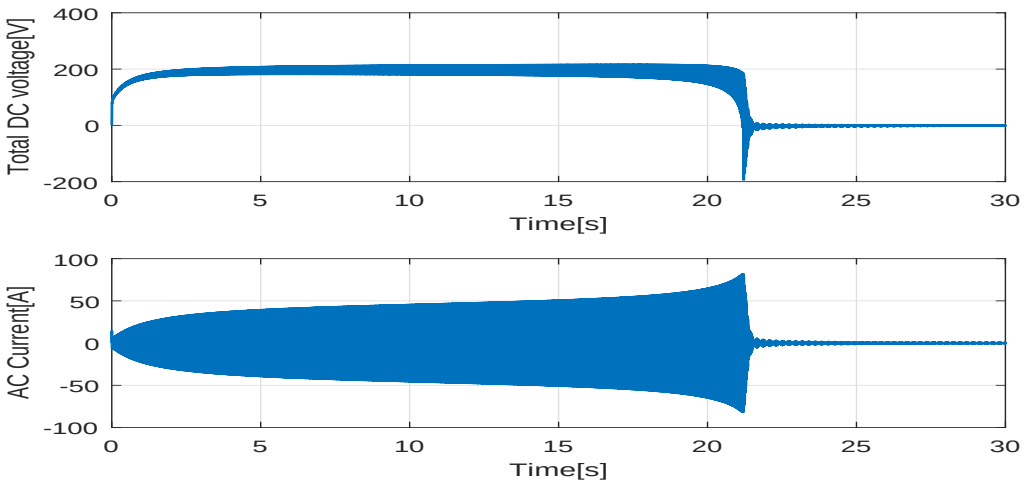

(b) Simulation results when V_{S1} is 56 V

Figure 6.2.2 Time responses of under and above V_{S1} threshold showing stable and unstable converter operations

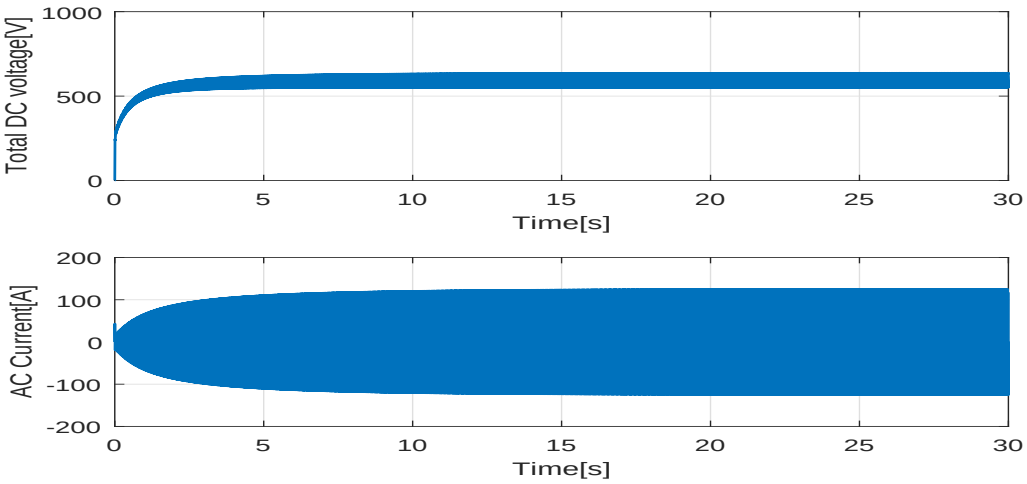

(a) Simulation results when V_{ref} is 599 V

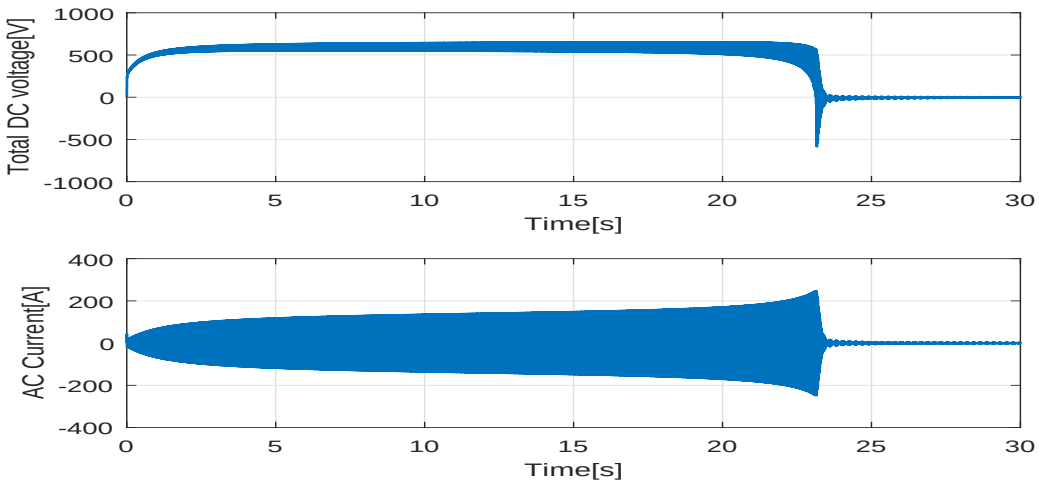

(b) Simulation results when V_{ref} is 601 V

Figure 6.2.3 Time responses of under and above V_{ref} threshold showing stable and unstable converter operations

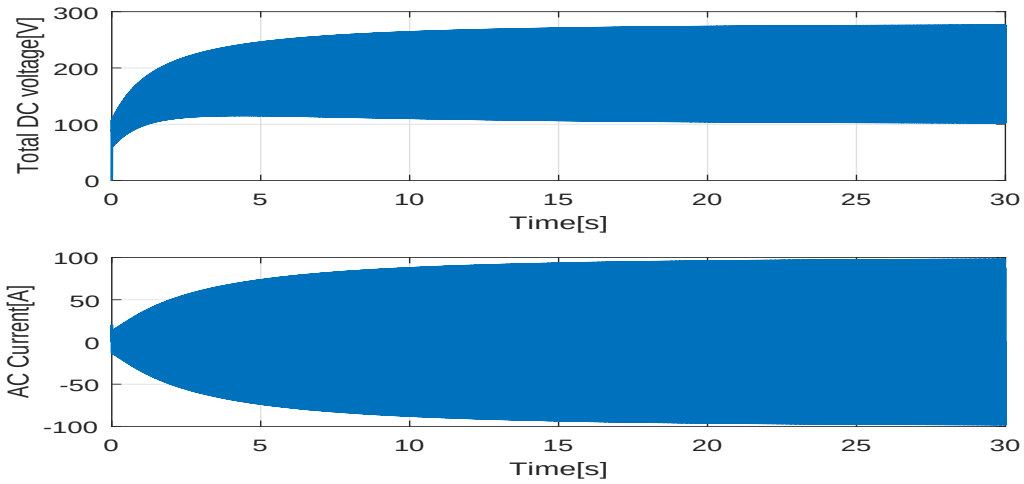

(a) Simulation results when R is 2.1Ω

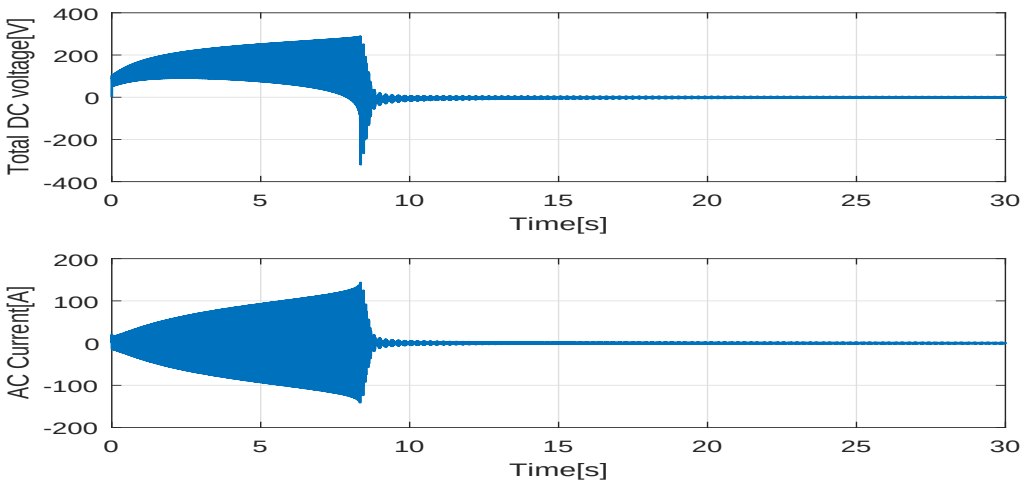

(b) Simulation results when R is 2.2Ω

Figure 6.2.4 Time responses of under and above R threshold showing stable and unstable converter operations

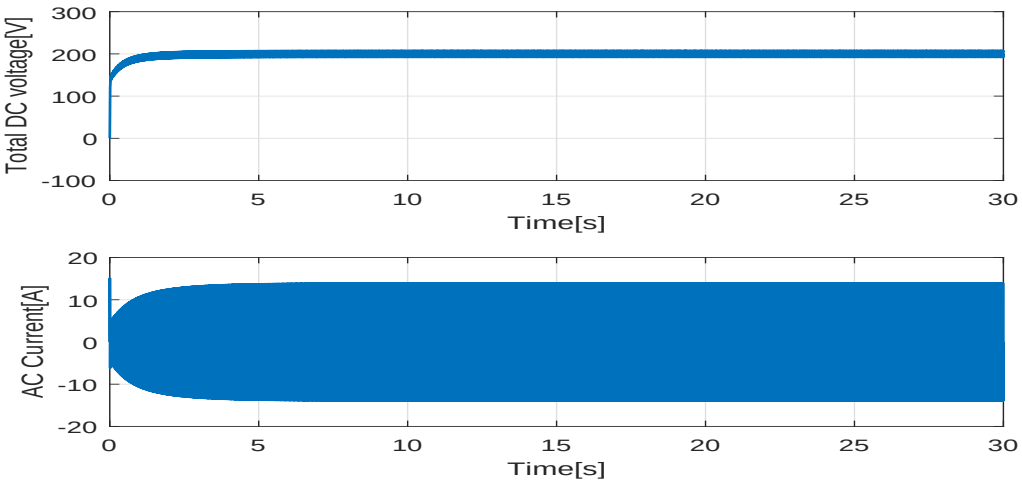

(a) Simulation results when r is 5.3Ω

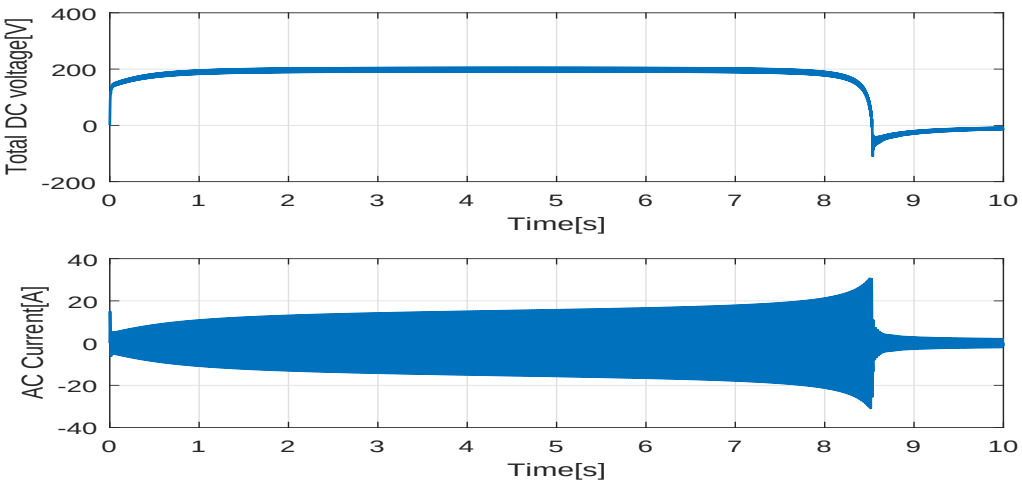

(b) Simulation results when r is 5.6Ω

Figure 6.2.5 Time responses of under and above r threshold showing stable and unstable converter operations

6.3 Stability Analysis of the Full System

In this section, a more detailed mathematical model is built. Compared to the simplified model, it additionally includes the PLL equation and the voltage at the point of common coupling. It is a seven order ODE system which includes the grid side inductance and more realistic control algorithm.

Represent the state variables as $\mathbf{x} = [V_C, I_L, U, V_\beta, D_\beta, \theta, \Gamma]^T$. Neglect the transients, assume that $x_i = \bar{x_i} + \Delta x_i, i = 1, 2, ...7$, where $\bar{x_i}$ is the steady state and Δx_i is the small signal perturbation. Hence the non-linear time periodic(NLTP) system can be linearised as a small signal linear time periodic(LTP) model shown in (6.3.1).

$$
\begin{aligned}
\Delta\dot{x}_1 &= -\frac{1}{RC}\Delta x_1 + \frac{3}{C}(\bar{m}\Delta x_2 + 3\Delta m\bar{x_2}) \\
\Delta\dot{x}_2 &= -\frac{1}{L+L_S}(\bar{m}\Delta x_1 + \Delta m\bar{x_1}) - \frac{r}{L+Ls}\Delta x_2 \\
\Delta\dot{x}_3 &= (-\frac{k_p}{CR} - k_i)\Delta x_1 - \frac{3k_p}{C}(\bar{m}\Delta x_2 + \Delta m\bar{x_2}) \\
\Delta\dot{x}_4 &= \Delta x_5 \\
\Delta\dot{x}_5 &= -\omega^2\Delta x_4 - \omega\Delta x_5 \\
\Delta\dot{x}_6 &= \Delta x_7 - k_p^{'}\sin(\bar{x_6})\Delta x_6 V_\alpha + k_p^{'}\cos(\bar{x_6})\Delta x_6\bar{x_4} + k_p^{'}\sin(\bar{x_6})\Delta x_4 \\
\Delta\dot{x}_7 &= -k_i^{'}\sin(\bar{x_6})\Delta x_6 V_\alpha + k_i^{'}\cos(\bar{x_6})\Delta x_6\bar{x_4} + k_i^{'}\sin(\bar{x_6})\Delta x_4
\end{aligned} \tag{6.3.1}
$$

$$
\begin{aligned}
\Delta m =& \frac{1}{V_{ref}}(A_s\cos(\bar{x_6} + \omega T_s) - \frac{L}{2T_s}x_3\bar{x_6}\cos(\bar{x_6} + 2\omega T_s) - \frac{L}{2T_s}\Delta x_3\sin(\bar{x_6} + 2\omega T_s) \\
&+ \frac{L}{2T_s}\Delta x_2 - r\bar{x_3}\Delta x_6\cos(\bar{x_6} + \omega T_s) - r\Delta x_3\sin(\bar{x_6} + \omega T_s))
\end{aligned} \tag{6.3.2}
$$

We may, therefore, determine stability by examining the magnitudes of the eigenvalues of the monodromy matrix, which is obtained by solving the small signal model for a fundamental period T_S. In the small signal model, it also contains steady state spectra that are solved in the last chapter for detailed model steady-state modelling.

Meanwhile, the known system eigenvectors are informative about the small signal stability of the system. From observing the corresponding eigenvectors, it can be

known that $\lambda_{1,2}$ are related to the DC-link voltage control strictly, λ_3 is associated with the interaction between the outer loop and inner loop, λ_{4-7} are mainly affected by the PLL.

The eigenvalue maps shown in the following part of the section are obtained from two aspects concerning investigating the stability. In subsection 6.3.1 the stability boundary regarding the outer-loop PI controller is examined, under the assumption that the grid is non-ideal and the inductance of the transmission line is 3 mH, and other parameters remained the same with the defined system configurations. It is found that by varying the PI bandwidth, the eigenvalues of the monodromy matrix would escape the unit circle at some point. The immigration path of the eigenvalue from inside the unit circle to the outside is shown with a proper range of PI bandwidth configurations. In subsection 6.3.2 the stability threshold regarding the PLL bandwidth under different grid conditions.

6.3.1 The Effect of PI Bandwidth on Stability

Fig.6.3.1 is the eigenvalue distribution map when PI bandwidth is increasing from 50 Hz to 80 Hz with the step of $10Hz$ and L_S is assumed as 3 mH. λ_1 is closely related to the outer control loop, and λ_1 equals $-0.1972+0.0952j$, $-0.0288+0.2186j$, 0.3675 and 1.0632(unstable) for 50 Hz, 60 Hz, 70 Hz, 80 Hz, respectively. It can be concluded that 80 Hz is the stability threshold for this configuration. In the next section simulation results will show when PI bandwidth varies from 60 Hz to 80 Hz what the time response of the system would evolve.

6.3.2 The Effect of Grid Strength and PLL Bandwidth On Stability

In this subsection, the relationship between the grid strength and the PLL bandwidth limit is studied. Three grid inductance values $L_S = 0, 3, 6$ mH due to the availability

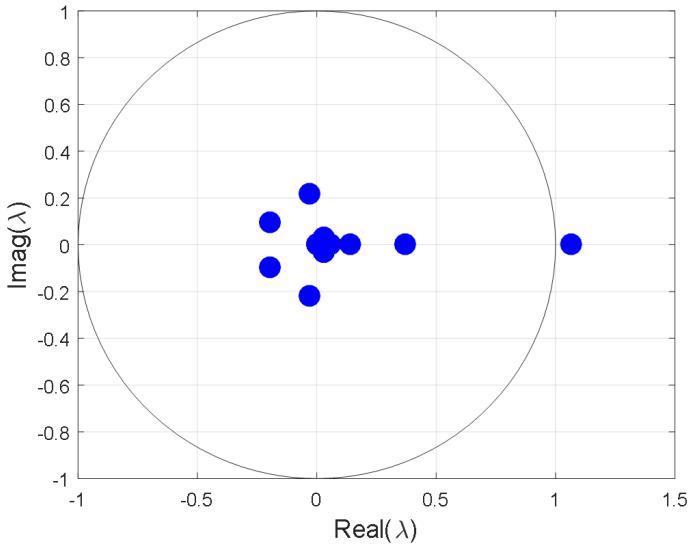

Figure 6.3.1 Eigenvalue map with increasing bandwidth of the DC-link PI controller from 50 Hz to 80 Hz.

in the lab is studied representing three different strength grids. Zero grid inductance stands for ideal grid; 3 mH grid inductance represents a more realistic grid condition; 6 mH stands for the relatively weak grid.

Fig.6.3.2a shows the eigenvalue map as PLL bandwidth increases in steps from 10 Hz to 50 Hz at an increment of 5 Hz when L_S is zero and mainly the conjugate eigenvalue pair λ_3, λ_4 are immigrating. The right side figure is the zoomed-in of λ_3 (the path of its conjugate part λ_4 is balanced in the plot) immigrating from inside the unit circle to outside the unit circle. The first eigenvalue which escapes the unit circle is when PLL bandwidth reaches 50 Hz, indicating the system losing stability.

In Fig.6.3.2b the PLL bandwidth is varied in steps from 15 Hz to 55 Hz at an increment of 5 Hz when L_S is 3 mH. The zoomed-in plot of λ_3 indicates that when PLL bandwidth reaches 55 Hz, it comes out of the unit circle.

Fig.6.3.2c demonstrates the eigenvalue map of the weak grid when L_S is 6 mH, and the PLL bandwidth is varied from 20 Hz to 60 Hz at an increment of 5 Hz. The zoomed-in plot of λ_3 indicates that when PLL bandwidth reaches 60 Hz, it comes out

of the unit circle.

In addition, the values of λ_3 in the right hand side of Fig.6.3.2 are listed in Table 6.1-6.3 for the last three bandwidths for aiding the interpretation of Fig.6.3.2. From the

Table 6.1 Eigenvalues of the closed-loop system with varying PLL bandwidths when the converter is connected to the ideal grid

PLL Bandwidth	$L_S = 0$	Magnitude
40 Hz	0.9745+0.2066j	0.9951
45 Hz	0.9825+0.1587j	0.9952
50 Hz	0.9981+0.0825j	1.0015

Table 6.2 Eigenvalues of the closed-loop system with varying PLL bandwidths when L_S equals 3 mH.

PLL Bandwidth	$L_S = 3$ mH	Magnitude
45 Hz	0.9979+0.0621j	0.9998
50 Hz	0.9985+0.0547j	0.9999
55 Hz	0.9995+0.0367j	1.0015

Table 6.3 Eigenvalues of the closed-loop system with varying PLL bandwidths when L_S equals 6 mH

PLL Bandwidth	$L_S = 3$ mH	Magnitude
50 Hz	0.9975+0.0645j	0.9996
55 Hz	0.9982+0.0587j	0.9999
60 Hz	0.9998+0.0448j	1.0016

eigenvalue analysis, we have obtained instability thresholds of PLL bandwidths under three different grid conditions. A general law can be summarised for the relationship between the grid strength and the stability breakpoint of the PLL bandwidth is that the weaker the grid is, the higher the PLL threshold bandwidth is. When it's ideal grid, the break point of PLL bandwidth is 50 Hz; when L_S is 3 mH, the threshold is 55 Hz; and when L_S is 6 mH, the system gets unstable until PLL bandwidth reaches 60 Hz.

The correctness of above prediction from the eigenvalue analysis is validated by both the simulations in the next section and experiments in the next chapter.

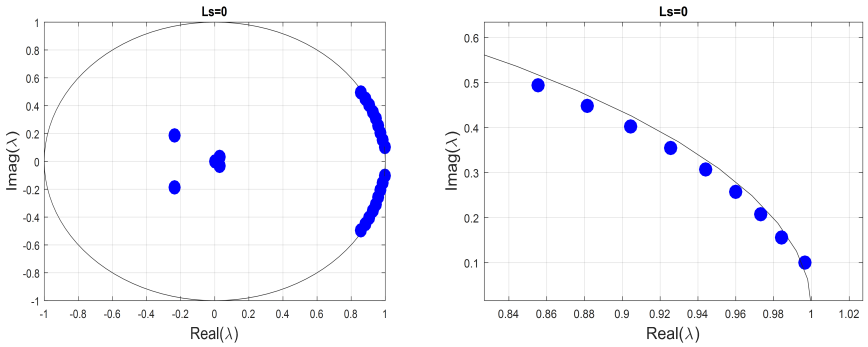

(a) Eigenvalue map with increasing PLL bandwidth when $L_S = 0$ mH.

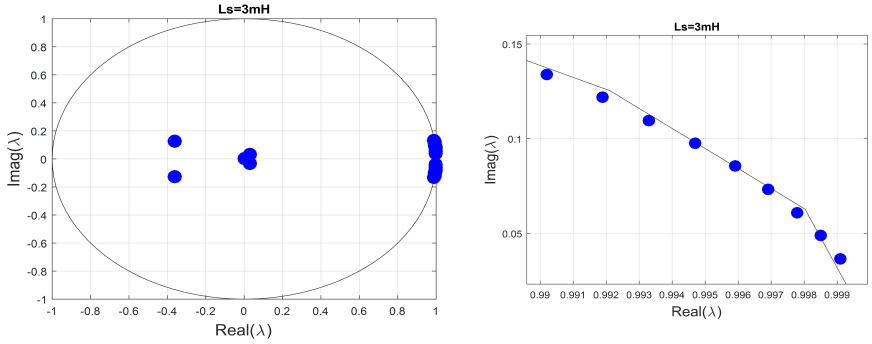

(b) Eigenvalue map with increasing PLL bandwidth when $L_S = 3$ mH.

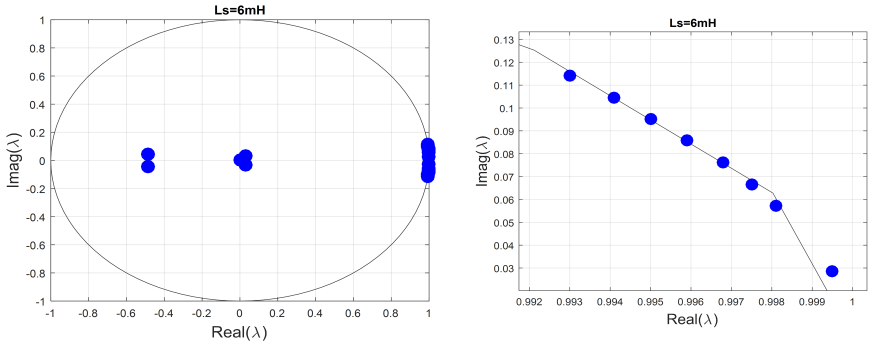

(c) Eigenvalue map with increasing PLL bandwidth when $L_S = 6$ mH.

Figure 6.3.2 Eigenvalue maps of varying PLL bandwidth regarding different grid strength.

6.4 Simulation Verification of the Parametric Thresholds

In this section, the aim is to use the system switching model to verify the thresholds of the PI bandwidth and PLL bandwidths under three grid conditions predicted by the stability analysis in section 6.3.

6.4.1 The Verification of PI Bandwidth Stability-Threshold

Fig.6.4.1 shows the simulation results (I_L, V_C, and V_{CONV}) from the switching model. Fig.6.4.1a shows the system response when PI bandwidth changes from 60 Hz, 70 Hz to 80 Hz each lasts for 1 s when L_S is 3 mH. During 0 s to 1 s, the system operates finely; during 1 s to 2 s, distortions are observed; during 2 s to 3 s, the current starts to diverge, the DC-link voltage and ac terminal voltage are distorted to a large extent.

6.4.2 The Verification of Grid Strength and PLL Bandwidth Stability-Threshold

Fig.6.4.2 indicates when PLL bandwidth varies from 40 Hz, 45 Hz to 50 Hz under ideal strong grid (L_S equals 0). Fig.6.4.3 demonstrates the system response when L_S equals 3 mH and PLL bandwidth changes from 45 Hz, 50 Hz to 55 Hz. Fig.6.4.4 shows the system response when L_S equals 6 mH and PLL bandwidth switches from 50 Hz, 55 Hz to 60 Hz. Each step lasts for one second, and the converter operates from stable to unstable. The overall time responses of the cell DC link voltage (20V/div), AC side current (10A/div), converter AC side input multilevel voltage (100V/div) are collected for each grid condition as well as the zoomed-in plot for each time step. It can be observed that as the grid side inductance increases from 0, 3 to 6 mH, representing the grid strength varying from ideal, practical to weak, the instability

point for PLL bandwidth is also increased. It can be assumed that there exists a relationship between the grid strength and PLL bandwidth regarding stability.

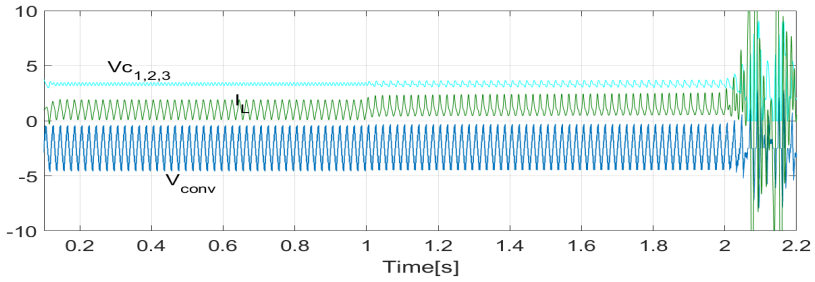

(a) Overall system response showing step changes of PI bandwidth.

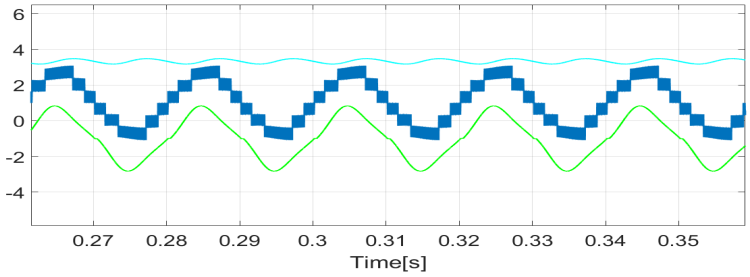

(b) Operation during PI bandwidth is 60 Hz.

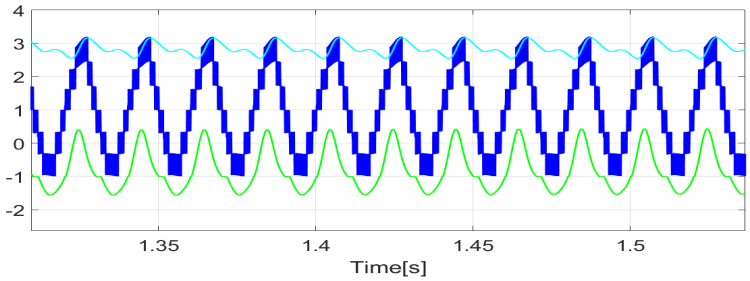

(c) Operation when PI bandwidth is 70 Hz.

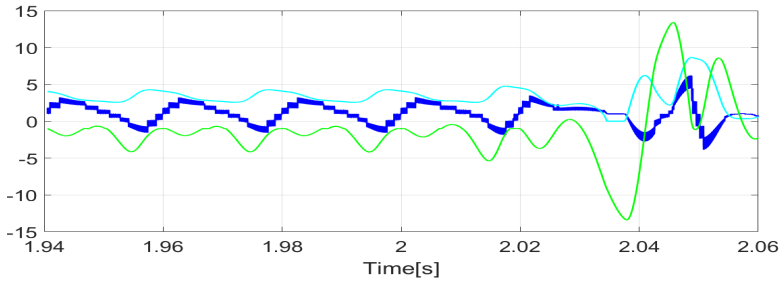

(d) Instant when system fails at 80 Hz.

Figure 6.4.1 Simulated time response of CHB converter operation with varying PI bandwidth condition

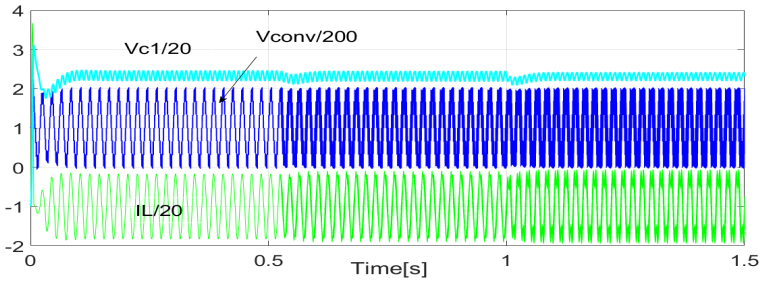

(a) Overall system response showing step evolutions of PLL bandwidth.

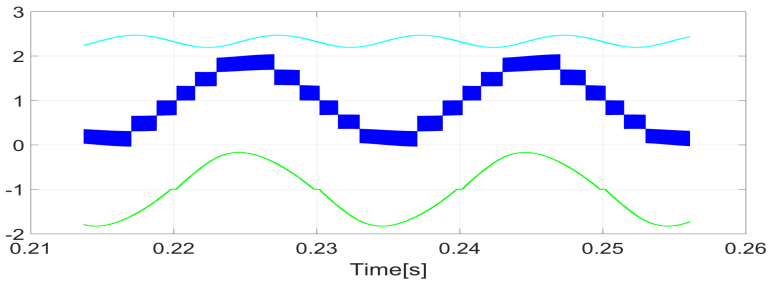

(b) Operation during PI bandwidth is 40 Hz.

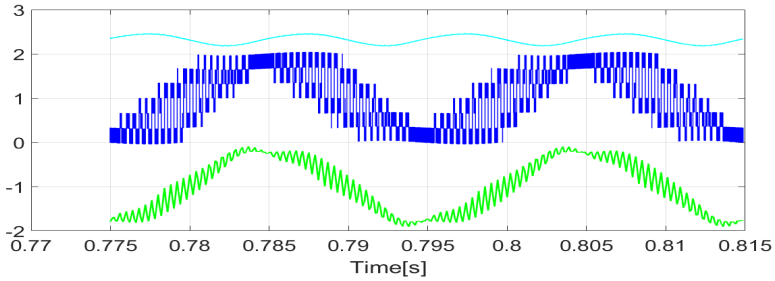

(c) Operation when PI bandwidth is 45 Hz.

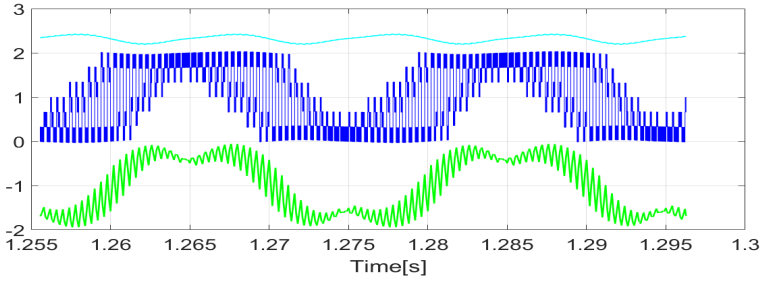

(d) Instant when system fails at 50 Hz.

Figure 6.4.2 Simulated time response of CHB converter operation of varying PLL bandwidths when $L_S = 0$

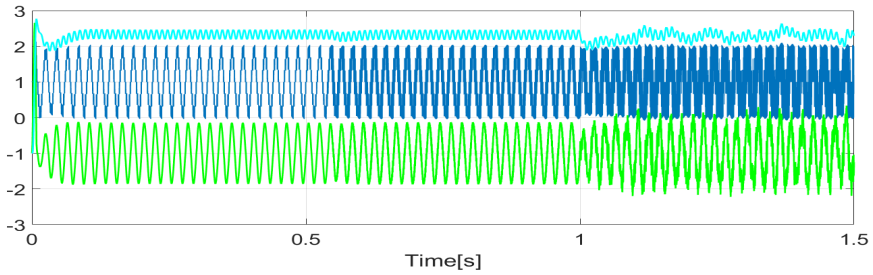

(a) Overall system response showing step evolutions of PLL bandwidth.

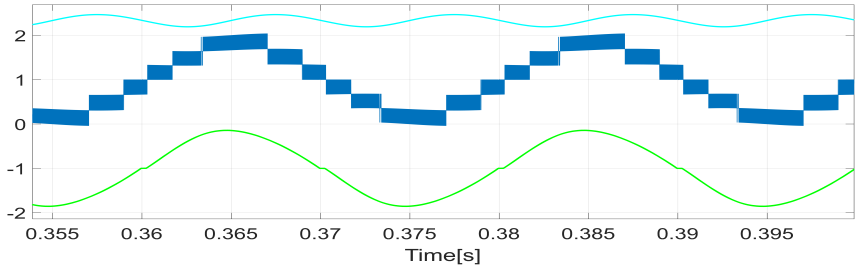

(b) Operation during PI bandwidth is 45 Hz.

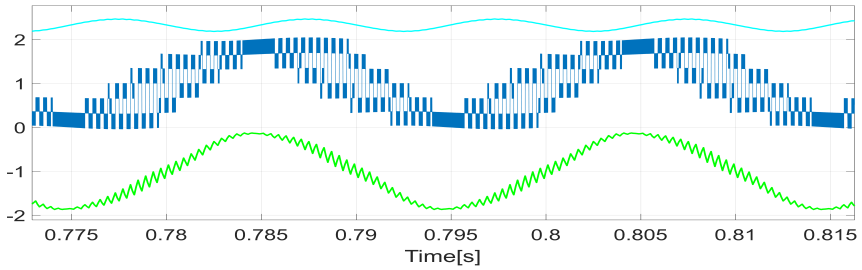

(c) Operation when PI bandwidth is 50 Hz.

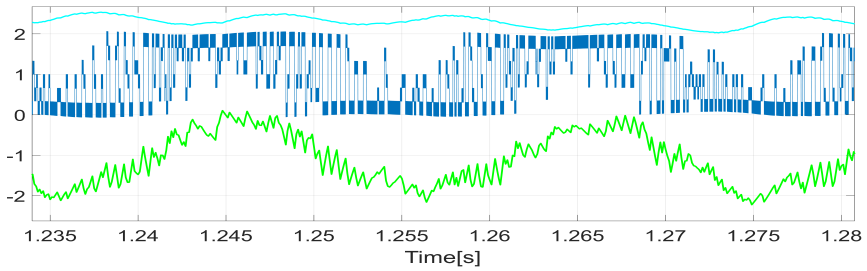

(d) Instant when system fails at 55 Hz.

Figure 6.4.3 Simulated time response of CHB converter operation of varying PLL bandwidth when $L_S = 3$ mH

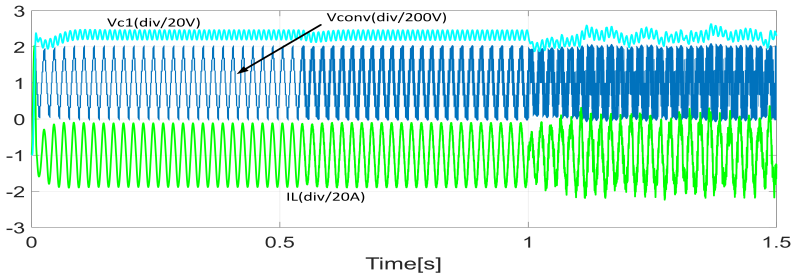

(a) Overall system response showing step evolutions of PLL bandwidth.

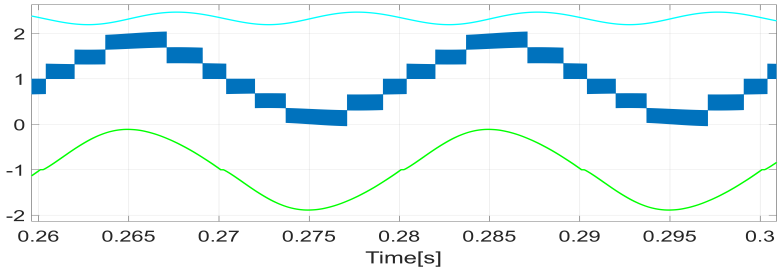

(b) Operation during PI bandwidth is 50 Hz.

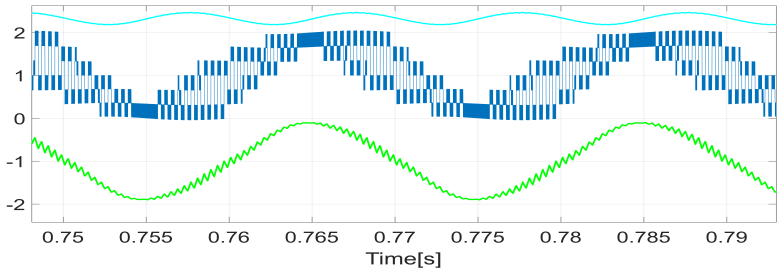

(c) Operation when PI bandwidth is 55 Hz.

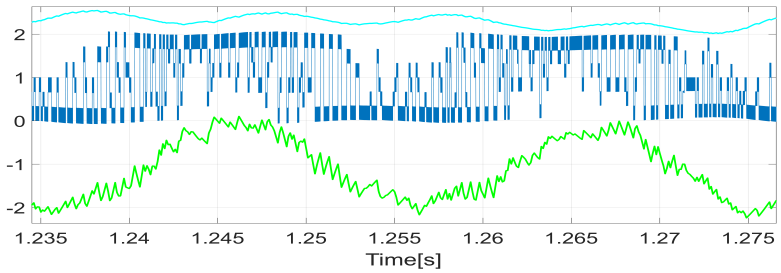

(d) Instant when system fails at 60 Hz.

Figure 6.4.4 Simulated time response of CHB converter operation of varying PLL bandwidth when $L_S = 6$ mH.

6.5 Summary

In this chapter, the stability analysis of the linear time-periodic model in terms of the small signal perturbations has been studied. The Floquet theory has been applied for the simplified system regardless of the grid side inductance to determine the stability of the system by observing the distribution of the Floquet multipliers regarding the unit cycle. The results have shown clear thresholds and stable ranges for some converter design parameters, such as the size of the DC resistive load, the AC side equivalent series resistance, the amplitude of the supply voltage and the reference of the total DC-link voltage controller. These stability thresholds have been verified by simulations to be validated. However, it is hard to validate them in the experiment because the there existing danger of capacitor voltage going to the negative or current flowing through the switching devices being higher than the nominal ratings.

Another case was studied when the CHB rectifier is connected to the weak grid. Weak grid refers to that the impedance between the grid and the converter is big so that the operation of the PLL would be affected. Under this condition, the DC-link voltage is unstable since a small perturbation is likely to make the system diverge. The possible reason is that the output phase angle from the PLL is distorted, resulting in a distortion in the reference current of the deadbeat control thus the whole control loop becomes unstable. Experiments in chapter 8 will verify these analytical results.

This analysing method has provided a powerful tool for carrying out the stability of more grid-connected converter prototypes since they are all non-linear time-periodic systems in nature from mathematical modelling. This technique can help engineers with clear stability boundaries during constraints design and selection. The disadvantage of this method is that it may contain too much calculus of the harmonic balance steady-state modelling.

Chapter 7

Converter Hardware Design and Practical Control Implementation

7.1 Overall Rig Structure

Fig7.1.1 shows the overall experiment setting up. The main part of the rig is protected inside a cover. The load power resistors and line inductor are laid on the ground. The sampled data is imported to computer from the control board. The computer acts the control actions via software depending on the feedback measurements. An electronic oscilloscope is available of observing real-time data. A programmable AC source machine is connected to the system as the system input, emulating a single-phase grid condition.

A zoomed-in photo of the central part of the rig is shown in Fig7.1.3. The CHB converter is made up of three H-bridge cells connected in series from the AC side, and their gate drive boards are supplied by an auxiliary power source. Six $1000\mu F$ $450V$ electrolytic capacitors are connected to the CHB on the DC side, two in parallel for each cell. An FPGA/DSP control platform is set up on the right of CHB sending switching signals to gate driver via fibre optic cables. A transducer station sits on the

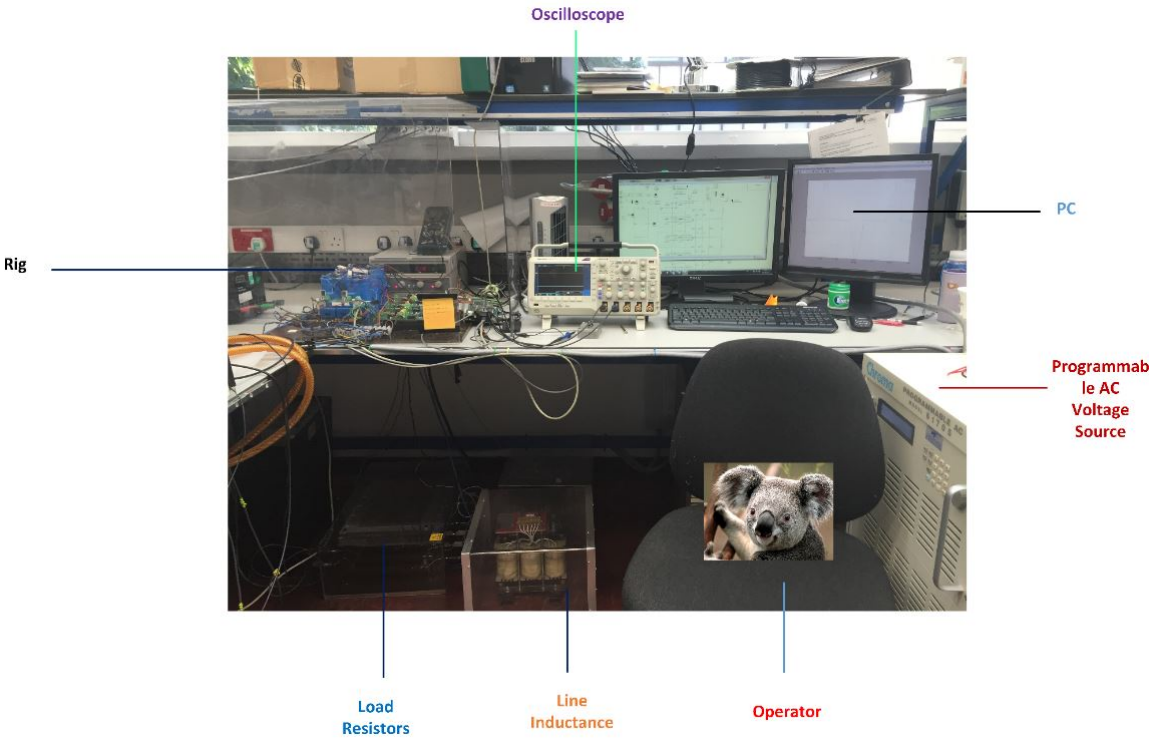

Figure 7.1.1 Overview of experiment set-up

left of the converter, consisting of four voltage sensors, three for capacitor voltages, one for the supply voltage (on strip board) and one current sensor (on PCB).

A functional block diagram is also illustrated in Fig.7.1.2. The hardware system consists of six parts as shown. There are both power flow and signal information communication between each part within the system.

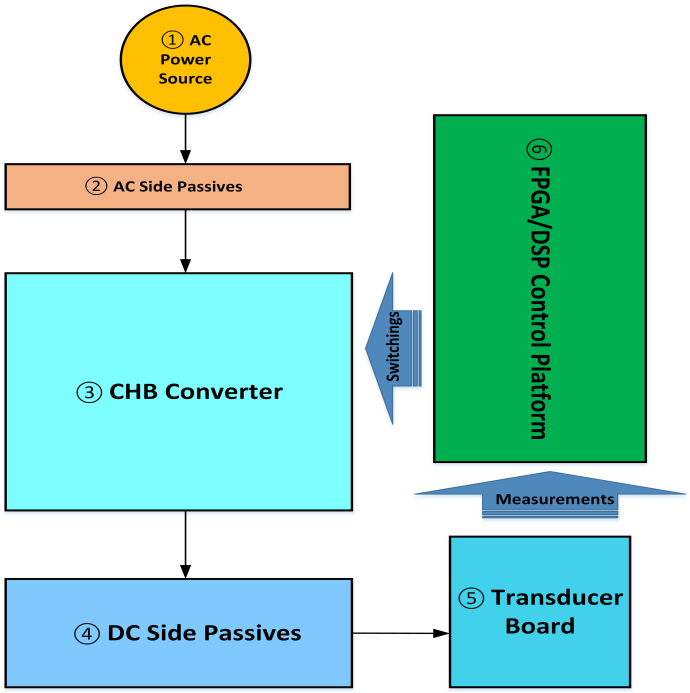

Figure 7.1.2 Functional block diagram of hardware subsystems

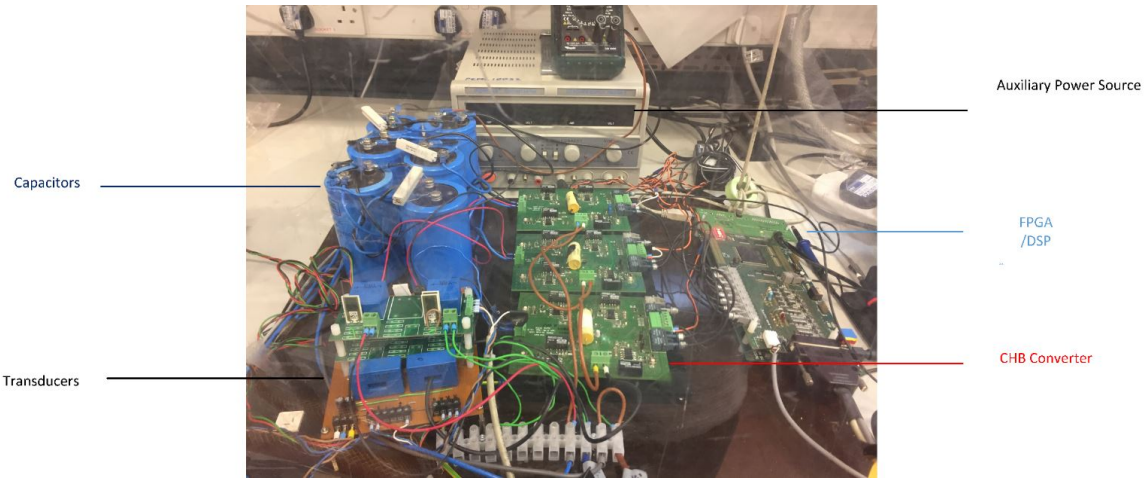

Figure 7.1.3 Photo of rig

7.2 Converter Design

7.2.1 IGBT Module

The 7-level CHB converter is built up with 3 H-bridge cells. The H-bridge power module designed in PEMC group is used [45]. The IGBT module used is Semikron SK30GH123 IGBT module 1200V 30A. It is a full-bridge power module containing four IGBTs with body diodes as shown in Fig.7.2.1. The IGBT power module is mounted to the gate drive circuit PCB, underneath pasted to the heat sink.

Figure 7.2.1 SEMIKRON SK30GH123 (a)power module and (b)pin configuration

7.2.2 Gate Drive Board

Each gate drive board requires the supply voltage of $0-5V$ provided by an auxiliary DC power supply. Hence each board has a circulating current of about $0.4A$, the supply power for three gate drive boards is approximately $6W$.

Each gate drive board contains four gate drive circuits for the full H-bridge power module. However, only two switching signals from the FPGA are required for each power module, served as the gating signals for the two upper switches, the other two for gating the lower switches are obtained by inverting them directly on the PCB.

The highlight of the gate drive circuit is shown in Fig.7.2.2, the switching signal

received from FPGA is inverted and sent to the optocoupler HCPL-3120, the optocoupler then converts the low-voltage gating signals to $\pm 15V$ signals which are suitable for driving IGBTs. It also provides insulation between the high voltage operating side and the low voltage gate drive side. The optocoupler is supplied by the DC-DC converter NMH0515SC which gives the $\pm 15V$ output from the nominal 5V input voltage.

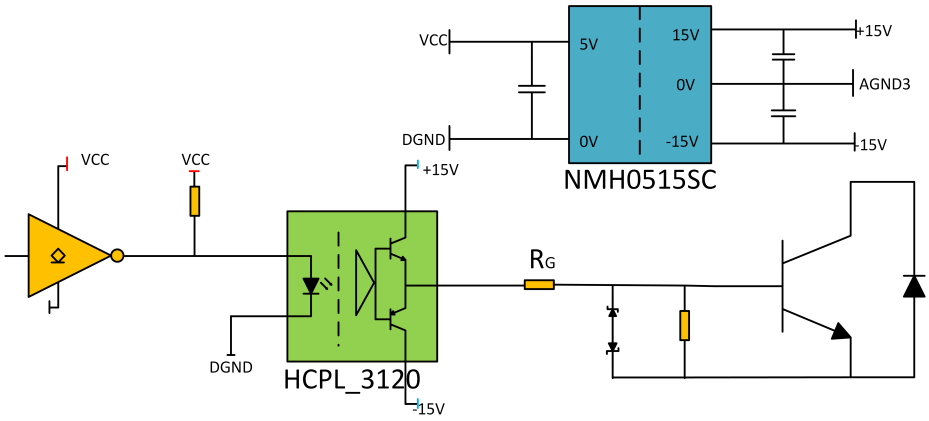

Figure 7.2.2 Highlight of the gate drive circuit

A resistor R_G (47Ω) is connected to the gate of IGBT to limit the current into the gate of the IGBT. The value of R_G affects the speed of turning on IGBT. The smaller R_G is, the shorter switching time and less switching loss are. R_G also helps to avoid the resonance which could happen because of the stray inductance and the parasitic capacitance around the IGBTs and inverse diodes. Hence it can't be too small, and there is a trade-off of its choice.

A pair of back to back Zenor diodes are connected between the gate and emitter of the IGBT to have over-voltage protection avoiding the voltages applied to the IGBT beyond $\pm 18V$. A $20k\Omega$ resistor is connected in parallel to the Zenor diodes, which is to assure that in the absence of the gate drive signal, the capacitance across the gate and emitter wouldn't unexpectedly turn on via the parasitic capacitances.

7.2.3 Dead Time Circuit

According to a method of calculating deadtime [118] and the nominal values of the IGBT module[119], the calculated dead time is around $0.5\mu s$. The actual dead time is set to be $1.5\mu s$ for enough safety margin.

The dead time circuit is integrated into the gate drive circuit. It consists of mainly an RC circuit as shown in Fig.7.2.3. When the input signal of the dead time circuit changes from low to high, the current flows through the trimmer, the capacitor is charging. Thus the RC circuit stops the rising edge of the output signal from changing too fast. On the other hand when the input signal changes from high to low, the current would go from the diode, the capacitor is discharging. A Schmitt trigger is used to after the RC circuit to convert the slow rising edges of the gating signals to fast edges, resulting in the gating signals with dead time, whose length is decided by the time constant of the RC circuit.

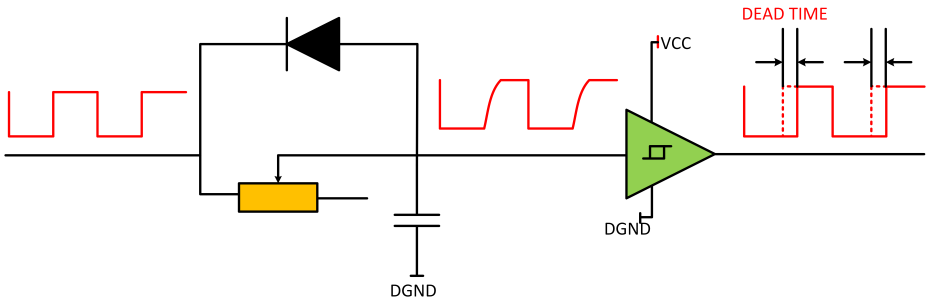

Figure 7.2.3 Dead time circuit

7.3 Transducers

The voltage transducer used is LEM LV-25P[120], which can measure either AC or DC voltages. The current transducer used is LEM LA-55P[121]. They are both Hall effect closed-loop compensated current transducer and supplied with ±15 V voltage.

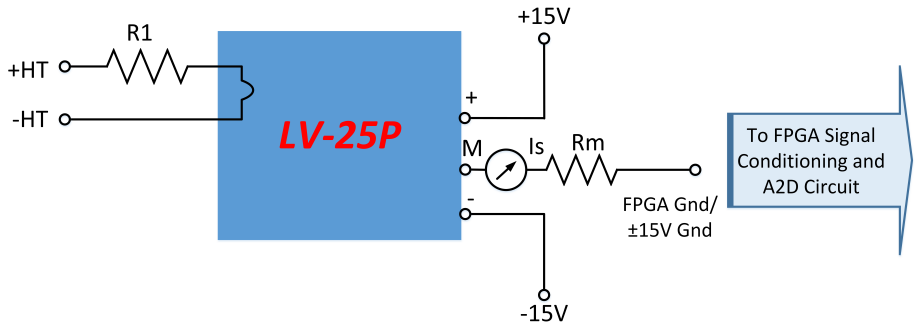

Figure 7.3.1 Voltage transducer LV-25P connection

The diagram of the voltage transducer is shown in Fig.7.3.1, a primary resistor R_1 on the high voltage measurement side and a burden resistor R_m on the output side, respectively. Their values need to be chosen with care. The transducer optimum accuracy is obtained at the nominal primary current of 10 mA according to the datasheet. Assume the measured voltage is around 200 V, the calculated value for the primary resistor is hence 20 $k\Omega$. In the experiment, we applied 23.5 $k\Omega$, by two 47 $k\Omega$ metal-plate cement type resistors connected in parallel.

The output of the transducer is a current signal, which needs to be converted to a voltage signal. This voltage signal is then sent to the signal conditioning and A2D circuit on the FPGA via a 25D-way connector. The converted voltage signal cannot beyond $5V$, which is the supply voltage of the FPGA board and the A2D converters. From the datasheet the current conversion ratio is 2500 : 1000, if the primary side is working with nominal current, the current on the secondary side would be 0.4 mA. In our case a 150 Ω burden/measuring resistor is soldered on FPGA, resulting in about $0.06V$ voltage as the input to the signal conditioning circuit.

The current transducer works similarly and is more straightforward. The primary nominal RMS current for LA-55P is 50 A. If consider the measured current to be 20 A, the number of turns on the primary side should be two to achieve the excellent accuracy. Similarly, at the output, a burden resistor is selected according to the conversion ratio.

It should be noted that transducers should be calibrated before being used to give the feedback measurements for the closed-loop control. The calibration process converts the output from the A2D converters to the real voltage or current values so that the DSP code can use them. The calibration is fulfilled by a Precision Voltage Source (PVS) and a low-power current generator.

7.4 Passive Components

7.4.1 Line Inductance Selection

The line inductor on the AC side has two main functions; the first is acting as the current smoothing circuit and, the other is for adjusting the power factor since by changing the voltage on the inductor the different power factor operations can be achieved.

To limit the switching ripple in the supply side current, the high-frequency switching ripple can cause Electromagnetic Interference (EMI) problem, the reactance of the inductor needs to be at the allowable size at the frequency of the ripple to avoid big voltage ripple, even though the amplitude of the ripple current is small. A method is to find out the most significant voltage harmonic and its magnitude by doing an FFT of the converter simpler model and then calculate the inductance with allowable current ripple according to Electromagnetic Compliance (EMC) standards. However, we use another simpler method by approximately evaluating the line inductance by (7.4.1) for a 3-cell CHB converter[122].

$$L_{min} = \frac{V_{ref}}{12 f_s I_{Lripple}} \tag{7.4.1}$$

where f_s is the switching frequency of the PWM, V_{ref} is the total DC-link voltage reference, and $I_{Lripple}$ is the current ripple.

Consider a nominal current of 20 A rms and limit current ripple at 2%, which would be 0.4 A. Assume V_{ref} as 200 V, and f_s as 5 kHz. Then according to (7.4.1), the

minimum inductance value needed is 8.3 mH. But according the components available in the lab, a bigger 11 mH inductor is used.

7.4.2 DC Capacitor Selection

Capacitors are served as DC side filter at the output of the rectifier. It converts the non-smooth DC current to smoother DC current. When designing the DC link capacitors, there are a few configurations need to be considered. The most important two are the voltage rating and capacitance value, the voltage rating needs to be selected according to the application, and the capacitance decides the size of the ripple.

The capacitors linked in the DC side of each isolated H-bridge, the DC voltage should be higher than the AC voltage to avoid over modulations. In this project the capacitors with a voltage rating of 450 V are used in the experiment, ensuring large enough safety margin for operation.

The DC current feeding the capacitor contains not only a DC component but also a twice the frequency of the grid current. This is a result of the interference of grid voltage and grid current at single phase operation. In this case, the DC current that feeds the capacitor can be calculated as:

$$I_{dc} = \frac{V_{Spk} I_{Lpk}}{2V_{ref}} \tag{7.4.2}$$

Where V_{Spk} and I_{Lpk} are the peak values of grid voltage and grid current, the ripple in the DC side voltage at frequency 2ω can be calculated from the current magnitude and the impedance of the capacitor (at frequency 2ω). Hence the capacitance can be calculated as:

$$C = \frac{I_{dc}}{2\omega V_{Cripple}} \tag{7.4.3}$$

Where $V_{Cripple}$ is the peak ripple (peak to peak is twice the value). Set the ripple of the capacitor voltage as 2%, take the reference of the DC link voltage as 200 V,

the ripple would be 4 V peak. With this assumption, the capacitor should have a capacitance of 4775 μF.

However, due to the available capacitors in the lab. In the experiment, two electrolytic 1000 μF capacitors are used in parallel on DC side of each cell, resulting in 2000 μF in total. Therefore, the actual ripple would be larger than the expected and have a 4% ripple.

For the safety consideration, a discharge resistor is connected to each load capacitor. Each capacitor bank is connected in parallel with 20 Ω 3000 W discharge power resistors, which are available in the lab. When powered off, the capacitor could find a way to dissipate the stored energy quickly via these resistors. The value of this resistor can't be too small; otherwise they would get burnt directly.

7.5 FPGA/DSP Control Platform

The control platform is a two-layer structure with Field Programmable Gate Array (FPGA) on top and Digital Signal Processor (DSP) on the bottom as indicated in Fig.7.5.1, connecting via a 32-bit wide External Memory Interface (EMIF) on the DSK. The DSP is used for calculations, and the FPGA board is for A2D function and generating PWM signals.

DSP employed is a high-speed Texas Instrument (TI) TMS320C6713 floating point DSP which runs at 225 MHz, and the DSP Starter Kit (DSK) is used. The DSK is a tabletop card to allow evaluating the specific characteristic of DSP. It also allows evaluators to expand the system in a variety of ways.

The FPGA chip applied is the Microsemi ProASIC3 A3P400[123], which contains 400,000 programmable system gates. The program, which can fulfil the basic requirements needed is loaded to the FPGA. The program includes a register set for controlling the A2D triggering and access to the sampled data, registers set for setting

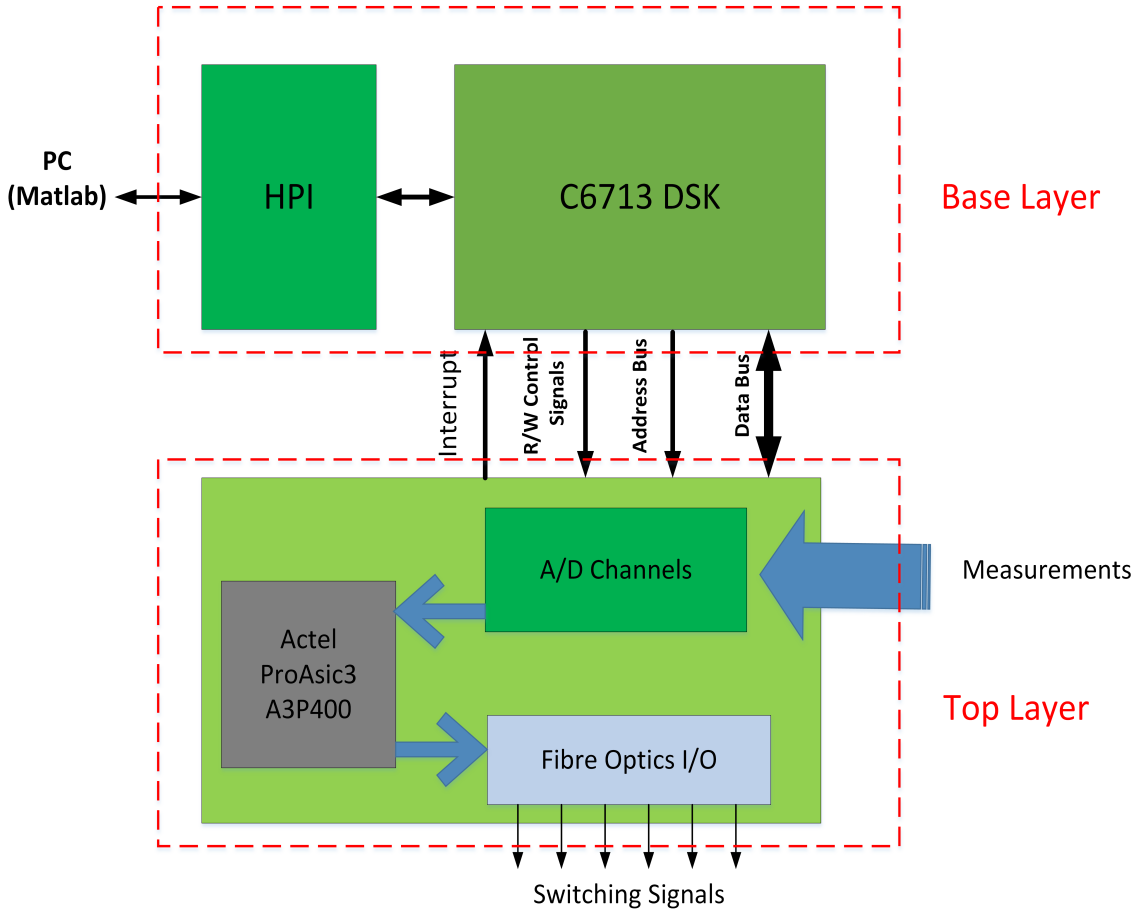

Figure 7.5.1 Schematic of hardware control platform

up an interrupt signal, PWM registers, and other assistant functions such as setting trips and LED display.

A daughter card is connected to the DSP to use the Host Port Interface (HPI) of the C6713, through its USB port, the data in DSP can be accessed and transferred to the computer without interrupting the Central Processing Unit (CPU) of the DSP. All of the accesses to the EMIF are clocked at up to 100 MHz. Through the HPI daughter card, the data from DSP is transferred to the computer in Matlab for saving and plotting.

The source code is compiled with specific configuration files in the TI Code Composer Studio(CCS) software. After compiling and debugging, an out file is generated and

downloaded to the DSP.

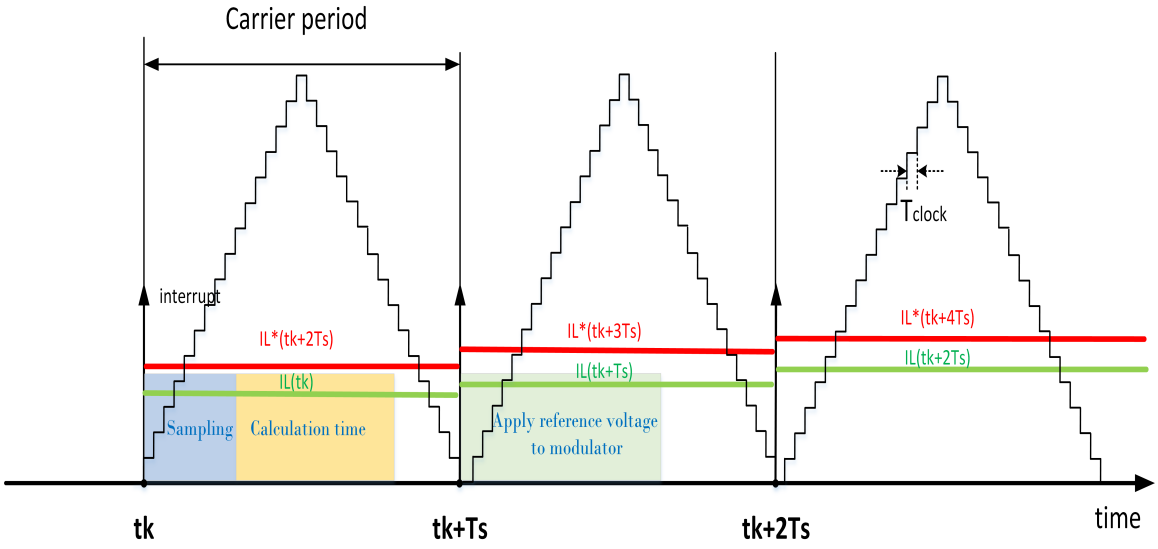

Figure 7.5.2 Digital implementation of dead beat control

The interrupt pulses are generated in FPGA by its clock, and the clock is provided initially by the clock on the FPGA board, whose frequency is 50 MHz. As Fig7.5.2 indicates, the interrupt period is defined to be the same with the period of the carrier. The PSCPWM is fulfilled in FPGA. FPGA UP/DOWN counters generate three phase-shifted triangle carrier waveforms. In our case, there is only one sampling during each interrupt. The sampling frequency is the same with the switching frequency.

The DSP enables the PWM interrupt and then waits for the interrupt to occur. After each pulse, the control is executed until the next pulse. As shown in Fig7.5.2 during each interrupt, the sampling would take place first, the measured data of V_S, V_{C1}, V_{C2}, V_{C3} and I_L are obtained by DSP. Then during the calculation time, DSP executes PI control and deadbeat control law.

The PI controller has been designed in continuous time domain, in order to be implemented in DSP, calculate the error signal of total voltage first, then multiply the error signal by the proportional coefficient k_p; The integral part is implemented with a trapezoidal formula, this integral signal is stored and summed up as time increases.

The proportional part adds the integral part as the output of the PI controller.

The improved deadbeat control law is implemented by considering the intrinsic delay of DSP. As shown in Fig.7.5.2. At time t_k, the sampled values of $V_S(t_k)$ and $I_L(t_k)$ are read, with the desired current reference for the next sampling time $t_k + T_S$ and at $t_k + 2T_S$, the desired voltage reference V^*_{CONV} is calculated, this is the average voltage that the converter applied from the AC side. At time $t_k + T_S$ this desired voltage is applied to the PWM modulator. Moreover, at $t_k + 2T_S$ the measured current would track the prediction made two samplings before.

The output of control is the desired PWM sinusoidal modulating signal. This signal is within the range from -1 to 1 before sent to FPGA they are scaled to the range from 0 to the amplitude of the carrier. Thus the active PWM signals are generated by the comparator in FPGA and over-modulation protection is also added.

The switching outputs are sent to the gate drive circuits of converter via fibre optic cables for its advantage of bringing fewer distortions to the signals, also providing an isolation interface between the control platform and converter.

7.6 Summary

In this chapter the experimental gate drivers, voltage and current transducers, and control platform, etc. are covered and demonstrated. The rig is in a fine mode that can be implemented with the designated control loops and the selected PSCPWM modulation technique with safety trips to test the CHB converter. Different settings can be varied in the control configurations so that the instability points of the parameter can be verified experimentally. The rig is expected to introduce as little disturbances to the waveform as possible. In chapter 8 the experimental results are shown indicating the excellent performance of this rig.

Chapter 8

Experimental Validations

8.1 Introduction

This chapter aims to validate the stability margins developed in the analysis of chapter 6 experimentally. This chapter is organised as follows. In section 8.2 it shows the experimental results of the stable operations of the control loop. The experimental waveforms are obtained by a Tektronix scope; the figures are sampled data taken from an oscilloscope and plotted in MATLAB rather than using screen plots. In section 8.3 the unstable experimental results are demonstrated with parameters in steps approaching the instability points. Figures in this section are scope screen plots.

The experiments were carried out with a single phase 7-level CHB converter as constant with that in the analysis. The AC voltage source is supplied by a programmable AC source, and the magnitude is configured to be $120Vrms$. The $200V$ total DC link voltage reference leads to a modulating index around 0.85. Thus a 7-level voltage can be applied by the converter on the AC side. The experimental waveforms are compared to the simulations where waveforms from the simulation are selected the same time interval in steady state.

8.2 Stable Operation of the System Experimental Results

In this section, the stable operation of the converter is implemented as well as the digital control algorithm is verified. Thus the rig is tested by assuming the CHB rectifier is connected to a strong grid, which in the experiment is realised by not connecting any supply inductance in the circuit.

The rig start-up condition is first recorded. When the converter is powered on, but no switching signals are given yet, the converter works like a diode bridge rectifier, the AC current and DC link voltage waveforms are as shown in Fig8.2.1 at this condition. After being activated by a mechanical switch, the control algorithm effects on the converter waveforms after a very short transient.

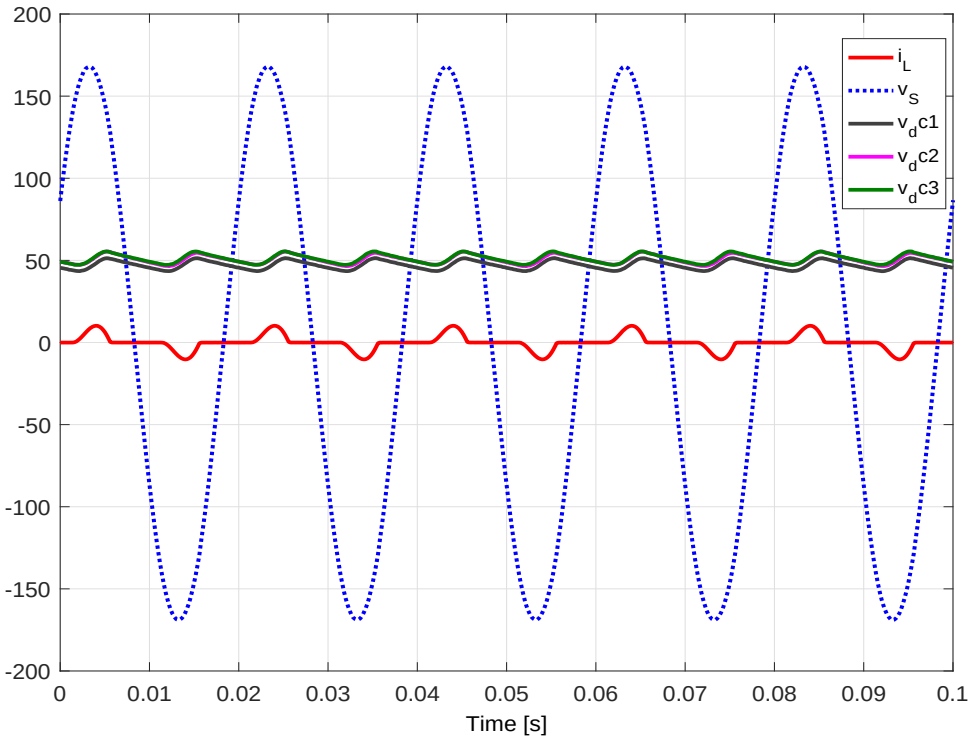

Figure 8.2.1 Experiment start-up waveforms

The results of outer loop total DC-link voltage controller is illustrated in Fig.8.2.2. Fig.8.2.2a shows the total DC link voltage control results with measured waveform with its reference. The average voltage has been controlled to its reference $200V$ in the steady state with the intrinsic 2nd order harmonic ripple. The ripple from the experiment is a bit bigger than that from the simulation due to the non-ideal passive component in reality.

Even though without a DC link voltage balancing control, the experiment results indicate that the DC voltage on each capacitor is balanced enough. This can be seen in Fig.8.2.2b the DC link voltages on each of the H-Bridge cell, each H-Bridge is around $66.67V$, respectively, and the results show the voltages are quite balanced with balanced loads. Thus we don't need a DC balance control for this study. However, even if the experiment results show that DC voltages unbalance become an issue, and balancing scheme has been added, it would appear transparent to the outer control loop so the theoretical analysis would still be valid.

The results of inner-loop current controller are depicted in Fig8.2.3. The measured current is plotted on top of the reference current from both simulation and experiment. It can be seen that the actual current tracks its sinusoidal reference quite well.

The multilevel voltage applied by the converter is depicted in Fig8.2.4 from both simulation and experiment.

Additionally, the output of the phase-locked loop is observed. It is exposed in Fig8.2.5 that the phase angle of the supply voltage is detected correctly.

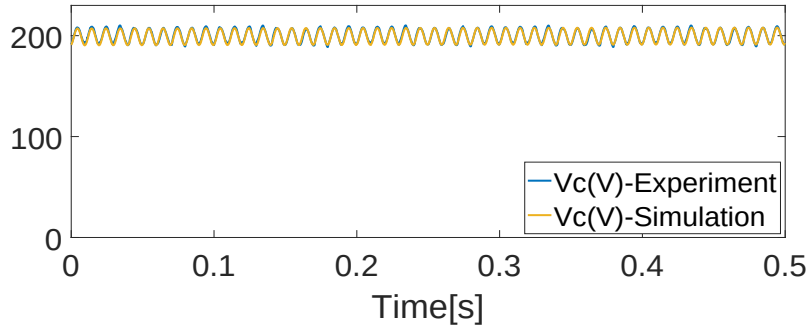

(a) Total DC-link Voltage when connected to a strong grid

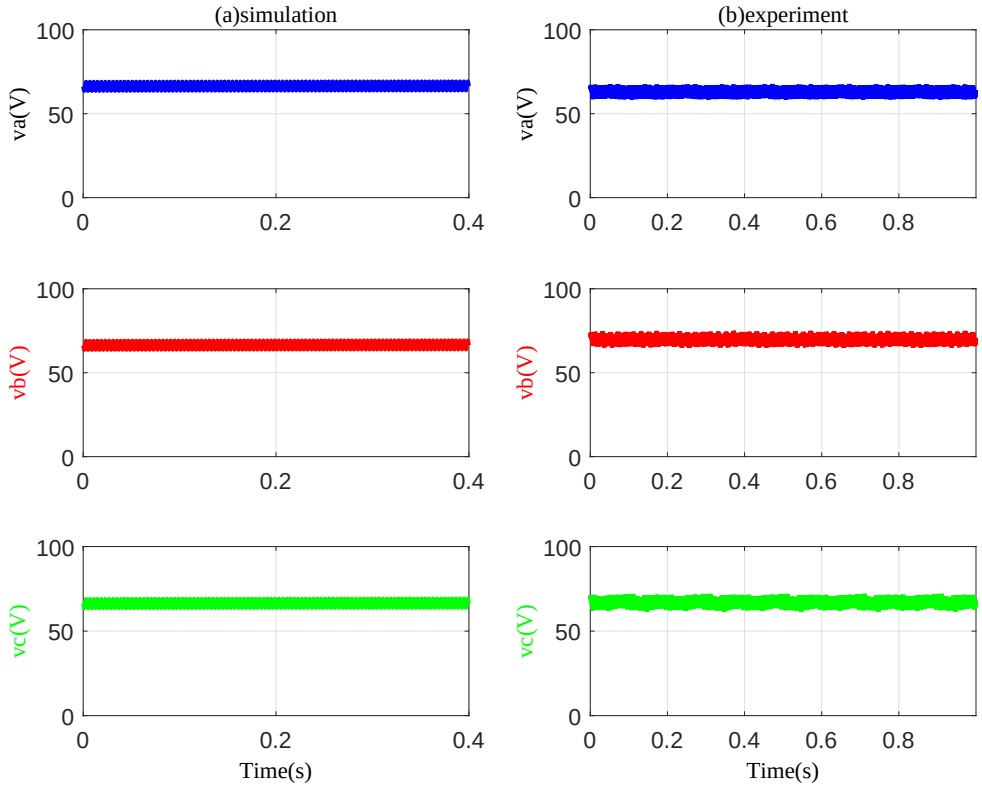

(b) Experimental DC link voltages on cells when connected to a strong grid

Figure 8.2.2 Steady-state experimental DC-link voltages.

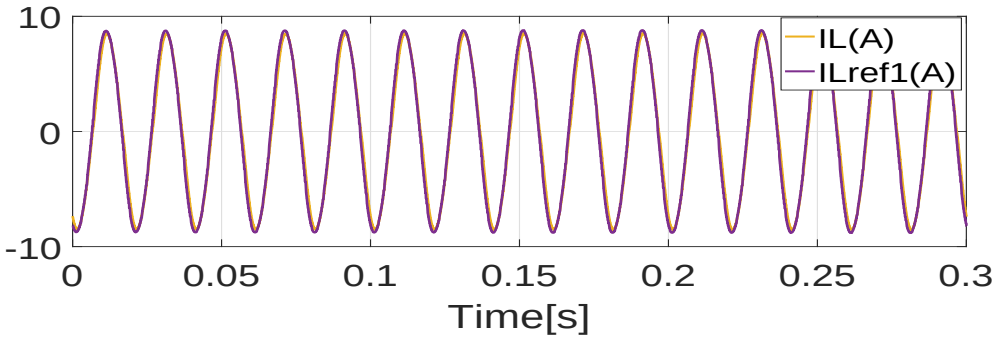

(a) Simulation Results

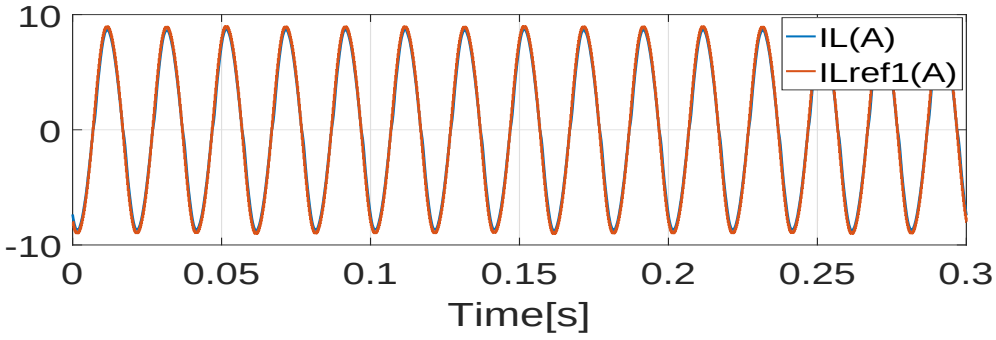

(b) Experiment Results

Figure 8.2.3 Results of current control: current reference and measured current when connected to a strong grid.

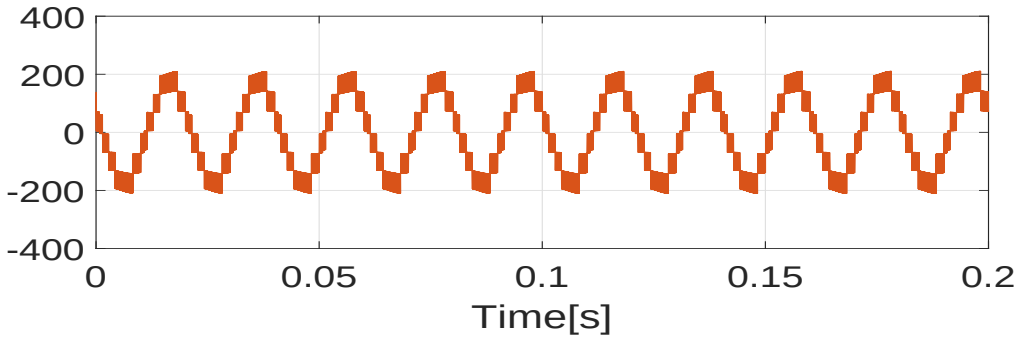

(a) Simulation Results

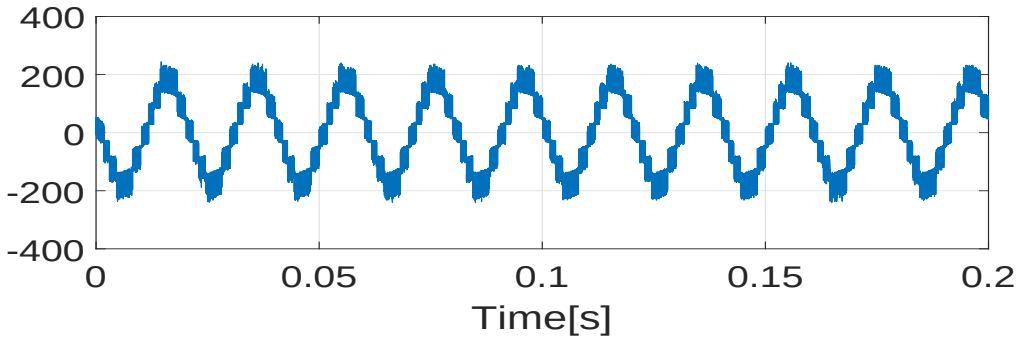

(b) Experiment Results

Figure 8.2.4 Waveform of converter applied voltage under strong grid condition.

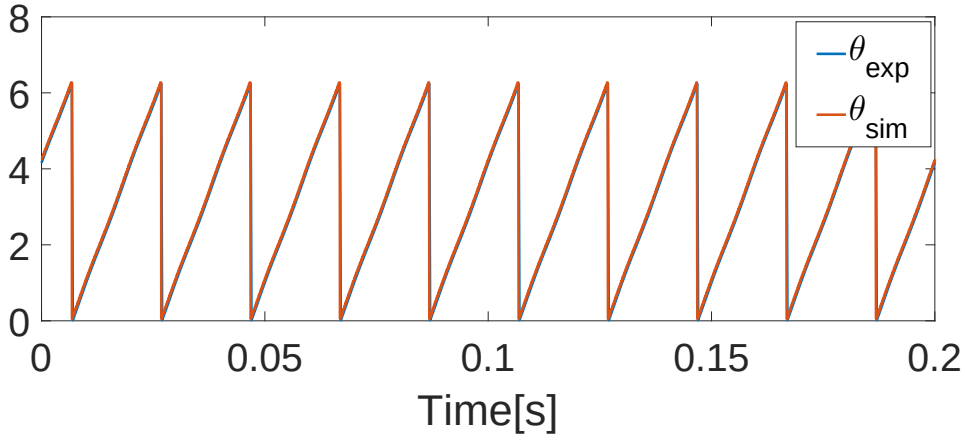

Figure 8.2.5 Output of PLL when CHB connected to strong grid

8.3 Experiment Results of the Unstable Operation of the System

In this section, instability thresholds of the parameters are investigated by experiments. The effect of PI controller bandwidth on the stability of the system is studied in section 8.3.1, and the joint effect of the grid inductance and PLL bandwidth is investigated in section 8.3.2. The values of parameters under study have been changed in steps gradually leading the system to instability.

In the following, in each figure, the data collected to demonstrate the condition of the converter are the DC voltage on cell 1 (light blue), the converter AC side current (green), and the AC side converter implied multilevel voltage (blue).

Hardware protection trips are set for maximum current and voltage as $\pm 25A$ and $\pm 250V$ for safety considerations. As indicated in Table 8.1 some main features of the used IGBT module SK30GH123, the maximum continuous collector current is $33A$. The reference voltage for the total DC-link voltage is chosen to be $200V$. Under this constraint the AC current is within the device safety rating, as well as the CHB converter is working is the 3-cell converter is generating a 7-level terminal voltage.

Table 8.1 IGBT Module SK30GH123

Descriptions	Values
IGBT maximum collector emitter voltage	$1200V$
IGBT maximum continuous collector current	$33A$
IGBT maximum gate emitter voltage	$\pm 20V$
IGBT operating temperature	-40 $150^{O}C$

8.3.1 The Experimental Results Showing Effect of Voltage PI Bandwidth on the Stability of the Closed-loop System

The analysis in chapter 6 indicates that when the converter is connected to a weak grid L_S equals 3 mH and all other parameters are unchanged as defined in the system parameter table, the system eigenvalue would escape the unit circle when PI bandwidth exceeds 80 Hz. In the case of different PI bandwidth for investigating the stability of the system, it is found that it doesn't matter what the PLL bandwidth is, the instability boundary of PI bandwidth is not affected by the PLL bandwidth.

The experimental verification of this analytical prediction is shown in Fig.8.3.1, where after the control has been activated, the PI bandwidth is changing as 60 Hz, 70 Hz and 80 Hz successively for one second each. It can be observed that the system operates well when PI bandwidth is 60 Hz and is strongly distorted when it's 70 Hz and finally becomes unstable when PI operates at 80 Hz when protection trips are activated due to over-current.

8.3.2 The Experimental Results Showing Effect of Grid Strength and PLL Bandwidth on the Stability of the Closed-loop System

As the eigenvalue stability analysis and the switching model simulations revealed, the PLL bandwidth limit is closely related to the grid strength. Data of three different strength grids 0 mH, 3 mH, and 6 mH have been collected in Fig.8.3.2, Fig.8.3.3 and Fig.8.3.4, respectively.

Fig.8.3.2 shows when the converter is connected to the ideal grid where grid inductance can be neglected. After the closed loop control has been applied to the system, the PLL bandwidth has been set as $40, 45, 50$ (Hz) in order (each lasts for 1 s). In Fig.8.3.2a the long-term response of V_C, I_L, V_{CONV} is shown. It can be observed that

the system stops working at 50 Hz because the amplitude of the ac current becomes big, so the system protection is activated. Fig8.3.2b shows the zoomed-in plot during the first step when PLL is working at 40 Hz and is stable. However, both the voltage and current get large oscillations at 45 Hz as indicated in Fig.8.3.2c. Finally, the waveforms get dramatically distorted and resulted in the system trip when PLL is 50 Hz, as given in Fig.8.3.2d.

Similarly, Fig.8.3.3 shows the experiment results when the VSC is connected to a grid for which the grid inductance is assumed to be 3 mH, and the PLL bandwidth is changing in step as $45, 50, 55$ (Hz) after each 1 second. From Fig.8.3.3a it can be seen that after PLL bandwidth has switched to be 55 Hz, the current and voltage start to diverge, and the trip has been activated. Fig.8.3.3b 8.3.3c 8.3.3d shows the zoomed-in operations during each configuration, respectively. The waveforms are distorted gradually as the PLL bandwidth increase and finally leading the system failed to work.

Finally, Fig.8.3.4 shows the experiment results when the VSC is connected to a grid for which the grid inductance is assumed to be 6 mH, which can be regarded as a weak grid, and the PLL bandwidth is changing in step as $50, 55, 60$ (Hz) after each 1 second. From Fig.8.3.4a it can be seen that after PLL bandwidth has switched to be 60 mH, the current and voltage start to diverge and the trip has been activated. Fig.8.3.4b 8.3.4c 8.3.4d shows the zoomed-in operations during each configuration, respectively. Also, the waveforms are distorted gradually as the PLL bandwidth increases and finally paused by the trip when reaching the instability point.

So far, the experimental results have verified the prediction from eigenvalue analysis and simulation results with the same instability points regarding the PI bandwidth and PLL bandwidth under different grid conditions. If comparing the simulation results from the last chapter with the experimental results shown here, it is shown that they match with each other. It can, therefore, be concluded that our stability analysis conducted is valid.

The reason for the observed instability is the interactions between the control parts. Although it has been mentioned previously, it is summarised again in here. Firstly the inductance of the grid transmission line brings distortion to the voltage at the point of common coupling. Thus the PLL gets interfered at the input and generates the erroneous output of phase angle of the grid voltage. Secondly, the current control loop gets affected by the wrong phase angle that PLL provides, and the current waveform would lose control and easily would increase its magnitude with time; thirdly, the inner loop current control furthermore interacts with the outer-loop DC voltage controller, leading to the DC-link instability.

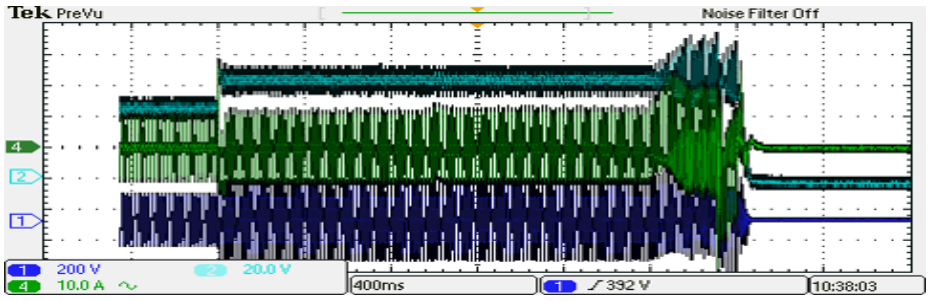

(a) Overall system response showing step changes of PI bandwidth

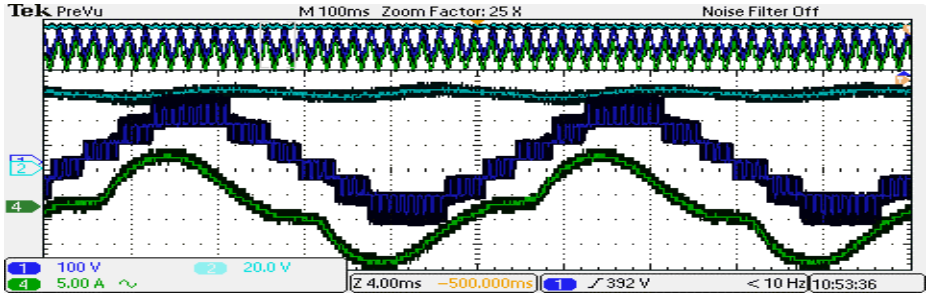

(b) Operation during PI bandwidth is 60 Hz

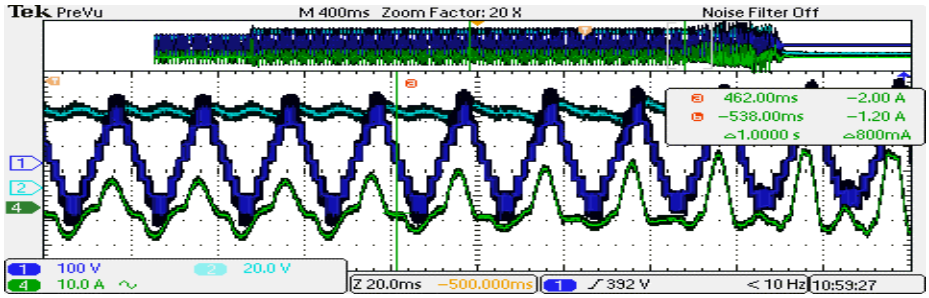

(c) Operation when PI bandwidth is 70 Hz

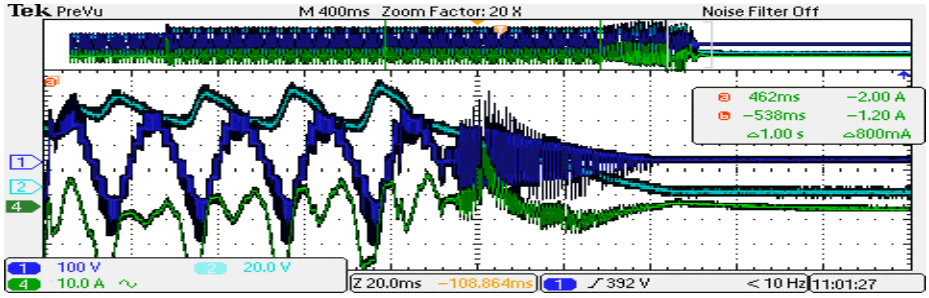

(d) Operation when PI bandwidth is 80 Hz

Figure 8.3.1 Experimental results of CHB converter operation time response with varying PI bandwidth, for verifying the analysed PI bandwidth instability threshold

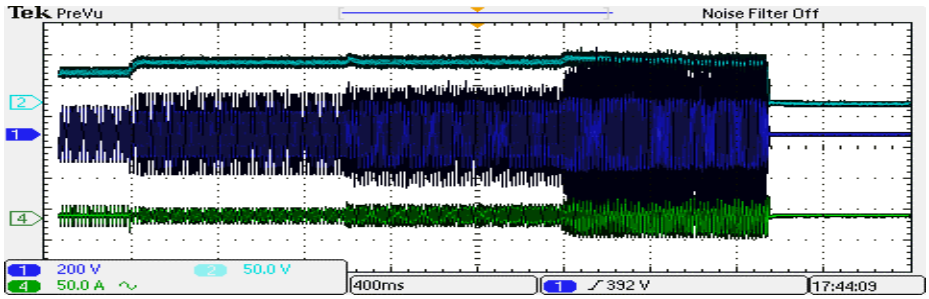

(a) Overall system response under step evolutions of PLL bandwidth

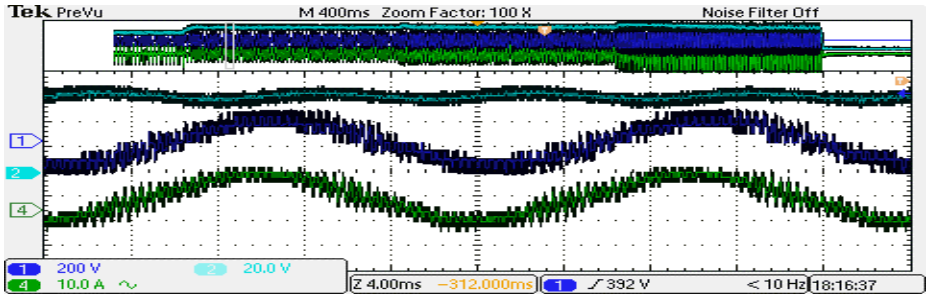

(b) Operation when PLL bandwidth is 40 Hz

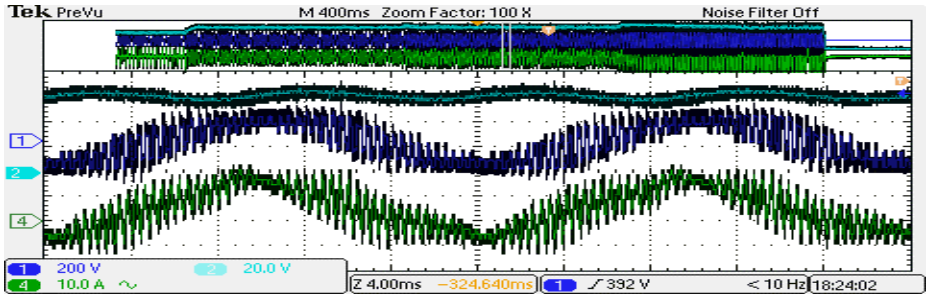

(c) Operation when PLL bandwidth is 45 Hz

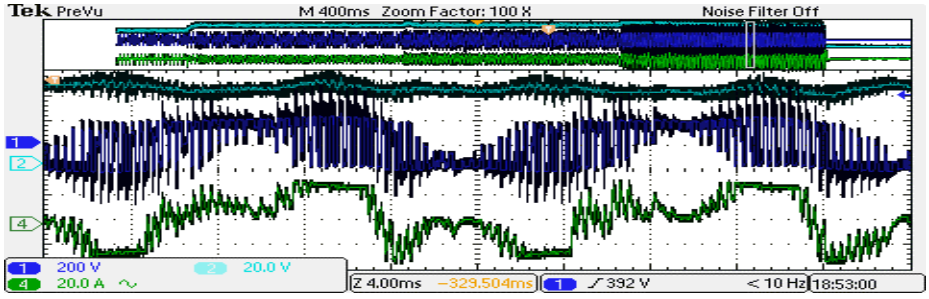

(d) operation when PLL bandwidth is 50 Hz

Figure 8.3.2 Experimental results of CHB converter operation time response with varying PLL bandwidth when grid inductance is negligible, for verifying the analysed PLL bandwidth instability threshold when grid inductance is negligible

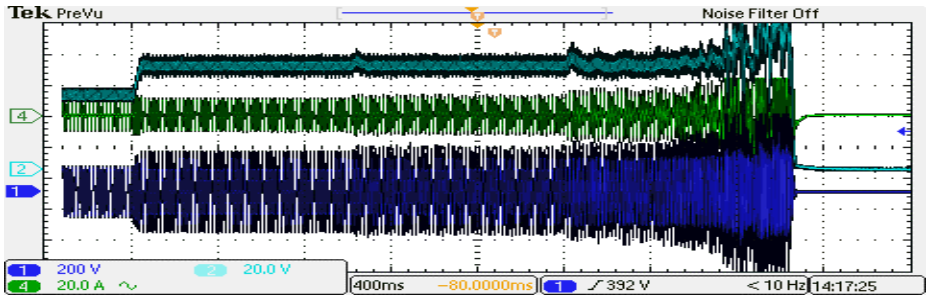

(a) Overall system response under step evolutions of PLL bandwidth

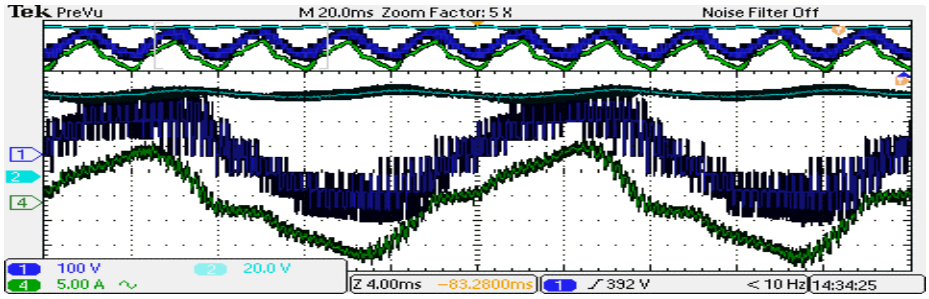

(b) Operation when PLL bandwidth is 45 Hz

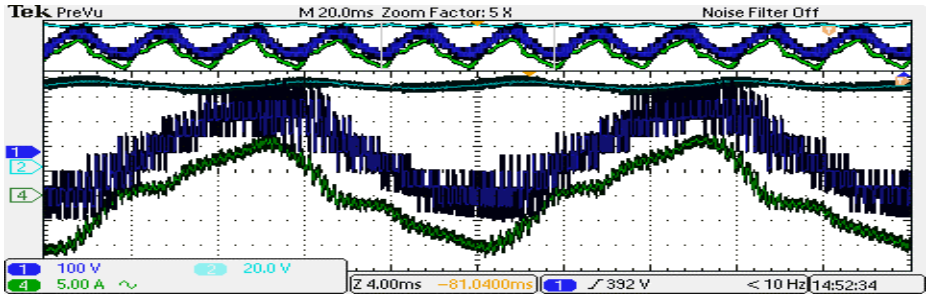

(c) Operation when PLL bandwidth is 50 Hz

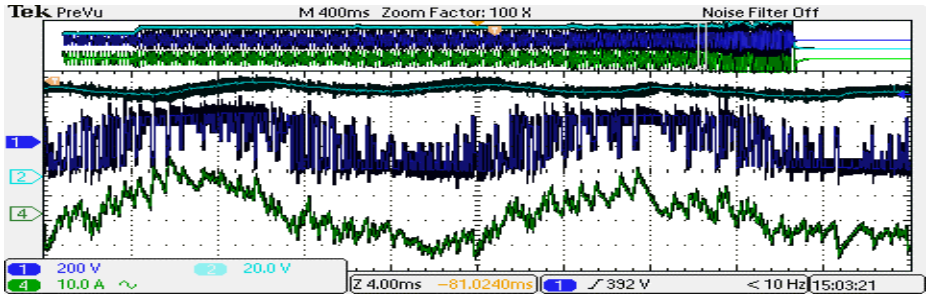

(d) Operation when PLL bandwidth is 55 Hz

Figure 8.3.3 Experimental results of CHB converter operation time response with varying PLL bandwidth when $L_S = 3$ mH, for verifying the analysed PLL bandwidth instability threshold when $L_S = 3$ mH

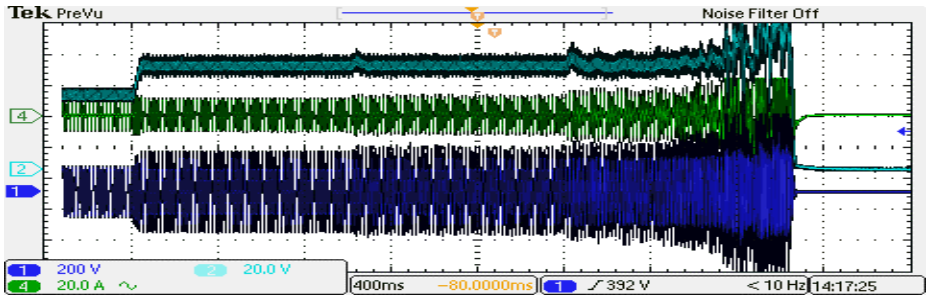

(a) Overall system response under step evolutions of PLL bandwidth

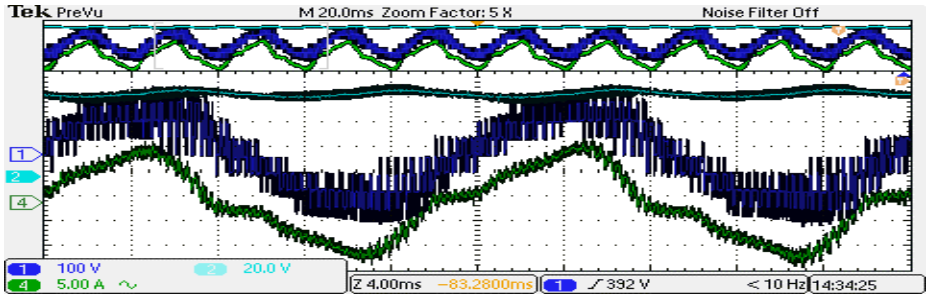

(b) Operation when PLL bandwidth is 50 Hz

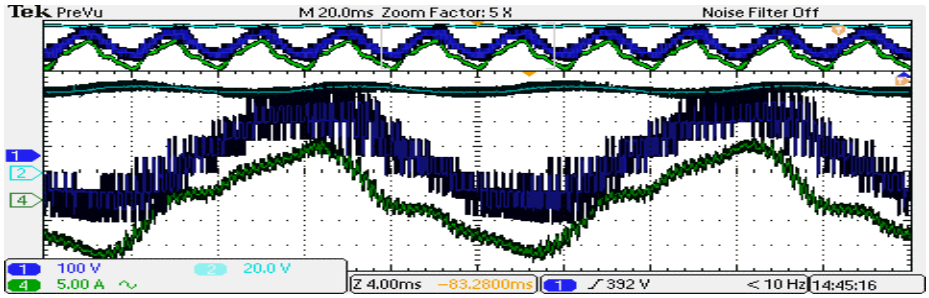

(c) Operation when PLL bandwidth is 55 Hz

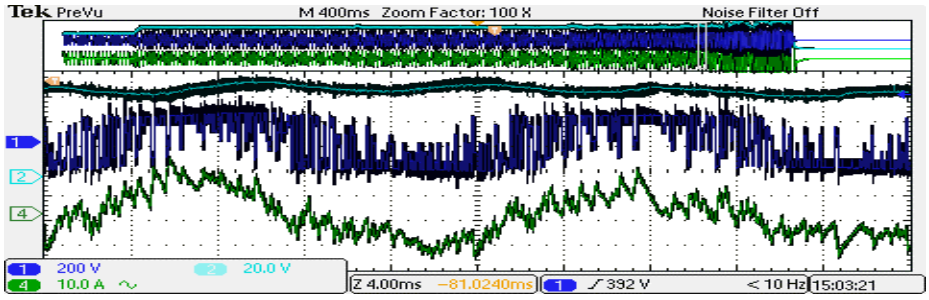

(d) Operation when PLL bandwidth is 60 Hz

Figure 8.3.4 Experimental results of CHB converter operation time response with varying PLL bandwidth when $L_S = 6$ mH, for verifying the analysed PLL bandwidth instability threshold when $L_S = 6$ mH

8.4 Summary

In this chapter, a rig of single-phase CHB rectifier with total DC-link voltage control and AC current has been tested either connected to the strong grid (zero impedance between the supply voltage and converter) or weak grid (large impedance between the supply voltage and converter). The size of the large impedance is used as the value predicted where the PLL starts to operate incorrectly, and the control loops lose its stability.

The experiment results agree with the simulation results for PI bandwidth and PLL bandwidth thresholds both in stable and unstable working conditions in chapter 6. Furthermore, the experiment results validate the stability analysis for seven-order weak grid system, proving that the analytic results regarding the stability are reasonable.

The experiments have been conducted for only a few numbers of cases due to the limitation of the availability of lab equipment. From both the simulation and experiment results, it can be concluded that the interaction between the control loops and grid inductance have a strong effect on the stability of the converter operation and there existing certain instability points for PI and PLL bandwidths beyond which the system would quickly go to unstable operation and got tripped. With our stability analysis method, these parametric boundaries can be accurately derived.

Chapter 9

Conclusions

Multilevel converters show an emerging technology in grid integration and HVDC applications due to their synthesised low-THD AC voltage or current waveforms. With also the benefit of generating high output voltage using low voltage rating devices, and producing high switching output voltage applying low switching frequency on each switching devices, thus multilevel converters have a broad application on high power medium or high voltage application.

Cascaded H-bridge converter stands out among other multilevel topologies for its inherent characteristic of modularity and less number of devices required. The CHB is usually controlled on both AC and DC sides to ensure the power flow as expected(for example, unity power factor operating) when connected to the grid. The design of CHB converters depends the goal of eliminating the switching ripple and achieve the desired operating point. However, the stability is not guaranteed by the design of system parameters, the control and converter hardware design can both lead the system to instability.

However, in the case of CHB converters applied in distributed power systems, the renewable resources such as wind turbines are typically located far away from the load centres and consumers. As a consequence, the high impedance of the long

transmission line makes the grid strength weak. The eigenvalue analysis undertaken in this thesis shows that there exists threshold value for the grid side inductance beyond which the control loops start to break down and to lead to the system operating unstably.

The reason is found that in the phase locked loop, the large impedance in the grid side introduces significant distortion in the input signal for the PLL. Thus the inner current control loop fails to work. As a result, the current magnitude will increase, and the interactions between the current controller and voltage controller lead to the instability in the DC link voltage, too. Thus the whole system gets unstable and collapse.

In this thesis, a more detailed modelling method for the multilevel converter being controlled is provided. From the stability analysis, there existing more clear specific thresholds for some system parameter values and the parameters within the controller design. Thus enhance the engineers to design the system with very clear stability margins. The modelling technique proposed is suitable for the time-periodic system so that the system can be directly modelled in the natural reference frame and the control loop and PLL can be included in the model easily. The eigenvalue analysis method provides a precise prediction of the threshold of the grid side inductance. The future work can be studied about other affecting factors in the system.

The modelling process always starts with the switching model of the power systems, which use the switching functions accurately describe the functionality of the power converters. However, for stability analysis, a much simpler but sufficient model the averaged model derived from the switching model is used. The harmonic balance technique is further applied to the averaged model for capturing the dominant spectra and obtaining the steady-state model. The simulation results of the switching model, the averaged model, and the steady-state model indicate a good match between them.

The Floquet theorem is then applied to justify the stability of the time-periodic steady state. Compute the small-signal model of the grid-connected CHB rectifier

with 2-loop control and PLL measuring the grid angle, which is a seven-order ODE system, for a fundamental period. Obtain the final matrix of the solution of ODE and calculate the eigenvalues of the matrix. If all the eigenvalues are inside the unit circle, the system is stable, if there is more than one eigenvalue escaping out of the unit circle the system is unstable.

By implementing the stability analysis, it is predicted that there existing instability point for the total DC-link voltage PI controller bandwidth; and also there existing the stable boundaries for PLL bandwidth under various grid strengths. An experimental rig has been set up to validate the analytical predictions. The parametric bandwidth has been arranged in step changes gradually approaching the instability point. The experimental results verified that the predicted thresholds exist and when exceeding these thresholds the system would become disturbed a lot and even active protective trips to stop the converter from working.

9.1 Summary of Achievements

Overall achievements of this thesis are summarised as below:

• A review of stability analysis methods for nonlinear systems has been given, including an example of perturbation theory applied to the DC-DC buck converter with CPL load causing the Hopf bifurcation.

• Presented a review of multilevel converter topologies, modulation, control in industry. The review has highlighted and briefly described the four most common topologies related to multilevel converters, such as NPC, flying capacitors, cascaded H-bridge and modular multilevel configuration.

• Implemented a 2-loop control scheme controlling total DC-link voltage and AC current for single-phase CHB rectifier, the control has been realised in the experiment and the achieved experimental results have been demonstrated. There is also a detailed description of the hardware set-up and how the proposed controller has been

implemented on a combined DSP/FPGA platform.

• Developed a mathematical model with the harmonic spectra of the open-loop CHB converter by applying the harmonic balancing technique. Developed the mathematical model incorporated the control scheme of CHB rectifier. The analysed steady state model solution matches accurately with the switching model simulation.

• Used the mathematical model to predict the constraints under which the instability would emerge. Hence brought more specific stable range for some converter design parameters and controller design parameters. The interactions between the control loops can be quickly investigated, in this case especially regarding the effect of the grid side inductance on the PLL and current control loops, the instability boundary of the PLL bandwidth is predicted.

• Implemented the experimental validation of the prediction of the stability boundary undertaken. Firstly the voltage controller PI bandwidth has been set as the parameter, thus it's varied in steps of one second duration approaching the threshold; secondly the PLL bandwidth is also set in step changes under different grid strength representing ideal, practical and weak grids, the experimental results show that the system would lose stability at the predicted unstable point.

9.2 Further Work

• The modelling and stability analysis methods can be applied to more multilevel converters such as M2LC. The theory has been applied to CHB converter, but it can be expanded to apply many more converter types for periodic systems.

• Multilevel converters controlled by more other modulation strategies and control schemes can be analysed and compared. In this thesis, the PSC-PWM is applied for the CHB converter, and DBC algorithm is applied for the current control. In the future work, various modulation and control strategies can be modelled and analysed.

Bibliography

[1] M. Guan and Z. Xu, "Modeling and control of a modular multilevel converter-based hvdc system under unbalanced grid conditions," *IEEE Transactions on Power Electronics*, vol. 27, pp. 4858–4867, Dec 2012.

[2] F. Katiraei, M. R. Iravani, and P. W. Lehn, "Small-signal dynamic model of a micro-grid including conventional and electronically interfaced distributed resources," *IET Generation, Transmission Distribution*, vol. 1, pp. 369–378, May 2007.

[3] P. Bresesti, W. L. Kling, R. L. Hendriks, and R. Vailati, "Hvdc connection of offshore wind farms to the transmission system," *IEEE Transactions on Energy Conversion*, vol. 22, pp. 37–43, March 2007.

[4] J. Qin, M. Saeedifard, A. Rockhill, and R. Zhou, "Hybrid design of modular multilevel converters for hvdc systems based on various submodule circuits," *IEEE Transactions on Power Delivery*, vol. 30, pp. 385–394, Feb 2015.

[5] P. Rao, M. L. Crow, and Z. Yang, "Statcom control for power system voltage control applications," *IEEE Transactions on Power Delivery*, vol. 15, pp. 1311–1317, Oct 2000.

[6] S. Kouro, M. Malinowski, K. Gopakumar, J. Pou, L. G. Franquelo, B. Wu, J. Rodriguez, M. A. Perez, and J. I. Leon, "Recent advances and industrial applications of multilevel converters," *IEEE Transactions on Industrial Electronics*, vol. 57, pp. 2553–2580, Aug 2010.

[7] Y. Yu, J. Yan, H. Fang, R. Yang, Y. Yu, and D. Xu, "Application and performance of a multilevel cascaded h-bridge converter on static var generator," in *Proceedings of The 7th International Power Electronics and Motion Control Conference*, vol. 4, pp. 2694–2698, June 2012.

[8] B. Tai, C. Gao, X. Liu, and J. Lv, "Combination system of var compensation and photovoltaic power generation based on modular multilevel converter," in *IECON 2015 - 41st Annual Conference of the IEEE Industrial Electronics Society*, pp. 002932–002937, Nov 2015.

[9] S. Falcones, X. Mao, and R. Ayyanar, "Topology comparison for solid state transformer implementation," in *IEEE PES General Meeting*, pp. 1–8, July 2010.

[10] "Ieee guide for planning dc links terminating at ac locations having low short-circuit capacities," *IEEE Std 1204-1997*, pp. 1–216, Jan 1997.

[11] V. Diedrichs, A. Beekmann, K. Busker, S. Nikolai, and S. Adloff, "Control of wind power plants utilizing voltage source converter in high impedance grids," in *2012 IEEE Power and Energy Society General Meeting*, pp. 1–9, July 2012.

[12] M. Liserre, R. Teodorescu, and F. Blaabjerg, "Stability of photovoltaic and wind turbine grid-connected inverters for a large set of grid impedance values," *IEEE Transactions on Power Electronics*, vol. 21, pp. 263–272, Jan 2006.

[13] A. Antonopoulos, L. ngquist, L. Harnefors, K. Ilves, and H. P. Nee, "Stability analysis of modular multilevel converters with open-loop control," in *IECON 2013 - 39th Annual Conference of the IEEE Industrial Electronics Society*, pp. 6316–6321, Nov 2013.

[14] N. R. Chaudhuri, R. Oliveira, and A. Yazdani, "Stability analysis of vector-controlled modular multilevel converters in linear time-periodic framework," *IEEE Transactions on Power Electronics*, vol. 31, pp. 5255–5269, July 2016.

[15] J. Sun, "Small-signal methods for ac distributed power systems x2013;a review," *IEEE Transactions on Power Electronics*, vol. 24, pp. 2545–2554, Nov 2009.

[16] S. Y. Elnaggar and G. N. Milford, "Stability analysis of nonlinear left handed transmission lines using floquet multipliers and bifurcation theory," in *2016 IEEE International Symposium on Antennas and Propagation (APSURSI)*, pp. 1093–1094, June 2016.

[17] J. Bian, H. Li, and T. Q. Zheng, "Stability analysis of grid-connected inverters with lcl-filter based on harmonic balance and floquet theory," in *2014 International Power Electronics Conference (IPEC-Hiroshima 2014 - ECCE ASIA)*, pp. 3314–3319, May 2014.

[18] L. Chen and K. Aihara, "Stability and bifurcation analysis of differential-difference-algebraic equations," *IEEE Transactions on Circuits and Systems I: Fundamental Theory and Applications*, vol. 48, pp. 308–326, Mar 2001.

[19] C. K. Tse and M. D. Bernardo, "Complex behavior in switching power converters," *Proceedings of the IEEE*, vol. 90, pp. 768–781, May 2002.

[20] Y. S. Apte, "Routh-hurwitz stability criterion and its equivalents," *India, IEE-IERE Proceedings* -, vol. 7, pp. 149–154, October 1969.

[21] H. H. Hwang and P. C. Tripathi, "Generalisation of the routh-hurwitz criterion and its applications," *Electronics Letters*, vol. 6, pp. 410–411, June 1970.

[22] K. Khatwani, "On routh-hurwitz criterion," *IEEE Transactions on Automatic Control*, vol. 26, pp. 583–584, Apr 1981.

[23] F. E. Bothwell, "Nyquist diagrams and the routh-hurwitz stability criterion," *Proceedings of the IRE*, vol. 38, pp. 1345–1348, Nov 1950.

[24] B. Wen, D. Boroyevich, P. Mattavelli, Z. Shen, and R. Burgos, "Experimental verification of the generalized nyquist stability criterion for balanced three-phase ac systems in the presence of constant power loads," in *2012 IEEE Energy Conversion Congress and Exposition (ECCE)*, pp. 3926–3933, Sept 2012.

[25] S. R. Hall and N. M. Wereley, "Generalized nyquist stability criterion for linear time periodic systems," in *1990 American Control Conference*, pp. 1518–1525, May 1990.

[26] C. A. Desoer and Y. T. Wang, "On the generalized nyquist stability criterion," in *1979 18th IEEE Conference on Decision and Control including the Symposium on Adaptive Processes*, vol. 2, pp. 580–586, Dec 1979.

[27] F. Guinjoan, J. Calvente, A. Poveda, and L. Martinez, "Large-signal modeling and simulation of switching dc-dc converters," *IEEE Transactions on Power Electronics*, vol. 12, pp. 485–494, May 1997.

[28] R. Zhang, M. Hu, Y. Zhang, W. Ma, and J. Zhao, "Control of bifurcation in the buck converter using novel resonant parametric perturbation," in *IECON 2017 - 43rd Annual Conference of the IEEE Industrial Electronics Society*, pp. 982–986, Oct 2017.

[29] M. L. Wardi, M. Amairi, and M. N. Abdelkrim, "Output regulation of nonlinear systems with fopi controller based on singular perturbation technique," in *2017 18th International Conference on Sciences and Techniques of Automatic Control and Computer Engineering (STA)*, pp. 18–23, Dec 2017.

[30] L. Liu, X. Mei, D. Dong, and H. Liu, "Perturbation methods for dynamic analysis of cracked beams," in *2011 International Conference on Consumer Electronics, Communications and Networks (CECNet)*, pp. 4264–4267, April 2011.

[31] S. Yamada and K. Bessho, "Harmonic field calculation by the combination of finite element analysis and harmonic balance method," *IEEE Transactions on Magnetics*, vol. 24, pp. 2588–2590, Nov 1988.

[32] J. Lu, S. Taghizadeh, M. J. Hossain, and X. Zhao, "Harmonic balance method used for harmonics calculation and prediction in power systems," in *2016 Australasian Universities Power Engineering Conference (AUPEC)*, pp. 1–6, Sept 2016.

[33] "Lyapunov a. m. the general problem of the stability of motion (in russian), doctoral dissertation, univ. kharkov 1892 english translations: (1) stability of motion, academic press, new-york london, 1966 (2) the general problem of the

stability of motion, (a. t. fuller trans.) taylor francis, london 1992. included is a biography by smirnov and an extensive bibliography of lyapunov's work.,"

[34] J. C. Willems, "The analysis of feedback systems," *Cambridge, MA: MIT Press*, 1971.

[35] P. Kundur, J. Paserba, V. Ajjarapu, G. Andersson, A. Bose, C. Canizares, N. Hatziargyriou, D. Hill, A. Stankovic, C. Taylor, T. V. Cutsem, and V. Vittal, "Definition and classification of power system stability ieee/cigre joint task force on stability terms and definitions," *IEEE Transactions on Power Systems*, vol. 19, pp. 1387–1401, Aug 2004.

[36] A. A. Fouad and V. Vittal, "Power system transient stability analysis using the transient energy function method," *Englewood Cliffs, NJ: Prentice-Hall*, 1991.

[37] C. K. Tse, Y. M. Lai, and H. H. C. Iu, "Hopf bifurcation and chaos in a free-running current-controlled cuk switching regulator," *IEEE Transactions on Circuits and Systems I: Fundamental Theory and Applications*, vol. 47, pp. 448–457, Apr 2000.

[38] J. Li, X. Zhou, and G. Dong, "Hopf bifurcation analysis on dynamic voltage stability of wind power systems with svc," in *2014 IEEE International Conference on Mechatronics and Automation*, pp. 1533–1537, Aug 2014.

[39] Y. Lu, H. Li, and W. Li, "Hopf bifurcation and its control in an induction motor system with indirect field oriented control," in *2009 4th IEEE Conference on Industrial Electronics and Applications*, pp. 3438–3441, May 2009.

[40] P. Panagis, F. Stergiopoulos, P. Marabeas, and S. Manias, "Comparison of state of the art multilevel inverters," in *2008 IEEE Power Electronics Specialists Conference*, pp. 4296–4301, June 2008.

[41] C. Iihami, K. Ersan, and B. Ramazan, "Review of multilevel voltage source inverter topologies and control schemes," Management 2011:(February):111428.

[42] J. S. Lai and F. Z. Peng, "Multilevel converters-a new breed of power converters," *IEEE Transactions on Industry Applications*, vol. 32, pp. 509–517, May 1996.

[43] J. Zhou and Z. Li, "Research on hybrid modulation strategies based on general hybrid topology of multilevel inverter," in *2008 International Symposium on Power Electronics, Electrical Drives, Automation and Motion*, pp. 784–788, June 2008.

[44] X. Yuan, "Analytical averaged loss model of a three-level t-type converter," in *7th IET International Conference on Power Electronics, Machines and Drives (PEMD 2014)*, pp. 1–6, April 2014.

[45] A. Watson, *Selective Harmonic Elimination Methods for a Cascaded H-Bridge Converter*. Ph.D. thesis, Dept. Elect. Eng., University of Nottingham, 2008.

[46] A. Nabae, I. Takahashi, and H. Akagi, "A new neutral-point-clamped pwm inverter," *IEEE Transactions on Industry Applications*, vol. IA-17, pp. 518–523, Sept 1981.

[47] T. A. Meynard and H. Foch, "Multi-level conversion: high voltage choppers and voltage-source inverters," in *Power Electronics Specialists Conference, 1992. PESC '92 Record., 23rd Annual IEEE*, pp. 397–403 vol.1, Jun 1992.

[48] L. Xu and V. G. Agelidis, "Active capacitor voltage control of flying capacitor multilevel converters," *IEE Proceedings - Electric Power Applications*, vol. 151, pp. 313–320, May 2004.

[49] C. Feng, J. Liang, V. G. Agelidis, and T. C. Green, "A multi-modular system based on parallel-connected multilevel flying capacitor converters controlled with fundamental frequency spwm," in *IECON 2006 - 32nd Annual Conference on IEEE Industrial Electronics*, pp. 2360–2365, Nov 2006.

[50] C. Hochgraf, R. Lasseter, D. Divan, and T. A. Lipo, "Comparison of multilevel inverters for static var compensation," in *Proceedings of 1994 IEEE Industry Applications Society Annual Meeting*, pp. 921–928 vol.2, Oct 1994.

[51] H. Kuhn, N. E. Ruger, and A. Mertens, "Control strategy for multilevel inverter with non-ideal dc sources," in *2007 IEEE Power Electronics Specialists Conference*, pp. 632–638, June 2007.

[52] S. Debnath, J. Qin, B. Bahrani, M. Saeedifard, and P. Barbosa, "Operation, control, and applications of the modular multilevel converter: A review," *IEEE Transactions on Power Electronics*, vol. 30, pp. 37–53, Jan 2015.

[53] S. Allebrod, R. Hamerski, and R. Marquardt, "New transformerless, scalable modular multilevel converters for hvdc-transmission," in *2008 IEEE Power Electronics Specialists Conference*, pp. 174–179, June 2008.

[54] J. Peralta, H. Saad, S. Dennetiere, J. Mahseredjian, and S. Nguefeu, "Detailed and averaged models for a 401-level mmc-hvdc system," in *2013 IEEE Power Energy Society General Meeting*, pp. 1–1, July 2013.

[55] S. Debnath and M. Saeedifard, "A new hybrid modular multilevel converter for grid connection of large wind turbines," *IEEE Transactions on Sustainable Energy*, vol. 4, pp. 1051–1064, Oct 2013.

[56] Q. Tu, Z. Xu, H. Huang, and J. Zhang, "Parameter design principle of the arm inductor in modular multilevel converter based hvdc," in *2010 International Conference on Power System Technology*, pp. 1–6, Oct 2010.

[57] K. Ilves, A. Antonopoulos, S. Norrga, and H. P. Nee, "Steady-state analysis of interaction between harmonic components of arm and line quantities of modular multilevel converters," *IEEE Transactions on Power Electronics*, vol. 27, pp. 57–68, Jan 2012.

[58] A. Das, H. Nademi, and L. Norum, "A method for charging and discharging capacitors in modular multilevel converter," in *IECON 2011 - 37th Annual Conference of the IEEE Industrial Electronics Society*, pp. 1058–1062, Nov 2011.

[59] X. Shi, B. Liu, Z. Wang, Y. Li, L. M. Tolbert, and F. Wang, "Startup schemes for modular multilevel converter under different load conditions," in *2015 IEEE*

Applied Power Electronics Conference and Exposition (APEC), pp. 2174–2180, March 2015.

[60] R. Picas, J. Pou, S. Ceballos, V. G. Agelidis, and M. Saeedifard, "Minimization of the capacitor voltage fluctuations of a modular multilevel converter by circulating current control," in *IECON 2012 - 38th Annual Conference on IEEE Industrial Electronics Society*, pp. 4985–4991, Oct 2012.

[61] R. Picas, J. Pou, S. Ceballos, J. Zaragoza, G. Konstantinou, and V. G. Agelidis, "Optimal injection of harmonics in circulating currents of modular multilevel converters for capacitor voltage ripple minimization," in *2013 IEEE ECCE Asia Downunder*, pp. 318–324, June 2013.

[62] M. Malinowski, K. Gopakumar, J. Rodriguez, and M. A. Perez, "A survey on cascaded multilevel inverters," *IEEE Transactions on Industrial Electronics*, vol. 57, pp. 2197–2206, July 2010.

[63] Z. Pan and F. Z. Peng, "A sinusoidal pwm method with voltage balancing capability for diode-clamped five-level converters," *IEEE Transactions on Industry Applications*, vol. 45, pp. 1028–1034, May 2009.

[64] L. M. Tolbert and T. G. Habetler, "Novel multilevel inverter carrier-based pwm methods," in *Conference Record of 1998 IEEE Industry Applications Conference. Thirty-Third IAS Annual Meeting (Cat. No.98CH36242)*, vol. 2, pp. 1424–1431 vol.2, Oct 1998.

[65] B. Mwinyiwiwa, Z. Wolanski, and B. T. Ooi, "Microprocessor implemented spwm for multiconverters with phase-shifted triangle carriers," in *Industry Applications Conference, 1997. Thirty-Second IAS Annual Meeting, IAS '97., Conference Record of the 1997 IEEE*, vol. 2, pp. 1542–1549 vol.2, Oct 1997.

[66] V. G. Agelidis and M. Calais, "Application specific harmonic performance evaluation of multicarrier pwm techniques," in *PESC 98 Record. 29th Annual IEEE Power Electronics Specialists Conference (Cat. No.98CH36196)*, vol. 1, pp. 172–178 vol.1, May 1998.

[67] S. Bifaretti, P. Zanchetta, A. Watson, L. Tarisciotti, A. Bellini, and J. Clare, "A modulation technique for high power ac/dc multilevel converters for power system integration," in *Energy Conversion Congress and Exposition (ECCE), 2010 IEEE*, pp. 3697–3704, Sept 2010.

[68] P. Kaurav and P. Bansal, "A reduced switched based three-phase asymmetrical cascade multilevel inverter with different modulation techniques," in *2015 International Conference on Electrical, Electronics, Signals, Communication and Optimization (EESCO)*, pp. 1–6, Jan 2015.

[69] A. K. Ranjan, D. V. Bhaskar, and N. Parida, "Analysis and simulation of cascaded h-bridge multi level inverter using level-shift pwm technique," in *2015 International Conference on Circuits, Power and Computing Technologies [ICCPCT-2015]*, pp. 1–5, March 2015.

[70] C. Feng, J. Liang, V. G. Agelidis, and T. C. Green, "A multi-modular system based on parallel-connected multilevel flying capacitor converters controlled with fundamental frequency spwm," in *IECON 2006 - 32nd Annual Conference on IEEE Industrial Electronics*, pp. 2360–2365, Nov 2006.

[71] M. Angulo, P. Lezana, S. Kouro, J. Rodriguez, and B. Wu, "Level-shifted pwm for cascaded multilevel inverters with even power distribution," in *2007 IEEE Power Electronics Specialists Conference*, pp. 2373–2378, June 2007.

[72] H. S. Patel and R. G. Hoft, "Generalized techniques of harmonic elimination and voltage control in thyristor inverters: Part i–harmonic elimination," *IEEE Transactions on Industry Applications*, vol. IA-9, pp. 310–317, May 1973.

[73] A. H. Bhat and P. Agarwal, "A generalized space vector modulation with simple control technique for balancing dc-bus capacitor voltages of a three-phase, neutral-point clamped converter," in *2006 International Conference on Power Electronic, Drives and Energy Systems*, pp. 1–6, Dec 2006.

[74] A. K. Gupta and A. M. Khambadkone, "A space vector pwm scheme for multilevel inverters based on two-level space vector pwm," *IEEE Transactions on Industrial Electronics*, vol. 53, pp. 1631–1639, Oct 2006.

[75] A. M. K. A. K. Gupta, "A space vector pwm scheme to reduce common mode voltage for a cascaded multilevel inverter," in *2006 37th IEEE Power Electronics Specialists Conference*, pp. 1–7, June 2006.

[76] Z. Bai, Z. Zhang, and Y. Zhang, "A generalized three-phase multilevel current source inverter with carrier phase-shifted spwm," in *2007 IEEE Power Electronics Specialists Conference*, pp. 2055–2060, June 2007.

[77] H. Hu, W. Yao, and Z. Lu, "Design and implementation of three-level space vector pwm ip core for fpgas," *IEEE Transactions on Power Electronics*, vol. 22, pp. 2234–2244, Nov 2007.

[78] G. Wang, S. Baek, J. Elliott, A. Kadavelugu, F. Wang, X. She, S. Dutta, Y. Liu, T. Zhao, W. Yao, R. Gould, S. Bhattacharya, and A. Q. Huang, "Design and hardware implementation of gen-1 silicon based solid state transformer," in *2011 Twenty-Sixth Annual IEEE Applied Power Electronics Conference and Exposition (APEC)*, pp. 1344–1349, March 2011.

[79] J. Clare, "Advanced power converters for universal and flexible power management in future electricity networks," in *2009 13th European Conference on Power Electronics and Applications*, pp. 1–29, Sept 2009.

[80] S. Bifaretti, P. Zanchetta, A. Watson, L. Tarisciotti, and J. Clare, "Advanced power electronic conversion and control system for universal and flexible power management," *Smart Grid, IEEE Transactions on*, vol. 2, pp. 231–243, June 2011.

[81] S. Bifaretti, P. Zanchetta, Y. Fan, F. Iov, and J. Clare, "Power flow control through a multi-level h-bridge based power converter for universal and flexible power management in future electrical grids," in *2008 13th International Power Electronics and Motion Control Conference*, pp. 1771–1778, Sept 2008.

[82] Q. Hao, B. T. Ooi, F. Gao, C. Wang, and N. Li, "Three-phase series-connected modular multilevel converter for hvdc application," *IEEE Transactions on Power Delivery*, vol. 31, pp. 50–58, Feb 2016.

[83] C. Oates, "Modular multilevel converter design for vsc hvdc applications," *IEEE Journal of Emerging and Selected Topics in Power Electronics*, vol. 3, pp. 505–515, June 2015.

[84] G. P. Adam, I. A. Abdelsalam, K. H. Ahmed, and B. W. Williams, "Hybrid multilevel converter with cascaded h-bridge cells for hvdc applications operating principle and scalability," *IEEE Transactions on Power Electronics*, vol. 30, pp. 65–77, Jan 2015.

[85] Y. H. Liu, J. Arrillaga, and N. R. Watson, "Cascaded h-bridge voltage reinjection," *IEEE Transactions on Power Delivery*, vol. 23, pp. 1200–1206, April 2008.

[86] Z. Chen, Z. Wang, Y. Liu, and Y. Luo, "A unipolar pwm strategy for hybrid cascaded multilevel converters," in *IECON 2014 - 40th Annual Conference of the IEEE Industrial Electronics Society*, pp. 1154–1160, Oct 2014.

[87] C. Marouchos and M. Darwish, "Teaching power electronics using the switching function approach," in *Universities Power Engineering Conference (UPEC), 2012 47th International*, pp. 1–7, 2012.

[88] M. Ciobotaru, S. Bifaretti, and P. Zanchetta, "Short circuit analysis of the uniflex-pm using stationary and natural reference frame control," *EPE Journal*, 2009.

[89] J. Rodriguez and P. Cortes, "Predictive control of power converters and electrical drives," *book*, 2012.

[90] I. S. Mohamed, S. A. Zaid, M. F. Abu-Elyazeed, and H. M. Elsayed, "Model predictive control-a simple and powerful method to control ups inverter applications with output lc filter," in *2013 Saudi International Electronics, Communications and Photonics Conference*, pp. 1–6, April 2013.

[91] P. Cortes, A. Wilson, S. Kouro, J. Rodriguez, and H. Abu-Rub, "Model predictive control of multilevel cascaded h-bridge inverters," *IEEE Transactions on Industrial Electronics*, vol. 57, pp. 2691–2699, Aug 2010.

[92] L. Tarisciotti, P. Zanchetta, A. Watson, J. Clare, and S. Bifaretti, "A comparison between dead-beat and predictive control for a 7-level back-to-back cascaded h-bridge under fault conditions," in *2013 IEEE Energy Conversion Congress and Exposition*, pp. 2147–2154, Sept 2013.

[93] S. K. Chung, "Phase-locked loop for grid-connected three-phase power conversion systems," *IEE Proceedings - Electric Power Applications*, vol. 147, pp. 213–219, May 2000.

[94] V. Kaura and V. Blasko, "Operation of a phase locked loop system under distorted utility conditions," in *Applied Power Electronics Conference and Exposition, 1996. APEC '96. Conference Proceedings 1996., Eleventh Annual*, vol. 2, pp. 703–708 vol.2, Mar 1996.

[95] L. N. Amuda, B. J. C. Filho, S. M. Silva, S. R. Silva, and A. S. A. C. Diniz, "Wide bandwidth single and three-phase pll structures for grid-tied pv systems," in *Conference Record of the Twenty-Eighth IEEE Photovoltaic Specialists Conference - 2000 (Cat. No.00CH37036)*, pp. 1660–1663, 2000.

[96] "A new single-phase pll structure based on second order generalized integrator," in *Power Electronics Specialists Conference, 2006. PESC '06. 37th IEEE*, pp. 1–6, June 2006.

[97] L. Tarisciotti, A. J. Watson, P. Zanchetta, S. Bifaretti, J. C. Clare, and P. Wheeler, "An improved dead-beat current control for cascaded h-bridge active rectifier with low switching frequency," in *6th IET International Conference on Power Electronics, Machines and Drives (PEMD 2012)*, pp. 1–6, March 2012.

[98] L. Tarisciotti, P. Zanchetta, A. Watson, J. Clare, S. Bifaretti, and M. Rivera, "A new predictive control method for cascaded multilevel converters with intrinsic modulation scheme," in *Industrial Electronics Society, IECON 2013 - 39th Annual Conference of the IEEE*, pp. 5764–5769, Nov 2013.

[99] L. Tarisciotti, A. Watson, P. Zanchetta, S. Bifaretti, J. Clare, and P. Wheeler, "An improved dead-beat current control for cascaded h-bridge active rectifier with low switching frequency," in *Power Electronics, Machines and Drives (PEMD 2012), 6th IET International Conference on*, pp. 1–6, 2012.

[100] A. J. Watson, P. W. Wheeler, and J. C. Clare, "A selective harmonic elimination system for restoring and equalising dc link voltages in a multilevel active rectifier," in *2007 European Conference on Power Electronics and Applications*, pp. 1–7, Sept 2007.

[101] L. Tarisciotti, P. Zanchetta, A. Watson, S. Bifaretti, J. Clare, and P. Wheeler, "Active dc voltage balancing pwm technique for high-power cascaded multilevel converters," *Industrial Electronics, IEEE Transactions on*, vol. 61, pp. 6157–6167, Nov 2014.

[102] S. Grillo, V. Musolino, G. Sulligoi, and E. Tironi, "Stability enhancement in dc distribution systems with constant power controlled converters," in *Harmonics and Quality of Power (ICHQP), 2012 IEEE 15th International Conference on*, pp. 848–854, June 2012.

[103] M. Molinas, D. Moltoni, G. Fascendini, J. A. Suul, and T. Undeland, "Constant power loads in ac distribution systems: An investigation of stability," in *2008 IEEE International Symposium on Industrial Electronics*, pp. 1531–1536, June 2008.

[104] A. B. Jusoh, "The instability effect of constant power loads," in *Power and Energy Conference, 2004. PECon 2004. Proceedings. National*, pp. 175–179, Nov 2004.

[105] M. Zhao, X. Yuan, J. Hu, and Y. Yan, "Voltage dynamics of current control time-scale in a vsc-connected weak grid," in *2016 IEEE Power and Energy Society General Meeting (PESGM)*, pp. 1–1, July 2016.

[106] Z. J. Z, "Impact of short circuit ratio and phase locked loop parameters on the small-signal behaviour of a vsc-hvdc converter," in *2016 IEEE Power and Energy Society General Meeting (PESGM)*, pp. 1–1, July 2016.

[107] T. Midtsund, J. A. Suul, and T. Undeland, "Evaluation of current controller performance and stability for voltage source converters connected to a weak grid," in *The 2nd International Symposium on Power Electronics for Distributed Generation Systems*, pp. 382–388, June 2010.

[108] Y. Huang, X. Yuan, J. Hu, and P. Zhou, "Modeling of vsc connected to weak grid for stability analysis of dc-link voltage control," *IEEE Journal of Emerging and Selected Topics in Power Electronics*, vol. 3, pp. 1193–1204, Dec 2015.

[109] F. S. Tsai, "Small-signal and transient analysis of a zero-voltage-switched, phase-controlled pwm converter using averaged switch model," *IEEE Transactions on Industry Applications*, vol. 29, pp. 493–499, May 1993.

[110] A. Abramovitz, "An approach to average modeling and simulation of switch-mode systems," *IEEE Transactions on Education*, vol. 54, pp. 509–517, Aug 2011.

[111] N. M. Wereley and S. R. Hall, "Frequency response of linear time periodic systems," in *29th IEEE Conference on Decision and Control*, pp. 3650–3655 vol.6, Dec 1990.

[112] H. Li, J. Shang, X. You, T. Zheng, B. Zhang, and J. L, "A novel stability analysis method based on floquet theory for cascaded dc-dc converters system," in *2015 IEEE Energy Conversion Congress and Exposition (ECCE)*, pp. 2679–2683, Sept 2015.

[113] S. Y. Elnaggar and G. N. Milford, "Stability analysis of nonlinear left handed transmission lines using floquet multipliers and bifurcation theory," in *2016 IEEE International Symposium on Antennas and Propagation (APSURSI)*, pp. 1093–1094, June 2016.

[114] F. Cappelluti, F. L. Traversa, F. Bonani, S. D. Guerrieri, and G. Ghione, "Floquet-based stability analysis of power amplifiers including distributed elements," *IEEE Microwave and Wireless Components Letters*, vol. 24, pp. 493–495, July 2014.

[115] A. N. Michel and L. Hou, "Floquet theory for linear periodic differential equations with discontinuous right-hand side," in *2009 IEEE International Conference on Control and Automation*, pp. 128–132, Dec 2009.

[116] M. Albani, F. Capolino, A. Cucini, S. Maci, F. Mariottini, E. Martini, A. Polemi, and A. Toccafondi, "An overview of the truncated floquet wave diffraction theory," in *2006 IEEE Antennas and Propagation Society International Symposium*, pp. 1237–1240, July 2006.

[117] H. Li, J. Bian, J. Shang, T. Q. Zheng, and R. Hao, "A novel stability analysis method for the dc-ac inverter with nonlinear loads based on harmonic balance and floquet theory," in *2015 9th International Conference on Power Electronics and ECCE Asia (ICPE-ECCE Asia)*, pp. 2382–2387, June 2015.

[118] Z. Xi, *How to calculate and minimize the dead time requirement for IGBTs properly.* Infineon, v1.0 ed., May 2007.

[119] SEMIKRON, *SK30GH123 SEMITOP IGBT Module*, 10 2005.

[120] LEM, *Voltage Transducer LEM LV 25-P Datasheet*, version 19 ed., August 2014.

[121] LEM, *Current Transducer LEM LA 55-P Datasheet.*

[122] J. J. Shea, "Transformer and inductor design handbook, 3rd ed. [book review]," *IEEE Electrical Insulation Magazine*, vol. 21, pp. 61–61, Jan 2005.

[123] Microsemi Corporation, *Microsemi ProASIC3 Flash Family FPGAs*, revision 18 ed., March 2016.

Appendix A

Matlab Codes For Buck CPL

```
%%%%%%%%%%%%%% Averaged Model #buckode454.m# %%%%%%%%%%%%%%%%%%%%%%%%%%
function dy = buckode454(t,y)
global R L C E PL D;
dy = zeros(2,1); % a column vector
dy(1) = (y(2) - y(1)/R-PL/y(1))/C;
dy(2) = (D*E-y(1))/L ;

%%%%%%%%%%%%% Linearization eigenvalue calculation #buck_hopf_eigenvalue.m#
global R L C E PL D P0;
%Draw the eigenvalue as PL is varied
%title: Locus of the complex eigenvalue pair corresponding to Table i
for PL=P0-5:0.5:P0+5  %PL=31 32 33 34 35 36 37
lamda1 = ((-1/C/R+PL/C/D^2/E^2) + sqrt((-1/C/R+PL/C/D^2/E^2)^2-4/L/C))/2;
lamda2 = ((-1/C/R+PL/C/D^2/E^2) - sqrt((-1/C/R+PL/C/D^2/E^2)^2-4/L/C))/2;
plot(real(lamda1),imag(lamda1),'b*');
hold on;
plot(real(lamda2),imag(lamda2),'r*');
hold on;
line([0 0],[-300 300]); %y axis
line([-5 5],[0 0]);     %x axis
```

```
xlabel('Re({\lambda})'),ylabel('Im({\lambda})'),
end

%%%%%%%%%%%%%%DISCOVER OF LIMIT CYCLE%%%%%%%%%%%%%%%%%
%ON THE PHASE PORTRAIT, DRAW THREE CASES (ALL START FROM
%THE SAME INITIAL POINT( Close to EQUILIBRIUM)):
%FIRST SET  PL=P0-1 (INSIDE LIMIT CIRCLE);
%SECOND SET PL=P0+1 (OUTSIDE LIMIT CIRCLE);
%THIRD SET  PL=P0   (EXACTLY ON LIMIT CIRCLE);
R=100;
L=37.5e-3;
C=420e-6;
E=120;                  %supply voltage
D=0.5;                  %duty cycle
P0  = D^2*E^2/R;        %threshold load power
Veq = D*E;              %equilibrium or leading order voltage
Ieq = 1;%2*D*E/R;          %equilibrium or leading order ncurrent
t_start = 0;
t_end   = 20;

options=odeset('RelTol',1e-6,'AbsTol',1e-6);
%starting inside limit cycle
PL=P0-1;
[T,Y]=ode45(@buckode454,[t_start t_end],[Veq Ieq],options);

    plot(Y(:,1),Y(:,2),'Linewidth',1.5,'color', [12 188 242] ./ 255);
    xlabel('vc[V]'),ylabel('iL[A]');
    hold on;
%starting outside limit cycle
    PL=P0+1;
    [T,Y]=ode45(@buckode454,[t_start t_end],[Veq Ieq],options);
    plot(Y(:,1),Y(:,2),'Linewidth',1.5);
```

```
%starting on limit cycle
    PL=P0;
    [T,Y]=ode45(@buckode454,[t_start t_end],[Veq Ieq],options);
    plot(Y(:,1),Y(:,2),'Linewidth',1.5);

clc,clear;
%This perturbation soution is not for all the initial conditions, but
%only for V,I One is from the equilibrium, the other is from the edge of
%limit cycle
global R L C E PL D ;
%SYSTEM CONFIGURATIONS
R=100;
L=37.5e-3;
C=420e-6;
E=120;                                  %supply voltage
D=0.6;          %D affects much as well!! %duty cycle
P0=D^2*E^2/R;                           %threshold load power
PL=P0-1;                                %actual power supplied

%PERTURBATION RESULTS
omega   = sqrt(1/L/C);
epsilon = 1e-4;                         %perturbation coefficient
P2      = (PL-P0)/epsilon^2;            %power error
Veq     = D*E;                          %equilibrium or leading order voltage
Ieq     = 2*D*E/R;                      %equilibrium or leading order ncurrent
t_start = 0;
t_end   = 5;
t       = linspace(t_start,t_end,1e4);
r       = sqrt(-R*C/3/L*P2);            %amplitude of A

V1 = 2*omega*L*r*sin(omega*t);
I1 = 2*r*cos(omega*t);
```

```
V2 = -2*1i*r^2*L^3*omega^3/3/Veq/R*exp(2*1i*omega*t)+...
2*1i*r^2*L^3*omega^3/3/Veq/R*exp(-2*1i*omega*t);
I2 = r^2*L^2*omega^2/3/Veq/R*exp(2*1i*omega*t)+...
r^2*L^2*omega^2/3/Veq/R*exp(-2*1i*omega*t)+P2/Veq+2*r^2*L^2*omega^2/Veq/R;

V_pert = Veq+epsilon*V1+epsilon^2*V2;
I_pert = Ieq+epsilon*I1+epsilon^2*I2;

%%%%%%%%% time response by solving system odes %%%%%%%%%
options = odeset('RelTol',1e-5,'AbsTol',1e-5);
V_start_range = 2*omega*L*epsilon*r;
I_start_range = 2*epsilon*r;

%THE INITIAL CONDITION HAS TO BE STARTING FROM LIMIT CYCLE
V_start1 = Veq-V_start_range;
I_start1 = Ieq;
%OR (the four initial conditions have the same results)
% V_start2 = Veq+V_start_range; I_start2 = Ieq;
% V_start3 = Veq; I_start3 = Ieq-V_start_range;
% V_start4 = Veq; I_start4 = Ieq+V_start_range;

[T,Y]=ode45(@buckode454,[t_start t_end],[V_start1 I_start1],options);

%plots
figure(1)
subplot(2,1,1);
       plot(T,Y(:,1),'Linewidth',1.5);
       title('Time Responses'),xlabel('Time[s]'),ylabel('vc[V]'),grid on
       hold on;
       plot(t,V_pert,'Linewidth',1.5);
```

```
        legend('Exact Solution','Perturbation Solution');
        xlim([0 0.1]);
subplot(2,1,2);
        plot(T,Y(:,2),'Linewidth',1.5);
        xlabel('Time[s]'),ylabel('iL[A]'),grid on
        hold on;
        plot(t,I_pert,'Linewidth',1.5);
        legend('Exact Solution','Perturbation Solution')
        xlim([0 0.1]);
figure(2)
        plot(Y(:,1),Y(:,2),'r','Linewidth',1.5),grid on
        title('Phase Portrait'),xlabel('VC[V]'),ylabel('IL[A]')
        hold on;
        plot(V_pert, I_pert,'Linewidth',1.5)
        legend('Exact Solution','Perturbation Solution')

%the bigger PL-P0 is, the larger the size of the limit circle is
%the size of limit circle decides the initial condition range
```

Appendix B

Matlab Scripts For CHB (Simplified Model)

```
%%%%%%%%%%%%%%%%%%%%%%%%%%%%%%%%%%%%%%%%%%%%%%%%%%%%%%%%%%%%%%%%%%%%%%%%
%%Open Loop Modelling
global R L C r Vs m ;
%define the time span and switching frequency
t_start=0;   %simulating start time
t_end=1;     %simulating  end  time
f0 = 50;     %grid frequency
fs = 5e3;    %switching frequency 5kHz
Ts = 1/fs;   %swiching period 200us
t  = t_start:Ts:t_end-Ts;   %simulating time span

%define the system parameters
C = 5e-3;            %cell DC capacitance
R = 20;              %cell DC LOAD
L = 11.75e-3;         %grid inductance
r = 0.6;             %grid inductance ESR
As= 120*sqrt(2);     %grid voltage peak amplitude
```

```
omega=2*pi*f0;       %grid frequency in rad/s
M = 0.8;             %modulation index
S = As*sin(omega*t); %grid voltage
mi= M*sin(omega*t);  %modulaing signal

%initial values for the system
m(1) =0;
VC(1)=0;
IL(1)=0;

%solve 2 converter odes for defined time span
for k=1:((t_end-t_start)/Ts-1)
m  = mi(k);
Vs = S(k);
[T,X]=ode45(@converterode,[k*Ts (k+1)*Ts],[VC(k) IL(k)]);

VC(k+1)=X(end,1);
IL(k+1)=X(end,2);
end

%%%%%%%%%%%%%%%%%%%%%%%%%%%%%%%%%%%%%%%%%%%%%%%%%%%%%%%%%%%%%%%%%%%%%%%%%%%%
%% Converter ODEs
function dy = converterode(t,y)
global R L C r Vs m ;
dy = zeros(2,1);
dy(1) = (3*m*y(2) - y(1)/R)/C;
dy(2) = (Vs-m*y(1)-r*y(2))/L ;
end

%%%%%%%%%%%%%%%%%%%%%%%%%%%%%%%%%%%%%%%%%%%%%%%%%%%%%%%%%%%%%%%%%%%%%%%%%%%%
%% Function of system ODEs
 function dy = systemodes(t,y)
 global R L C r Sk mk Kp Ki Vref;
```

```
 dy = zeros(5,1); % a column vector
 dy(1) = (mk*y(4)-y(1))/R/C;
 dy(2) = (mk*y(4)-y(2))/R/C;
 dy(3) = (mk*y(4)-y(3))/R/C;
 dy(4) = (Sk-mk*(y(1)+y(2)+y(3)))/L-r*y(4)/L ;
 dy(5) = -Kp/C*(3*mk*y(4)-(y(1)+y(2)+y(3))/R)
         +Ki*(Vref-(y(1)+y(2)+y(3)));
 end

%%%%%%%%%%%%%%%%%%%%%%%%%%%%%%%%%%%%%%%%%%%%%%%%%%%%%%%%%%%%%%%%%%%%%%%%%%%
%% 7-Order Matrix Truncated Model
%system parameters
C = 5e-3;            %cell DC capacitance
R = 20;              %cell DC LOAD
L = 5e-3;            %grid inductance
r = 0.6;             %grid inductance ESR
Vs= 120*sqrt(2);     %grid voltage peak amplitude
omega=2*pi*50;       %grid frequency in rad/s
m1 = 0.4;            %modulation index
k=1;

for m1=[0.1,0.2,0.3,0.4,0.5,0.6,0.7,0.8,0.9]
M    =[ -m1/2 L*omega    r         m1/2      0         0          0;
       0        r      -L*omega    0    -m1/2        0          0;
       0        0        0       -m1/2      0       3*L*omega   r;
       0        0        0          0     m1/2       r        -3*L*omega;
       1/R      0       3*m1        0       0        0          0;
       0      3*m1/2     0     2*C*omega   1/R     -3*m1/2      0;
       0        0      -3*m1/2    1/R   -2*C*omega  3*m1/2      0];

a = [-Vs/2; 0; 0; 0; 0;0 ;0];
x = linsolve(M, a);
```

```
% results
V0 = x(1);
V2 = 2*sqrt(x(4)^2+x(5)^2);
I1 = 2*sqrt(x(2)^2+x(3)^2);
I3 = 2*sqrt(x(6)^2+x(7)^2);

V0_MATLAB(k)=V0;
V2_MATLAB(k)=V2;
I1_MATLAB(k)=I1;
I3_MATLAB(k)=I3;
k=k+1;
end

%%%%%%%%%%%%%%%%%%%%%%%%%%%%%%%%%%%%%%%%%%%%%%%%%%%%%%%%%%%%%%%%%%%%%%%
clear;clc;
global   C R L Ts  r  As Vref kp ki omega;
%define the time span and switching frequency
t_start=0;  %start time
t_end=5;  %end time
fs=5e3;   %switching frequency 5kHz
Ts=1/fs;   %swiching period 200us
t= t_start:Ts:t_end-Ts;   %time span

%define the system parameters
C=2e-3;
R=20;
L=11.75e-3;
omega=2*pi*50;
r=0.6;
As=120*sqrt(2);
```

```
%set the reference value for the total dc link voltage
Vref=300;
kp = 0.0166;           % proportional constant
ki = 0.374;            % proportional constant

%initial values for the system
VC(1)=0;
IL(1)=0;
u(1)=kp*(Vref-0);

[T,X]=ode45(@plant_bai,[t_start t_end],[VC(1) IL(1) u(1)]);
VC=X(:,1);
IL=X(:,2);
U =X(:,3);

subplot(2,1,1);
plot(T,VC,'Linewidth',1);
xlabel('Time[s]');
ylabel('Total DC voltage[V]');
grid on;
subplot(2,1,2);
plot(T,IL,'Linewidth',1);
ylabel('AC Current[A]');
xlabel('Time[s]');
grid on;

%%%%%%%%%%%%%%%%%%%%%%%%%%%%%%%%%%%%%%%%%%%%%%%%%%%%%%%%%%%%%%%%%%%%%%%%%%%%
function dy = plant_bai(t,y)
global R L C r As kp ki Vref Ts omega;
Vs = As*sin(omega*t);
m = 1/Vref*(Vs-r*y(2)-L/Ts*(y(3)*sin(omega*(t+Ts))-y(2)));
```

```
dy = zeros(3,1); % a column vector
dy(1) = (3*m*y(2) - y(1)/R)/C;
dy(2) = (Vs-m*y(1)-r*y(2))/L ;
dy(3) = -kp/C*(3*m*y(2)-y(1)/R)+ki*(Vref-y(1));
end

%%%%%%%%%%%%%%%%%%%%%%%%%%%%%%%%%%%%%%%%%%%%%%%%%%%%%%%%%%%%%%%%%%%
%%Algorithm of The Closed Loop
 global  S C R L Ts w r t_start t_end As Vref mk Sk Kp Ki;
 %define the time span and switching frequency
 t_start = 0;                    %start time
 t_end   = 1;                    %end time
 fs      = 5e3;                  %switching frequency 5kHz
 Ts      = 1/fs;                 %swiching period 200us
 t       = t_start:Ts:t_end-Ts;  %time span
 %define the system parameters
 C       = 2e-3;                %cell's DC capacitance Farads
 R1      = 20;                   %cell's DC resistance ohms
 L       = 11.75-3;               %AC input inductance Henri
 omega   = 2*pi*50;              %supply frequency, rad/s
 r       = 0.6;                 %supply series resistance ohms
 As      = 120*sqrt(2);          %peak of supply voltage
 S       = As*sin(w*t);
 %set the control parameters for the PI controller
 % of total dc link voltage control
 Vref    = 200;                  %reference value
 Kp      = 0.0166;                %proportional constant
 Ki      = 0.374;                 %integral constant
 %initial values for the system
 m(1)    = 0;
 Vc1(1)  = 0;
 Vc2(1)  = 0;
```

```
Vc3(1)  = 0;
IL(1)   = 0;
u(1)    = Kp*(Vref-(Vc1(1)+Vc2(1)+Vc3(1)));
%solve system odes and implement control
for k=1:((t_end-t_start)/Ts-1)
mk      = m(k);
Sk      = S(k);
[T,X]   = ode45(@systemodes,[0 k*Ts (k+1)*Ts],[Vc1(k) Vc2(k)
          Vc3(k) IL(k) u(k)]);
Vc1(k+1)= X(end,1);
Vc2(k+1)= X(end,2);
Vc3(k+1)= X(end,3);
IL(k+1) = X(end,4);
 u(k+1) = X(end,5);
Vc(k+1) = Vc1(k+1)+Vc2(k+1)+Vc3(k+1);
I_reference(k+1)=u(k+1)*sin(w*(k+1)*Ts);
m(k+1)  = (S(k+1)-L/Ts*(I_reference(k+1)-IL(k+1))-
           r*IL(k+1))/Vref;
end
plot(t,Vc,'r',t,IL,t,u,'Linewidth',2),grid on
title('closed loop control')

%%%%%%%%%%%%%%%%%%%%%%%%%%%%%%%%%%%%%%%%%%%%%%%%%%%%%%%%%%%%%%%%%%%%%%%
%% Algorithm of matrix A(t)
function dx = At(t,x)
global C R L w r Ts Kp Ki Vref As
u0=(As/Vref-sqrt(As^2/Vref^2-8*r/3/R))/(2*r/Vref);
iL=u0*exp(1i*w*Ts)/(1+1i*w*Ts);
%As_threshold=sqrt(8*r/3/R)*Vref;
Am=As/Vref-(r+L*1i*w)*u01*exp(1i*w*Ts)/
(1i*w*Ts+1)/Vref;
S2=-3*Am*iL/4/(C*w-1i/2/R);% equa 2)
```

```
 %u2=-(1i*w*Kp+Ki/2)*S2/1i/w;
 %U=u01-0.5*1i*u2*exp(2i*w*t)+0.5*1i*conj(u2)*exp(-2i*w*t);
 IL=-0.5*1i*iL*exp(1i*w*t)+0.5*1i*conj(iL)*exp(-1i*w*t);
 IL=real(IL);
 mk=-0.5*1i*Am*exp(1i*w*t)+0.5*1i*conj(Am)*exp(-1i*w*t);
 mk=real(mk);
 S=Vref+0.5/1i*S2*exp(2*1i*w*t)-0.5/1i*conj(S2)*exp(-2*1i*w*t);
 S=real(S);
 %solve the matrix as 3 odes
 dx = zeros(3,1);
 deltamk=1/Vref*(-r*x(2)-L/Ts*(x(3)*sin(w*(t+Ts))-x(2)));
 dx(1)=(3*mk*x(2)+3*deltamk*IL-1/R*x(1))/C;
 dx(2)=(-r*x(2)-mk*x(1)-deltamk*S)/L;
 dx(3)=-Kp/C*(3*mk*x(2)+3*deltamk*IL-1/R*x(1))-Ki*x(1);

%%%%%%%%%%%%%%%%%%%%%%%%%%%%%%%%%%%%%%%%%%%%%%%%%%%%%%%%%%%%%%%%%%%%%%%
%% Algorithm for Calculating the Eigenvalues
 clc;clear;
 global C R L w r Ts Kp Ki Vref As
 options = odeset('RelTol',1e-6,'AbsTol',1e-6);
 [T,X1] = ode45(@At,[0 0.02],[1 0 0],options); %a(T)
 [T,X2] = ode45(@At,[0 0.02],[0 1 0],options); %b(T)
 [T,X3] = ode45(@At,[0 0.02],[0 0 1],options); %c(T)
 format short
 xmat=[X1(end,:)' X2(end,:)' X3(end,:)'];  %monodromy matrix
 eiv=eig(xmat,'nobalance');
 eiv1=eiv(1);
 eiv2=eiv(2);
 eiv3=eiv(3);
```

Appendix C

Matlab Scripts of the Full Model

Parameters

```
% clc;clear;
global R L C r As Vref fs Ts omega phg rs Ls N;
global kp ki kp_pll ki_pll
global kp0 ki0 kp1 ki1 kp2 ki2 kp3 ki3 kp4 ki4 kp5 ki5 kp6 ki6 kp7 ki7
global kp8 ki8 kp9 ki9 kp10 ki10 kp11 ki11 kp12 ki12 kp13 ki13
global kp_pll0 ki_pll0 kp_pll1 ki_pll1 kp_pll2 ki_pll2 kp_pll3 ki_pll3
global kp_pll4 ki_pll4 kp_pll5 ki_pll5
%%%%%%%%%%%%%%%%%%%%%%%%%%% PLL %%%%%%%%%%%%%%%%%%%%%%%%%%%%%%%%%%%%
kp_pll0 = 9.2;
ki_pll0 = 422.3;

kp_pll1 = 47.1239;    %15Hz
ki_pll1 = 7.6926e3;

kp_pll2 = 62.8319;    %20Hz
ki_pll2 = 1.3676e4;
```

```
kp_pll3 = 78.5398;    %25Hz
ki_pll3 = 2.1368e4;

kp_pll4 = 94.2478;    %30Hz
ki_pll4 = 3.0770e4;

kp_pll5 = 109.9557;   %35Hz
ki_pll5 = 4.1882e4;

kp_pll6 = 125.6637;   %40Hz
ki_pll6 = 5.4703e4;

kp_pll7 = 141.3717;   %45Hz
ki_pll7 = 6.9233e4;

kp_pll8 = 157.0796;   %50Hz
ki_pll8 = 8.5473e4;

kp_pll9 = 172.7876;   %55Hz
ki_pll9 = 1.0342e5;

kp_pll10 = 188.4956;   %60Hz
ki_pll10 = 1.2308e5;

kp_pll11 = 204.2035;   %65Hz
ki_pll11 = 1.4445e5;

kp_pll12 = 219.9115;   %70Hz
ki_pll12 = 1.6753e5;

kp_pll13 = 235.6194;   %75Hz
```

```
ki_pll13 = 1.9231e5;

kp_pll14 = 251.3274;   %80Hz
ki_pll14 = 2.1881e5;

kp_pll15 = 282.7433;   %90Hz
ki_pll15 = 2.7693e5;

kp_pll16 = 314.1593;   %100Hz
ki_pll16 = 3.4189e5;

kp_pll   = kp_pll1;
ki_pll   = ki_pll1;

%%%%%%%%%%%%%%%%%%%%%%%% PI %%%%%%%%%%%%%%%%%%%%%%%%%%%%%%%%%%%%%%%%%\
kp0 = 0.0166;
ki0 = 0.374;

kp1 = 0.0170;     %15Hz
ki1 = 5.9138;

kp2 = 0.0275;     %20Hz
ki2 = 10.1643;

kp3 = 0.0379;     %25Hz
ki3 = 15.5545;

kp4 = 0.0484;     %30Hz
ki4 = 22.0844;

kp5 = 0.0589;     %35Hz
```

```
ki5 = 29.7539;

kp6 = 0.0631;     %37Hz
ki6 = 33.1408;

kp7 = 0.0693;     %40Hz
ki7 = 38.5630;

kp8 = 0.0903;     %50Hz
ki8 = 59.6002;

kp9 = 0.1112;     %60Hz
ki9 = 85.1959;

kp10 = 0.1322;    %70Hz
ki10 = 115.3503;

kp11 = 0.1531;     %80Hz
ki11 = 150.0632;

kp12 = 0.1741;     %90Hz
ki12 = 189.3347;

kp13 = 0.1950;     %100Hz  This won't work because PI plant is not valid until 100
ki13 = 233.1647;

kp   = kp3;
ki   = ki3;
%%%%%%%%%%%% OTHER CONFIGURATIONS %%%%%%%%%%%%%%%%%%%%%%%%%%%%%%%%%%%%%%%%%%%%
As   = 120*sqrt(2);
Vref = 200;
```

```
R    = 20;
C    = 2e-3;

L    = 1.153e-3;%3e-3;%10.8e-3;%;
r    = 0.6;

%%%%%%%%%%%GRID INDUCTANCE%%%%%%%%%%%%%%%%%%
% Ls=0e-3;
% rs=0;% keep resistance values fixed, their effects can be neglected

% Ls=1e-3;
% rs=0.4;

Ls  = 6e-3;
rs  = 0.8;
%%%%%%%%%%%%%%%%%%%%%%%%%%%%%%%%%%%%%%%%%%%%%%
fs=10e3;Ts=1/fs;
omega=2*pi*50;phg=0;
f0=50;T0=1/f0;

%%%%%%%%% device %%%%%%%%%%%%%%%%%%%%
```

```
fpga_clk=10e6;
uplim=fpga_clk/2/fs;
shift=uplim/2;

N=3;
```

seven_state_variables_average_model

```
global   C R L Ts r As kp ki omega Kp_pll Ki_pll Vc_ref phg;
%define the time span and switching frequency
f0=50;
t_start=0;   %start time
t_end=3;     %end time
fs=5e3;      %switching frequency 5kHz
Ts=1/fs;     %swiching period 200us
t= t_start:Ts:t_end-Ts;   %time span
phg=0;
%define the system parameters
C  = 2e-3;R = 20;L  = 11.75e-3;
omega= 2*pi*f0; r  = 0.6; As = 120*sqrt(2);

%DC link PI controller
Vc_ref = 200;
kp     = 0.0166;  %0.024358;
ki     = 0.374;   %1.0588;

%PLL configs
Kp_pll = 9.2;
Ki_pll = 422.3;
```

```
%initial values for the system
y1(1)= 0;y2(1)= 0;y3(1) = kp*(Vc_ref-0);
y4(1)=0; y5(1)=0;y6(1)=0;y7(1)=0;
%PI and plant
[T,Y]=ode45(@plant_ODE_continuous,[t_start t_end],[y1(1) y2(1) y3(1) y4(1)
 y5(1) y6(1) y7(1)]);
y1=Y(:,1);y2=Y(:,2);y3=Y(:,3);
y4=Y(:,4);y5=Y(:,5);y6=Y(:,6);
y7=Y(:,7);
```

ss_symbolic_seven

```
function dy = plant_ODE_continuous(t,y)
global R L C r kp ki Vc_ref Kp_pll Ki_pll m  omega As Ts phg;
Vs = As*sin(omega*t+phg);
Valpha=Vs;
i_L_ref1= y(3)*sin(y(6)+omega*Ts);
i_L_ref2=  y(3)*sin(y(6)+2*omega*Ts);
Vs_pk = sqrt(Vs^2+y(4)^2);
Vs_ref =  Vs_pk*sin(y(6)+omega*Ts);
%calculations
Vconv_ref = Vs_ref-L/2/Ts*(i_L_ref2-y(2))-r*i_L_ref1;
m = Vconv_ref/Vc_ref;
% if (m >1)
%     m =1;
% else if (m <-1)
%         m =-1;
%     end
% end
% m=1/Vc_ref*(As*sin(y(6)+omega*Ts)-L/2/Ts*(y(3)*sin(y(6)+2*omega*Ts)-y(2))
%-r*y(3)*sin(y(6))+omega*Ts);
dy = zeros(7,1); % a column vector
```

```
dy(1) = -y(1)/R/C+3*m*y(2)/C ;%plant
dy(2) = -m/L*y(1)-r/L*y(2)+Vs/L ;
dy(3) = (kp/C/R-ki)*y(1)-3*m*kp/C*y(2)+ki*Vc_ref;%PI
dy(4) = y(5);  %Vbeta%PLL
dy(5) = -omega^2*y(4)-omega*y(5)+omega^2*Vs;
dy(6) = y(7)+Kp_pll*cos(y(6))*Vs+Kp_pll*sin(y(6))*y(4);  %use vd to get angle
dy(7) = Ki_pll*cos(y(6))*Vs+Ki_pll*sin(y(6))*y(4);
end

clear;clc;
% THIS WORKS--THE METHOD FOUND TO SPEED UP WORKS
% syms m_1a m_1b I_L1a I_L1b U_0 V_C0 x_41a x_41b x_51a x_51b As C R L omega
% r Ts Vref N phg
% eqns = [m_1a*I_L1a+m_1b*I_L1b==2*V_C0/N/R
%        r*I_L1a-omega*L*I_L1b==As-m_1a*V_C0
%        r*I_L1b+omega*L*I_L1a==-m_1b*V_C0
%        V_C0==Vref
% (r-L/Ts)*I_L1a==As*cos(omega*Ts+phg)-m_1a*V_C0-L/Ts*U_0*cos(omega*Ts+phg)
% (r-L/Ts)*I_L1b==As*sin(omega*Ts+phg)-m_1b*V_C0-L/Ts*U_0*sin(omega*Ts+phg)
%        x_51a==-omega*x_41b
%        x_51b==omega*x_41a
%        -x_41b==As
%        x_41a==0
%    ];
% [m1az,m1bz,IL1az,IL1bz,U0z,VC0z,x_41az,x_41bz,x_51az,x_51bz] = solve(eqns,
 [m_1a,m_1b,I_L1a,I_L1b,U_0,V_C0,x_41a,x_41b,x_51a,x_51b])

%%%%%%% copy down the results%%%%%%%%%%%%
t_start=0;   %start time
t_end=2;     %end time
fs=5e3;      %switching frequency 5kHz
Ts=1/fs;     %swiching period 200us
```

```
t= t_start:Ts:t_end-Ts;   %time span
kp_pll = 9.2; ki_pll = 422.3; As = 120*sqrt(2);
kp  = 0.0166;   %0.024358;;
ki  = 0.374;   %1.0588;
R=20;C=2e-3;L=11.75e-3;r=0.6;Vref=200;
omega=2*pi*50;Ts=1/5000;phg =0;
V_S1=As; N=3;
m1a  = eval(m1az);
m1b  = eval(m1bz);
IL1a = eval(IL1az);
IL1b = eval(IL1bz);
U0   = eval(U0z);
VC0=Vref;
x_41a=0;x_41b=-As;
x_51a=As*omega;x_51b=0;
IL1=IL1a+1j*IL1b;
m1=m1a+1j*m1b;
VC2=-3*m1*IL1/4/(C*omega-1j/2/R);
x_41=x_41a+1j*x_41b;
x_51=x_51a+1j*x_51b;
x1=VC0*ones(size(t))+(VC2*exp(2j*omega*t)-conj(VC2)*exp(-2j*omega*t))/2j;
x2=(IL1*exp(1j*omega*t)-conj(IL1)*exp(-1j*omega*t))/2j;
x3=U0*ones(size(t));
x4=(x_41*exp(1j*omega*t)-conj(x_41)*exp(-1j*omega*t))/2j;
x5=(x_51*exp(1j*omega*t)-conj(x_51)*exp(-1j*omega*t))/2j;
m=(m1*exp(1j*omega*t)-conj(m1)*exp(-1j*omega*t))/2j;
x1=real(x1);x2=real(x2);x3=real(x3);m=real(m);
plot(t,x1,t,x2,t,x3,t,m);
```

```
%%%%%%%%%%%%%%%%%%%%%%%%%%%%%%%%%%%%%%%%%%%%%%%%%%%%%%%%%%%%%%%%%%%%%%%%%%%%
hold on;clear;
% clc;
global R L C r As kp ki Vref Ts omega kp_pll ki_pll phg N rs Ls;
%%%%%%%%%%%%PLL%%%%%%%%%%%%%%%%
kp_pll = 9.2;
ki_pll = 422.3;
As = 120*sqrt(2);
%%%%%%%%%%%%PI%%%%%%%%%%%%%%%%%
kp = 0.0166;
ki = 0.374;
R=20;
C=2e-3;
r=0.6;rs=0.4;% keep resistance values fixed, their effects can be neglected
L=10.35e-3;%1.153e-3
Ls=0;%10.75;

Vref=330;
fs=5e3;
omega=2*pi*60;Ts=1/fs;phg =0;
f0=50;T0=1/f0;N=3;

% for Ls=10e-3:0.1e-3:11e-3
% for Vref=300:10:350
options = odeset('RelTol',1e-4,'AbsTol',1e-4);
[T1,X1]=ode45(@seven_ss_weak,[0 0.02],[1 0 0 0 0 0 0],options);
[T2,X2]=ode45(@seven_ss_weak,[0 0.02],[0 1 0 0 0 0 0],options);
[T3,X3]=ode45(@seven_ss_weak,[0 0.02],[0 0 1 0 0 0 0],options);
[T4,X4]=ode45(@seven_ss_weak,[0 0.02],[0 0 0 1 0 0 0],options);
[T5,X5]=ode45(@seven_ss_weak,[0 0.02],[0 0 0 0 1 0 0],options);
[T6,X6]=ode45(@seven_ss_weak,[0 0.02],[0 0 0 0 0 1 0],options);
```

```
[T7,X7]=ode45(@seven_ss_weak,[0 0.02],[0 0 0 0 0 0 1],options);

ymat = [X1(end,:)' X2(end,:)'  X3(end,:)'  X4(end,:)'  X5(end,:)'
        X6(end,:)'  X7(end,:)' ];
eiv = eig(ymat)
% figure(2);
zgrid([],[]); %draws unit circle
hold on;
plot(real(eiv),imag(eiv),'bo','MarkerEdgeColor','b',...
               'MarkerFaceColor','b',...
                'MarkerSize',10,'Linewidth',2),grid on;
                title('eigenvalue 3');
              xlabel('Real({\lambda})','Fontsize',14)
              ,ylabel('Imag({\lambda})','Fontsize',14);
              grid on;
%     hold on;
% end
```